Studies on the Optimum Geometry for a Nuclear Resonance Fluorescence Detection System for Nuclear Security Applications

2014

HANI HUSSEIN NEGM

KYOTO UNIVERSITY

ABSTRACT

A non-destructive inspection of special nuclear materials (SNMs), such as ^{235}U and ^{239}Pu, is crucial to thwarting nuclear proliferation and terrorism in addition to securing the energy supply from nuclear fission in worldwide. The promise of the nuclear resonance fluorescence (NRF) as a non-destructive assay (NDA) technique in safeguard/homeland security applications lies in its potential to quantify directly a specific isotope in an assay target. In NRF measurements, nuclear resonances are excited by an external photon beam leading to the emission of γ-rays with specific energies, which are a fingerprint of the emitting isotope. The angular distribution of re-emitted photons is governed by the angular momenta of the states involved in the process. Moreover, the elastic and inelastic scattering of photons from atoms provide background for the detection of characteristic NRF γ-rays, whereas the physical properties of these scattering mechanisms cause the angular distribution of the background intensity. The detection of NRF γ-rays should to be a function of both the interrogating γ-beam energy spectrum and the geometry configuration of the detection system. The main challenge in NRF measurements achieving precise and accurate measurements lies in accruing sufficient counting statistics in a reasonable measurement time. Consequently, the optimization of the geometric configuration of the detector system for NRF measurements and the characteristic of the interrogating γ-ray beam are essential for the NDA of SNMs. In this work, we will establish the essential optimum condition to design an inspection system for the SNMs based on the NRF interaction. For the evaluation of the system, a Monte Carlo

radiation transport code (MCRT), GEANT4, has been developed to calculate the NRF reaction beside the atomic interactions. The physical processes due to the non-resonant photons, primarily Compton scattering, that contribute in the background of NRF measurements are described and investigated using a Monte Carlo simulation, the GEANT4 toolkit. The NRF is simulated with consideration of the angular distributions of resonance emissions, the effects of nuclear recoil, and thermal motion. As the result of simulation study we found that the measuring resonant emissions of the NRF reaction at backward angles (relative to the interrogation beam) yields less atomic scattering background and relatively high NRF yield with respect to the forward scattering angles.

The detection of NRF signals, which have a low yield, is required a detection system with a high efficiency and a good resolution. Thus, We are planning to use the $LaBr_3$:Ce detector as a unit structure in the detector array for an inspection of SNMs by NRF technique. The $LaBr_3$:Ce detector considerable a good candidate in nuclear applications due to the interesting scintillator properties, which have been reported on, compared to other conventional scintillators, such as energy resolution, decay time, material density and etc. The study on the energy response function (ERF) of $LaBr_3$:Ce detector especially in the energy range around 2 MeV is significantly important, in which the numerous of the excitation energies in the SNMs such as ^{235}U and ^{239}Pu are existing. The ERF of the $LaBr_3$:Ce detector was investigated and performed with a Monte Carlo simulation using GEANT4. The consideration for self-contamination is taken into account in the simulation, which was found within the $LaBr_3$:Ce detector at levels as high as

2.8 MeV, where the interested excitation energies of the SNMs are existing. As the result of simulation study of the ERF of the LaBr$_3$:Ce, the dominate radioactive isotopes in the background spectrum of LaBr$_3$:Ce originated from the meta-stable isotope [138]La over the energy region from 0 to ~ 1550 keV, which has an activity of 1.42 ± 0.12 Bq/cc, and the [227]Ac chain over the energy region from ~ 1600 to 2800 keV, which has an activity of 1.37 ± 0.08 × 10^{-2} Bq/cc. The activities of the minor contamination from the [226]Ra and [228]Th chains were 3.41 ± 0.24 × 10^{-4} and 2.2 ± 0.3 × 10^{-3} Bq/cc, respectively. In advanced, the ERF code is used to analysis the NRF spectrum of the [238]U that measured in the HIγS facility to addresses 8 NRF excitation levels for the [238]U around 2.5 MeV.

Because of, the attenuation and the self-absorption processes through the target for the incident γ-rays and the scatetring NRF γ-rays, an analytical model for the NRF reaction yield (NRF RY model) is deduced to optimize the detection system in terms of the target thickness. The NRF RY model is investigated for the scattering resonance emissions in all possible directions (backward, forward, and ninety-degree scattering angles) to calculate the expected yield of the NRF reaction and to interpreter the saturation of the NRF yield as a function of the target thickness that is expected from the simulation and the experimental results. In which, the two NRF experiments were conducted to study the target thickness dependence. The first one was carried out on the heavy material, [208]Pb, at relatively high energy (7.3 MeV), at the laser Compton backscattering (LCS) γ-ray beam line of the New-SUBARU at the SPRING-8 facility (Japan). The second NRF experiment was performed on a nuclear material [238]U at approximately 2.5 MeV, at the LCS γ-

ray line of the HIγS facility at Duke University (USA). Both of the two experiments were carried out for different target thicknesses. The validity of the NRF reaction yield model was verified by both results of the experiments on ^{208}Pb and ^{238}U. Moreover, the MC simulation using the developed code of the GEANT4 was performed for the NRF interaction of both of the experimental setups for a wide range of the target thicknesses. The simulation results have been validated by the experimental data as well, verified by the analytical model of the NRF reaction yield (NRF RY Model). The scattering NRF γ-rays were measured by both of the HPGe detectors and the LaBr$_3$:Ce detector array. In addition, we proposed a new technique to calculate the NRF cross-section based on the fitting of the saturation curve of the experimental data of the NRF yield with the target thickness by the NRF RY model. The proposed technique offers more accurate NRF cross-section than that from the absolute measurements, because the new method only need the relative measurements for different thickness target.

Furthermore, the MC simulation using GRANT4 was performed for the realistic inspection system for the highly enriched uranium (HEU) of 93% inside a standard 20' container. The detection system is based on the LaBr$_3$:Ce detector array at backward angle of 180° relative to the incident beam that consist of a 100 detector as 10 × 10 matrix with spacing 10 mm. The NRF excitation energy of 1733 keV for ^{235}U is selected. As the result of simulation study, the 100 detector of the LaBr$_3$:Ce could measure the NRF yield for a 1 kg of the HEU at 1.5 m from the target center with the incident energy spread (ΔE/E) 1% for the incident flux of 3.33 × 10^6 photon/sec over a 10 min .

ACKNOWLEDGMENTS

I would like to thank all who contributed to this work, especially my supervisor Prof. Hideaki Ohgaki for his guidance, support, and his valuable discussions, which brought this work to its current level. I have a great deal of gratitude and appreciation for him.

I would like to thank Prof. Yasuyuki Shirai and Prof. Kazunari Matsuda for their valuable comments and review of my dissertation.

I would like to thank the scientists of the Institute of Advanced Energy, Kyoto University, especially our lab staff, Prof. T. Kii, Dr. I. Daito, Dr. H. Zen, and Prof. K. Masuda, for their guidance and support during my study.

I would like to thank the scientists at the Japan Atomic Energy Agency (JAEA), mainly Dr. N. Kikuzawa for his guidance regarding the Monte Carlo simulation GEANT4, and Dr. T. Hayakawa, Dr. T. Shizuma, and Prof. R. Hajima for their discussion about the experimental and simulated results. I would like to express my thanks to Dr. I. Daito, Dr. T. Hayakawa, and Dr. T. Shizuma for helping me to achieve the NRF experiments at the New SUBARU facility and the HIγS facility. In addition, special thanks are due to the staff of the New SUBARU and the HIγS facility at Duke University for their help with performing the NRF experiments. I would also like to thank

ABBREVIATIONS LIST

CERN: The European Organization for Nuclear Research.

D-D: D-D neutrons generated.

DFELL: Duke Free Electron Laser Laboratory.

DNA: Delayed Neutron Analysis.

DSP: Digital Signal Processing module.

EM: ElectroMagnetic model.

ENSDF: Evaluated Nuclear Structure Data File.

ERF: Energy Response Function.

FEL: Free Electron Laser.

FWHM: Full Width at Half Maximum.

GEANT: GEneration ANd Tracking [In the late 1970s, at the beginning of GEANT1], GEometry ANd Tracking [Currently].

GEANT4:   A Monte Carlo software toolkit to simulate the passage of particles through matter.

GPS: General Particle Source.

HE: High Energy.

HEP: High Energy Physics.

HEU: Highly Enriched Uranium.

HIγS: High Intensity γ-ray Source.

HPGe: High Purity Germanium.

IAEA: International Atomic Energy Agency.

IEC: Inertial Electrostatic Confinement.

JAEA: Japan Atomic Energy Agency.

JST:	Japan Science and Technology.
KEK:	The High Energy Accelerator Research Organization, Japan.
KERMA:	Kinetic Energy Released to Matter (measuring transferred energy from radiation to matter).
KN:	Klein-Nishina.
LaBr$_3$:Ce:	Scintillator Detector.
LCS:	Laser Compton BackScattering.
LE:	Low Energy.
LINAC:	Linear Accelerator.
MC:	Monte Carlo.
MCA:	Multichannel Analyzer.
MCRT:	Monte Carlo Radiation Transport.
MoU:	Memorandum of Understanding.
NDA:	Non-Destructive Assay.
New-SUBARU:	The name of the synchrotron light source that was constructed at the SPring-8 site.
NRF:	Nuclear Resonance Fluorescence.
NRF RY Model:	NRF Reaction Yield Model.
OK:	Optical Klystron.
OO:	Object-Oriented.
PD:	Polarization Degree.
PMT:	Photo Multiplier Tube.
PSA:	Pulse Shape Analysis.
QM:	Quasi-Monochromatic.
R&D:	Research and Development.

RE: Reaction Events.

RTA: Real Time Analysis.

RY: Reaction Yield.

s/n: Signal-to-Noise.

SEMP: Standard ElectroMagnetic Processes.

SNIP: Statistics-sensitive Non-linear Iterative Peak-clipping.

SNMs: Special Nuclear Materials.

SPring-8:   Super Photon RING-8 GeV.

SR: Synchrotron Radiation.

TSB: Technical Steering Board.

TUNL: Triangle Universities Nuclear Laboratory.

WGPu: Weapons-Grade Plutonium.

WGU: Weapons-Grade Uranium.

XRF: X-ray Fluorescence.

CONTENTS

CHAPTER 1

Introduction

An overview of the nuclear power will be introduced. The great concern in the development of nuclear materials and the related applications is the possibility of smuggling special nuclear materials (SNMs) in large cargo containers with sufficient shielding by lead, which presents a dire scenario for world commercial flow. Efforts around the world have been made to develop inspection systems against this threat. The potential of nuclear resonance fluorescence (NRF) as a tool for the inspection system of the SNMs is presented. The objective and an overview of this dissertation are introduced in the last section.

7.3 Nuclear Power Overview

Nuclear power continues to play an important role in global clean electricity production despite the accident at the Fukushima Daiichi Nuclear Power Plant in 2011. The total nuclear power capacity was slightly lower than in previous years due to the permanent shutdown of 13 reactors in 2011, including 8 in Germany and 4 in Japan, in the wake of the accident. However,

there were 7 new grid connections compared to 5 in 2010, 2 in 2009 and none in 2008 [1]. At the same time, in 2012, nuclear power global generating capacity grew to 372.1 GW(e) with 437 reactors in operation at the end of 2013. Three new reactors were connected to the grid, and two reactors that had been in 'long-term shutdown' were restarted. Only 3 reactors were permanently shut down in 2012 compared with 13 in 2011 [2].

Current Nuclear Power Plants use low enriched ^{235}U fuels. However, there were tons of stocks of weapon-grade ^{235}U materials in the world. The Atomic Energy Act of 1954 defined ^{235}U and ^{239}Pu as Special Nuclear Materials (SNMs) [3]. The element ^{235}U enriched to 20% was defined as Highly Enriched Uranium (HEU); ^{235}U enriched to 90% is usually used in nuclear weapons, therefore they are sometimes called as weapon-grade ^{235}U (WGU). However, in this thesis we simply call "HEU" includes weapon-grade ^{235}U. In addition, ^{239}Pu with a concentration of 93% is used in weapons-grade plutonium (WGPu) [4]. One unit of a nuclear weapon can be produced with approximately 26 kg of HEU or ~ 5 kg of WGPu [4].

Terrorist attacks have become a serious threat, and this threat continues to grow, especially after the attack on the World Trade Center in the USA. Attempts can be made to load SNMs (HEU and WGPu), radioactive materials, or/and explosives materials onto various forms of transport to other destinations, including aircrafts and ships, in a concealed manner among personal baggage or hidden in a cargo container. The international smuggling of weapons grade nuclear material presents significant security challenges. The International Atomic Energy Agency (IAEA) reported that

182 confirmed incidents involved nuclear material, with 18 incidents involving HEU or WGPu between January 1993 and December 2003 [5]. However, the practical implementation of a 100%-accurate security screening for SNMs and explosive contents in the cargo containers at seaports may be impossible because of the sheer number of containers, by using current means of the imaging systems Moreover in the fact they are unable to identify the isotopic compositions of the materials.

In addition, HEU has considerably stronger properties of self-shielding for passive detection because of its high density and relatively low radiation energy, 185 keV in ^{235}U. Where, the thickness of HEU that attenuates a given type of radiation by a factor of ten is approximately 3 mm, and the smallest size of HEU that can be used for an explosion is approximately 10 to 38 cm in diameter [4]. Besides, the neutron emission from the natural fission of ^{235}U is also a negligible ~ 0.006 n/s per kg [6,7].

Efforts are being made to find accurate, efficient, and practical ways to prevent smuggling of SNMs. In addition, these potential threats encourage many laboratories around the world to develop inspection systems for hidden SNMs. The utilization of bremsstrahlung γ-rays [8,9] and neutrons [10,11] as probes for measuring the isotopic composition of heavily shielded materials has been demonstrated. However, further developments are needed to construct a practical inspection system. The bremsstrahlung γ-rays generally produce a large background noise and cause low signal-to-noise (S/N) ratio in measured spectrum because of their wide spread nature of energy spectrum. On the other hand, the neutron multiple scattering inside

the materials leads to difficulty to distinguish with probe neutrons and induced neutrons. Recently, Pruet *et al*. proposed the novel nondestructive detection method for [235]U concealed in a cargo transporter of using laser Compton scattering (LCS) γ-rays [12]. The LCS γ-ray source belongs to a new class of machines that produce energy-tunable, monochromatic γ-rays by the scattering of short-duration laser pulses from relativistic electrons [13-15]. This process is known as Thomson or inverse Compton scattering and produces γ-rays pulses that have beam-like characteristics and exhibit exceptional brightness or high photon density.

Under the "Research and Development (R&D) for the Implementation of the Anti-Crime and Anti-Terrorism Technologies for a Safe and Secure Society" that is being promoted by the Japan Science and Technology (JST) Agency, we have been developing an active non-destructive inspection system to detect the hidden nuclear material in a cargo container at the seaports [16-18]. This system is based on a hybrid technique between a neutron and gamma, which consists of a fast pre-screening using D-D neutrons generated by an inertial electrostatic confinement (IEC) device [19,20] and a post-screening based on NRF using quasi-monochromatic γ-rays generated by LCS because of its high selectivity and high penetration of the shielding.

7.4 Potential of NRF for the SNMs Inspection

NRF technique has been introduced as a powerful tool to identify the isotopic composition of material based on nuclear energy levels. NRF is a

phenomenon in which a photon of an appropriate energy excites a nucleus to a higher state, which subsequently decays to the ground state or a lower-lying state by emitting a γ-ray with an energy equal to the energy difference between the resonance state and the lower state [21,22]. The relative simplicity of the interaction in the NRF experiment can yield the following spectroscopic information: level excitation energy, E_i, integrated NRF cross-section, I_s, spin of the transition state, J, state parity, π, transition width ratio, Γ_0^2/Γ, and reduced excitation probabilities, Γ_0. Because of the uniqueness of the resonance energies, these resonance photons can be used as signatures for isotope identification. Thus, NRF is able to measure the isotopic content for any element with an atomic number greater than that of helium. NRF may be useful to identify threats such as conventional explosives, SNM, toxic materials, and chemical weapons. Bertozzi has pursued the application of NRF for homeland security applications [8,9]. His approach involves exposing materials to an intense photon beam with a continuous energy distribution and detecting the emitted resonance photons unique to each isotope.

In addition, the NRF measurements have advantages in light of the LCS γ-ray source. For instance, the LCS γ-ray source can produce energy-tunable, monochromatic, and polarized γ-rays by the scattering of lasers from relativistic electrons. The NRF using the LCS γ-ray source has certain merits; at first the elemental and isotopic composition of materials can be determined through heavy shields such as thick iron plates [23] because the energies of the LCS γ-rays are of the order of MeV. Second, the scattering NRF γ-rays can be measured with a high S/N ratio because the LCS γ-ray source can produce

5

a quasi-monochromatic photon beam. Third, a 100% linear polarized γ-ray beam can be generated, which causes the angle distribution for the scattering NRF γ-rays. With NRF measurements, we can obtain a unique fingerprint of each nuclide because the energies of the states excited by NRF are a function of the atomic number and mass of the nuclide of interest. However, the drawback of the NRF is its very small cross-section, in order of μb. Therefore, to utilize the LCS γ-ray for the active probe of the inspection of hidden special nuclear materials (SNMs) [23], a well-designed detection system is indispensable. For this purpose, a numerical simulation code, which can treat the NRF, is required to assist the design work. In addition, the angular distribution of outgoing γ-rays depends upon the mode of the photon reaction as well as polarization axis of the incident LCS γ-ray beams. As well the thickness dependence of SNM target should be examined, because a certain amount of SNM material, which should cause strong attenuation in and out going γ-rays, is required to construct hazardous matter.

7.5 Objectives and Thesis Overview

This thesis research addresses the challenges in the detection of hidden SNMs in cargo containers for homeland security applications. The work focuses on photon interrogation techniques based on NRF interaction whereby resonance photons are collected. Specifically, we are primarily interested in the NRF calculations by the Monte Carlo simulation using Geant4 to optimize the detection system for SNMs. In addition, there is an analytical calculation for the reaction yield of the NRF scattering γ-rays in terms of the target thickness. Furthermore, the challenges of measuring the

NRF γ-rays using the scintillator detector, namely, the LaBr$_3$:Ce, have been addressed after studying the energy response function (ERF) of the LaBr$_3$:Ce detector including its internal activities. Measuring the NRF excitation levels of the ^{238}U was performed with the HPGe detector and LaBr$_3$:Ce detector array. The LaBr$_3$:Ce could be a good candidate after developing an analysis code including the ERF. In addition to measuring the excitation levels for nuclear material, we observed 11 transitions of the NRF line from the ^{238}U, and four of them are newly detected. In addition, the NRF cross-sections for the NRF excitation levels of ^{238}U were calculated by the common method with the absolute values of the incident γ-ray beam, detection efficiency, and the effective angular distribution of the scattering NRF γ-rays. Moreover, we have proposed a new method to calculate the NRF cross-section of the excitation levels based on fitting the experimental data of the NRF yield with the target thickness. The method could be an improvement the accuracy of the NRF cross-sections because this method did not require the absolute measurements of the effective incident flux in the resonant window, the detection efficiency of the detection system that depends on the geometry complications of the measuring system, and the effective angular distribution of the scattering NRF γ-rays. On the other hand, apart from these features that could minimize the uncertainty in the NRF cross-sections for the transition states, our method precisely addresses the attenuation component and the self-absorption of the NRF γ-rays, which depend on the NRF absorption cross section.

In the first chapter, an overview of the nuclear power and technology is presented that is concerned with the nuclear materials and the radioactive

isotope. Then, the potential and the merits of NRF as a tool for addressing the SNMs are introduced as a powerful technique for isotopic identification, whereby the NRF is considered as a fingerprint of the isotope. In this chapter, we also depicted the motivation and purpose of this thesis.

Chapter two is aimed to present the photon interaction processes that are related by the NRF interaction and its detection as well that are necessary for photon transport calculations. Because measuring NRF γ-rays includes the scattering of the non-resonant photons due to the elastic and inelastic interactions, the processes are introduced with the corresponding cross-sections. As well, the NRF interaction with its cross-section and angular distribution is presented.

Chapter three is aimed to study the optimum geometry configuration of the inspection system. In this regard, we introduce an overview of the MC simulation toolkit GEANT4. Then, the atomic scattering calculations specific to the Compton scattering to minimize the count rate in the detection system, which came from the scattering Compton photons and the recoil charged particles of the electrons, are addressed. The optimization of the geometric detection system for the atomic and the NRF scattering γ-rays was analyzed using the MC simulation toolkit Geant4. In this chapter, we will demonstrate that the non-resonant photons scatter for the most part in the forward direction (small scattering angles) relative to the interrogating beam, while; at large angles, the intensity and energy are reduced. Moreover, the resonant photons of the scattering NRF γ-rays are for the most part scattered in backward than forward directions – relative to the interrogating beam. This

trend indicates that the detection of the scattering NRF γ-rays would be better at large scattering angles (backward) relative to the interrogation beam.

An analytical model for the NRF interaction is introduced in chapter four in order to study the target thickness dependence on the NRF reaction yield. The model is based on the attenuation of the incident γ-rays prior to an emission of the NRF γ-rays and the self-absorption of the scattering NRF γ-rays before leaving the target material. Moreover, the relationship between the effective length for the NRF interaction and the attenuation length of the γ-rays through the target material was deduced. The NRF yield equation for the thick and thin target was deduced in all possible scattering angles (forward, backward, and ninety degree).

In Chapter five, the energy response function (ERF) of the recently developed scintillator of the LaBr$_3$:Ce detector will be introduced in order to assessment the response function of the LaBr$_3$:Ce and the contamination of the self-activity within the detector. In advanced, the ERF code will be used to analysis the NRF spectra. The self-activities of the LaBr$_3$:Ce detector were taken into account, which originate from the meta-stable isotope of the ^{138}La and the ^{227}Ac-decay chain. The LaBr$_3$:Ce detector has been introduced with attractive scintillation properties amongst the others in terms of the energy resolution and material density, decay time and so on. The LaBr$_3$:Ce detector with an energy response function code would be a good candidate for use in the interrogation systems for the SNMs in addition to the HPGe detectors.

To study the target thickness dependence on the NRF reaction yield, the NRF measurements on the depleted uranium (DU) and lead targets were

presented in chapter six. In addition to the experimental measurements, the MC simulation was used to extend the results for a wide range of the target thickness to better understand the NRF yield behavior. To interpret the experimental results, the NRF reaction yield model was introduced in addition to both of the experimental and simulation results to reproduce and fit the data. Based on the experimental data and the NRF RY model, we proposed the new method to determine the NRF cross-section without absolute measurements, which is needed in the common method. In addition, the NRF RY was studied with different target thicknesses of the DU and natural lead.

Finally, the summary and the conclusion of this work will be presented in chapter 7. As well, the realistic simulation for the inspection system for the SNMs has been achieved. The simulation was performed on the 1 kg of the HEU within the standard 20′ container with a detector array of the 100 LaBr$_3$:Ce detector. The different detector size is calculated for the detector array. In addition, different incident energy spread is simulated. The simulation results shows the ability of the LaBr$_3$:Ce array detector to measure the scattering NRF γ-rays.

CHAPTER 2

Photon Interactions and Cross-Sections

The physical process of the photon interaction with materials can be divided into absorption and scattering due to interactions with atomic electrons or with nuclear material. The scattering process is the main process in the nuclear resonance fluorescence for materials assay, due to its contribution in the background spectrum of the NRF and significant effect on the s/n ratio. In this chapter, the physics are discussed in the context of the non-destructive assay measurements and calculations using NRF. The chapter begins by describing the photo-atomic absorption, scattering, and pair production that are necessary for photon transport calculations, together with the related cross-section data. Thereafter, the photonuclear scattering process, NRF, is discussed. Note that many parts of the atomic interactions in this chapter are based on these references [24- 30].

Classification of Photon Interactions

The interaction of photons with matter can be classified according to:

2. The type of target, *e.g.*, electrons, atoms, or nuclei, with which the photons interact, and

3. The type of event, e.g., scattering, absorption, pair production, *etc.*, that takes place.

The classifications of the photon interaction with matter based on the absorption and scattering of the electronic or nuclear component are presented in Table 2.1 [31]. The most important interactions for photons are:

o The photoelectric effect, σ_{pe},

o Compton scattering, σ_{CS}, and,

o Electron-positron pair production, σ_{pair}.

Rayleigh scattering, σ_R, is usually of minor importance for the broad beam conditions typically found in shielding but must be known (as data files for the radiation transport simulation code) for the interaction of the attenuation coefficient data.

The photonuclear effect, $\sigma_{ph.n}$, is for the most part restricted to the region of the giant resonance at approximately 10 to 30 MeV, at which, at the resonance peak, it may amount to as much as 10 percent of the total "electronic" cross-section. Elastic nuclear scattering, inelastic nuclear scattering and Delbrück scattering are negligible processes in photon interaction spectroscopy. Elastic nuclear scattering is regarded as a nuclear analog to very low energy Compton scattering by an electron. In this process, a photon interacts with a nucleon in such a manner that a photon is re-emitted with the same energy.

Table 2.1

Classification of elementary photon interaction with atomic electrons, nucleus, or the surrounding electric field of them.

Type of Interaction / Interaction with:	Absorption	Scattering	
		Elastic (coherent)	Inelastic (Incoherent)
Atomic electrons	Photoelectric effect $\sigma_{pe} \begin{cases} \sim Z^4\,(LE) \\ \sim Z^5\,(HE) \end{cases}$	*Rayleigh scattering* $\sigma_R \sim Z^2\,(LE)$	*Compton scattering* $\sigma_{CS} \sim Z$
Nucleus	Photonuclear reactions (γ,n), (γ,p), Photo-fission, *etc.* $\sigma_{ph.n} \sim Z$	Elastic nuclear scattering $(\gamma,\gamma) \sim Z^2$ *Nuclear Thomson scattering*	Inelastic nuclear scattering (γ,γ') *Nuclear resonance* $\sim NRF$
Electric field surrounding charged particles	Electron-positron pair production in field of nucleus, $\sigma_{pair} \sim Z^2$ $(h\nu \geq 1.02\ MeV)$ Electron-positron pair production in electron field, $\sigma_{trip} \sim Z^2$ $(h\nu \geq 2.04\ MeV)$ Nucleon-antinucleon pair production $(h\nu \geq 3\ GeV)$	Delbrück scattering	
Mesons	Photo-meson production, $(h\nu \geq 150\ MeV)$	Modified (γ,γ)	

During inelastic nuclear scattering, the nucleus is raised to an excited level by absorbing a photon. The excited nucleus subsequently de-excites by emitting a photon of equal or lower energy. The phenomenon of photon scattering by the Coulomb field of a nucleus is called Delbrück scattering (also nuclear potential scattering). It can be thought of as virtual pair production in the field of the nucleus – that is, pair production followed by annihilation of the created pair.

We should mention here our interest in the energy in the 2 MeV region for the scattering NRF γ-rays and the relevant process in this energy range, which includes many excitation levels in the SNMs such as ^{235}U and ^{239}Pu. Therefore, the processes of interest should be mainly the photoelectric effect, Compton scattering, pair production, and the discrete NRF transitions in this region.

o **Photoelectric Effect**

The photoelectric effect was reviewed historically by Hubbell in NSRDS-NBS 29 [24]. In the atomic photoeffect, a photon disappears, and an electron is ejected from an atom. The photo-electron carries the energy of the absorbed photon subtracted from the binding energy. The *K*-shell electrons are the most tightly bound and are the most important contributions to the atomic photoeffect cross-section in most cases. However, if the photon energy drops below the binding energy of a given shell, an electron from that shell cannot be ejected. Hence, particularly for medium- and high-Z elements, a plot of σ_{pe} versus the photon energy exhibits the characteristic saw-tooth

absorption edges, as displayed in Fig. 2.4, because the binding energy of each electron subshell is attained, and this process is permitted to occur. The order of magnitude of the photoelectric atomic-absorption cross-section is:

$$\sigma_{pe} \begin{cases} \sim Z^4/(hv)^3 & \Rightarrow \quad \{Low\ Energy\ (LE)\} \\ \sim Z^5/hv & \Rightarrow \quad \{High\ Energy\ (HE)\} \end{cases} \tag{2.1}$$

o **Compton Scattering**

In Compton scattering, a photon collides with an electron, loses some of its energy and is deflected from its original direction of travel (Fig. 2.1). The basic theory of this effect, assuming the electron to be initially free and at rest, is described well by Klein and Nishina [32].
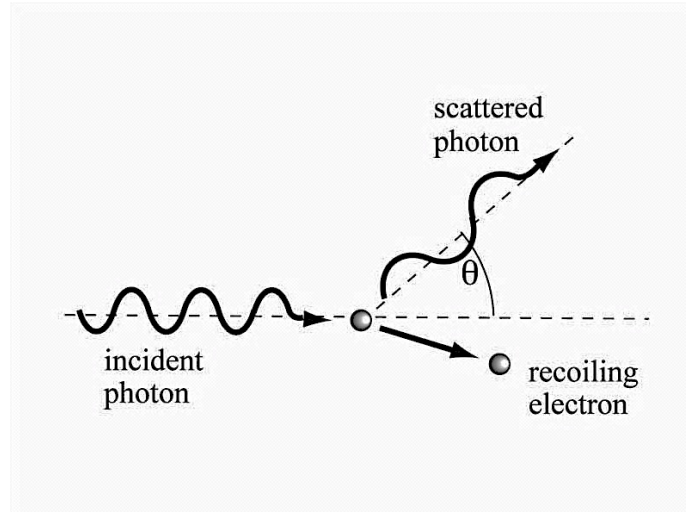
Fig. 2.1: *Compton scattering with a free electron at rest.*

The relation between photon deflection and energy loss for Compton scattering is determined from the conservation of momentum and energy between the photon and the recoiling electron. This relation can be expressed

as:

$$E_s = \frac{E_0}{1+\left(E_0/m_e c^2\right)\left(1-\cos\theta\right)}, \tag{2.2}$$

$$E_r = E_0 - E_s = E\frac{\left(E/m_e c^2\right)\left(1-\cos\theta\right)}{1+\left(E/m_e c^2\right)\left(1-\cos\theta\right)} \tag{2.3}$$

where E_0 is the energy of the incident photon, E_s is the energy of the scattered photon, E_r is the energy of the recoil electron, m_e is the rest mass of an electron, and c is the speed of light. The relation between the photon scattering angle, θ, and the electron recoil angle, φ, is deduced as

$$\tan\varphi = \frac{1}{1+\left(E_0/m_e c^2\right)}\cot\left(\frac{\theta}{2}\right). \tag{2.4}$$

For un-polarized photons, the differential cross-section for the Compton scattering or the Klein-Nishina angular distribution function per steradian of solid angle Ω can be calculated using:

$$\frac{d\sigma_{cs}^{KN}(\theta)}{d\Omega} = \frac{r_0^2}{2}\frac{1+\cos^2\theta}{\left[1+E_s\left(1-\cos\theta\right)\right]^2}\left[1+\frac{E_s^2\left(1-\cos\theta\right)^2}{\left(1+\cos^2\theta\right)\left[1+E_s\left(1-\cos\theta\right)\right]}\right]$$

$$= \frac{r_0^2}{2}\left(\frac{k}{k_0}\right)^2\left(\frac{k}{k_0}+\frac{k_0}{k}-\sin^2\theta\right) \qquad \left(cm^2 sr^{-1} electron^{-1}\right), \tag{2.5}$$

where $k_0 = \frac{E_0}{m_e c^2}$, and, $k = \frac{E_s}{m_e c^2}$,

where r_0 is the classical electron radius. This angular distribution is displayed in Fig. 2.2 [33].
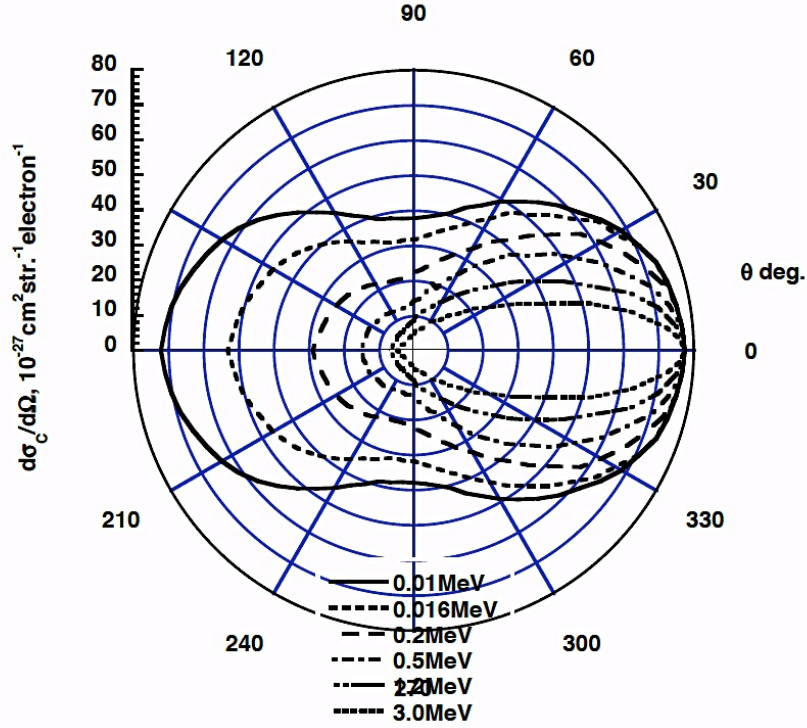
Fig 2.2: *Differential cross-section of Compton scattering [33].*

The classical electron radius, also known as the Lorentz radius or the Thomson scattering length, is based on a classical (*i.e.*, non-quantum) relativistic model of the electron. According to modern research, the electron is assumed to be a point particle with a point charge and no spatial extent [34]. However, the classical electron radius is calculated as:

$$r_e = \frac{1}{4\pi\varepsilon_0} \frac{e^2}{m_e c^2} = 2.8179403267(27) \times 10^{-15} \, m \tag{2.6}$$

where e is the electric charge and ε_0 is the permittivity of free space [35].

Integration of Eq. (2.6) over all angles gives the total Klein-Nishina (KN) cross-section,

17

$$\sigma_{cs}^{KN} = 2\pi r_0^2 \left\{ \frac{1+k}{k^2} \left[\frac{2(1+k)}{1+2k} - \frac{\ln(1+2k)}{k} \right] + \frac{\ln(1+2k)}{2k} - \frac{1+3k}{(1+2k)^2} \right\} \tag{2.7}$$

$$\left(cm^2 electron^{-1} \right)$$

This equation is plotted for a wide range of E in Fig 2.3. We should note that this graph for a free electron and the Compton scattering cross-section differs when the scattering material is comprised of atoms containing bound electrons.

Polarization Effects

Linear polarization is important in low-energy photon transport because photons are linearly polarized in scattering; further, the Compton and Rayleigh scattering of linearly polarized photons are anisotropic in their azimuthal distributions in the low-energy region. For linearly polarized photons with a free electron, the Klein-Nishina angular distribution function per steradian of solid angle is [32]

$$\frac{d\sigma_{cs}^{KN}}{d\Omega} = \frac{r_0^2}{4} \left(\frac{k}{k_0} \right)^2 \left(\frac{k}{k_0} + \frac{k_0}{k} + 4\cos^2\Theta - 2 \right) \tag{2.8}$$

Here, Θ is the angle between the incident polarization vector ($\vec{e}_0$) and the scattered polarization vector ($\vec{e}$). According to Heitler [36], two directions are considered for $\vec{e}$, i.e., $\vec{e}$ either in the same plane as $\vec{e}_0$ ($\vec{e}_\parallel$) or perpendicular to $\vec{e}_0$ ($\vec{e}_\perp$). The elastic scattering of a photon by one electron is called Thomson scattering. The Thomson-scattering cross-section per electron for a linearly polarized photon is [37]

$$\frac{d\sigma_T}{d\Omega} = r_0^2 \cos^2\Theta \tag{2.9}$$
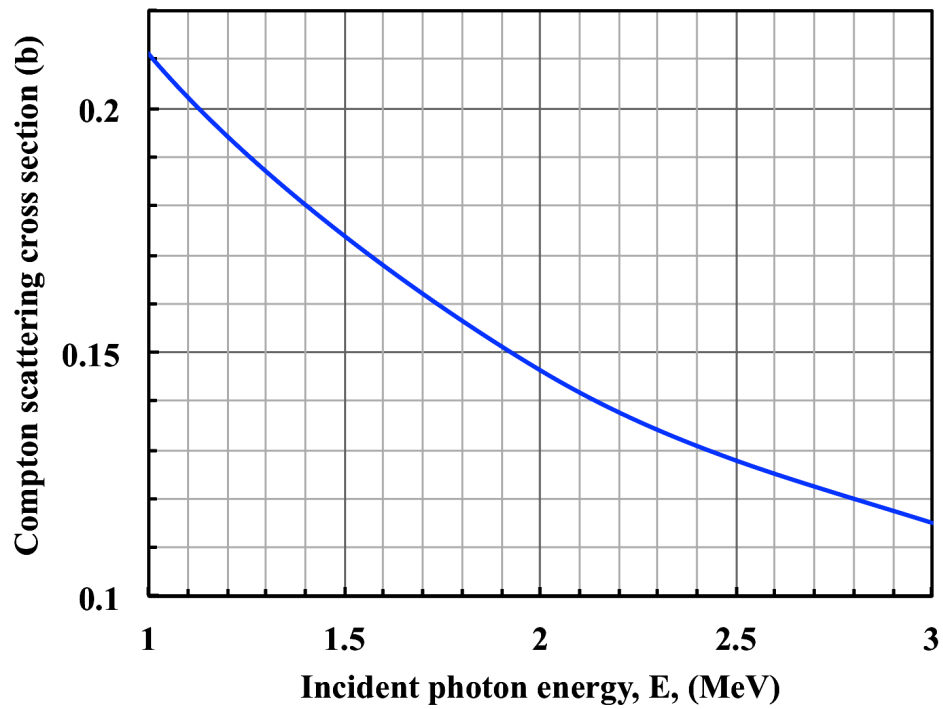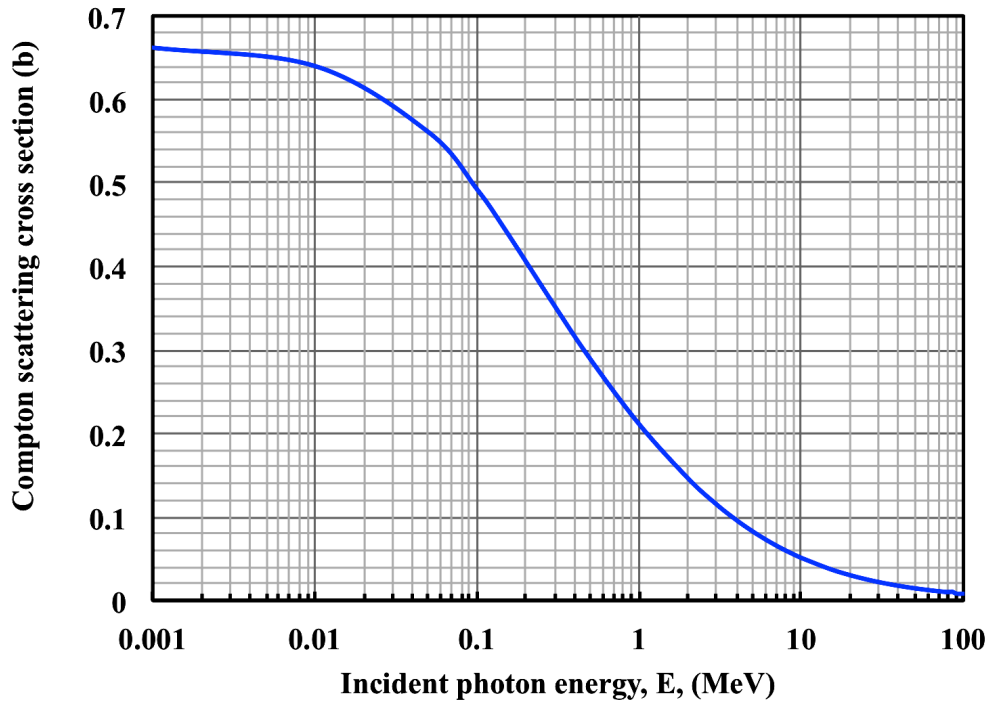
Fig 2.3: *Compton scattering cross section vs. incident photon energy for photons incident upon a single free electron. The upper values for a wide energy range from 1 keV to 100 MeV. The lower graph for the interested energy region is approximately 2 MeV.*

o **Rayleigh Scattering**

Rayleigh scattering is a process by which photons are scattered by bound atomic electrons and in which the atom is neither ionized nor excited. This process occurs for the most part at low energies and for high-Z material, in the same region in which electron-binding effects influence the Compton-scattering cross section. In practice, it is necessary to consider the charge distribution of all electrons at once. This can be done approximately through the use of an "atomic form factor", $F(q,Z)$, based on the Thomas-Fermi, Hartree, or other models of the atom. The square of this form factor, $[F(q,Z)]^2$, is the probability that the Z electrons of an atom take up the recoil momentum, q, without absorbing any energy. In this process, q is well represented by the following equation because it is assumed that $k_0 - k = 0$:

$$q = 2k\sin\frac{\theta}{2}. \tag{2.10}$$

The differential Rayleigh scattering cross-section for un-polarized photons is

$$\frac{d\sigma_R(\theta)}{d\Omega} = \frac{r_0^2}{2}\left(1+\cos^2\theta\right)\left[F(q,Z)\right]^2 \qquad \left(cm^2 sr^{-1} atom^{-1}\right). \tag{2.11}$$

o **Electron-Positron Pair Production**

In this effect, which is the most likely photon interaction at high energies, a photon disappears in the field of a charged particle, and an electron-positron pair appears. For the reaction $M_1 + M_2 \rightarrow M_3 + M_4 + M_5 + Q$, it can be demonstrated from the conservation of energy and momentum that

the threshold energy for the reaction in laboratory system is

$$T_{th}^{lab} = \frac{Q}{2M_2 c^2} \left[Q - 2\left(M_1 c^2 + M_1 c^2 \right) \right] \tag{2.12}$$

when M_2 is at rest. In a pair-production reaction ($\gamma + M \rightarrow M + m_e + m_e + Q$),

$$M_1 = 0$$
$$M_2 = M_3 = M,$$
$$M_4 = M_5 = m_e$$

so that:

$$Q = 2m_e c^2 \left(-T_{th}^{CM} \right) \tag{2.13}$$

and

$$T_{thh}^{lab} = \frac{2m_e c^2 \left(2m_e c^2 + Mc^2 \right)}{Mc^2} \tag{2.14}$$

Thus:

- Pair production in the field of a nucleus of mass M $\left(M \gg m_e c^2 \right)$:

$$T_{th}^{lab} = \frac{2m_e c^2}{Mc^2} \left(Mc^2 \right) = 2m_e c^2 = 1.022 \ MeV \tag{2.15}$$

- Pair production in the field of an electron $\left(M = m_e \right)$:

$$T_{th}^{lab} = \frac{2m_e c^2}{m_e c^2} \left(m_e c^2 + m_e c^2 \right) = 4m_e c^2 = 2.044 \ MeV \tag{2.16}$$

The cross-section σ_n for pair production in the field of a nucleus varies as

$$\sigma_n \sim Z^2. \tag{2.17}$$

For low photon energies,
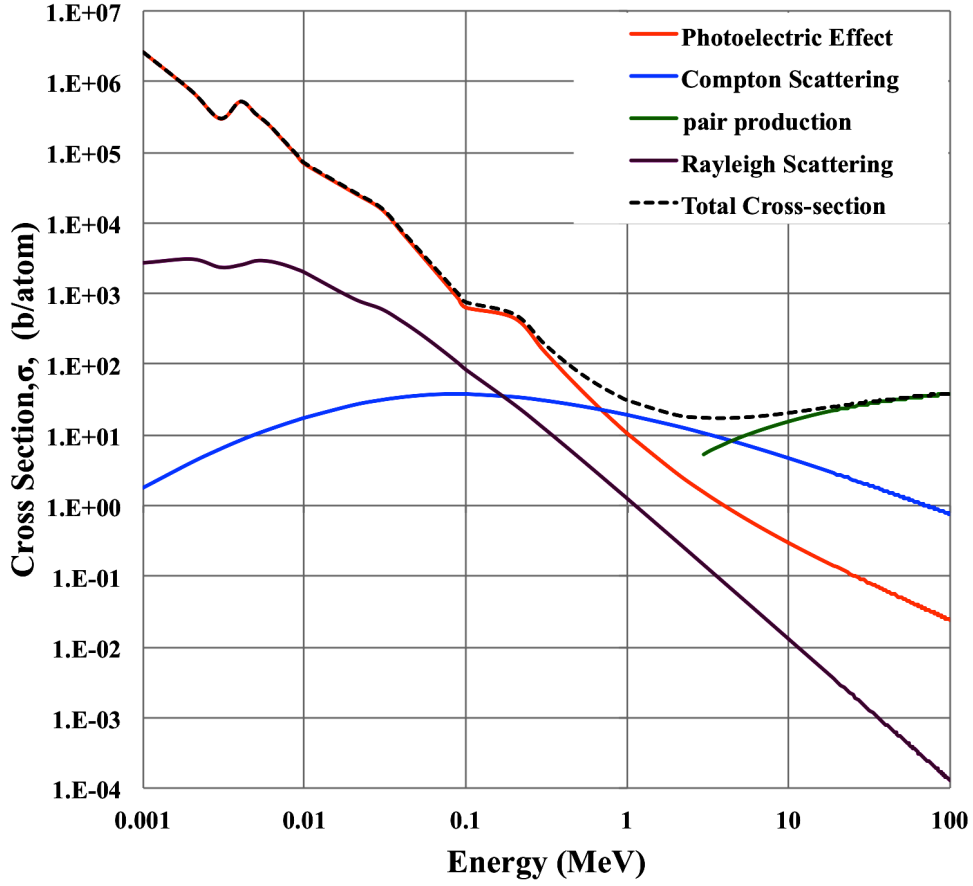
Fig. 2.4: *Photon cross-sections of uranium for photon energies between 1 keV and 100 MeV, showing the photoelectric effect, Compton scattering, pair production, Rayleigh scattering, and the total cross-section.*

$$\kappa_n \left(= \frac{N_A}{uA} \sigma_n \right) \sim \ln(h\nu). \tag{2.18}$$

For high energies [32],

$$\kappa_n \sim \frac{7}{9X_0} \tag{2.19}$$

where X_0 is the radiation length of the material. The cross section, σ_{trip} (triplet), in the field of one of the atomic electrons varies as Z times the square of the unit charge, or

$$\sigma_{trip} \sim Z \tag{2.20}$$

and is of minor importance, except for the lowest-Z materials. Examples for the photon interaction cross-sections for a photon with uranium material are displayed in Fig. 2.4.

o **Mass Attenuation and Energy-Absorption Coefficients**

■ **Mass attenuation coefficient, μ/ρ**

A narrow beam of monoenergetic photons with an incident intensity I_0, penetrating a layer of material with mass thickness x and density ρ, emerges with intensity I, given by the exponential attenuation law,

$$\frac{I}{I_0} = \exp\left[-(\mu/\rho)x\right]. \tag{2.21}$$

This equation can be rewritten as

$$\mu/\rho = x^{-1} \ln\left(\frac{I}{I_0}\right). \tag{2.22}$$

from which μ/ρ can be obtained from the measured values of I_0, I and x.

The theoretical value of μ/ρ is defined with the total cross-section per atom, σ_{tot}, which is related to μ/ρ according to

$$\frac{\mu}{\rho} = \frac{N_a}{uA}\sigma_{tot}.$$

(2.23)

In this equation, N_a is Avogadro's number (6.022045×10^{23} mol^{-1}), u is the atomic mass unit ($1/12$ of the mass of an atom of nuclide ^{12}C), A is the relative atomic mass of the target element. The total cross-section can be written as the sum over contributions from the principal photon interactions,

$$\sigma_{tot} = \sigma_{pe} + \sigma_{coh} + \sigma_{incoh} + \sigma_{pair} + \sigma_{trip} + \sigma_{pn.n}.$$

(2.24)

where σ_{coh} and σ_{incoh} is the coherent and incoherent scattering cross-section respectively.

Photonuclear absorption can contribute as much as 5 – 10% to the total photon interaction cross-section in a fairly narrow energy region, usually somewhere between 5 and 40 MeV. This cross-section has not been included in the theoretical tabulations of the total cross section because of the difficulties due to (a) the irregular dependence of both the magnitude and resonance-shape of the cross section as a function of both Z and A; (b) the gaps in the available information, much of which is for separated isotopes or targets otherwise differing from natural isotope mixtures; and (c) the lack of theoretical models for $\sigma_{pn.n}$ comparable to those available for calculations of the other cross sections of interest. μ/ρ without including photonuclear absorption is calculated according to:

$$\frac{\mu}{\rho} = \frac{N_a}{uA}\left(\sigma_{pe} + \sigma_{coh} + \sigma_{incoh} + \sigma_{pair} + \sigma_{trip}\right). \tag{2.25}$$

- ## Mass Energy-Absorption Coefficient μ_{en}/ρ

The mass energy-absorption coefficients, μ_{en}/ρ (cm^2/g or m^2/kg, ρ is a density of the medium), is a useful parameter in computations of energy deposited in media subjected to photon irradiation. μ_{en}/ρ can be described more clearly through the use of an intermediate quantity, the mass energy-transfer coefficient μ_{tr}/ρ.

The mass energy-transfer coefficients, μ_{tr}/ρ, when multiplied by the photon energy flounce Ψ ($\Psi = \Phi E$, where Φ is the photon flounce and E is the photon energy), gives the dosimetric quantity *kerma*. Kerma has been defined [38] as the sum of the kinetic energies of all those primary charged particles released by uncharged particles (here photons) per unit mass. Thus, μ_{tr}/ρ takes into account the escape of secondary photon radiations produced at the initial photon-atom interaction site plus, by convention, the quanta of radiation from the annihilation of positrons (assumed to have come to rest) originating in the initial pair-production interactions.

Hence, μ_{tr}/ρ is defined as

$$\frac{\mu_{tr}}{\rho} = \frac{N_a}{uA}\left(f_{pe}\sigma_{pe} + f_{incoh}\sigma_{incoh} + f_{pair}\sigma_{pair} + f_{trip}\sigma_{trip}\right). \tag{2.26}$$

In this expression, coherent scattering has been omitted because of the negligible energy transfer associated with it, and the factor f represents the average fraction of the photon energy, E_0, that is transferred to the kinetic energy of charged particles in the remaining types of interactions. These energy-transfer fractions are given by:

$$f_{pe} = 1 - \left(X/E_0 \right), \tag{2.27}$$

where X is the average energy of fluorescence radiation emitted per absorbed photon,

$$f_{incoh} = 1 - \left(\langle E_s \rangle + X \right)/E_0, \tag{2.28}$$

where $\langle E_s \rangle$ is the average energy of the Compton-scattered photon. In addition,

$$f_{pair} = 1 - 2m_e c^2/E_0, \tag{2.29}$$

and

$$f_{trip} = 1 - \left(2m_e c^2 + X \right)/E_0, \tag{2.30}$$

The mass energy-absorption coefficient involves further emission of radiation produced by charged particles in traveling through the medium and is defined as:

$$\mu_{en}/\rho = (1-g)\mu_{tr}/\rho. \tag{2.31}$$

The factor g represents the average fraction of the kinetic energy of secondary charged particles (produced in all types of interactions) that is

26

subsequently lost in the radiative energy-loss processes as the particles slow to rest in the medium. The evaluation of g is accomplished by integrating the cross-section for the radiative process of interest over the differential track-length distribution established by the particles in the course of slowing down.

o   **Photonuclear Interaction**

- **Integrated NRF Cross-Section**

Nuclear resonance fluorescence (NRF) is the incoherent absorption and emission of γ-rays from a nucleus. In the NRF process, an incident γ-ray of energy, E_x, excites the nucleus into a higher energy state, typically populating a $\Delta J = 1$ level, where J is total angular momentum, (a $\Delta J = 2$ level is much less probable). Afterward, the nucleus de-excites, and if $E_x < S_n$, where S_n is the neutron separation energy, signature γ-rays are emitted, populating the ground state or lower-lying excited states. Because the momentum transfer associated with NRF is small, dipole ($L = 1$) excitations are highly favored over quadrupole ($L = 2$) ones, making it a good probe for studying M1 and E1 excitations in nuclei.

The interaction cross-section for a state that undergoes the NRF of a γ-ray as the nucleus transition from an excited state to the ground state is given by the Breit-Wigner form [21]:

$$\sigma_{NRF}(E) = \frac{\pi}{2} g \left(\frac{\hbar c}{E} \right)^2 \frac{\Gamma^2}{(E - E_r)^2 + (\Gamma/2)^2} \tag{2.32}$$

where E denotes the incident photon-energy, and E_r represents the resonant energy. $\hbar$ is the Plank's constant. Γ indicates the sum of the partial width of different de-excitation states, *i.e.*, Γ is a total width of the NRF transitions defined as

28

$$\Gamma = \sum_i \Gamma_i = \Gamma_1 + \Gamma_2 + ... + \Gamma_n \tag{2.33}$$

which is related to the state's mean lifetime, τ, by

$$\Gamma = \hbar/\tau \tag{2.34}$$

where Γ_n is the nth partial width for the decay from the nth level. g is a statistical factor, which depends on the total angular momentum numbers of the ground-state, J_0, and the excited-state, J_i, by the following expression.

$$g = \frac{2J_i + 1}{2J_0 + 1} \tag{2.35}$$

Generalizing Eq. (2.32) to de-excitations other than those proceeding exclusively to the ground state, the cross-section of a de-excitation to the ith state is:

$$\sigma_i(E) = \frac{\pi}{2} g \left(\frac{\hbar c}{E} \right)^2 \frac{\Gamma_0 \Gamma_i}{(E - E_r)^2 + (\Gamma/2)^2} \tag{2.36}$$

Summing over all possible values of i for a given nucleus, the resonance absorption cross-section of γ-rays with energy E is:

$$\sigma_{abs}(E) = \frac{\pi}{2} g \left(\frac{\hbar c}{E} \right)^2 \frac{\Gamma_0 \Gamma}{(E - E_r)^2 + (\Gamma/2)^2} \tag{2.37}$$

where Γ_0 is the partial width of the state for decay by γ-ray emission to the ground state. The resonance reaches a maximum value when $E = E_r$, and thus,

$$\sigma_{abs}^{\max}(E) = 2\pi g \left(\frac{\hbar c}{E_r} \right)^2 \frac{\Gamma_0}{\Gamma} \tag{2.38}$$

▪ Doppler Broadening and Nuclear Recoil

The Doppler effect is an important consideration for NRF measurements because the spectral lines appear wider than they actually are. This is due to the thermal motion of the nuclei. Each nucleus moves with a velocity v, thereby shifting the rest of energy E to E'.

$$E' = \frac{E(1+v/c)}{\sqrt{1-(v/c)^2}} \approx E(1+v/c). \tag{2.39}$$

where $c \gg v$. If the velocities are well described by a Maxwellian distribution function, the likelihood of a nuclei having a component of v parallel to the source direction is:

$$w(v)dv = \sqrt{\frac{M}{2\pi k_B T}} \exp\left(-\frac{Mv^2}{2k_B T} \right) dv, \tag{2.40}$$

where M is the nuclear mass, T is the absolute temperature of the material, and k_B is Boltzmann's constant. The energy distribution in terms of the velocity distribution of Eq. (2.39) is given by:

$$w(E')dE' = \frac{1}{\Delta\sqrt{\pi}} \exp\left(-\frac{E'-E}{\Delta} \right)^2, \tag{2.41}$$

and $\quad \Delta = \dfrac{E}{c}\sqrt{\dfrac{2k_B T}{M}}$ (2.42)

where Δ indicates the standard deviation of the distribution. The Doppler width, Γ_D, of a broadened resonance is given by

$$\Gamma_D = 2\sqrt{2\ln 2}\,\Delta = 2.355\Delta.$$ (2.43)

In case of the ^{238}U target, a Doppler width for the emission line of 2468 keV is 1.99 eV at the absolute temperature of 300 K, where the intrinsic width is in order of meV. Moreover, the effective temperature, T_{eff}, of the solid target is in general considerably higher than the actual absolute temperature T [39]. Therefore, a correction to absolute temperature must be made as follows:

$$\frac{T_{eff}}{T} = 3\left(\frac{T}{\Theta_D}\right)^3 \int_0^{\Theta_D/T} t^3\left(\frac{1}{e^t-1}+\frac{1}{2}\right)dt$$ (2.44)

where Θ_D represents the Debye temperature, which is a physical property of a material. The Doppler shifted energy distribution should be averaged over the NRF cross-section to obtain the Doppler broadened cross-section as follows:

$$\sigma_{NRF}^D = \int \sigma_{NRF}(E')w(E')dE' = \frac{\sqrt{\pi}}{2\Delta}\sigma_{NRF}^{\max}\Gamma\exp\left[-\left(\frac{E'-E}{\Delta}\right)^2\right]$$ (2.45)

Substituting $\sigma_{NRF}^{\max}$ from Eq. (2.38) in Eq. (2.45) yields:

$$\sigma_{NRF}^{D}(E) = \pi^{3/2}g\left(\frac{\hbar c}{E_r}\right)^2 \frac{\Gamma_0}{\Delta}\exp\left[-\left(\frac{E-E_r}{\Delta}\right)^2\right] \qquad (2.46)$$

An additional important term is the recoil energy of the nuclei after an emission of the NRF γ-rays, whereby a part of the emitted γ-energy goes to the recoil nucleus. This is in general, sufficient and larger than the level (intrinsic or Doppler) width; thus, the scattered NRF γ-rays cannot be absorbed again by the mother isotope state. The recoiling energy can be expressed by

$$E_{recoil} = \frac{E_r^2}{Mc^2} \qquad (2.47)$$

where for the emission line of 2468 keV of the ^{238}U nucleus, the recoil energy is deduced as 13.74 eV, which represents several orders of the Doppler width for this transition level. This means that the emission γ-rays are unable to make resonance again for the emission level. In the next subsection, we will introduce the NRF angular distribution for scattering NRF γ-rays.

▪ NRF γ-rays Angular Distribution

The angular distribution of the scattering NRF γ-rays will be sampled from correlation functions, $W(\Theta)$, appropriate to the multipolarities of the electromagnetic radiation. In general, more than one electric and magnetic multipole satisfies the selection rules governing a particular transition and can thus contribute [22,40] with relative intensities that depend upon the

detailed overlap of the initial and final states of nuclear wave functions. Thus, the resulting angular distribution is a superposition of the distributions for the contributing multipoles. It is anticipated that in many cases in which both electric and magnetic multipoles can contribute to the same transition, the mixing ratio is unknown in the majority of cases.

The angular distribution of the emitted NRF γ-rays photons is represented by a correlation function, $W(\Theta)$, evaluated with respect to the direction of the incident photon. The correlation function depends upon the multipolarities of the electromagnetic radiation involved in the emission transition. Because the NRF interaction commonly occurs between the levels that differ in angular momenta by two or less, the angular correlation function $W(\Theta)$ of scattered photon, γ_2, with respect to the incoming photon, γ_1, (incident beam), in cases of $L \leq 2$, can be written as [40]:

$$W(\Theta) = \sum_{v=0,2,4} A_v(1)A_v(2)P_v(\cos\Theta) \tag{2.48}$$

where Θ is the scattering angle between the incident and scattered photon, and $P_v(\cos\Theta)$ are the Legendre functions. The coefficients $A_v(1)$ represent the photons in the entrance channel having multi-polarity l_1 or $l_1' = l_1 + 1$ and a mixing ratio δ_1. Similarly, $A_v(2)$ describes the scattered photons having multi-polarity l_2 or $l_2' = l_2 + 1$ and a mixing ratio δ_2. The mixing ratios are defined as:

$$\delta_{1(2)} = \frac{<\Psi_f|l'_{1(2)}|\Psi_i>}{<\Psi_f|l_{1(2)}|\Psi_i>}. \tag{2.49}$$

The coefficients $A_v(1)$ and $A_v(2)$ can be expressed in terms of F-coefficients as:

$$A_v(1) = \left(\frac{1}{1+\delta_1^2}\right)\left[F_v\left(l_1 l_1 J_0 J\right)\right] + 2\delta_1 F_v\left(l_1 l'_1 J_0 J\right) + \delta_1^2 F_v\left(l'_1 l'_1 J_0 J\right), \tag{2.50}$$

$$A_v(2) = \left(\frac{1}{1+\delta_2^2}\right)\left[F_v\left(l_2 l_2 J_f J\right)\right] + 2\delta_2 F_v\left(l_2 l'_2 J_f J\right) + \delta_2^2 F_v\left(l'_2 l'_2 J_f J\right) \tag{2.51}$$

The angular distribution of photons scattered off an even–even nuclei through pure dipole transitions with a spin sequence of $(0 \rightarrow 1 \rightarrow 0)$ for a non-polarized γ-ray beam is given by:

$$W(\Theta)_{Dipole} = \frac{3}{4}\left(1 + \cos^2\Theta\right). \tag{2.52}$$

Whereas, the angular distribution for a pure quadrupole transitions with a spin sequence of $(0 \rightarrow 2 \rightarrow 0)$ is given by

$$W(\Theta)_{Quadrupole} = \frac{5}{4}\left(1 - 3\cos^2\Theta + 4\cos^4\Theta\right). \tag{2.53}$$

Fig. 2.5 presents the angular distribution function, $W(\Theta)$, of a dipole transition with a spin sequence of $(0 \rightarrow 1 \rightarrow 0)$, as well as a quadrupole transition with spin sequence of $(0 \rightarrow 2 \rightarrow 0)$ for an even-even isotope, such as ^{238}U transitions, in a case in which the incident γ-rays photons is un-polarized.
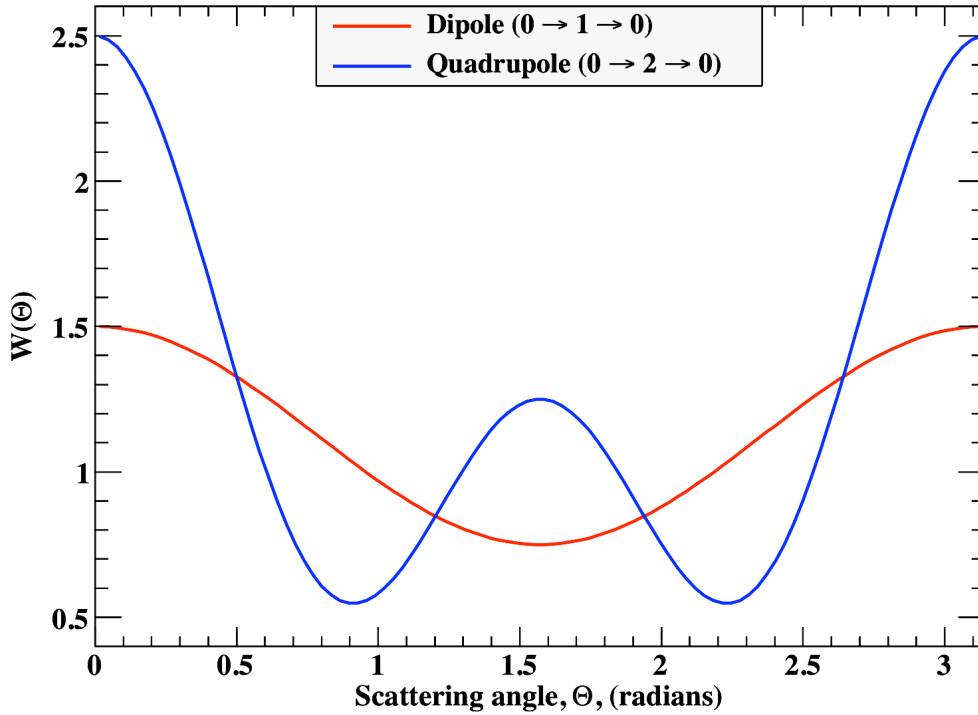
Fig. 2.5: *the angular distribution function,* $W(\Theta)$, *for photon transitions between levels of spin* $(0 \rightarrow 1 \rightarrow 0)$ *and* $(0 \rightarrow 2 \rightarrow 0)$.

Moreover, the angular distribution of γ-rays in the case of a linearly polarized γ-ray beam of both:

- *Dipole transitions:* given by,

$$W(\Theta,\phi)_{Dipole} = W_{Dipole}(\Theta) \mp \frac{3}{4}(1-\cos^2\Theta)\cos 2\phi, \qquad (2.54)$$

where the minus sign for electric dipole (E1) and the plus sign for magnetic dipole (M1), and,

- *Quadrupole transitions:* given by,

35

$$W(\Theta,\phi)_{Quadrupole} = W(\Theta)_{Quadrupole} \pm \frac{5}{4}\left(1 - 5\cos^2\Theta + 4\cos^4\Theta\right)\cos 2\phi \qquad (2.55)$$

Moreover, in the general case of $L = 1$ a dipole transition for which there is no mixing transition between M1 and E2, *i.e.*, the maxing ratio of M1/E2 equals zero, the angular correlation function is given by

$$W(\Theta,\phi)_{Dipole} = 1 + \left(F_2\right)^2\left[P_2 \mp \frac{1}{2}P_2^{(2)}\cos 2\phi\right] \qquad (2.56)$$

where the F-coefficients can be found in various compilations (e.g., Siegbahn 1965 [41]; Wapstra et al. 1959 [42]), and

$$P_2 = \frac{1}{2}\left(3\cos^2\Theta - 1\right) \qquad (2.57)$$

$$P_2^{(2)} = 3\left(1 - \cos^2\Theta\right) \qquad (2.58)$$

For quadrupole transitions with $L = 2$, the general equation for the angular distribution is:

$$\begin{aligned}W(\Theta,\phi)_{Quadrupole} &= 1 + \left(F_2\right)^2\left[P_2 \pm \frac{1}{2}P_2^{(2)}\cos 2\phi\right]\\ &\quad + \left(F_4\right)^2\left[P_4 \mp \frac{1}{12}P_4^{(2)}\cos 2\phi\right],\end{aligned} \qquad (2.59)$$

where:

$$P_4 = \frac{1}{8}\left(35\cos^4\Theta - 30\cos^2\Theta + 3\right), \qquad (2.60)$$

$$P_4^{(4)} = -\frac{105}{2}\cos^4\Theta + 60\cos^2\Theta - \frac{15}{2}. \qquad (2.61)$$

In case of the consideration of the E2 transition only the angular distribution of quadrupole transitions will becomes

$$W(\Theta,\phi)_{Quadrupole} = 1 + \left(F_2\right)^2 \left[P_2 + \frac{1}{2} P_2^{(2)} \cos 2\phi \right]$$
$$+ \left(F_4\right)^2 \left[P_4 - \frac{1}{12} P_4^{(2)} \cos 2\phi \right],$$

(2.62)

If there is a maxing ratio between M1 and E2, the dipole transition ($L = 1$) is given by

$$W(\Theta,\phi)_{E1/M1} = 1 + \left(A_2\right)^2 P_2 + A_2 a_2 \cos 2\phi P_2^{(2)},$$

(2.63)

where:

$$A_2 = \left(\frac{1}{1+\delta^2}\right)\left[F_2\left(j_i j_f 11\right) + 2\delta F_2\left(j_i j_f 12\right) + \delta^2 F_2\left(j_i j_f 22\right) \right],$$

(2.64)

$$a_2 = \left(\frac{1}{1+\delta^2}\right)\left[\frac{1}{2} F_2\left(j_i j_f 11\right) - \frac{1}{3}\delta F_2\left(j_i j_f 12\right) + \frac{1}{2}\delta^2 F_2\left(j_i j_f 22\right) \right].$$

(2.65)

CHAPTER 3

Monte Carlo Simulation to Optimize the NRF Detection System

The promise of NRF as a non-destructive assay (NDA) technique in safeguard applications lies in its potential to directly quantify a specific isotope in an assay target. Optimization of geometric configuration of the detector system for NRF measurements as well as interrogating γ-beam characteristics are the key technology for NDA of SNMs such as ^{235}U and ^{239}Pu. In NRF measurements, resonances are excited by an external photon beam leading to the emission of γ-rays with specific energies, which are the fingerprint of the emitting isotope [22]. The angular distribution of re-emitted photons is governed by the angular momenta of the states involved in the process [40]. Moreover, the elastic and inelastic scattering of photons from atoms provide background for the detection of characteristic NRF γ-rays. However, physical properties of these scattering mechanisms cause the background intensity for the detection of NRF γ-rays to be a function of both the interrogating γ-beam energy spectrum and the geometry configuration of the detection setup. The main challenge in NRF measurements achieving precise and accurate

measurements lies in accruing sufficient counting statistics in a reasonable measurement time.

In this chapter, the Monte Carlo (MC) simulation using the Geant4 toolkit has been performed to calculate the NRF interaction to optimize the setup of the measuring system [43,44]. First, an overview of the Geant4 will be introduced. Therewith, the atomic scattering calculations in terms of the Compton scattering will be presented to minimize the background of the Compton-scattering γ-rays and charged particles "*i.e.*, electrons", in the NRF measurements. Afterward, a MC simulation using Geant4 will be introduced for the NRF interaction and its angular distribution to optimize the detection system setup for scattering NRF γ-rays in forward, backward, and ninety-degree directions.

1.1. Geant4 Scope of Application

Geant4 [45-47] is a free software package composed of tools that can be used to accurately simulate the passage of particles through matter. All aspects of the simulation process have been included in the toolkit:

   i.   The geometry of the system,

  ii.   The materials involved,

 iii.   The fundamental particles of interest,

  iv.   The generation of primary events,

   v.   The tracking of particles through materials and electromagnetic fields,

  vi.   The physics processes governing particle interactions,

vii.   The response of sensitive detector components,

viii.   The generation of event data,

ix.   The storage of events and tracks,

x.   The visualization of the detector and particle trajectories, and

xi.   The capture and analysis of simulation data at different levels of detail and refinement.

At the heart of Geant4 is an abundant set of physics models to handle the interactions of particles with matter across a very wide energy range. Data and expertise have been drawn from many sources around the world, and in this respect, Geant4 acts as a repository that incorporates a large part of all that is known about particle interactions.

Geant4 is written in C++ and exploits advanced software-engineering techniques and object-oriented technology to achieve transparency. For example, the way in which cross sections are input or computed is separated from the way in which they are used or accessed. The user can overload both of these features. Similarly, the computation of the final state can be divided into alternative or complementary models, according to the energy range, the particle type, and the material. To build a specific application, the user-physicist chooses from among these options and implements code in user action classes supplied by the toolkit. A serious problem with previous simulation codes was the difficulty of adding new or variant physics models; development was difficult due to the increased size, complexity and interdependency of the procedure-based code. In contrast, object-oriented

methods help manage complexity and limit dependencies by defining a uniform interface and common organizational principles for all physics models. Within this framework, the functionality of models can be more easily recognized and understood, and the creation and addition of new models is a well-defined procedure that entails little or no modification to the existing code.

1.1.1. History of Geant4

These ideas first appeared in two studies conducted independently at CERN and KEK in 1993. Both groups sought to investigate how modern computing techniques could be applied to improve the existing FORTRAN-based Geant3 simulation program. Activities were merged in the fall of 1994, and a formal proposal, RD44, to construct an entirely new program based on object-oriented technology was submitted to CERN's Detector Research and Development Committee. The initiative grew to become a large international collaboration of physicist programmers and software engineers from a number of institutes and universities participating in a range of high-energy physics (HEP) experiments in Europe, Japan, Canada and the United States. *The objective was to write a detector simulation program that had the functionality and flexibility necessary to meet the requirements of the physics experiments. The initial scope quickly widened when it became apparent that such a tool would also benefit the nuclear, accelerator, space and medical physics community, with more individuals joining from these fields of science.*

The RD44 project represented a pioneering effort in redesigning a major CERN software package for a modern object-oriented (OO) environment based on C++. The R&D phase was completed in December 1998 with the delivery of the first production release. The collaboration was subsequently renamed Geant4 and re-instated on the basis of a formal Memorandum of Understanding (MoU) signed by many of the same national institutes, laboratories and large HEP experiments that had participated in RD44. The agreement addresses the program management, maintenance and user support during the production phase and the continued development and refinement of the toolkit. It is subject to tacit renewal every two years and sets forth a collaboration structure defined by a Collaboration Board (CB), a Technical Steering Board (TSB) and several working groups.

The collaboration now profits from the accumulated experience of many contributors to the field of Monte Carlo simulation of physics detectors and physical processes. While geographically distributed software development and large-scale object-oriented systems are no longer a novelty, Geant4, in terms of the size and scope of the code and the number of contributors, may well represent the largest and most ambitious project of its type outside the corporate world. A clean overall problem decomposition has led to a clear hierarchical structure of domains. Every section of the Geant4 software, which corresponds to a releasable component (library), is individually managed by a working group of experts. In addition, there is a working group for each of the activities: testing and quality assurance, software management and documentation management. A release coordinator heads each group. This consequent distribution of responsibility among a relative

large number of people permits a support structure by which outside users can address questions directly to the appropriate expert.

1.1.2.   Overview of Geant4 Functionality

The Geant4 class category diagram is displayed in Fig. 3.1. Categories at the bottom of the diagram are used by virtually all-higher categories and provide the foundation of the toolkit; the following is a description for each one.

1. Global: category covers the system of units, constants, numerics and random number handling. The two categories of:

2. Materials & Particles: implement facilities necessary to describe the physical properties of particles and materials for the simulation of particle-matter interactions.

3. The geometry: the module that offers the ability to describe a geometrical structure and propagate particles efficiently through it. Above these reside the categories required to describe the tracking of particles and the physical processes they undergo. The

4. Track: category contains classes for tracks and steps, used by the

5. Processes: category, which contains implementations of models of physical interactions: electromagnetic interactions of leptons, photons, hadrons and ions, and hadronic interactions. All processes are invoked by the
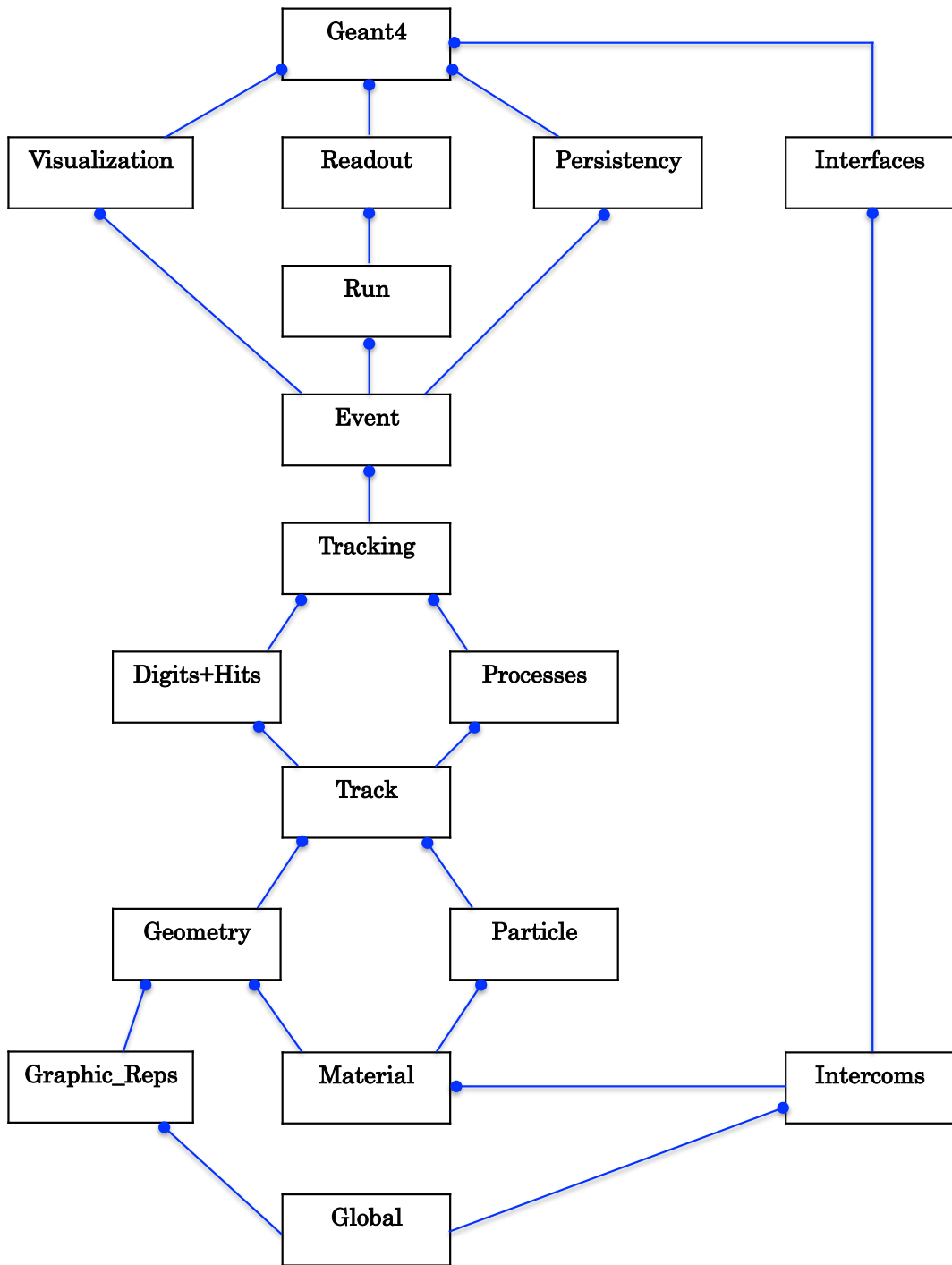
Fig. 3.1: *Geant4 class categories* [45].

6. Tracking: category, which manages their contribution to the evolution of a track's state and provides information in sensitive volumes for hits and digitization. Above these the

7. Event: category, which manages events in terms of their tracks and the

8. Run: category manages collections of events that share a common beam and detector implementation.

9. Readout: category allows the handling of pile-up.

Finally, the capabilities that use all of these categories and connect to facilities outside the toolkit through abstract interfaces, provide visualization, persistency and user interface capabilities.

1.1.3.   Developed NRF Interaction Code

The NRF process interaction developed in Geant4 by the Japan Atomic Energy Agency (JAEA) group [48] consists of a set of C++ classes. There are three classes: fission, inelastic, and elastic scattering for calculation of hadrons. Three classes are added, namely, UserGammaElasticProcess, UserGammaCrossSectionDataStore, and UserGammaElasticCrossSection-Data. These classes are extensions to calculate the NRF process, for which we should prepare an input data files containing the resonant information of the transition levels; these data are: the excitation energy, the spin, parity, width of transition state, and the cross-section of the NRF; these data should prepared for each transition. We added the effect of the angular distributions of resonance emissions that depends on the polarization degree of the incident beam and the spin sequence (dipole, quadrupole or mixing of them)

of the transition stats. Additionally, the nuclear recoil reaction is added to prevent the resonance by the emitted NRF γ-rays again for the mother isotope state. The Doppler width was also taken into account of the resonance state. The track of each photon and its energy changes are traced, taking into account the atomic processes and nuclear reactions. The NRF class category diagram is displayed in Fig. 3.2.
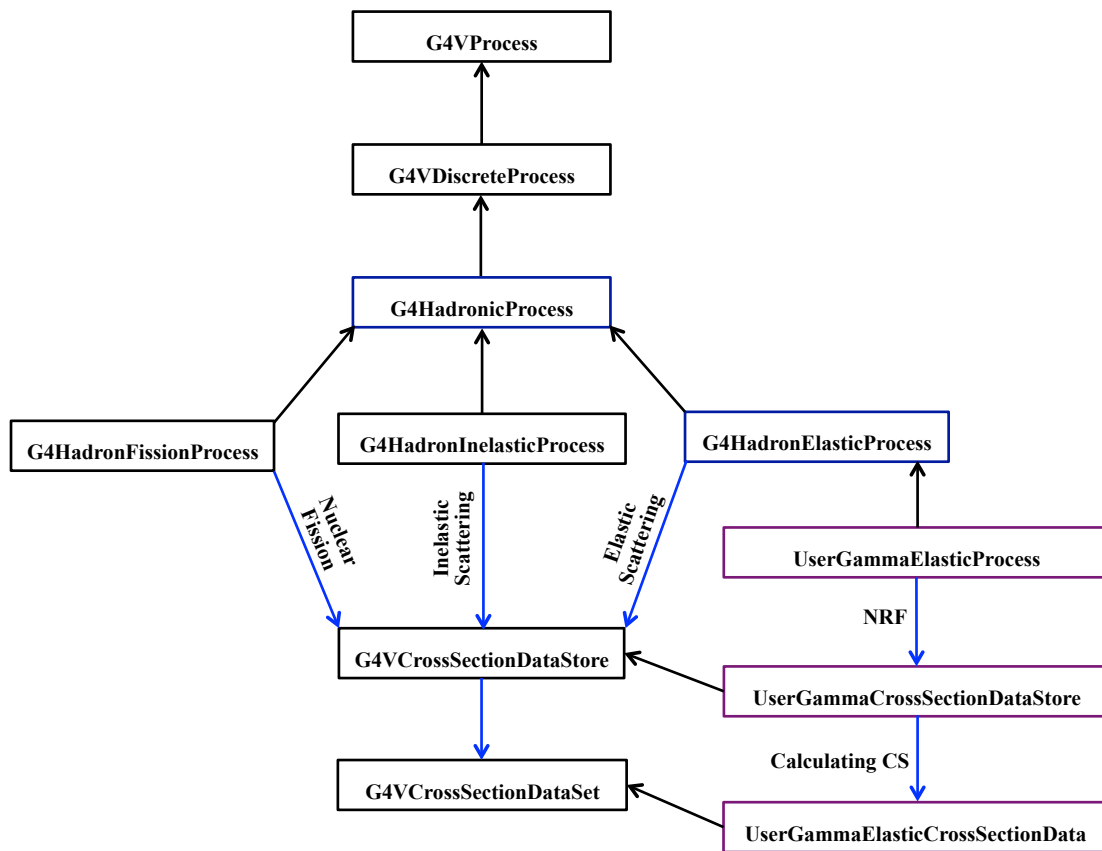
Fig. 3.2: *The NRF process class developed in Geant4.*

1.2. Incoherent Scattering

The non-resonant (elastic and inelastic) scattering photons may provide a background for the detection of the NRF scattering γ-rays, particularly from the Compton scattering. This background would directly affect the signal-to-noise (s/n) ratio of the detected signal. However, the physical properties of these scattering interactions cause the background intensity for the detection of the NRF γ-rays to be a function of the geometry of the detection setup and energy of the interrogating beam.

Compton scattering involves the inelastic scatter of a photon due to interaction with an electron. The kinematics of the collision and the differential cross-section for Compton scattering are presented in section (2.2). In this section, the Compton scattering photons and charged recoil electrons calculations will be introduced in terms of energy and the scattering angle.

These calculations could minimize the detection count rate of the non-resonant scattering photons and optimize the detection system for measuring the resonance photons, which will also be discussed in the next section.

The relations derived for the Compton energy in Eq. (2.2) assumed that the electron is free. The real description of the kinematics of inelastic scattering of a photon due to interaction with an atomic electron would necessarily include the binding energy of the electron. However, given that we are most interested in MeV-energy photons, the binding of outer-shell electrons to atoms is typically several eV, and even the K-shell electrons of

uranium have a binding energy of only 116 keV [49]. We conclude that the real kinematics experienced by MeV-photons when undergoing inelastic scattering due to atomic electrons can be considered very similar to those described by Eqs. 2.2 through 2.4.
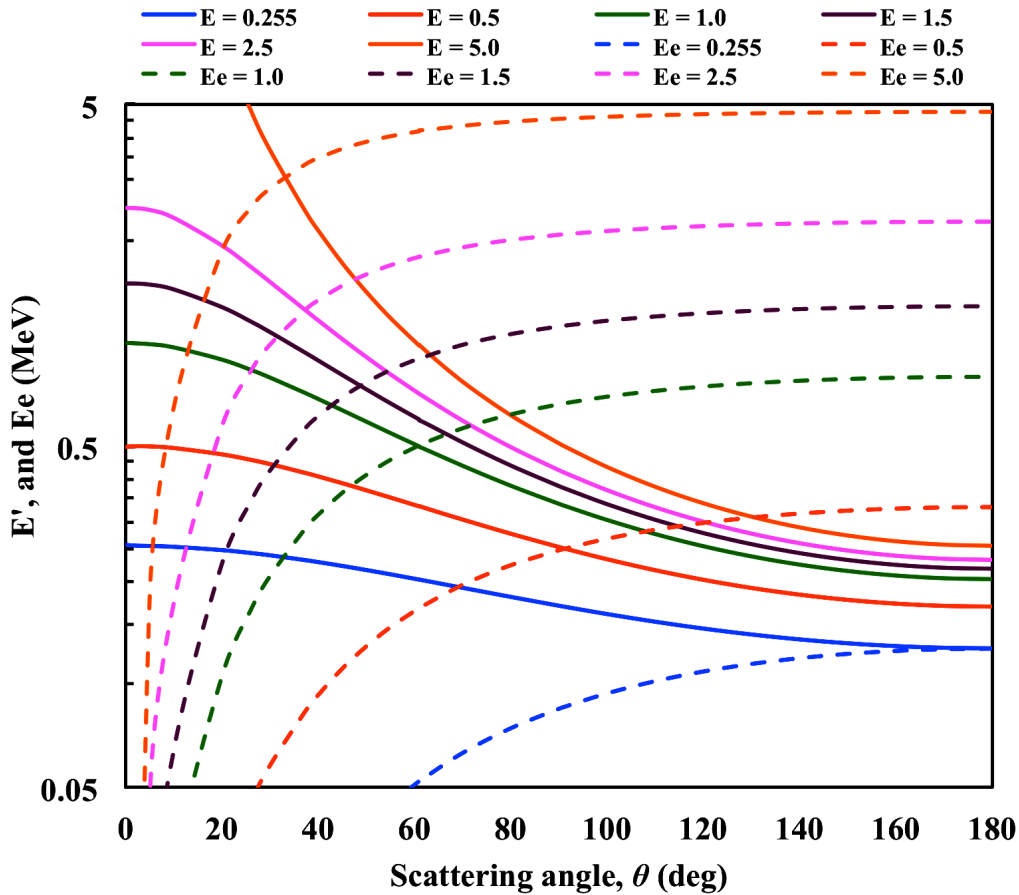
Fig. 3.3: *Energies of Compton-scattered photons, E', and Compton recoil electrons energies, E_e, as a function of the photon scattering angle, θ, for various initial photon energies, E = 0.255, 0.5, 1, 1.5, 2.5, and 5 MeV.*

The energy of emitted photons is plotted as a function of angle and various incident energies as presented in Fig. 3.3. The energy of a scattered photon drops below 1 MeV for a photon of E = 5.0 MeV at an angle for which $\theta \geq 53.8$ deg, while for a photon of E = 1 MeV, the energy drops below 0.5 MeV at an angle for which $\theta \geq 61$ deg. Moreover, for Compton scattering of a

100 MeV photon, the energy of the scattered photon drops below 1 MeV at $\theta \geq 61$ deg. This indicates that Compton scattering cannot produce high-energy photons in large angles relative to the initial photon trajectory.
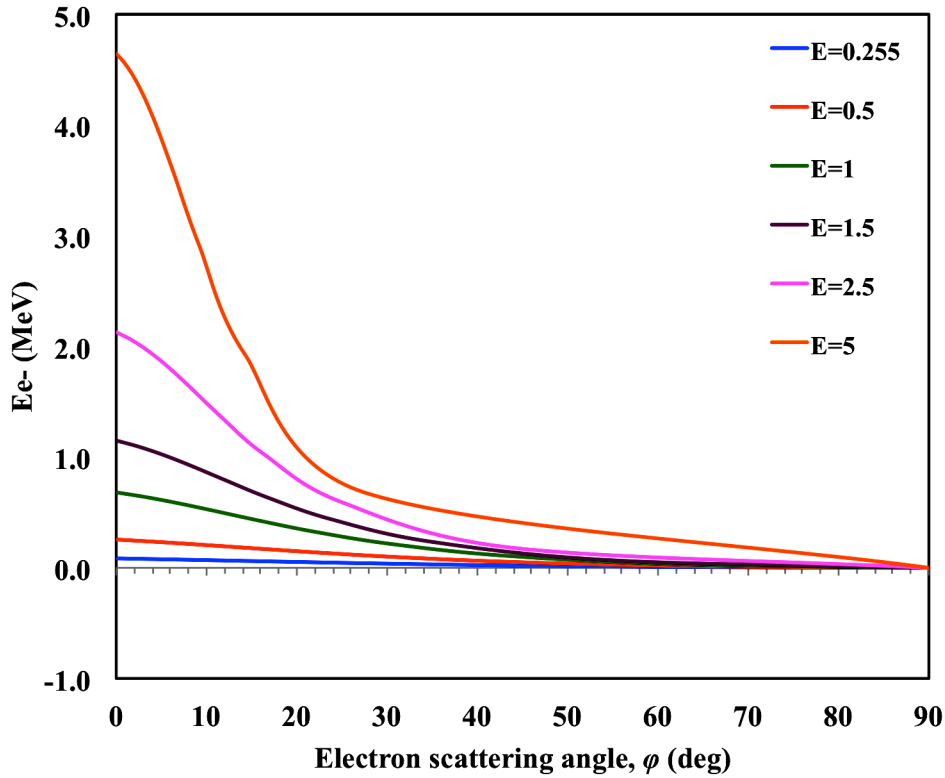
Fig. 3.4: *Energies of Compton electrons as a function of angle relative to the incident photon trajectory for various initial photon energies, E = 0.255, 0.5, 1, 1.5, 2.5, and 5 MeV.*

The dashed curves in Fig. 3.3 correspond to energies of electrons emitted during the Compton scattering of a photon of energy, *E*, scattered into the angle *θ*. These curves indicate that while Compton scattering cannot produce high-energy secondary photons in large scattering angles, the energies of Compton electrons can remain quite high. However, Eq. 2.4 indicates that the Compton electron is always emitted in relatively forward directions and that the emission is symmetric at approximately *φ* = 0. Fig 3.4

presents the same Compton electron energies as those displayed in Fig 3.3 but as a function of the Compton electron angle, φ. From this, we can see that energetic Compton electrons are only emitted in small angles relative to the direction of the incident photon.
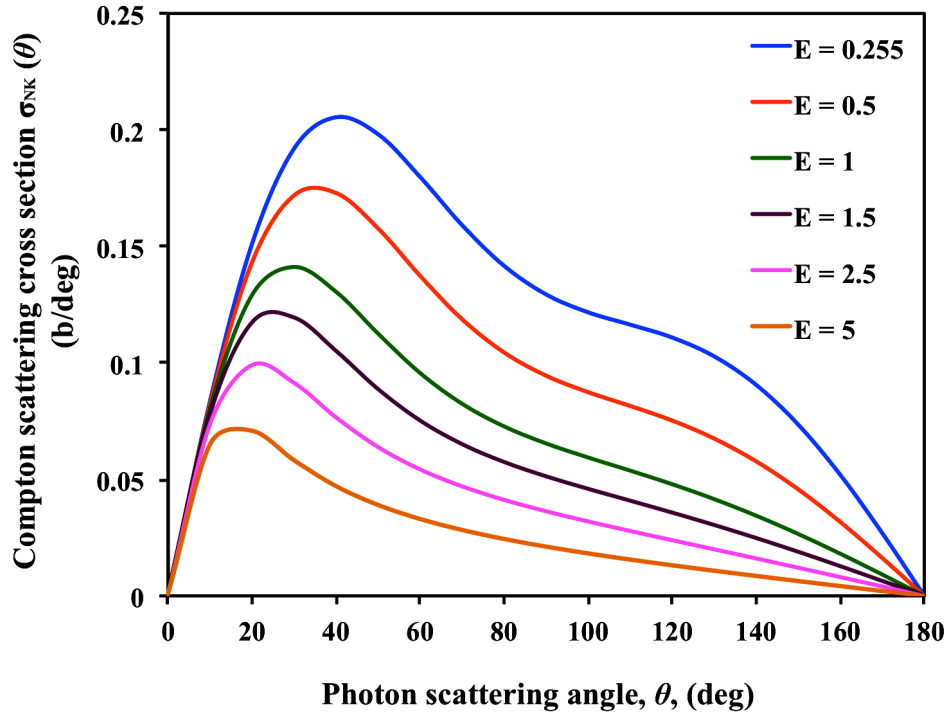
Fig. 3.5: *The KN differential scattering cross section for photon scattering of angle, θ, for incident photons of energy, E = 0.255, 0.5, 1, 1.5, 2.5, and 5 MeV.*

For further examination, the Compton angle-differentiated cross section reported by Eq. (2.5) is plotted versus θ for a range of incident photon energies, E, in Fig 3.5. Clearly, for E ≥ 1 MeV incident photons, Compton scattering predominantly produces scattered photons in forward directions.

Consequently and based on the above calculations, Compton scattering is predominantly forward directed; there is a non-negligible probability of scattering photons into the backwards direction. It should be remembered,

however, that Fig 3.2 indicates the energy of Compton backscattered photons is below 500 keV for incident photon energies of interest for any angle for which $\theta \geq 61\,\mathrm{deg}$. Therefore, the measurements of NRF γ-rays at backwards angles, relative to the incident beam direction, yield backgrounds that are significantly reduced relative to a comparable setup with the measurement of forward-directed photons.

1.3. Scattering of NRF γ-rays

The optimum geometric configuration of the detector system for NDA for SNMs by measuring scattering NRF γ-rays has been studied. To demonstrate the optimum scattering angle of NRF γ-rays with respect to the incoherent scattering and the self-absorption, a MCRT code, Geant4, has been developed to calculate NRF interaction. The simulation performed for the detector array consisting of eight LaBr$_3$:Ce (1.5″ × 3″) detectors positioned at 5 cm from the center of the target. Seven detectors are positioned at a seven scattering angles relative to the incident beam by a 45°-stepping angle, as well one detector is at 90° perpendicular on the incident beam. The HEU (90% - ^{235}U) is used as a target with different thicknesses at the resonant energy level of 1733 keV.

1.3.1.   Geometric Configuration of NRF Setup

Geant4 provides an efficient virtual environment to model the high-energy physics interactions between particles and matter over a wide range of energies. It provides several powerful tools for developing radiation sources, detectors, and a variety of complex shapes. The main classes in the simulation setup that was modeled are in three parts:

2. The Detector Construction Class, which contains the geometry and materials of the detector setup and the target. A virtual LaBr$_3$:Ce detector array consisting of 7 detectors were used. Each detector with a 1.5″ in diameter by 3″ in length. The detector array was positioned at 5 cm around the target, in the scattering plane φ = 90° relative to the γ-beam

direction with stepping scattering angle $\theta = 45^\circ$, as well one detector is at 90° perpendicular on the incident beam, as presented in Fig. 3.6. An high enrichment uranium (HEU) target (^{235}U – 90% + ^{238}U – 10%), as the SNM, was used as the interrogation target. Different target thicknesses varying from 1.0 μm to 5.0 cm with sectional area of 2.54 cm × 2.54 cm were measured.
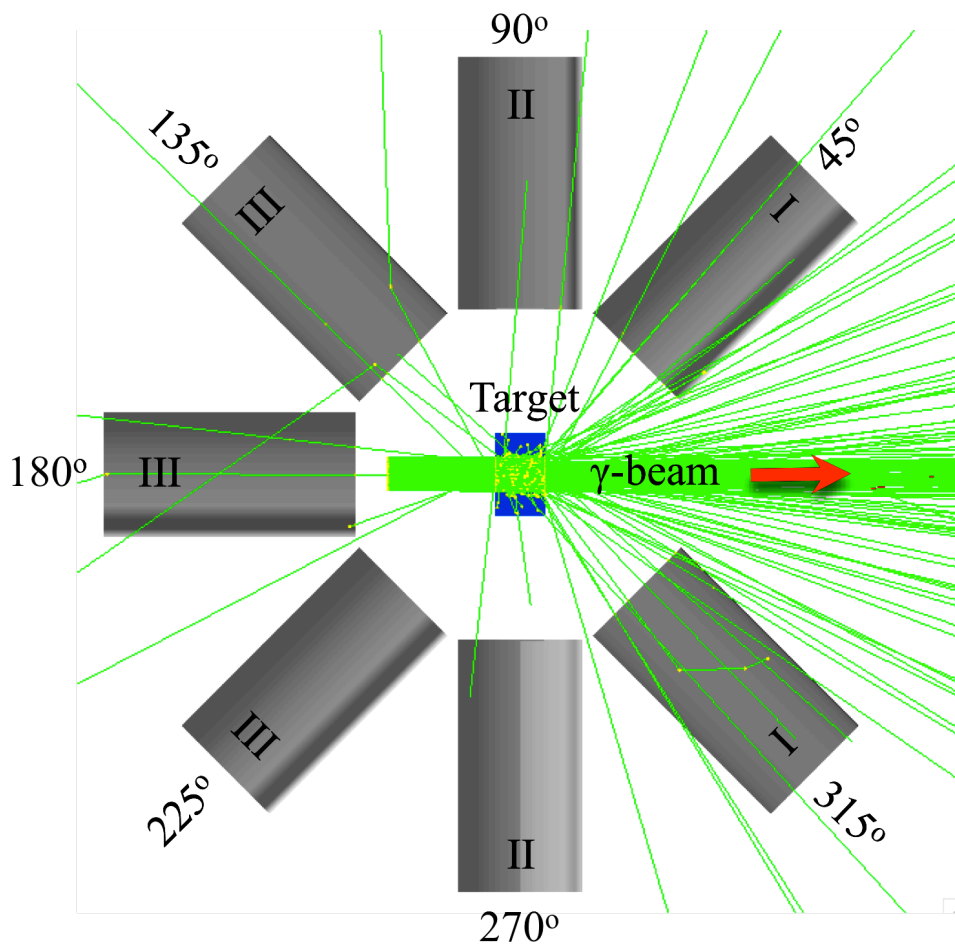
Fig. 3.6: *Schematic view of the geometric configuration of LaBr₃:Ce detector array of the NRF setup in scattering plane θ, as well the γ-ray track, where the green lines indicate the scattering γ-rays by the HEU target. There are three sets of the detector position as marked by: I – for forward scattering, II – for the 90º scattering, and III – for backward scattering, relative to the incident beam direction, which is marked as the red arrow.*

2. The Physics List Class, which contains implementations of the models of physical interactions: electromagnetic interactions of leptons, photons, hadrons and ions and hadronic interactions. The simulation carried out for standard electromagnetic (EM) interaction with matter and its decay, as well the photonuclear process, which implements the NRF interaction.

2. The Primary Generator Action Class, which simulates the incident beam that irradiates the target. The interrogation beam was assumed with high intensity mono-energetic γ-ray with incident photon numbers of 2×10^9 with a 100% linear polarized beam. We assumed the existing LCS γ-ray beam of the HIγS facility at Duke University [50]. The beam size/diameter of the γ-ray is assumed to be 19.05 mm. The incident beam energy was assumed to correspond to a resonant energy level of ^{235}U of 1733 keV [51-53]. The maximum value of the NRF cross-section of ~ 30 b.eV in the calculation was chosen amongst the reported values. The nuclear level width was assumed by the intrinsic/natural width. The calculation was made on the two values of the standard deviation (σ) of incident γ-ray energy. The first is assumed to be σ = 10 eV, and this value could enhance the reaction yield of scattering NRF γ-rays in addition to reducing computation time because the σ is comparable with the resonant window of the resonance energy level. The second value was assumed to be 1% from the incident energy, i.e., σ = 7.37 keV, (FWHM = 17.33 keV), which can be obtained from the HIγS facility. The γ-beam profile of incident energy and its cross-sectional profile are presented in Fig. 3.7.
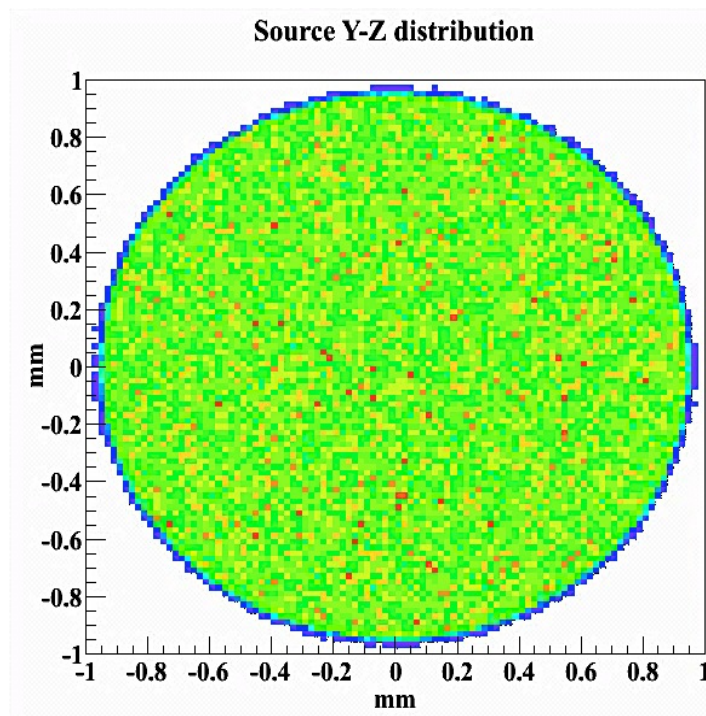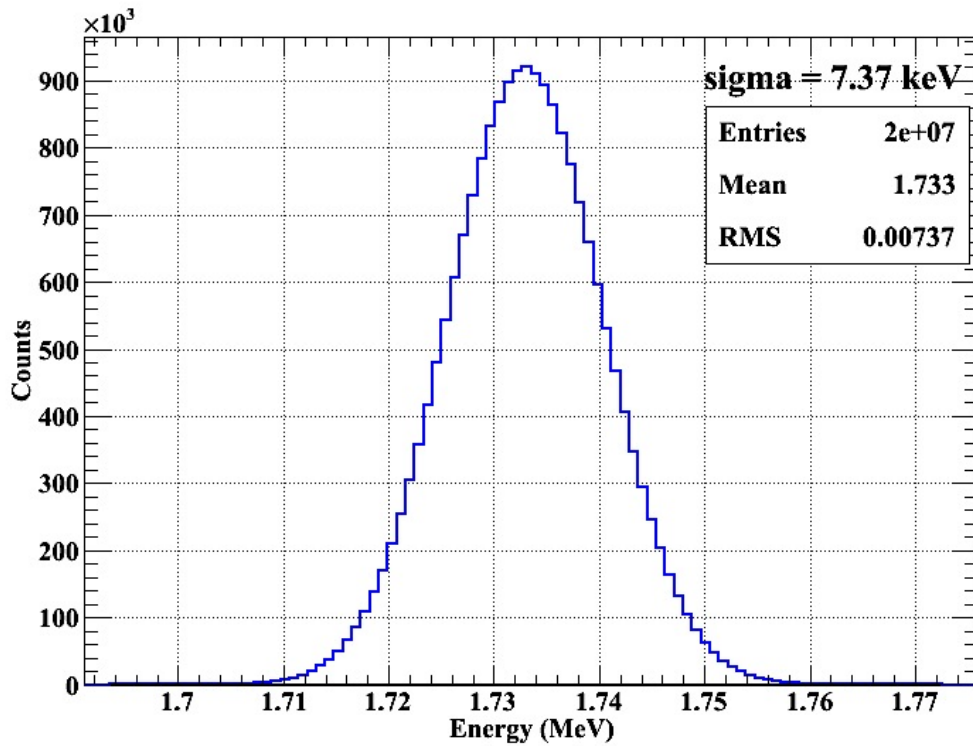
Fig. 3.7: *LCS γ-beam profile for incident energy of 1733 keV with energy spread of FWHM = 17.33 keV (uper graph), while the cross-sectional profile for the beam size of 19.05 mm is displayed in the lower graph.*

Scattering NRF γ-rays were divided into three sets of measurements as displayed in Fig 3.6. The first set is for forward measurements, which was performed by two detectors at 45°, and 315° as marked by "I". The second set was placed at ninety-degrees by two detectors marked "II" at 90° and 270°. The third set consisted of three detectors marked "III" at 135°, 180°, and 225° for backward measurements. The simulation was carried out for EM and NRF interactions. The detection system based on the LaBr$_3$:Ce detector would record the scattering γ-rays by the detectors at seven scattering angles. The γ-ray energy spectra will be stored in the data files for each detector for each run. The simulation was performed for different thicknesses; for each thickness, the energy spectra are collected.

1.3.2.   Results and Discussion

1.3.2.1. NRF Reaction Yield vs. Scattering Angle

As seen in Fig. 3.8, a collection of four energy spectra for scattering NRF γ-rays at different scattering angles were observed from the ^{235}U target (3.0 mm in thickness). A resonant energy of the NRF state of 1733 keV was selected in the simulation. The energy spread (standard deviation, σ) of incident γ-ray was 10 eV. Two pairs of these spectra, at backward scattering angles of 135° and 180°, have NRF peaks with a high-count rate relative to the other two spectra at 90° and forward angle at 45°. This trend of different yields with the scattering angles contributed to the attenuation of the incident beam energy through the target thickness and the self-absorption of emitted NRF γ-rays.
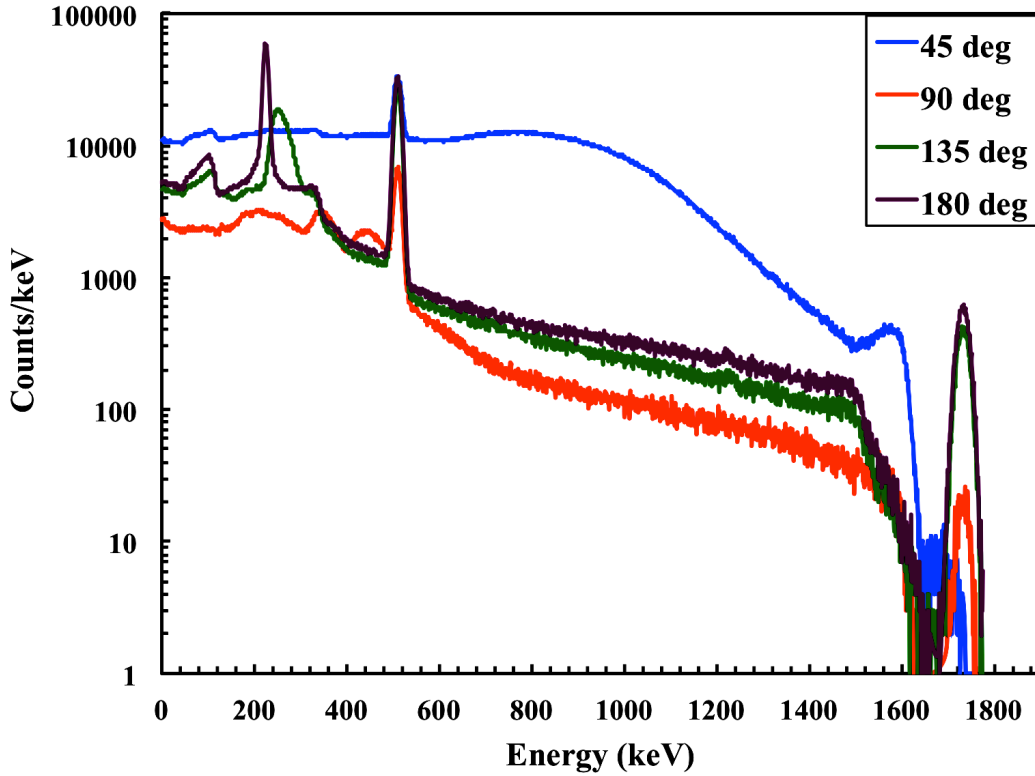
Fig. 3.8: *Energy spectra of scattering NRF γ-rays at different scattering angles from θ = 45º through 180º, respectively. The ²³⁵U target was of a 3.0 mm thickness. The resonant energy of the transition line was at 1733 keV. The beam energy spread (standard deviation) with σ = 10 eV.*

Thus, in case of the forward scattering, the resonant photons energy was reduced by attenuation based on the target thickness. Therefore, the NRF yield from the front surface to the beam has the highest number of resonant photons energies, which has a high probability of making the NRF interactions. The other factor that reduces the yield of measuring NRF γ-rays is the self-absorption of the emitted NRF γ-rays after the NRF interaction through the target prior to measuring it. These reasons could explain the different count in each of the cases of the scattering of the NRF γ-rays. For this purpose, an analytical model for the NRF reaction yield was deduced in chapter 4 to interpret this behavior of the NRF yield with the target thickness.
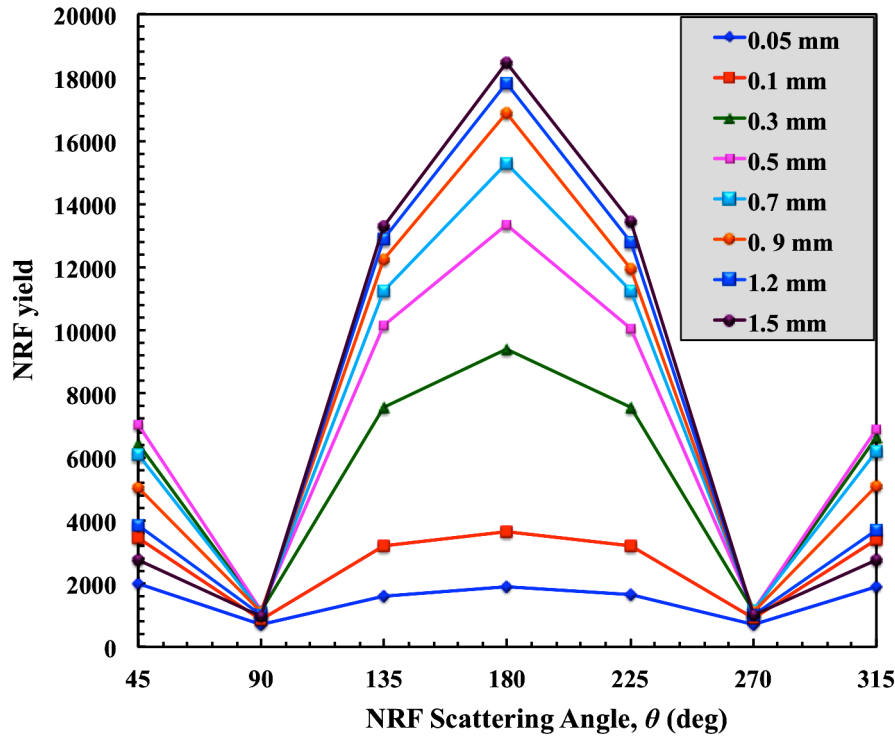
Fig. 3.9: *Scattering NRF yield of [235]U (1733 keV) vs. the 7 scattering angles for different target thicknesses as depicted in the figure.*

For further examination, an NRF experiment with several thicknesses of [238]U in the HIγS facility at Duke University has been presented in chapter 6. Moreover, the NRF γ-ray measurements at backward angles relative to the incident beam yields Compton scattering spectrums that are significantly reduced relative to a comparable setup with measurement of forward-directed photons, as discussed analytically in section 3.2.

For further examination, the NRF yield is plotted versus the scattering angles (the angular distribution) for the different target thicknesses as displayed in Fig. 3.9. This figure indicates that the maximum yield for the scattering NRF γ-rays is approximately the scattering angle of the 180° backward angle, while the NRF yields attain the minimum value at the scattering angle of 90°.

1.3.2.2.   NRF Reaction Yield vs. Target Thickness

Fig. 3.10 displays the relation between the yields of NRF γ-rays at different target thicknesses with different scattering angles. This figure indicates that the yields of scattering NRF γ-rays at backward angles between 135° and 180° are significantly higher than the forward angles and 90° measurements – relative to the incident beam direction. However, for thin targets – relative to the target mass number – the count rate of the NRF γ-rays at forward and backward angles may be the same. This demonstrated that the attenuation of γ-rays through the thin targets due to the attenuation of incident flux and the self-absorption could be ignored. On the other hand, the background yields due to the Compton scattering still in the forward measurements are great relative to the backward measurements.
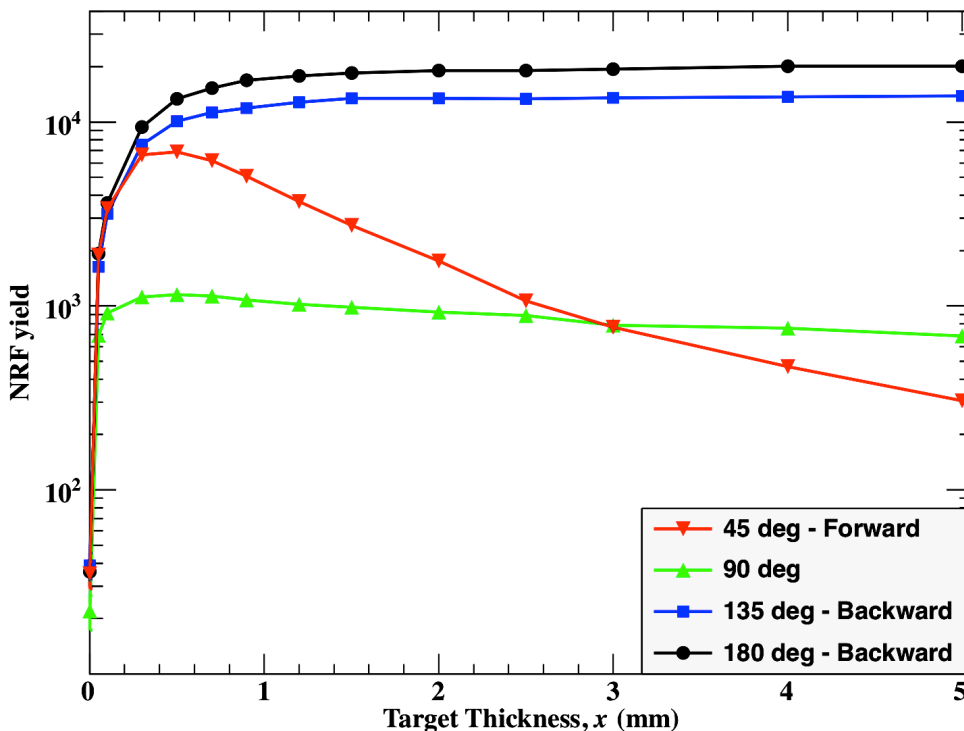
Fig. 3.10: *Scattering NRF yield of* ^{235}U *(1733 keV) vs. target thickness for forward (at 45°), ninety-degree, and backward (at 135° and 180°) configuration of detectors relative to incident beam.*

Consequentially, the preferable setting for measuring the scattering NRF γ-rays is in the backward angles, based on all calculations of the Compton scattering and the NRF scattering γ-rays and in light of the attenuation and the self-absorption of the γ-rays through the target material. We should mention that, in real experimental conditions, the detection of NRF γ-rays is affected by many other parameters, such as detection efficiency and dead time of the measuring system, which contribute by a negative NRF yield response. Therefore, a number of corrections should be taken into account with the NRF signal analysis.

1.3.2.3. NRF Reaction Yield vs. Spread of Incident Energy

Fig. 3.11, displays the comparison between the NRF reaction yields for two cases of the energy spread at a scattering angle of $\theta = 135^o$, in the same conditions, whereby the peak areas of the NRF signal in the cases of $\sigma = 10$ eV and 7.37 keV are 13564.7 ± 116.5 and 68.53 ± 17.01, respectively. It is obvious that the signal-to-noise ratio (S/N) of NRF γ-ray is affected by the energy spread (FWHM of energy) of the incident beam. This trend demonstrated that the condition of the beam has an effect on the NRF reaction yield, where the NRF yield is inversely proportional to the energy spread. In addition, with the smallest incident beam energy spread, the atomic scattering would be reduced to a greater degree than the broader one. This is one of the bigger challenges for measuring the scattering NRF yield in the proper time with suitable statistics in the count rate.
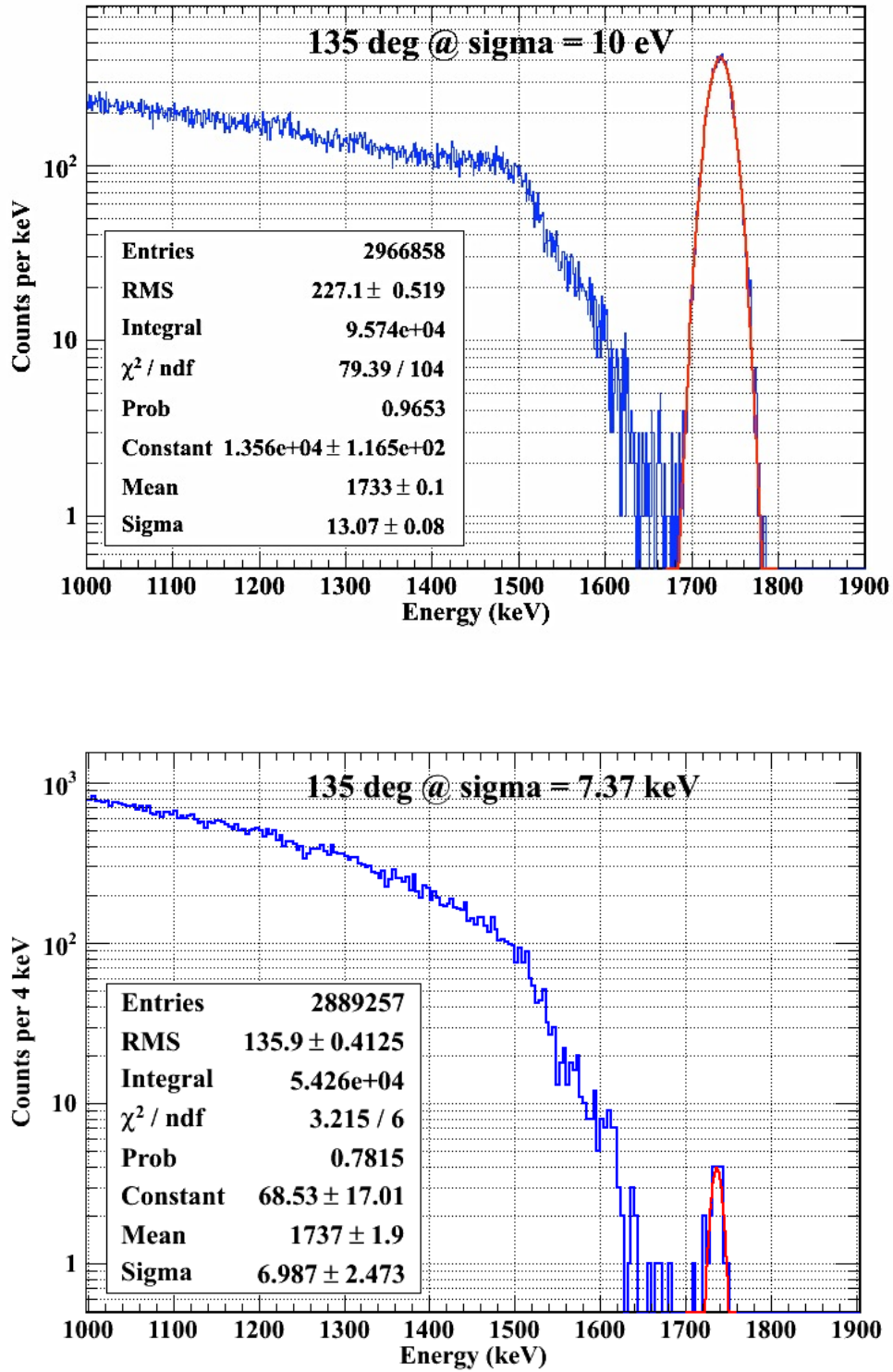
Fig. 3.11: *Energy spectrum of scattering NRF γ-rays of ²³⁵U for the transition line of 1733 keV with thickness 3 mm. The scattering angle was θ = 135°. Two values of the energy spread were selected, σ = 10 eV (upper spectrum) and σ = 7.37 keV (lower spectrum).*
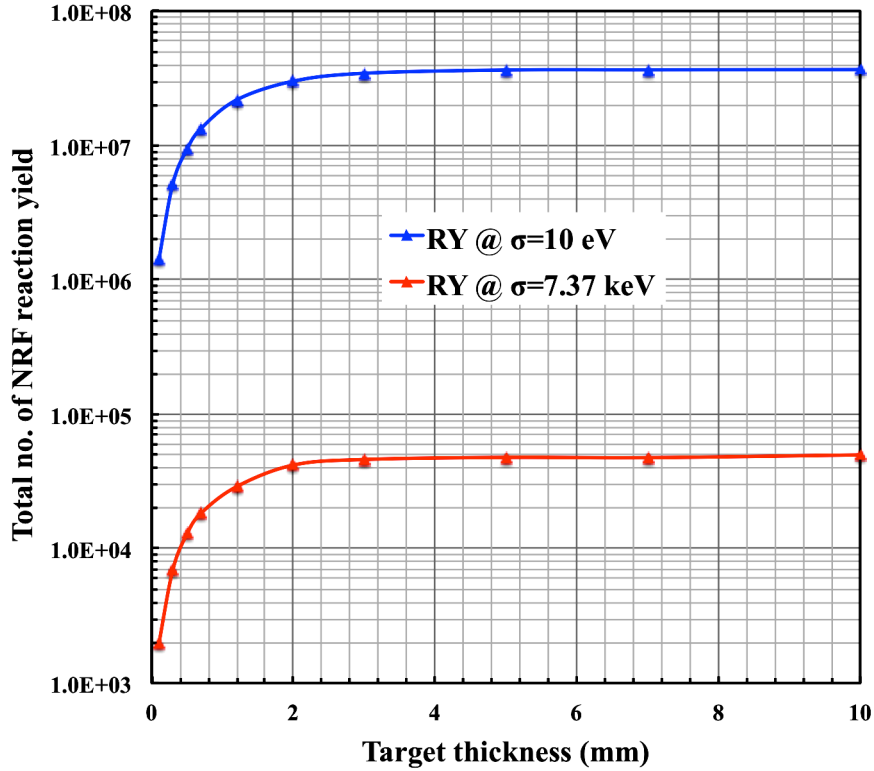
Fig. 3.12: *NRF reaction events number (at the interaction point) of ^{235}U of the transition state of 1733 keV. The incident beam energy spread was σ = 10 eV (Blue data) and 7.37 keV (Red data).*

Moreover, Fig. 3.12 demonstrates the effect of energy spread on the NRF reaction events (RE) number at the interaction point (without any absorption). These curves indicate that the NRF reaction yield increased with target thickness before reaching the saturation. The saturation trends of the NRF reaction occur because of the attenuation and the self-absorption of the γ-rays before and after the NRF interaction, as in the preceding discussion. The correlation between the effective-flux (the number of photons that induce the nucleus to make a resonance to specific state) and the energy spread (FWHM) can be put in the following form:

62

$$\Phi_{effective} = \frac{\Gamma_D}{FWHM} \Phi_{incident} ,\qquad\qquad (3.1)$$

where $\Phi_{effective}$ is the effective flux and Γ_D indicates the Doppler width of the resonance state, while $\Phi_{incident}$ is the incident flux that has an energy spread that is FWHM. Therefore, the reaction yield of the NRF is correlated by the energy spread by a function of (1/FWHM).

1.3.2.4. NRF Reaction Yield vs. Incident Flux

To more examine the relationship between the incident flux and the NRF reaction yield the simulation was performed for the different incident flux of 6.25×10^7, 1.25×10^8, 2.5×10^8, 5.0×10^8, 1.0×10^9, and 2.0×10^9. Fig 3.13 presents the effects of the incident flux on the reaction yield (events) of the NRF interaction. This figure demonstrated that the NRF reaction yield is directly proportional to the incident beam flux as presented in Fig. 3.14. Fig. 3.14 displays the linear fitting for the relation between the NRF reaction yield and the incident flux; this means that the NRF reaction yield linearly increases with the incident flux. The characteristics of the γ-ray source are considered the most challenging issue in the detection systems that are based on measuring the scattering NRF γ-rays in terms of the flux and its energy spread. As presented in Fig. 3.10, Fig. 3.13, and 3.14, the characteristics of γ-ray source are much more important in designing a detection system for the inspection purpose, which is considered a much more significant parameter in the inspection time estimation.
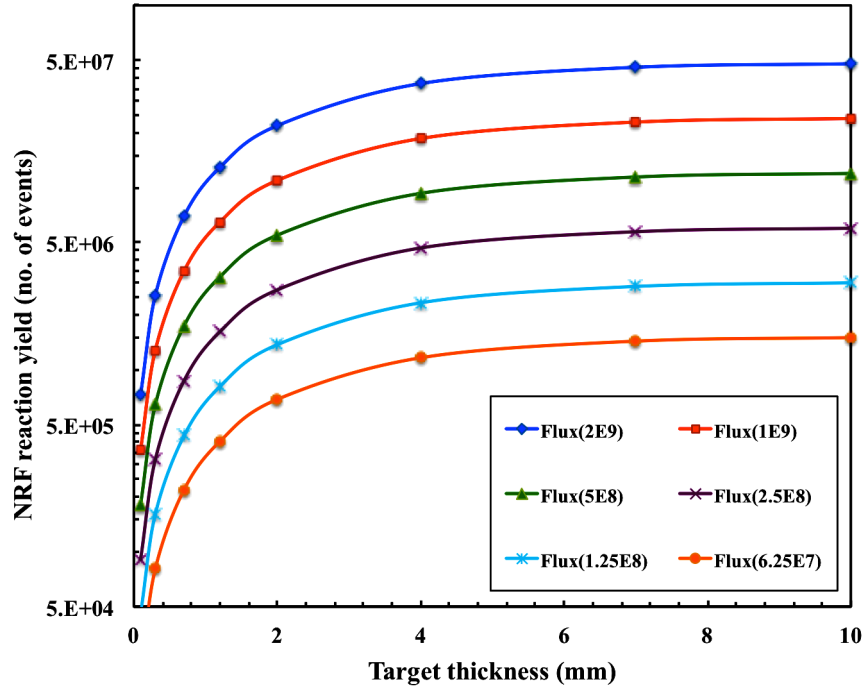
Fig. 3.13: *The NRF reaction yield (no. of events through the target) vs. the target thickness for a different incident beam flux of 2×10^9, 1×10^9, 5×10^8, 2.5×10^8, 1.25×10^8, and 6.25×10^7.*
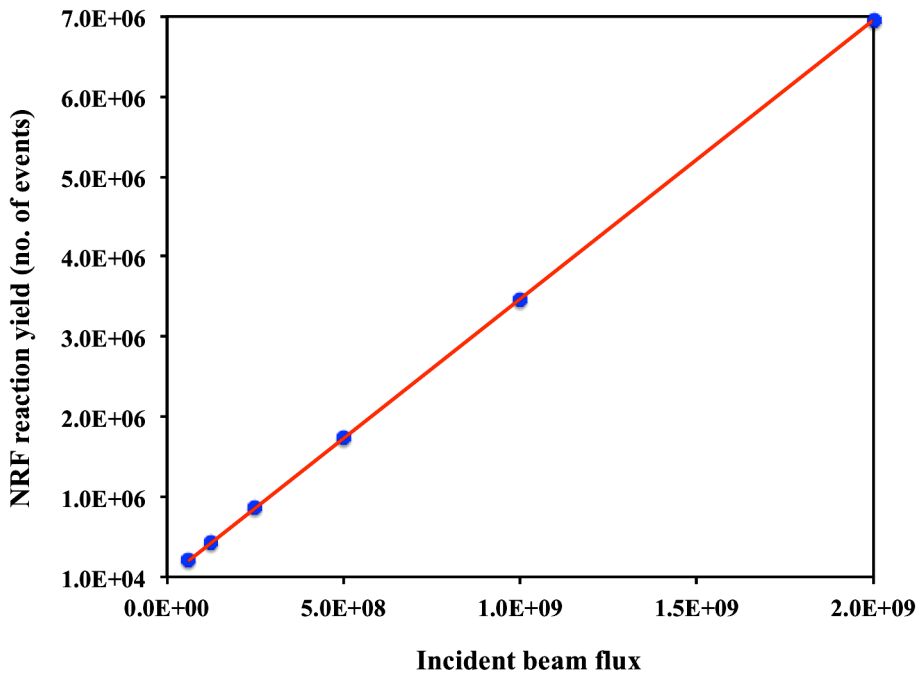
Fig. 3.14: *The NRF reaction yield (no. of events through the target) vs. the incident beam flux. The red line indicates the linear fitting for the simulation data. (The target thickness is 7 mm).*

1.3.2.5. Polarization Degree

The scattering NRF γ-rays have an angular distribution based on the polarization of the incident beam. Whereas, the simulation was performed for the incident beam with 100% linearly polarized that is perpendicular on the plane of detector setup. The polarization degree (asymmetry) can be calculated from measurement observation in the azimuthal plane (the plane that is a perpendicular on the incident beam direction) as following [22]:

$$P_\gamma = \frac{N_\perp\left(\Theta = 90^o, \Phi = 90^o\right) - N_\parallel\left(\Theta = 90^o, \Phi = 0^o\right)}{N_\perp\left(\Theta = 90^o, \Phi = 90^o\right) + N_\parallel\left(\Theta = 90^o, \Phi = 0^o\right)} \tag{3.2}$$

where $P_\gamma(E_\gamma)$ is the polarization degree (PD), $N_\perp$ ($N_\parallel$) is the NRF yield in the perpendicular (parallel) plane relative to the polarization of incident γ-beam. The Θ is the scattering plane angles, and Φ is azimuthal plane angles. The NRF yield as a function of the target thickness for a three scattering angles of the azimuthal plane are displayed in Fig. 3.15. The simulation results of the NRF yield in the Fig 3.15 are almost constant for the different scattering angles in the azimuthal plane in which the PD is 0.061. On the other hand, in the case of odd-A nuclei (such [235]U) the angular distribution that due to the half-integer spins involved in the cascade is nearly isotropic [22], this fact is clearly observed by the simulated result of the NRF yield in the azimuthal plane as shown in Fig 3.15 as well the PD quantity. Consequently, the angular distribution due to the polarized beam could be calculated well in the simulation code of NRF interaction.
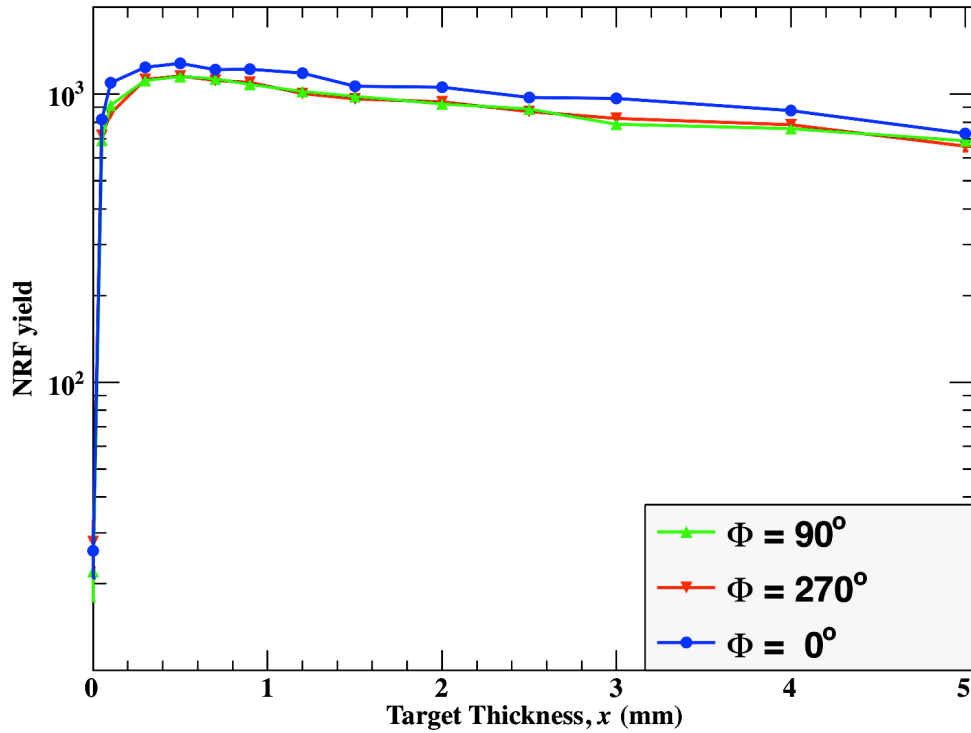
Fig. 315: *NRF yield for three scattering angles in the azimuthal plane for different target thickness of the HEU.*

1.4. Conclusion

A numerical study has been conducted for the NRF process and the Compton scattering to optimize the geometric configuration of the detector system setup for NRF measurements by using the Monte Carlo simulation toolkit GEANT4. Measurements of NRF γ-rays at backwards angles – relative to the interrogating beam direction – yield backgrounds that are significantly reduced relative to a comparable setup with measurement of forward–directed photons. For a heavy nuclei target, in this study, we assumed HEU (^{235}U) 90% with 10% of ^{238}U and a relatively low incident γ-ray energy (1733 keV), which the target absorption plays a significant role before and after the NRF process.

In this situation, backward-angle measurements are the optimum geometric configuration of the detector system for NRF γ-rays. In addition, the characteristic of incident beam flux in terms of the energy spread and the incident number demonstrated that the NRF yield was significantly affected by these terms. The γ-ray source with a much more intense number of incident photons with the smallest energy spread is preferable for designing the inspection system with a reasonable measuring inspection time. The PD for the HEU (even-odd nucleus) is calculated using MC simulation code of the NRF interaction that is verified by the theoretical principle.

CHAPTER 4

Analytical Model for the NRF

Reaction Yield

[Target Thickness Dependence]

In this section, we introduce an analytical model for the NRF reaction yield (NRF RY model) [54,55]. This model is used to interpret the saturation behavior that was deduced using the Monte Carlo simulation in chapter 3 and to describe the experimental measurements of the NRF reaction yield, which is presented in chapter 6. Additionally, the NRF RY model is useful to predict the expected yield of the NRF reaction, primarily for assaying nuclear materials. The NRF RY model is introduced for the thick and thin targets. The relationship between the NRF effective thickness and the total attenuation length due to the attenuation and the self-absorption component is deduced in the terms of the attenuation factors. The new technique is introduced to determine the NRF cross-section.

4.1 NRF Reaction Yield

To estimate the reaction yield of the NRF interaction with the isotope of interest (IOI), we assume the slab geometry that is presented in Fig. 4.1. The reaction yield of the NRF interaction caused by the incident γ-ray flux Φ_i can be described as follows.

i.   The incident beam flux Φ_i is attenuated prior to releasing the NRF γ-rays at a depth of x by an attenuation factor of $\left\{\exp\left[-\mu_i(E_i)\cdot r_i\right]\right\}$, where $\mu_i(E_i)$ is the linear attenuation coefficient for the electronic $\left\{\mu_e(E_i)\right\}$ and nuclear $\left\{\mu_n(E_i)\right\}$ interactions. E_i is the incident γ-ray energy, and r_i represents the incident pass length.

ii.   If the incident energy (E_i) or a portion of it is within the nuclear level width (Γ) of the IOI, $\left\{(E_r - \Gamma/2) \leq E_i \leq (E_r + \Gamma/2)\right\}$, then the NRF interaction will occur with the probability of the absorption NRF cross-section, σ. The released NRF γ-rays will have the angular distribution $W(\theta)$. These NRF γ-rays will undergo self-absorption by the electronic interaction in the target material prior to leaving it, by an attenuation factor of $\left\{\exp\left[-\mu_s(E_r)\cdot r_s\right]\right\}$, where $\mu_s(E_r)$ is the linear attenuation coefficient for the electronic interaction $\left\{\mu_e(E_r)\right\}$, E_r is the resonant energy of the NRF γ-rays for a particular level of the IOI, and r_s is the scattering pass length. Additionally, the intensity of the NRF γ-rays depends on the number of nuclei (N) per cm^3 of the IOI in the target.
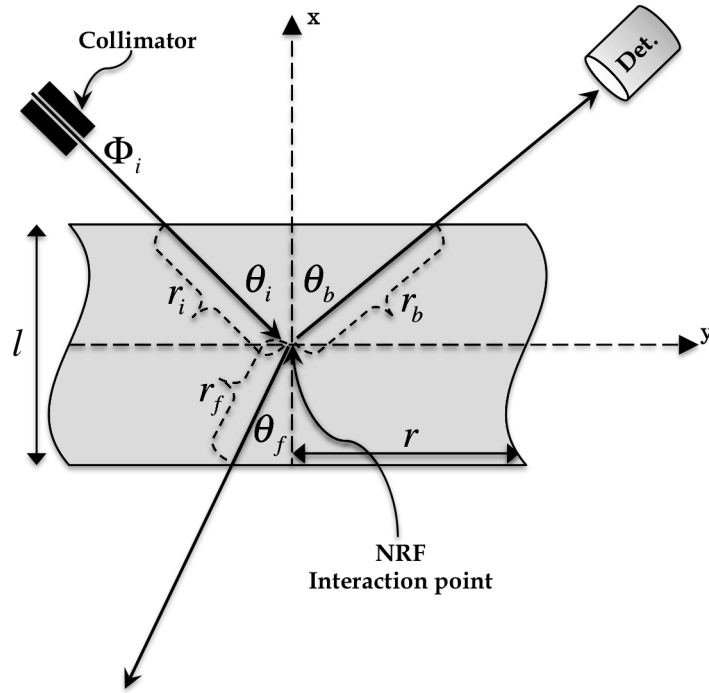
Fig. 4.1: *Schematic view of the slab geometry for the NRF interaction point and the scattering γ-rays in the backward and forward directions.*

iii. The measured scattering yield of the NRF γ-rays released from the target is dependent on the detection efficiency of the detector, $\varepsilon(E_r)$, and the fraction of the solid angle subtended by the detector, $(\Omega/4\pi)$.

Consequently, the NRF yield can be given by the following expression:

$$d^2Y = \left[\Phi_i \cdot e^{-\mu_i(E_i)\cdot r_i} \right] \cdot \left[N \cdot dx \cdot \sigma(E_i) \cdot dE \cdot W(\theta) \cdot e^{-\mu_s(E_r)\cdot r_s} \right] \cdot \left[\varepsilon(E_r) \cdot \frac{\Omega}{4\pi} \right] \qquad (4.1)$$

By integrating the reaction yield over the target thickness, x, and the incident γ-ray energy, E_i, we obtain the following equation:

$$Y = \left[\Phi_i \cdot N \cdot W(\theta) \cdot \varepsilon(E_r) \cdot \frac{\Omega}{4\pi} \right] \cdot \left[\int \sigma(E_i) \cdot dE \right] \cdot \left[\int e^{-\mu_i(E_i)\cdot r_i} \cdot e^{-\mu_s(E_r)\cdot r_s} \cdot dx \right] \qquad (4.2)$$

The first term of this equation represents the absolute values of the incident flux, the detection efficiency and the effective angular distribution, which depend on the polarization degree of the incident γ-rays, the type of the nucleus (even-even, odd-odd, or even-odd), and the spin sequence between the transition states (dipole, quadrupole, or mixing). The second term represents the integration over the incident energy within the nuclear-level width of the IOI. The third term represents the integration over the target thickness in terms of the attenuation and the self-absorption of the γ-rays through the target material.

4.2   NRF Attenuation Term

The attenuation factor for the scattering NRF γ-rays depends on the target geometry and the detector position. The attenuation factor consists of two components, the non-resonant component by the electronic interaction before and after the NRF interaction, and the resonant attenuation by the nuclear interaction via the absorption of the NRF. The self-absorption effects of the resonance must be corrected numerically, especially for the thick targets and the strong NRF transitions, for which the attenuation factor is more significant. However, the merit of the thin targets analysis is that the self-absorption of the NRF γ-rays can be neglected. Another feature for the measurements of the thin targets is the low scattering background.

• **Backward Scattering**

The analytical model is introduced to study the attenuation and self-absorption of the incident γ-rays and the scattering NRF γ-rays. We assumed the incident flux, Φ_i, with an angle θ_i relative to the perpendicular axis on the target surface, as shown in Fig. 2, and an incident pass length of $r_i = x / \cos(\theta_i)$. Supposing an incident energy within the nuclear level width (Γ), the NRF γ-rays will be scattered in all of the possible directions with an angular distribution of $W(\theta)$. We assume that the backward scattering has an angle θ_b, and that the scattering length is $r_b = x / \cos(\theta_b)$. Thus, the attenuation term for the backward scattering will be as follows:

$$\int e^{-\mu_i(E_r)\cdot r_i} e^{-\mu_s(E_r)\cdot r_b}\, dx = \int e^{-\mu_i(E_r)\frac{x}{\cos(\theta_i)}} e^{-\mu_s(E_r)\frac{x}{\cos(\theta_b)}}\, dx \tag{4.3}$$

By integration over the target thickness l, we obtain the following expression:

$$\Rightarrow \int_0^l e^{-\left(\mu_i(E_r)\cdot\sec(\theta_i)+\mu_s(E_r)\cdot\sec(\theta_b)\right)x}\, dx$$

$$= \frac{1 - e^{-\left(\mu_i(E_r)\cdot\sec(\theta_i)+\mu_s(E_r)\cdot\sec(\theta_b)\right)l}}{\mu_i(E_r)\cdot\sec(\theta_i)+\mu_s(E_r)\cdot\sec(\theta_b)} \tag{4.4}$$

$$= \frac{1 - e^{-\mu(E_r)\cdot l}}{\mu(E_r)}$$

where $\mu(E_r) = \mu_i(E_r)\cdot\sec(\theta_i)+\mu_s(E_r)\cdot\sec(\theta_b)$ (4.5)

is the total attenuation, $\mu_i(E_r)$ is the attenuation for the incident γ-rays of the electronic $\{\mu_e(E_r)\}$ and the nuclear absorption by the NRF $\{\mu_{NRF}(E_r)\}$; *i.e.*

$\mu_i(E_r) = \mu_e(E_r) + \mu_{NRF}(E_r)$, and $\mu_s(E_r)$ is the attenuation for the scattering NRF γ-rays for the electronic interaction only for $\{\mu_s(E_r) = \mu_e(E_r)\}$, where $\mu_e(E_r)$ and $\mu_{NRF}(E_r)$ can be expressed according to the following equation:

$$\mu_e(E_r) = \frac{N_a}{M} \sum_n \sigma_n^a(E_r) \tag{4.6}$$

where M is the effective mass number of the target material, N_a is Avogadro's number, σ_n^a is the atomic cross-section of the interaction type n, e.g., n denotes Compton scattering, the photoelectric effect, pair production, etc. In addition, the following equation is true:

$$\mu_{NRF}(E_r) = \frac{N_a}{M_{IOI}} \sigma_{NRF}^{ij} \tag{4.7}$$

where σ_{NRF}^{ij} represents the cross-section of the NRF transition line j of the ith isotope, and M_{IOI} is the atomic mass of the IOI.

• Forward Scattering

In the case of forward scattering, the total attenuation factor is given by replacing the scattering angle θ_b with θ_f, (see Fig. 4.1), therefore obtaining the following equation:

$$\mu(E_r) = \mu_i(E_r) \cdot \sec(\theta_i) + \mu_s(E_r) \cdot \sec(\theta_f). \tag{4.8}$$

The total attenuation term, which is given by Eq. (4.4), represents the effective thickness of the NRF interaction through the target thickness (later, we will present the relationship between the effective thickness and the attenuation length of the NRF γ-rays).

When the incident γ-rays are parallel to the x-axis $(\theta_i = 0)$, the total attenuation factor will be in the following form:

$$\mu(E_r) = \mu_i(E_r) + \mu_s(E_r) \cdot \sec(\theta)$$

$$= \mu_e(E_r) + \mu_{NRF}(E_r) + \mu_e(E_r) \cdot \sec(\theta) \qquad (4.9)$$

$$= \mu_e(E_r)(1 + \sec(\theta)) + \mu_{NRF}(E_r)$$

where θ represents θ_b or θ_f.

• Ninety-Degree Scattering

For a scattering angle of 90º and an incident angle θ_i equal to zero, we assume a fixed shape. Assuming a cylindrical shape with thickness l and radius r, the attenuation term will be in the following form:

$$\Rightarrow \frac{1 - e^{-(\mu_{NRF}(E_r) + 2\mu_e(E_r))l}}{\mu_{NRF}(E_r) + 2\mu_e(E_r)} e^{-\mu_e(E_r) \cdot r} \qquad (4.10)$$

where l represents the thickness of the target, and r indicates the length from the beam center to the boundary of the shape in the ninety-degree direction. For example, in the cube, l and r represent the side length of the cube, whereas in case of the sphere, l and r represent the sphere radius.

• Integration Over the Incident Energy

Because of the resonance that occurs within a narrow energy window, the range of the level width Γ, the integration of the cross-section over the incident energy, will change over the range of $(E_r - \Gamma_D/2)$ to $(E_r + \Gamma_D/2)$, considering the thermal motion and the Doppler width, thus obtaining the following expression:

$$\int_{(E_r-\Gamma_D/2)}^{(E_r+\Gamma_D/2)} \sigma(E_i) \cdot dE = \Gamma_D \cdot \sigma_{NRF}(E_r) \tag{4.11}$$

where Γ_D is the Doppler width of a broadened resonance level, which is given by Eq. (2.43).

4.3 Integrated NRF Reaction Yield

The integrated NRF reaction yield is given by substituting Eq. (4.4 or 4.10) and Eq. (4.11) into Eq. (4.2), thus obtaining the NRF reaction yield, Y, in the following form:

$$Y = \left[\Phi_i \cdot \Gamma_D \cdot N \cdot \sigma_{NRF}(E_r) \cdot W(\theta)\right] \cdot \left[\varepsilon(E_r) \cdot \frac{\Omega}{4\pi}\right] \cdot \left[\frac{1 - e^{-\mu(E_r) \cdot l}}{\mu(E_r)}\right] \tag{4.12}$$

This equation consists of three terms. The first term represents the absolute values of the incident beam flux within the level transition, the NRF cross-section, and the NRF angular distribution. The second term represents the detection efficiency for the detection system. The third term represents the

attenuation term due to the attenuation and self-absorption of the γ-rays before and after the NRF interaction.

4.4 Effective Thickness of the NRF Interaction

The last term in Eq. (4.12) of the attenuation represents the effective thickness of the NRF interaction within the target thickness as follows:

$$x_{effective} = \frac{1 - e^{-\mu(E_r) \cdot l}}{\mu(E_r)} \tag{4.13}$$

If the thickness $l \geq x^{Max}$ where $\left\{ \exp\left[-\mu(E_r) \cdot x^{Max} \right] \to 0 \right\}$, then the maximum effective thickness becomes the following:

$$x_{effctive}^{Max} \approx \frac{1}{\mu(E_r)} = \chi_0, \tag{4.14}$$

where χ_0 is the total attenuation length for the γ-rays before and after the NRF interaction, indicating that the maximum effective length is equal to the total attenuation length. Using this expression, we can estimate the maximum effective length for the NRF interaction in the interrogation sample by knowing the electronic attenuation in the material sample and the resonance cross-section of the transition level.

Consequently, the maximum value for reaction yield of the NRF interaction can be approximated according to the following expression:

$$Y^{Max} \approx \Phi_i \cdot \Gamma_D \cdot N \cdot \sigma_{NRF}(E_r) \cdot W(\theta) \cdot \varepsilon(E_r) \cdot \frac{\Omega}{4\pi} \cdot \chi_0 \qquad (4.15)$$

Therefore, the yield of the NRF reaction has a maximum value that depends on the attenuation length through the target due to the atomic and nuclear absorption. However, for thin targets, the attenuation term (the effective thickness) can be approximated according to the following expression:

$$\frac{1 - e^{-\mu(E_r)l}}{\mu(E_r)} \approx \frac{1 - (1 - \mu(E_r) \cdot l)}{\mu(E_r)} = l \qquad (4.16)$$

Thus, the reaction yield of the NRF interaction for thin targets can be approximated as a linear function in the following form:

$$Y \approx \Phi_i \cdot \Gamma_D \cdot N \cdot \sigma_{NRF}(E_r) \cdot W(\theta) \cdot \varepsilon(E_r) \cdot \frac{\Omega}{4\pi} \cdot l \qquad (4.17)$$

Thus, the NRF yield for a thin target shows a nearly linear behavior. Because the attenuation factor depends on the strength (the cross-section) of the NRF transition, the reaction yield for the thin targets and the relatively low cross-section for the transition NRF, the attenuation can be ignored, which simplifies the NRF yield calculated by Eq. (4.17).

4.5 NRF Reaction Yield in the Fitting Form

The NRF RY model can be expressed in the form of the fitting parameters C_0, C_1 and C_2, which can be used to fit the experimental or the

simulation results to extract the attenuation factors. In the case of backward or forward scattering with a scattering angle of θ based on Eq. (4.12), the reaction yield can be expressed in the following form:

$$Y = C_0 \cdot \frac{1 - e^{-\left[C_1(1+\sec(\theta))+C2\right]x}}{C_1\left(1+\sec(\theta)\right)+C2}$$ (4.18)

In contrast, for the scattering NRF γ-rays with an angle of 90°, the following equation is applied:

$$Y = C_0 \cdot \frac{1 - e^{-(2C_1+C_2)x}}{2C_1 + C_2} e^{-C_1 \cdot r},$$ (4.19)

where

$$C_0 = \Phi_i \cdot \Gamma_D \cdot N \cdot \sigma_{NRF}(E_r) \cdot W(\theta) \cdot \varepsilon(E_r) \cdot \frac{\Omega}{4\pi} \cdot \prod_k \exp(-\mu_k x_k),$$ (4.20)

$C_1 = \mu_e(E_r)$, and $C_2 = \mu_{NRF}(E_r)$,

where $\prod_k \exp(-\mu_k x_k)$ is the multiplicand of the attenuations of the absorbers, k, that are situated in front of the detector.

Using these equations, we can determine the total attenuation factor from the fitting parameters and the NRF attenuation factor from the parameter C_2, therefore enabling the calculation of the NRF cross-section using C_2, and Equation (4.7).

Fig. 4.2 represents the NRF reaction yield versus the target thickness, assuming that C_0 and C_1 in Eq. (4.18) are equal to unity, *i.e.*, the total

attenuation is equal to one in the units of the target thickness presented in the figure. This figure shows a saturation behavior for the NRF reaction yield as a function of the target thickness. The curvature of the saturation curve depends on the total attenuation factor of the atomic and the NRF absorption. Consequently, we expect a saturation behavior for the NRF reaction yield for the NRF interaction through the target material.
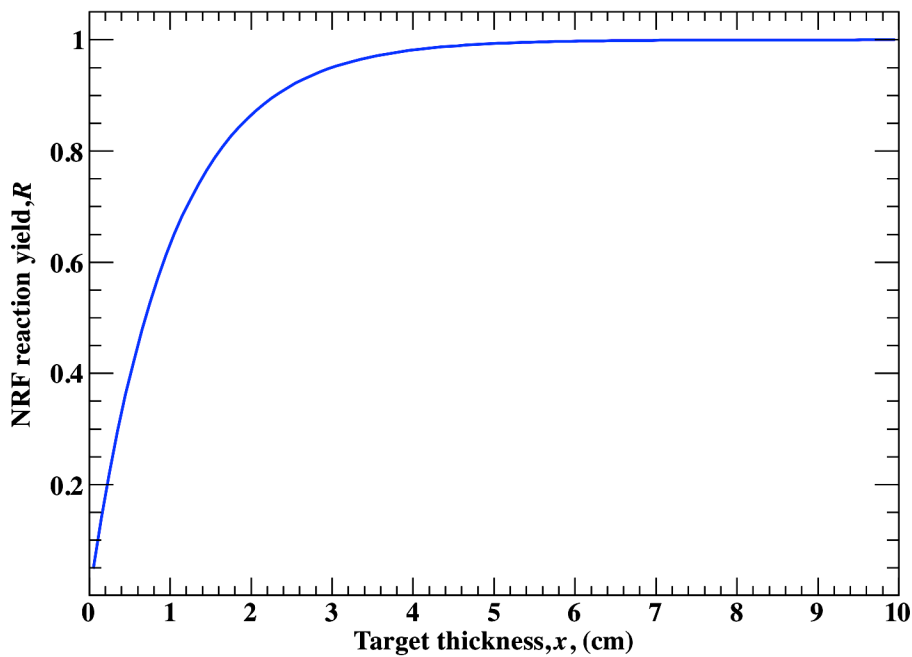
Fig. 4.2: *The expected saturation curve for the NRF reaction yield for the total attenuation factor of 1.0 cm^{-1}.*

In chapter 6, we introduce the experimental results of the NRF reaction yield for different target thicknesses of the depleted uranium. The NRF RY model will be used to reproduce the experimental and the simulation data.

We should emphasize that the NRF RY model can determine the NRF cross-section based on the attenuation factor of the NRF interaction, which is

determined from the fitting parameters of the experimental saturation curve. The merit of this method is that the cross-section can be determined without any absolute measurements for the incident flux and the detection efficiency of the detector array or the flux monitors along with the effective angular distribution of the scattering NRF γ-ray. This new technique will be used along with the absolute measurement technique (the knowing method) to determine the NRF cross-section in section 6.2.

4.6 Conclusion

An analytical model for the NRF reaction yield has been derived. The main term of the NRF RY model is the attenuation term, which determines the behavior of the NRF yield with the target thickness. The NRF yield has a linear trend for the thin targets and the smallest transition probability (NRF cross-section). However, the NRF yield has a saturation tendency for the thicker targets. The maximum effective thickness for the NRF interaction is approximately equals the attenuation length (atomic and nuclear absorption) of the γ-rays through the target. A new technique for estimation the NRF cross-section is introduced, which based on the fitting the experimental NRF yield using the NRF RY model to extract the NRF attenuation factor that leads to determine the NRF cross-section directly without the absolute measurements.

CHAPTER 5

The ERF of the LaBr$_3$:Ce Detector Using GEANT4

We are planning to use the LaBr$_3$:Ce detector in a detector array of an inspection system for the special nuclear materials (SNMs), such as ^{235}U and ^{239}Pu, by the NRF technique using the laser Compton backscattering (LCS) γ-ray beam. To study the possibility of using a LaBr$_3$:Ce detector to measure the NRF with the laser Compton scattering (LCS) γ-rays, the Energy Response Function (ERF) was determined using a Monte Carlo (MC) simulation toolkit, GEANT4 [56], which considers the internal radioactivity sources, and in which the LaBr$_3$:Ce detector has internal radioactivity sources of a meta-stable isotope ^{138}La (T$_{1/2}$=1.02×10^{11} y) and an α-decay chain from ^{227}Ac (T$_{1/2}$=21.77 y). The measurement spectra were used to calibrate the simulation up to 2.8 MeV. The quenching factor of the α-particles was deduced and showed a second-order polynomial response to their emission energies. The ERF that was reproduced from the MC code is reasonably consistent over the energy range of interest. The internal radiation activities (the count rate per cm^3) of the LaBr$_3$:Ce crystal were deduced as 1.44±0.12 Bq/cc.

A NRF spectrum of [238]U was measured using the LCS γ-ray of approximately 2.5 MeV at the HIγS facility of Duke University. The ERF code was applied to calculate this NRF spectrum; this will be introduced in the next chapter. The background originating from the internal and external radioactivity was evaluated.

5.1   Introduction

Recently, a nondestructive measurement method for shielded special nuclear materials (SNMs), such as [235]U or [239]Pu, has been proposed [12,23,57,58]. The special nuclear materials are measured using the nuclear resonance fluorescence (NRF) measurement technique with an energy tunable laser Compton-scattering (LCS) γ-ray source [12,23,58-60]. In previous studies, it has been considered that the scattered γ-rays are measured using highly pure germanium (HPGe) semi-conductor detectors because the energy resolution of the HPGe detector is excellent, typically $dE/E \sim 0.2\%$ at 1.33 MeV. The development of cerium-doped lanthanum halide crystals has gained special interest because of their excellent scintillator properties compared with NaI(Tl) and other scintillation crystals. Among the cerium-doped lanthanum halide crystals, $LaBr_3$:Ce is the most promising crystal with a high light output of approximately 63 photons/keV, a fast rise time of approximately 16 ns, a density of 5.08 g/cm^3, and an emission wavelength of 380 nm [61,62]. The high Z of the La atom makes the $LaBr_3$:Ce crystal a good γ-ray and β-particle detector. $LaBr_3$:Ce has been introduced for γ-ray spectral analysis because its photo peak resolution is

more than two-fold better than that for the conventional NaI(Tl) scintillation detectors (approximately 3% compared with 7% at the ^{137}Cs line of 662 keV).

In our previous study, we have proposed the use of the cerium-doped lanthanum halide crystal scintillator as LaBr$_3$:Ce instead of the HPGe detectors [17]. Furthermore, we have studied the performance and feasibility of the LaBr$_3$:Ce detector in a detector array for the inspection system of the SNMs using NRF with the LCS γ-ray beams [17,63,64]. However, there is one disadvantage because of the series of the self-activity/contamination of the radioisotope in the LaBr$_3$:Ce detector up to 2.8 MeV. The LaBr$_3$:Ce and LaCl$_3$:Ce detectors have two different types of contamination. One type is a meta-stable isotope ^{138}La. The isotopic abundance of ^{138}La is only 0.089%, and the half-life is $1.02\pm0.01\times10^{11}$ years [65]. In the energy region of 1.8 – 2.8 MeV, a bump appears, which has been considered an overlap of the α-particle peaks [66]. With the α-γ coincidence measurements, certain peaks among the bump are assigned to unstable isotopes as ^{227}Th, ^{223}Ra, ^{219}Rn, ^{211}Bi [67,68]. It has been concluded that the dominant source of the α-particles is the decay chain of a contaminated element ^{227}Ac ($T_{1/2}$=21.77 y), which is the chemical homologue of La. However, because the α-emitters occasionally decay to the ground state without any γ-ray emission, the detailed structure of the bump at approximately 2 MeV remains unestablished. In this energy region, there are many resonant energy levels of special nuclear materials, such as ^{235}U and ^{239}Pu; these levels are key for their nondestructive detection. Therefore, the study on the energy response function (ERF) of the LaBr$_3$:Ce detector is important, particularly over the energy range of 1.8 – 2.8 MeV [63,64].

In this chapter, the developed ERF of the LaBr$_3$:Ce detector using a Monte Carlo simulation toolkit, known as GEANT4 [45,46] is demonstrated. Then, the ERF code is used to investigate the precise ERF of the internal contamination and the expected radiation activities in the LaBr$_3$:Ce detector.
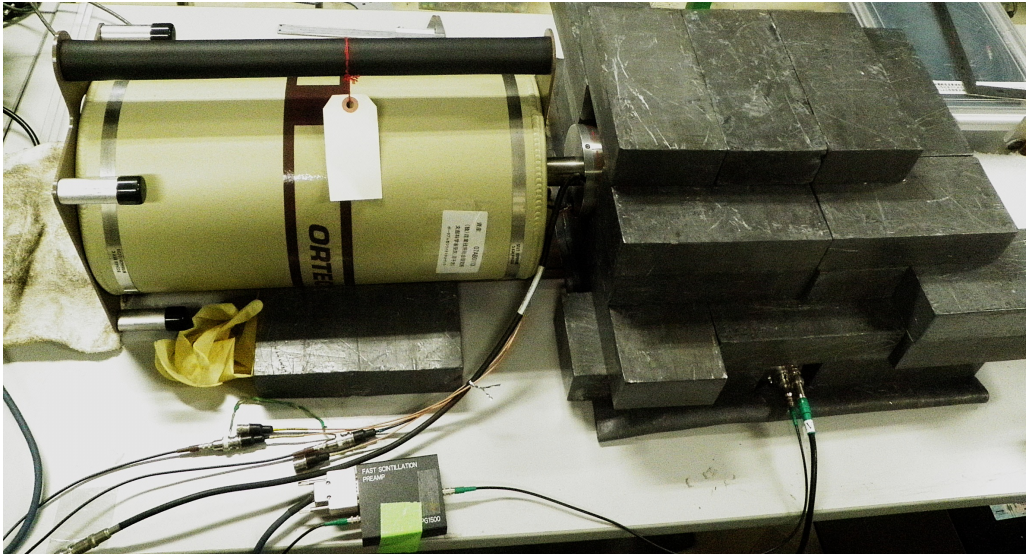
Fig. 5.1: *the experimental setup for the LaBr$_3$:Ce detector with the HPGe (120%) detector to measure the background of the LaBr$_3$:Ce.*

5.2   The ERF Measurement

The γ-ray spectra were measured using a LaBr$_3$:Ce detector, the Saint-Gobain BrilLanCe 380 (3.81 cm in diameter and 7.62 cm in length), which was connected to a 1.5″ photomultiplier (R9420, Hamamatsu) and a digital signal-processing (DSP) unit (Model AU8008, TechnoAP). The DSP unit was used to process the signals from the LaBr$_3$:Ce detector. The energy spectra were calibrated using the standard γ-ray sources, ^{137}Cs and [60]Co. The LaBr$_3$:Ce detector was placed in a lead box of 10-cm thickness. The γ-ray sources were placed 2.0 cm from the front surface of the detector. The geometry

configuration for the experimental setup of the LaBr$_3$:Ce detector with the HPGe (120% - relative efficiency) detector, to measuring the background of LaBr$_3$:Ce, is shown in Fig. 5.1.

5.3 MC Simulation, GEANT4

The ERF of the LaBr$_3$:Ce detector was performed using the MC simulation GEANT4 toolkit. GEANT4 is a software package composed of tools, which can be used to accurately simulate the passage of particles through matter. There are three main classes in the code of the ERF of the LaBr$_3$:Ce detector. The first class is called a detector construction, which describes the geometrical structure of the experimental setup and the detector, as provided by the manufacturer. The second class is the physics list [69], which contains implementations of the models of the physical interactions, as follows: the electromagnetic (EM) interactions of the leptons, photons, hadrons and ions, and the hadronic interactions. The third class is the primary generator action, which implements the facilities required to describe the physical properties of the particles. The general particle source (GPS) module [70] was used as a particle generator, which can be used to create a certain source shape with a specific position, angle and energy distribution, among others. In the case of the internal activity, a volume cylindrical source was created as the same size/shape of the crystal of LaBr$_3$:Ce, and in the case of the standard radioactive source (such as ^{137}Cs), an isotropic point source was created.

The GEANT4 toolkit provides a radioactive-decay module [69] using the data provided by the Evaluated Nuclear Structure Data File (ENSDF) [70]. The radioactive-decay module generates all of the decay components that are radiated from a specified radioisotope source. In the present study, we used the radioactive-decay module to generate the spectra for the chosen isotopes or radioactive chains, such as ^{238}U, ^{235}U, or ^{232}Th, inside or outside of the detector.
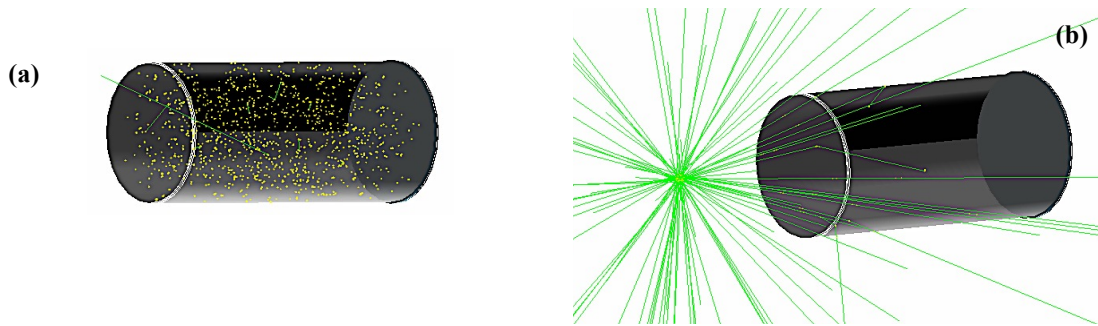
Fig. 5.2: *Three-dimensional view of the LaBr₃:Ce detector. (a) In the case of the internal activity by the α-particles, and (b) in the case of an isotropic γ-ray source in front of the detector.*

Fig. 5.2 presents the GEANT4-simulated three-dimensional view of LaBr₃:Ce with the exact specifications that the manufacturer provided and the tracking of the α-particles inside of the detector as a volume source, as shown in Fig. 5.2 (a), whereas in Fig. 5.2 (b), it is an isotopic source with the γ-rays tracking through the detector. The simulations were performed for 10^7-10^8 events to reduce the statistical uncertainty considering all of the possible physics processes. The secondary production threshold for the γ-rays was set at 10 keV. All of the data analyses in this study were performed using the ROOT analysis toolkit [71].

The differential pulse height spectrum corresponding to a particular energy E_0 of the incident particles is called the *response function* of the detector. We denote this function as $F(E, E_0)$. The energy response function of a LaBr$_3$:Ce detector for the incident energy E_0 has been assumed a Gaussian energy distribution in the simulation code, which can be expressed by the following equation:

$$F(E, E_0) = \frac{N_0}{\sigma\sqrt{2\pi}} \exp\left(\frac{(E - E_0)^2}{2\sigma^2}\right)$$ (5.1)

where E_0 is the average energy of the pulse height (the peak center of the incident energy), σ is the standard deviation of the pulse height, and N_0 is the total number of pulses. The statistical uncertainty of the pulse height is reflected by the width (the energy resolution, R) of the response function. This width (ΔE) is typically measured at the half-height of the peak (or the so-called full width at half maximum, FWHM). The energy resolution, R, is a function of the energy distribution of the pulse height E as follows [72]:

$$R = a + \frac{b}{\sqrt{E}}$$ (5.2)

where the parameters a and b are the fitting parameters of the experimental spectra. For the charged particles, their energy distribution becomes broader when they pass through matter. Therefore, the distribution of the pulse heights that are caused by the interaction of those particles with a detector material also widens. Thus, different parameter values of a and b were set in the simulation code of the ERF, where the parameter b was 0.77 keV$^{1/2}$ for the γ-rays and 1.85 keV$^{1/2}$ for the α-particles.

In the next section, the experimental and simulated results of the γ-ray standard source, ^{137}Cs, is presented to benchmark the ERF simulation code using GEANT4. Subsequently, the simulation code of the ERF is used to reproduce the ERF because of the internal contaminations of the internal activities and the external background contribution due to the natural background radiation from ^{40}K and ^{208}Tl.

5.4   Results and Discussion

5.4.1   The ERF of Standard Sources

Fig. 5.3 shows the ERF of ^{137}Cs (662 keV) from the measurement and the MC simulation code GEANT4, which are clearly consistent with each other. The simulated energy spectrum was generated for a number of events, which were evaluated using the activity of the ^{137}Cs source and the measurement of the live time. The source shape is a point source with the isotropic radiation as it displayed by the Fig 5.2 (b). The peak at approximately 210 keV was attributed to the backscattering γ-rays from the lead shield on which the source–detector setup was placed. The ratio between the internal and external activities was adopted using the multiple Gaussian fitting for the experimental spectrum, as described in the following section. Note that the simulation spectrum for ^{60}Co can also reproduce the measured spectrum as presented by the Fig. 5.4. Consequently, we can successfully reproduce the energy spectrum of any radioactive-isotope using the ERF simulation code, which is based on GEANT4, according to the available radioactive decay data.
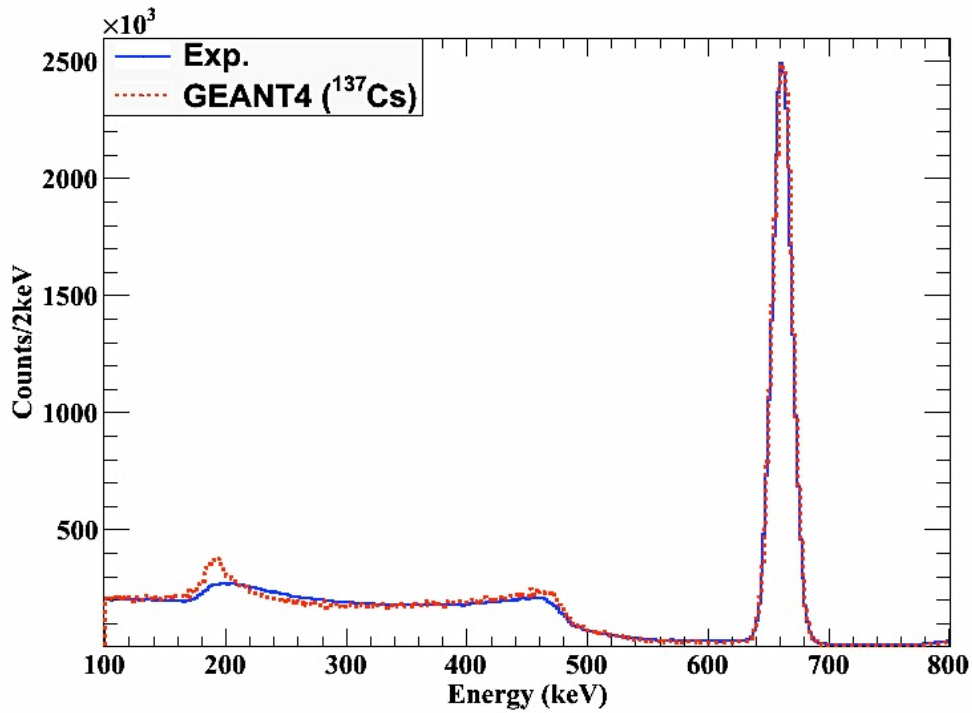
Fig. 5.3: *Comparison between the experimental and the simulated ERF of the LaBr₃:Ce detector to measure the γ-line of a standard γ-ray source of ¹³⁷Cs.*
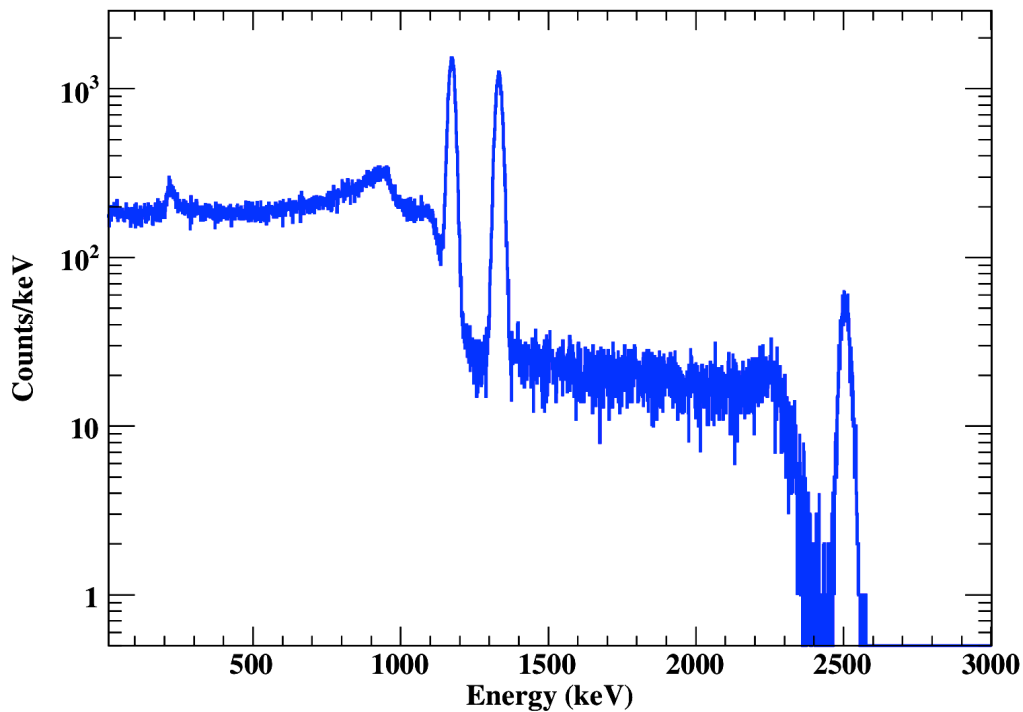
Fig. 5.4: *The ⁶⁰Co simulation spectrum as the ERF for the LaBr₃:Ce detector using the simulation code of the ERF that devolved in GEANT4. The source strength is 1 MBq. The source-detector distance is 2 cm. The source shape is a point source.*

5.4.2 The ERF for the Internal Activities/Contributions

The background spectrum of LaBr$_3$:Ce, which is caused by the internal contamination of the radioactive isotopes, consists of two major types of contamination. The first type is from an unstable isotope, ^{138}La, which is present in natural La with an abundance of 0.089% and a half-life of 1.02 × 10^{11} years. The second type is the contamination of the element ^{227}Ac (21.77 years), which is the chemical homologue of La.

The BG spectrum can be divided into the following two regions according to the contamination type: the first region ranges from 0 to ~ 1600 keV, which includes the contributions of the X-ray, γ-ray, and β-particle emitters. The second region ranges from ~ 1600 to 2800 keV, which includes the contributions of the α-particle emitters.

5.4.2.1 *The ERF of the contributions of the X-ray, γ-ray, and β-particle emitters*

Fig. 5.5 shows the expected contributions for each isotope in the background spectrum of the LaBr$_3$:Ce detector, which is simulated using the ERF simulation code, in the experimental background spectrum from the X-ray, γ-ray, and β-particle emitters. The primary contamination of the internal sources is the meta-stable isotope ^{138}La. ^{138}La has two decay modes as presented in Fig. 5.6; one decay mode is caused by electron-capture (EC) with a Q value of 1738 keV, and the second decay mode is caused by β-emission with a Q value of 1044 keV. Moreover, the decay modes are described in Eqs.

(5.3) and (5.4). All of the byproducts and features of the ¹³⁸La–decays clearly appeared in the background spectrum of LaBr₃:Ce, where the peak at approximately 1460 keV consists of three peaks, as shown in Fig. 5.7. The first peak at ~1438 keV is caused by the γ-ray emission from a daughter nucleus ¹³⁸Ba. The second peak at 1461 keV is attributed to the natural ⁴⁰K isotope as an external contribution, and the third peak at ~1470 keV is attributed to the pile-up/coincidence between the γ-ray line of ¹³⁸Ba and its X-ray emission from an atomic shell by approximately 32 keV energy according to the atomic shell emission K_α or K_β.
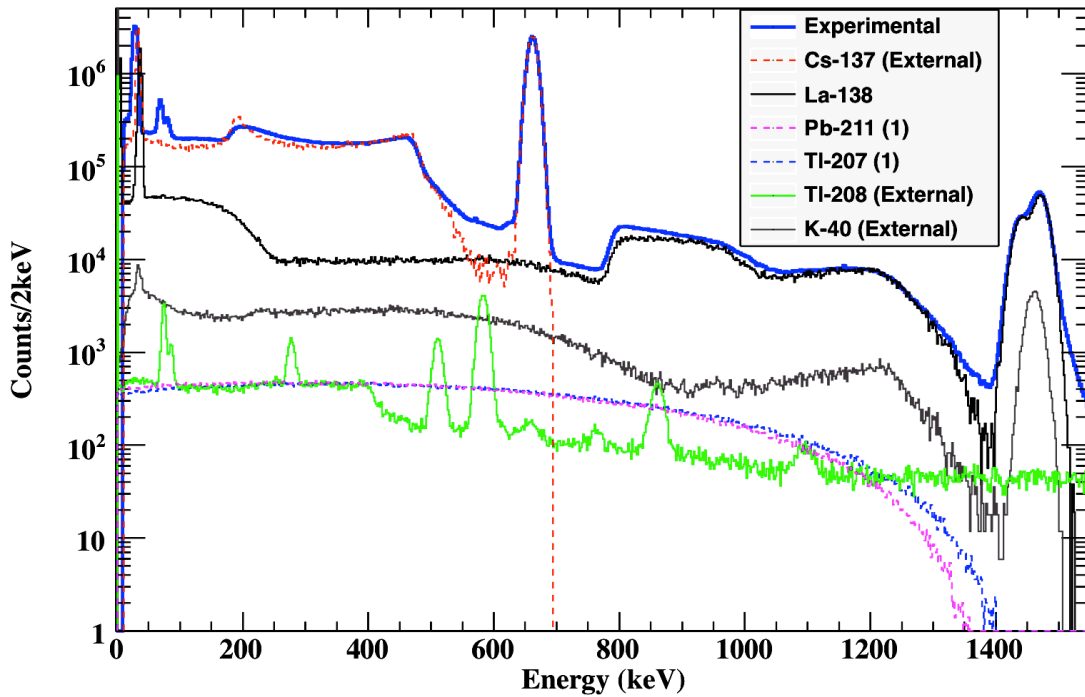
Fig. 5.5: *Simulation of the ERF of the expected contributions in the experimental background spectrum for the expected isotopes of the internal contributions and the external natural radiation sources. The internal contributions were from ¹³⁸La, ²¹¹Pb, and ²⁰⁷Tl. The external contributions were from ⁴⁰K, ²⁰⁸Tl, and ¹³⁷Cs (the standard source for calibration). The numbers between the brackets indicate the relative strength of the radioactive chains, see Fig. 5.9.*
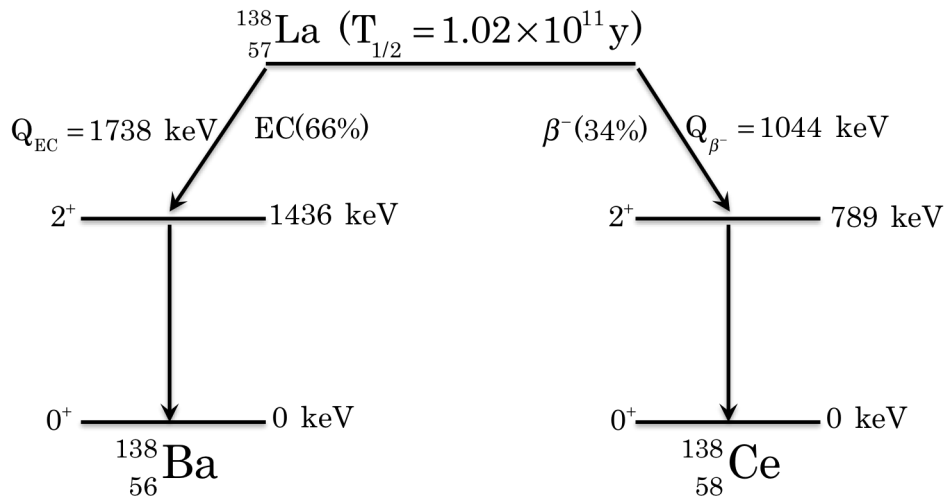
Fig. 5.6: ^{138}La *partial decay scheme.*
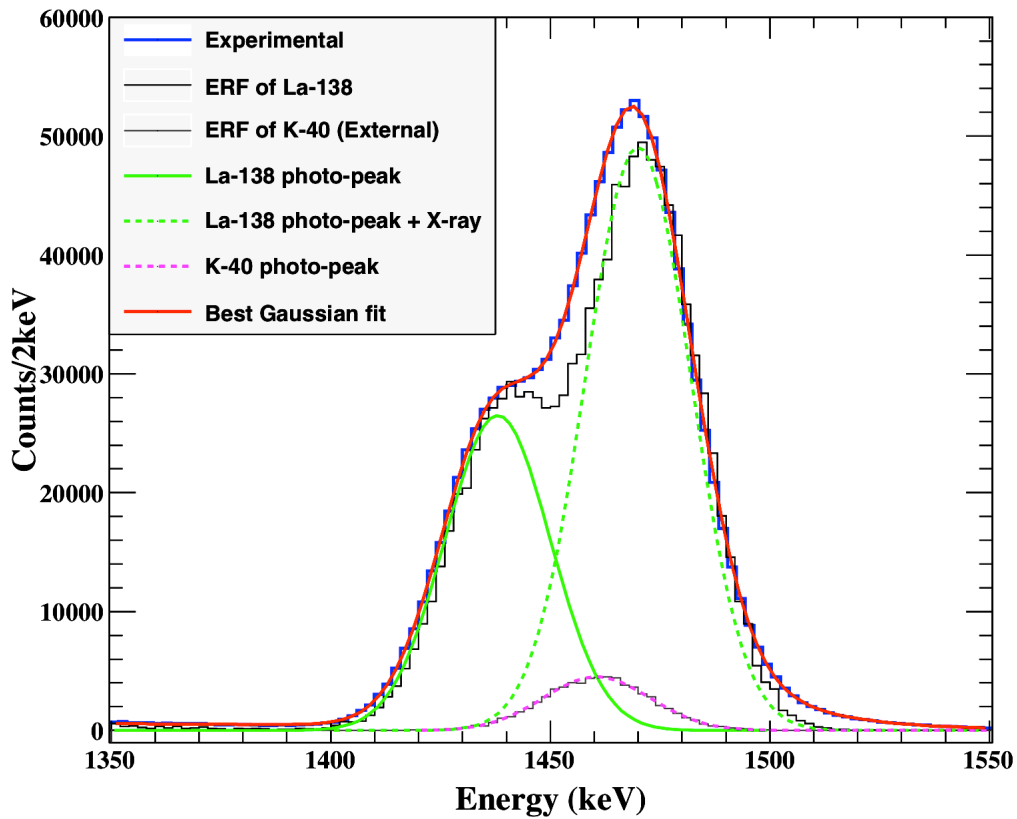
Fig. 5.7: *The best fit for the background peak at approximately 1460 keV using three Gaussian peaks, the photo-peak of ^{138}La, the photo-peak of ^{138}La plus the released atomic X-ray, and the ^{40}K photo-peak. Furthermore, the simulated ERF for the ^{138}La (as an internal source) and ^{40}K (as an external source) isotopes with the expected intensities in the background peak (the entire energy spectra are presented in Fig. 5.5).*

$$^{138}_{57}\text{La} + e^- \xrightarrow{\text{EC (66\%)}} {}^{138}_{56}\text{Ba} + \gamma - \text{ray (1436 keV)} + \text{X} - \text{ray} (\sim\!32\text{ keV}) \qquad (5.3)$$

$$^{138}_{57}\text{La} \xrightarrow{\beta^- - \text{decay (34\%)}} {}^{138}_{58}\text{Ce} + \beta^- (\sim\!255\text{ keV}) + \gamma - \text{ray (789 keV)} \qquad (5.4)$$
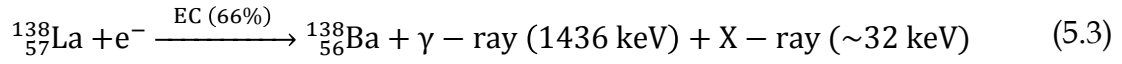
Note that all of the features and decay modes of the simulated ^{138}La spectrum are consistent with the experimental energy spectrum in terms of the decay mode, strength, and energy resolution, as shown in Figs. 5.5 and 5.7. The strengths of the ^{138}La and ^{40}K isotopes in the background spectrum were adapted according to the best fit to the entire peak at approximately 1460 keV using three Gaussian peaks, as shown in Fig. 5.7. The relative intensities of these three peaks of energies, specifically 1438, 1461, and 1470 keV, are 33.07, 5.69, and 61.24 %, respectively. In addition, the expected activity for ^{138}La (as an internal contamination source) was 123±11 Bq (1.42±0.11 Bq/cc).

Furthermore, the activity of ^{138}La inside the LaBr$_3$:Ce crystal can be calculated from its natural abundance (a_{La138} = 0.089%), half-life ($t_{1/2}$ = 1.02±0.01 × 10^{11} years [65]), and the lanthanum mass, m_{La}, which can be calculated from the mass of lanthanum bromide, m_{LaBr_3}, and the molecular-weight of lanthanum (mw_{La138}= 138.9 g/mol) and bromine (79.9 g/mol), which is 160.6 g for the current volume of the LaBr$_3$:Ce crystal. The activity or decay rate in Bq can be described as follows:

$$A = N\lambda = m_{La}\, a_{La138}\, A_v\, \ln(2)\, /(mw_{La138} t_{1/2}) \qquad (5.5)$$

where A_v is Avogadro's number. According to Eq. (5.5), the activity is 134 Bq (1.54 Bq/cc). The theoretically calculated activity is consistent with the evaluated value that was deduced from the strength of the ERF of ^{138}La within the statistical error.

Another significant peak in the ^{138}La spectrum is at ~789 keV, which is attributed to the pile-up/coincidence of the γ-line of ^{138}Ce with an energy of 789 keV and the β-continuum decay from ^{138}La with a β_{max} value of 255 keV. In addition, the structure of this β-continuum decay appears at the beginning of the ^{138}La spectrum with an endpoint energy of ~255 keV.

Other candidates for the internal activities are the β-decays of ^{211}Pb (β_{max} = 1367 keV, 100%) and ^{207}Tl (β_{max} = 1418 keV, 100%). The origin of ^{211}Pb and ^{207}Tl is the radioactive decay chain of ^{227}Ac, which contaminates the LaBr$_3$:Ce crystal and clearly appears at approximately 2 MeV in the α-peaks as described later. The strength of both of the β-particle emitters was adjusted from the best fitting condition of the α-emitters for an entire radioactive chain ^{227}Ac, which is discussed in the next section. The strength of ^{208}Tl (as an external contribution) was adjusted from the best fit for its photo-peak at 2614 keV with the experimental spectrum.

5.4.2.2 *The ERF of the contributions from the α-particle emitters.*

To interpret the type of α-emitter radioactive chain that contaminates the LaBr$_3$:Ce crystal, the actual ERF of the α-emitters from the natural chains

(^{238}U, ^{235}U, and ^{232}Th) in the LaBr$_3$:Ce detector is simulated and presented in Fig. 5.8. This figure clearly shows that the ERF of the ^{227}Ac-chain is the best candidate in the internal background of the LaBr$_3$:Ce detector according to the literature [67,68] because the four most significant peaks of the ^{227}Ac-chain correspond to the significant peaks in the background spectrum of the LaBr$_3$:Ce. Moreover, the α-energy shifted to the low energy because of the quenching of ionization of the charged particles. Because the ionization-quenching [73] ratio strongly depends on the scintillator, the experimental data are indispensable. To deduce the quenching ratio of the α-particle energies using the LaBr$_3$:Ce detector, let us assume that the internal background of LaBr$_3$:Ce corresponds to the α-energy of the ^{227}Ac-chain. An equivalent α-energy in the background energy spectrum was deduced from the best fit for nine peaks in the background spectrum (Fig. 5.9). These fitting parameters are shown in Table 5.1 in the last three columns, and the first three columns show the corresponding radioactive isotopes with its actual α-energy and transition intensity. Using these equivalent energies and their corresponding α-energies, the quenching curve for the α-particles through LaBr$_3$:Ce was deduced, as shown in Fig. 5.10. The best fit for the quenching curve of the α-particles through LaBr$_3$:Ce was found in the second-polynomial form, as follows:

$$E_{equivalent} = a_0 + a_1 E_\alpha + a_2 E_\alpha^2 \tag{5.6}$$

where a_0, a_1, and a_2 are the fitting parameters with values of 1.103 MeV, 4.813 × 10^{-3}, and 2.783 × 10^{-2} MeV^{-1}, respectively.
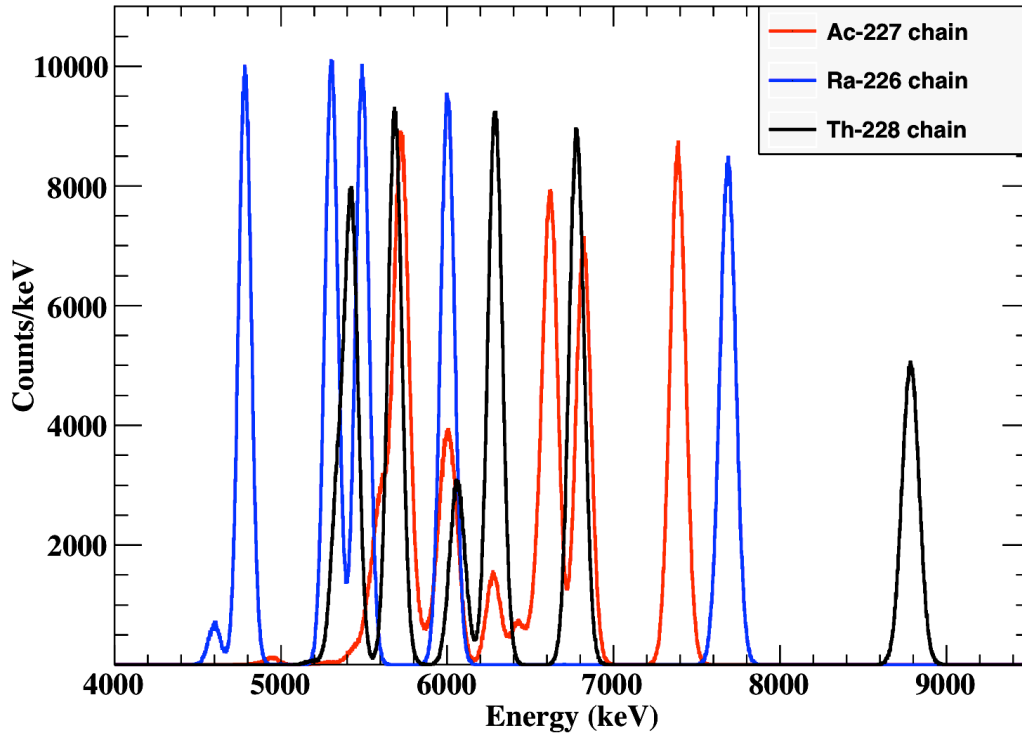
Fig. 5.8: *The simulated ERF for the α-emitters in the decay chains of ²²⁷Ac, ²²⁶Ra, and ²²⁸Th. The spectrum structure of the ²²⁷Ac chain notably resembles the background spectrum of LaBr₃:Ce in the second energy region, as shown in Fig. 5.9.*
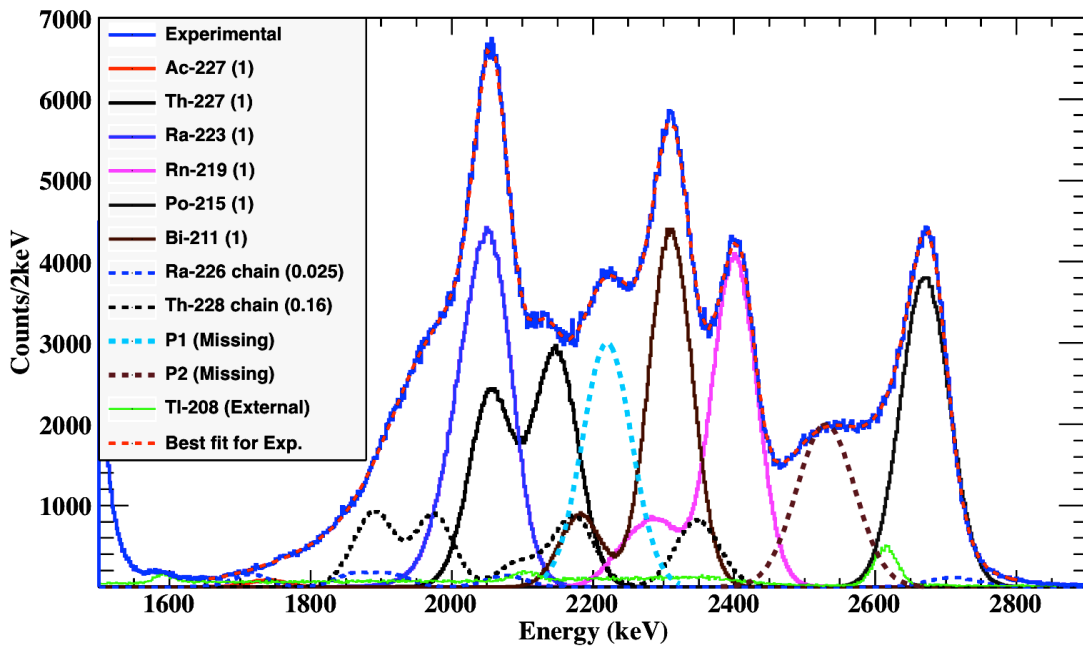
Fig. 5.9: *The comparison between the ERF of the experimental background spectrum of LaBr₃:Ce and the expected contributions that were simulated using GEANT4. The numbers between the brackets indicate the relative strength of the radioactive chains.*
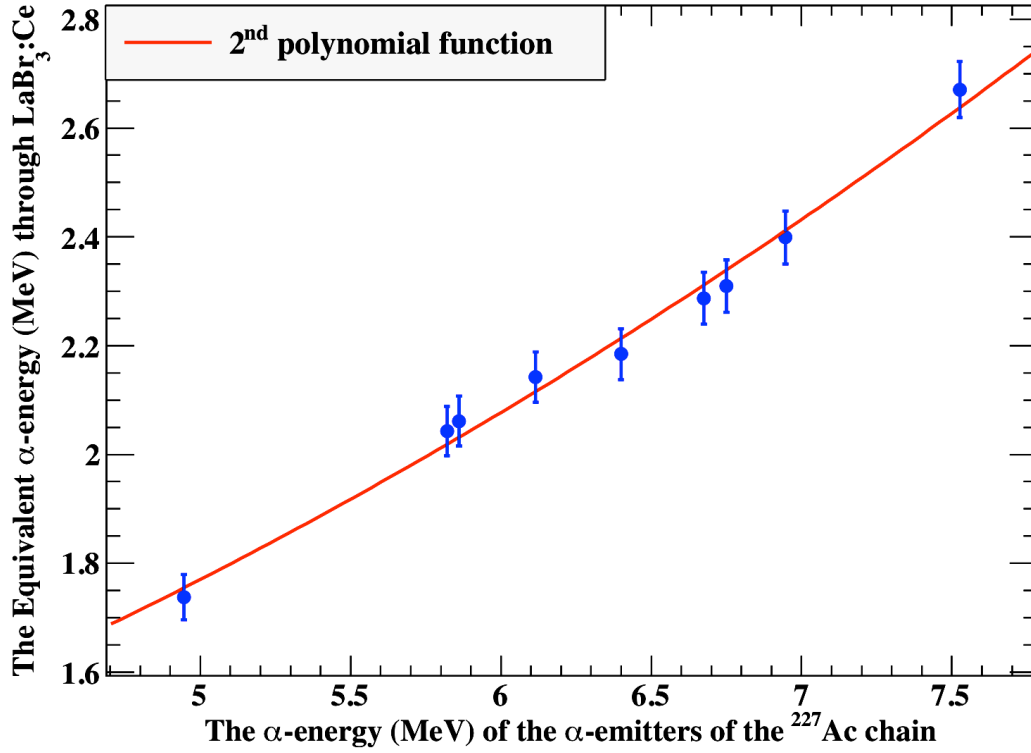
Fig. 5.10: *Quenching curve for the α-particles of the Ac-227 chain inside of the LaBr₃:Ce crystal. The α-emitters of the ^{227}Ac chain are ^{227}Ac, ^{227}Th, ^{223}Ra, ^{219}Rn, ^{215}Po, and ^{211}Bi, with Q-values of 5042.19, 6146.43, 5979.3, 6946.1, 7526.3, and 6750.3 keV, respectively. The points in the graph correspond to the highest transition intensities for the α-energy of each isotope in the decay chain of ^{227}Ac.*

Because of the determination of the quenching factor/ratio, the ERF for the α-particles through LaBr₃:Ce can be correctly reproduced by any α-emitters over the energy range of 4.9 to 7.5 MeV. In addition, the ERF of the natural chains was simulated to identify the contribution of the ^{226}Ra (^{238}U) and ^{228}Th (^{232}Th) chains in the background spectrum of LaBr₃:Ce. The relative strength of the different radioactive chains was adjusted using the best-fitting parameters of the entire background energy spectrum in the second region in which we assumed the equilibrium condition for each chain.

Fig. 5.9 shows the experimental background spectrum of LaBr$_3$:Ce and the simulated ERF for all of the expected contributions in the background spectrum in the second energy region. The dominant contribution in this energy region is the ^{227}Ac decay chain in which all of the features of the decay chain of ^{227}Ac exist in the background spectrum from the shape, relative spacing, and relative intensities of the decay transition of each isotope of this chain. The other chains of ^{238}U and ^{232}Th contribute significantly less than the ^{227}Ac decay chain. The expected relative strengths for the ^{227}Ac, ^{232}Th, and ^{238}U chains were 1.0, 0.16, and 0.025, respectively, as shown in Fig. 5.9. The activity of the major contamination, which came from the ^{227}Ac chain, is $1.37\pm0.08\times10^{-2}$ Bq/cc.

There are two β-emitters in the tail of the ^{227}Ac chain (with $\beta_{max} \sim 1400$ keV), as follows: ^{211}Pb and ^{207}Tl. These β-emitters should appear in the background spectrum with the same strengths as the ^{227}Ac chain, as shown in Fig. 5.5. In addition, the contribution of the natural ^{208}Tl considers its peak contribution in the last peak of the background spectrum of ^{215}Po at approximately 2.614 MeV. In addition, there is a peak in the background spectrum at approximately 1.592 MeV, which can be attributed to the double scape peak of the ^{208}Tl, and the simulated ERF for the ^{208}Tl appears to have the same peak at approximately 1.592 MeV. Consequently, we can reproduce the background spectrum of LaBr$_3$:Ce. However, two peak sources of approximately 2.22 and 2.53 MeV remain unknown, which may be attributed to the deficiency in the radioactive-decay data used by GEANT4.

Table 5.1

Summaries of α-emitters of the ^{227}Ac decay chain, energy, and transition intensity in the first three columns. Columns four to six are the fitting parameters of nine Gaussian functions in the BG spectrum of the LaBr$_3$:Ce that correspond to the α-energies of the isotopes of the ^{227}Ac chain. The relationships between the α-energy and its equivalent are shown in Fig. 5.10.

^{227}Ac-chain isotopes	α-energy E_α (MeV)	Transition intensity (%)	Peak height H (count)	Equivalent α-energy $E_{equivalent}$ (MeV)	Standard deviation σ (keV)
Ac-227	4.946	1.0	81.0	1.738	26.8
Ra-223	5.821	51.6	4287.1	2.043	38.4
Th-227	5.860	20.3	2492.9	2.061	34.0
Th-227	6.116	23.8	2986.0	2.142	34.3
Bi-211	6.399	16.2	886.3	2.184	30.7
Rn-219	6.675	12.9	4339.3	2.310	31.3
Bi-211	6.750	83.5	873.5	2.287	43.0
Rn-219	6.946	79.4	4004.7	2.399	33.1
Po-215	7.526	99.9	3808.6	2.671	34.5

5.5   Conclusion

We proposed the use of the LaBr$_3$:Ce detectors for nuclear resonance fluorescence with the laser Compton scattering γ-ray beam. Because the LaBr$_3$:Ce crystals include two types of contaminations, the energy spectrum with the LaBr$_3$:Ce scintillator is complex. The first type is a stable isotope of ^{138}La, and the other type is the α-emitters. We studied the ERF of a LaBr$_3$:Ce

detector using the developed GEANT4 simulation code and the newly measured experimental spectra. The simulation code was benchmarked by a γ-ray standard source (^{137}Cs) and showed good consistency in the energy resolution, peak strength, etc. The simulation code was modified to calculate the ERF of the α-particles by including the quenching term. Because of the best fit of the background spectrum and the simulation results, the dominate radioactive isotopes in the background spectrum of LaBr$_3$:Ce originated from the meta-stable isotope ^{138}La over the energy region from 0 to ~ 1550 keV, which has an activity of 1.42 ± 0.12 Bq/cc, and the ^{227}Ac chain over the energy region from ~ 1600 to 2800 keV, which has an activity of 1.37 ± 0.08 × 10^{-2} Bq/cc. The activities of the minor contamination from the ^{226}Ra and ^{228}Th chains were 3.41 ± 0.24 × 10^{-4} and 2.2 ± 0.3 × 10^{-3} Bq/cc, respectively. However, the source of the two peaks at approximately 2.22 and 2.53 MeV remains unknown, which may be attributed to the deficiency in the radioactive-decay transition data that were used in GEANT4. In the next chapter, the feasibility of using a LaBr$_3$:Ce detector to measure the NRF excitation levels of ^{238}U is investigated by applying the ERF simulation code.

CHAPTER 6

NRF Measurements

For an inspection system of hidden nuclear materials, a certain amount of SNMs with a high purity is the target object. Thus, in this chapter, we will study the dependence of the NRF reaction yield on the target thickness. The study of the NRF yield dependence on the target thickness of the SNMs is helpful for the evaluation of a number of parameters of an inspection system (such as the number of detectors needed, time estimation, and etc.) and its performance. Additionally, we study the saturation behavior/trend for the scattering NRF γ-rays with the target thickness, which is expected from the simulation results that were presented in chapter 3 and the analytical model of the NRF reaction yield that was presented in chapter 4. Therefore, two NRF experiments were conducted. The first experiment was performed on the heavy material, ^{208}Pb, at a relatively high energy (7.3 MeV), with a LCS γ-ray beam line of the New-SUBARU (Fig. 6.1) at the SPRING-8 facility (Japan) [54]. The second NRF experiment was performed on a nuclear material, ^{238}U, at approximately 2.5 MeV, with a LCS γ-ray line of the High Intensity γ-ray Source (HIγS) facility (Fig. 6.2) at Duke University (USA) [55].
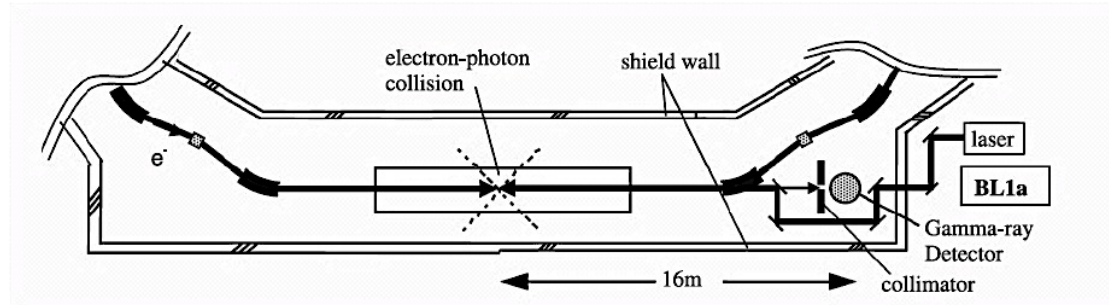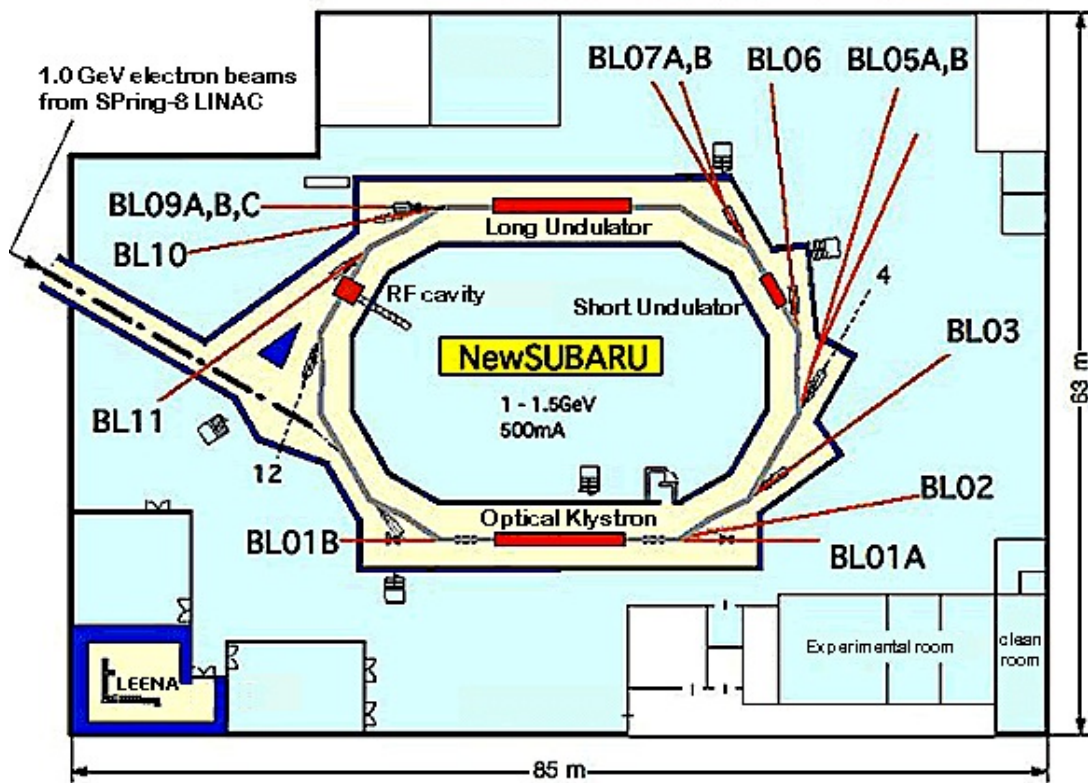
Fig. 6.1: *Layout of the storage ring of New-SUBARU Synchrotron Radiation (SR) Facility. The New-SUBARU is a 1.5 GeV electron storage ring with a circumference of about 119 meters that provides light beam in the region from VUV to soft X-ray using SPring-8's 1 GeV linac as an injector. Our experiment was performed in the beam-line 01A (BL1a). BL1a is used to generate laser-Compton γ-rays of 1 – 40 MeV. These are generated by backward Compton scattering with relativistic electrons in New-SUBARU and photons from external lasers. The γ-ray beam is a very unique light source having the positive characteristics of tunable energy, quasi-monochromaticity, tunable, polarization and beam directivity. The γ-ray is used in various studies: photo-nuclear reaction, electron pair creation, nuclear transmutation and CT-imaging.*
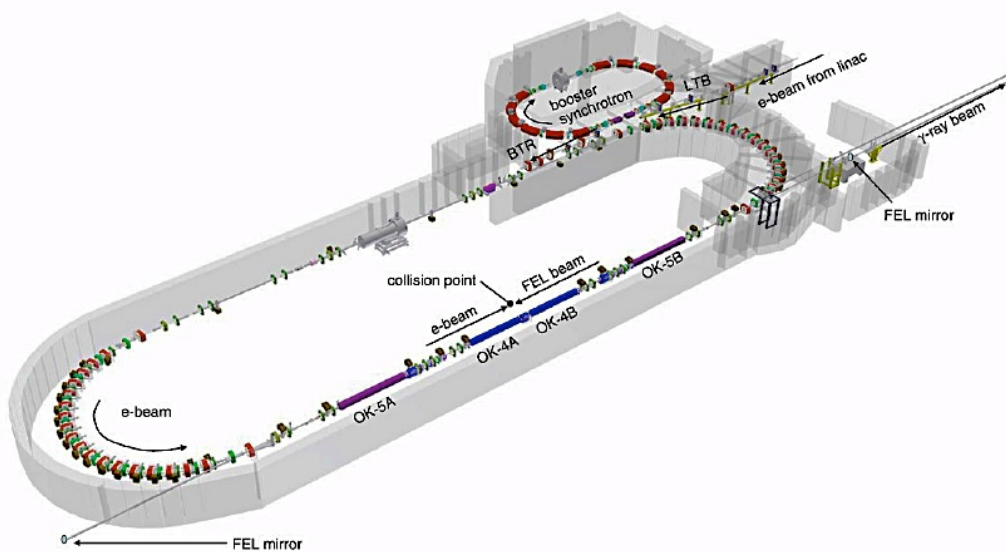
Fig. 6.2: *Layout of the HIγS facility that operated by Triangle Universities Nuclear Laboratory (TUNL) at the Duke Free Electron Laser Laboratory (DFELL). HIγS is a Free-Electron Laser (FEL) based Compton backscattering γ-ray source. The DFELL houses an accelerator based photon source in a 52,000 square-foot facility. There are two types of primary photon beams available at the DFELL: the HIγS with energies from 2 to 60 MeV and an optical beam with continuous tunable wavelength from IR to VUV. Both photon beam types are produced by an electron storage ring free electron laser (FEL) and its undulators. The FEL consists of electromagnetic undulators that are installed in the straight section of the 1.2-GeV racetrack-shaped storage ring. The undulators form the active elements of optical klystron (OK) FELs with a long optical cavity of 53.7 m. A nearly monoenergetic γ-ray beam is produced by intracavity Compton backscattering of the photons in the optical cavity by the stored electrons. The HIγS can produce γ-rays between 1 and 100 MeV with linear and circular polarizations with a very high degree of polarization. Total γ-ray intensities can reach over 1 billion photons/second at some energies with few percent energy resolution. These characteristics make HIγS the world's most intense polarized γ-ray source.*

Both of the two experiments were performed for different target thicknesses. The validity of the NRF reaction yield model (NRF RY model) was verified by both of the experimental results on ^{208}Pb and ^{238}U. Moreover, the MC simulation using the developed code of the GEANT4 was performed for the

NRF interaction of both of the experimental geometries for a wide range of the target thicknesses. The simulation results were validated by the experimental data and verified by the analytical model of the NRF RY. The scattering NRF γ-rays were measured by the HPGe detectors and the LaBr$_3$:Ce detector array. We present a new technique/method to estimate the NRF cross-section, which is based on the NRF attenuation factor that is obtained using the NRF RY model. The new technique provides accurate values for the NRF cross-section without the requirement of the absolute measurements of the incident flux, detection efficiency, and the effective angular distribution, among others.

6.1   NRF Experiment on ^{208}Pb

The motivation of this experiment is, to study the dependence of the NRF yield on the ^{238}U/^{235}U target with different thicknesses is preferable. But, the NRF experiment on a nuclear material is difficult in Japan. Instead of uranium target, we used the lead target as heavy nucleus. Moreover, to test the NRF RY model on the first experimental data. To this end, an NRF experiment has been performed using a laser Compton backscattering γ-ray beam line in New-SUBARU for a known resonance level of 7332 keV in the heavy nucleus ^{208}Pb. Cylindrically shaped natural lead targets with a 5.0 mm radius and different thicknesses of 10.0, 14.4, and 30.5 mm were irradiated using the LCS γ-ray energy of about 7.4 MeV. The NRF yield was measured using two HPGe detectors with relative efficiencies of 120% and 100% positioned at scattering angles of 90° and 130° relative to the incident γ-ray beam, respectively. As a result, the NRF yield exhibited a saturation behavior

for the thick lead target. In the next subsection the experimental setup will be introduced for the NRF experiment on the ^{208}Pb at resonant state of 7332 keV for a different target thicknesses.

6.1.1   Experimental Setup

NRF measurements of ^{208}Pb were performed at the LCS γ-ray beam line (BL1) at New-SUBARU [74], which based on the Compton backscattering of laser photons with the electrons stored in a storage ring. The LCS γ-ray energy that irradiated the target was generated with almost 100% linear-polarized photons with energy of about 7.4 MeV. The γ-beam is collimated with a circular lead collimator that is 3 mm in diameter, which is located at approximately 16 m downstream from the collision point, where the electrons collide with the laser photons and confines the beam spot to a certain size of photons per second to have an energy spread (FWHM) of approximately 10% on the target. Three shaped, natural lead targets with thicknesses of 10, 14.4, and 30.5 mm and a radius of 5.0 mm were used. The NRF γ-rays were measured using two HPGe detectors with relative efficiencies of 120% and 100% situated at 90° and 130° with respect to the incident beam axis, respectively, and focused on the geometric center of the Pb target. A 5.0 mm sheet of lead was placed in front of each detector to attenuate the low energy part of the γ-rays scattered by the target to reduce the count rate of the HPGe detector. The experimental setup is shown in Fig 6.3.
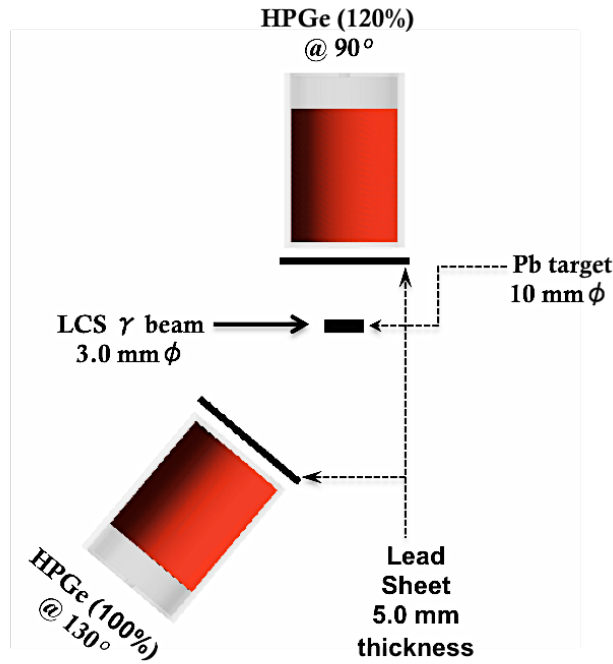
Fig 6.3: *Schematic drawing of experimental setup for the NRF measurements of the* ²⁰⁸*Pb target by the HPGe detectors with relative efficiencies of 120% and 100% at two scattering angles of 90° and 130°, respectively. The lead target was placed at the center of geometry. The LCS γ-rays from a beam 3 mm in diameter. There are two absorber sheets of lead with a thickness of 5 mm in front of each detector.*

6.1.2   Experimental Results

Typical spectra of the NRF measurements of ^{208}Pb at a resonance energy of 7.332 MeV are shown in Fig. 6.4. The upper spectrum is taken with the HPGe detector at the scattering angle 90° for the Pb target with thickness of 14.4 mm, and the lower energy spectrum is that measured at the scattering angle 130° for the same target thickness. In addition, the two NRF resonance levels were observed with 7.083 and 7.063 MeV beside the interested level 7332 keV. The remaining peaks in the spectra are the single (S) and double (D) escape peaks of the NRF γ-rays of the observed states as displayed in the Fig 6.4.
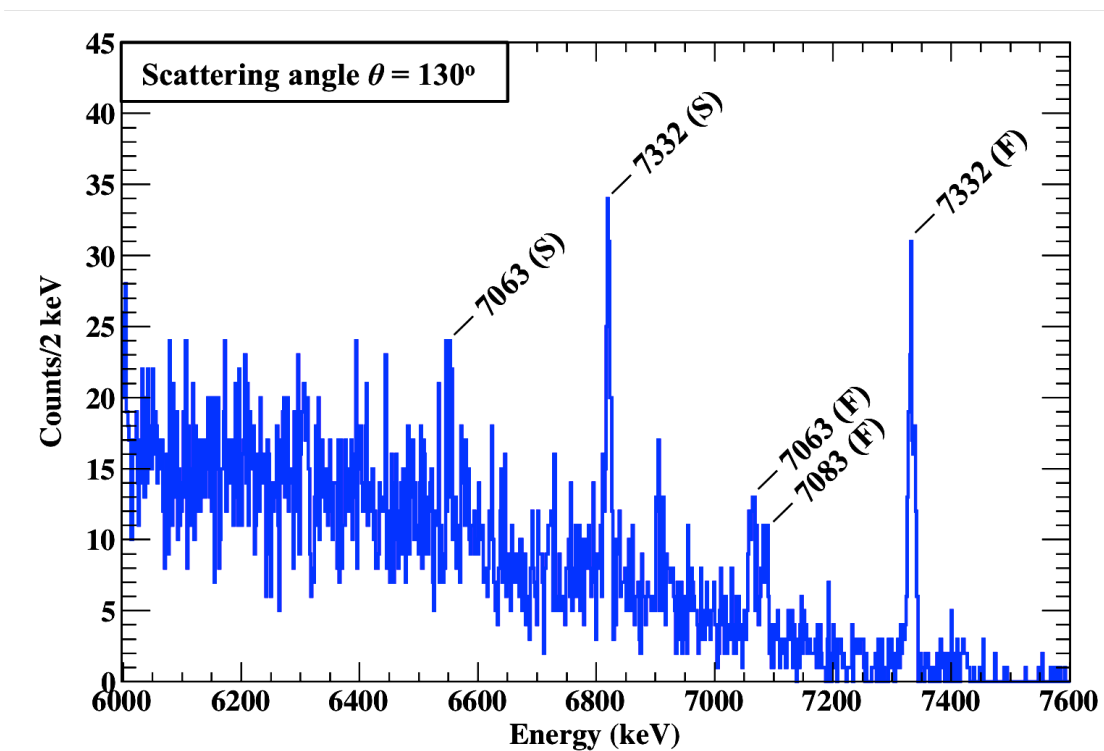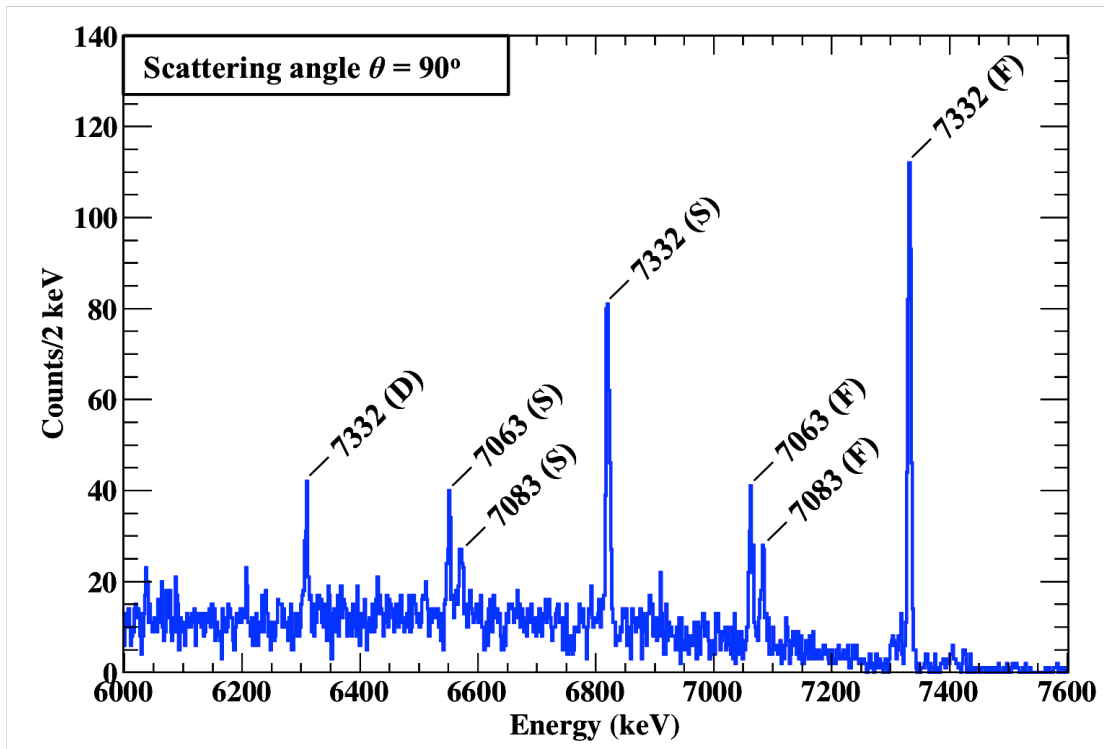
Fig. 6.4: *Measured γ-ray energy spectra of ^{208}Pb for a 14.4-mm-thick target. The upper spectrum is for the 90° scattering angle, and the lower figure is for the 130° scattering angle. There are a three NRF photo-peak marked by (F) as well as the single and double escape peaks marked by (S) and (D), respectively.*
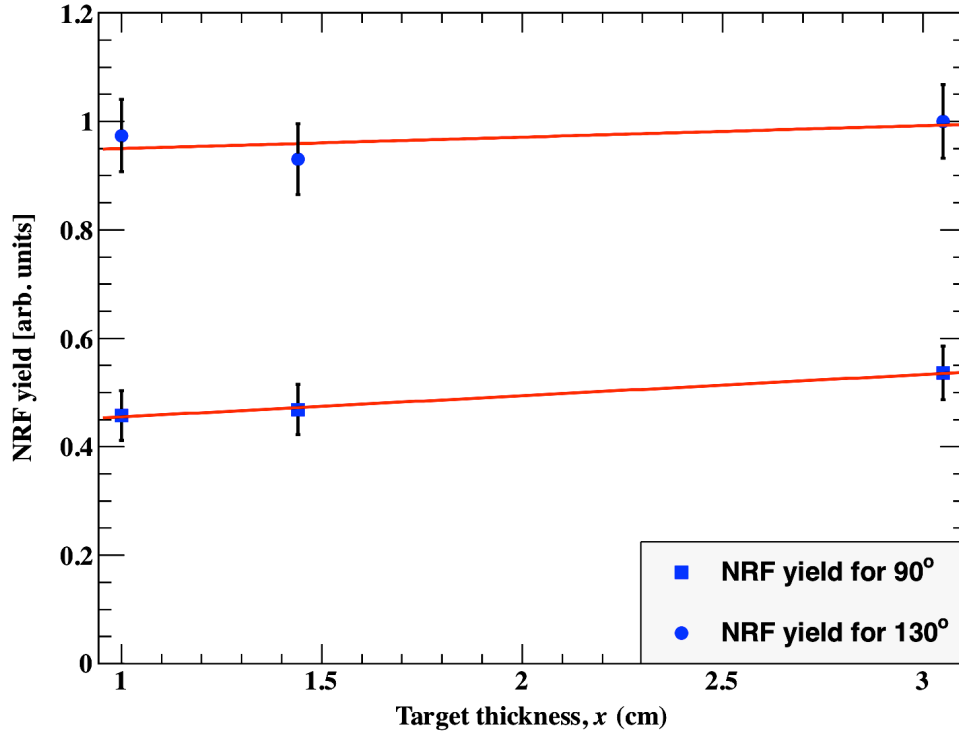
Fig. 6.5: *The normalized NRF yield with the target thickness of ^{208}Pb at a resonance energy of 7332 keV for the three thickness x = 1.00, 1.44, and 3.05 cm.*

In this study, we focused on the 7332 keV energy level. The normalized NRF yield of all the runs is illustrated in Fig 6.5. The normalization was performed with respect to the measurement live time and the total flux of the incident γ-ray beam. The detection efficiency of the HPGe detectors was calibrated using ^{60}Co, subsequently extended to high energies using GEANT4. Primarily, the detection efficiency is calibrated by the standard γ-ray source of the ^{60}Co for the low energy. Because of, there are no standard sources for the high-energy region of interest; the detection efficiency is calculated for the ^{60}Co and the high-energies using the GEANT4 simulation for the same geometry of the experimental setup. The experimental and the simulated results were in the consistence with each other as presented in the Fig 6.6. Therefore, the simulation code of the GEANT4 is used to calculate the detection efficiency for a wide energy range up to the high energy of interest that displayed in Fig 6.7.
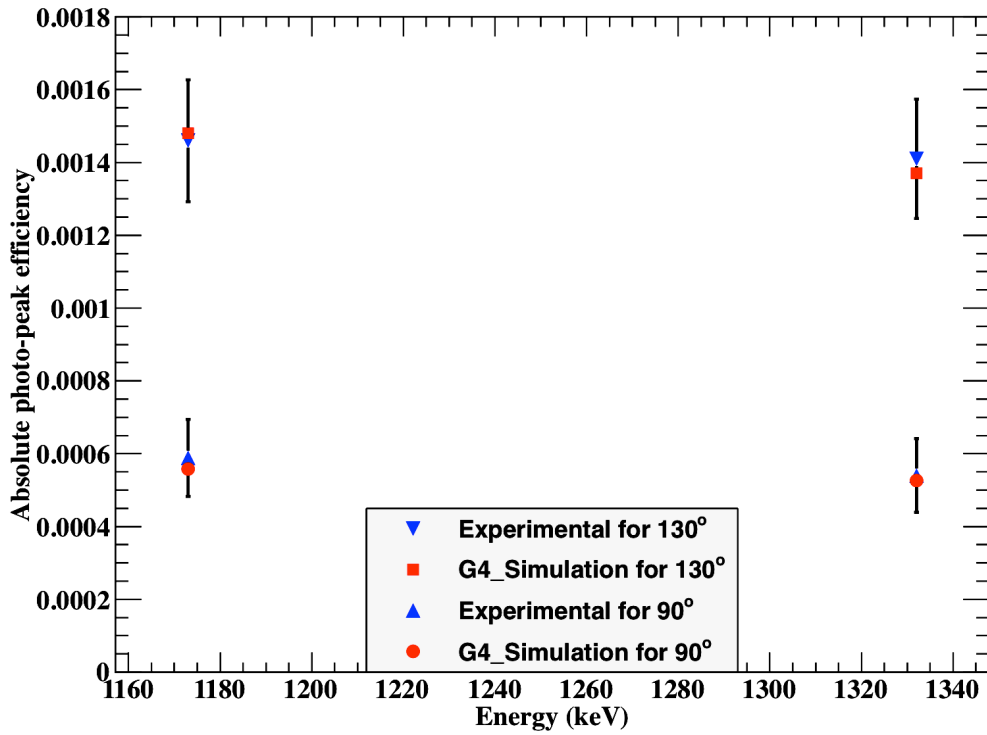
Fig. 6.6: *Absolute photo-peak efficiency of the HPGe detectors at the scattering angles of 90° and 130° for the measurement of the γ-lines of ^{60}Co as well the simulated by the GEANT4 for the same geometry and source.*
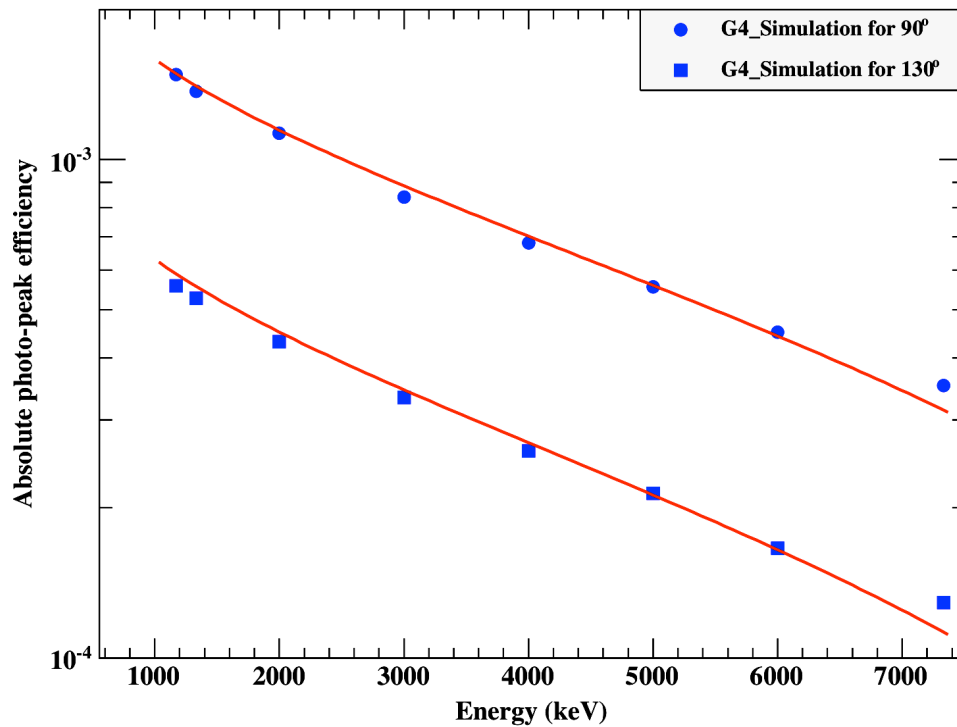
Fig. 6.7: *The simulated of the absolute photo-peak efficiency for the wide energy range up to 7332 keV for the HPGe detectors that is positioned at the scattering angles of 90° and 130°.*

Fig. 6.5 shows the relationship between the NRF reaction yield of ^{208}Pb and target thickness. The NRF yield of ^{208}Pb in this thickness range shows almost constant yield, it means that these measurements were inside the saturation region of the NRF reaction yield. The saturation is due to the attenuation and the self-absorption of the incident and scattering γ-rays through the target material as described in Chapter 4.

6.1.3   NRF Simulation Using GEANT4 for ^{208}Pb

To more examine the relation between the NRF yield and the target thickness of the lead, the simulation was applied using the developed GEANT4 code for a wide range of the lead target thicknesses for the same geometry as in the experimental setup as described above. The energy spread (at FWHM) was assumed to be 36.66 keV, this is less than the experimental energy spread in which was ~700 keV for the incident beam energy 7.4 MeV, to reduce the computation time.

Fig. 6.8 shows the simulation results of the scattered NRF γ-rays at the two scattering angles of 90° and 130° for the different target thicknesses as well as the experimental results. The NRF RY model applied for these experimental and simulation conditions are shown by the red curves in Fig. 6.8. The simulation results are in good agreement with the experimental data. In addition, the NRF RY model is in reasonable agreement for both the experimental and simulation data. The NRF yield shows a saturation behavior after a certain thickness, which can be expected from the NRF RY model because of the attenuation term.
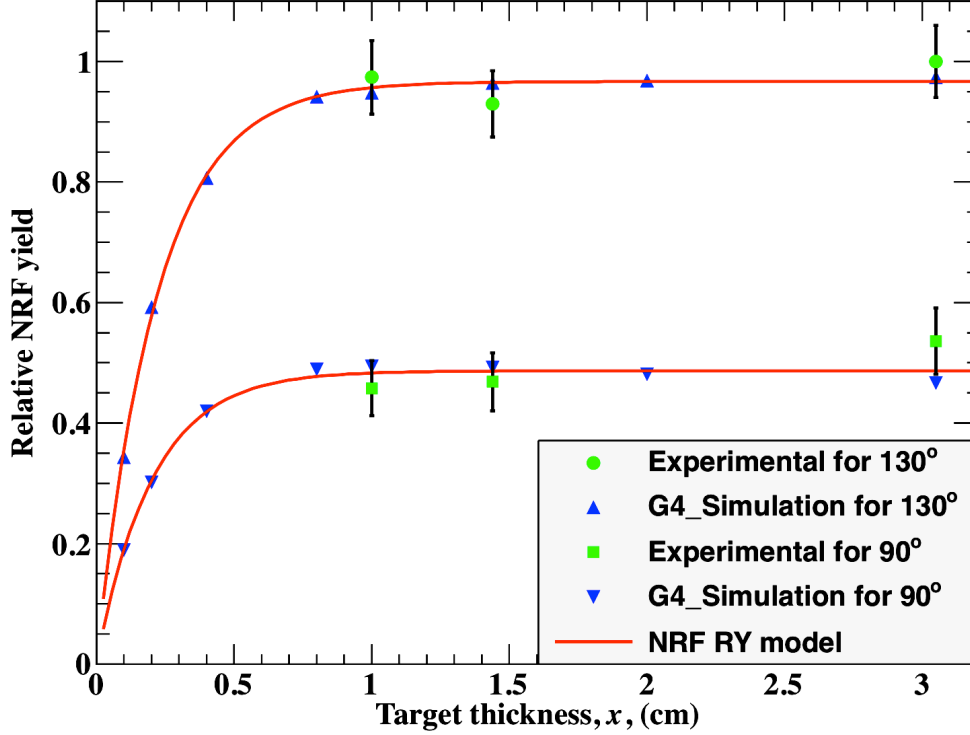
Fig. 6.8: *The relative NRF yield of ^{208}Pb, for the resonance state 7332 keV, as a function of the target thickness, where two sets of the data are shown. The experimental (for thicknesses of x = 10, 14.4, and 30.5 mm) and simulated (for target thicknesses of x = 1, 2, 4, 8, 10, 14.4, 20, and 30.5 mm) results at the two scattering angles 90° and 130°. In addition, the NRF RY model was verified for both angles displayed by the red curve.*

As described in this section, the GEANT4 calculation and the NRF RY model can be acceptable for the evaluation of the NRF yield even for different target thicknesses. In the next section, we will introduce the estimation of the NRF reaction yield from ^{235}U by GEANT4 and the NRF RY model.

6.1.4   Expected NRF RY for SNM – ^{235}U

The GEANT4 simulation was performed for the ^{235}U target at resonance energy of 1.733 MeV [51]. We assumed the same geometry as above (lead target) for the HEU target with an enrichment of 93% ^{235}U and 7% ^{238}U. Additionally, we added a third detector at 45° (forward scattering) with

respect to the incident γ-beam. The different target thicknesses were tested, x = 1, 2, 4, 8, 16, and 32 mm. The 1733 keV resonance has a natural width Γ = 0.0225 eV and a Doppler width Γ_D = 1.4024 eV caused by the thermal motion of the nucleus at 300 K. The recoil energy of the ^{235}U nucleus at this resonant energy is 6.86 eV. Because the natural level width is very small, the level width of the resonant state was set in the simulation equal to the Doppler width, to takes into account the thermal motion effect. However, the energy level-width is less than the recoil energy, it means that, there is no multiple resonance. The energy spread of the incident LCS γ-ray beam is assumed to be 8.665 keV, and the beam is 6 mm in diameter.

6.1.4.1 *Simulation Results of ^{235}U*

The NRF events inside the target are shown in Fig. 6.9 for a target thickness of 32 mm. This illustrates that NRF γ-rays are preferentially produced in the first layers of the thicker targets because of the low NRF energy of ^{235}U, and the attenuation processes. Therefore, for inspection systems, backward angles will be preferred to forward angles to avoid the self-absorption of scattered NRF γ-rays through the thicker SNM itself, which is clearly indicated in Fig. 6.9. Fig. 6.10 shows the simulation results of the different scattering angles for the various target thicknesses. The scattering angles were at 45º – forward scattering, 90º – scattering, and 130º – backward scattering. The relative NRF count rate was calculated with respect to the effective incident flux in the resonant window, which was calculated by multiplying the total incident flux by the ratio of the level width and the beam energy width.
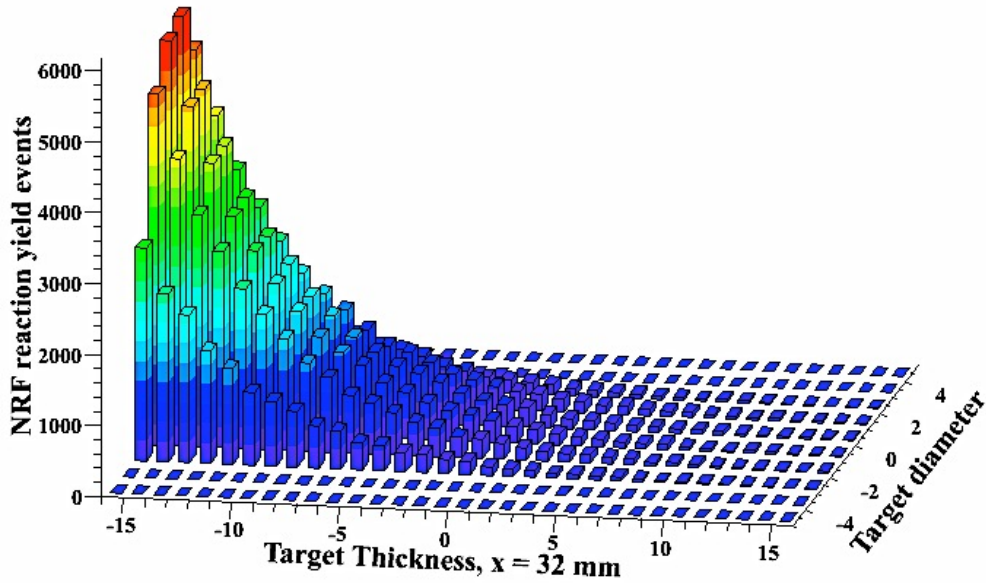
Fig. 6.9: *NRF reaction yield events through the ^{235}U target of a length x = 32 mm for a diameter of 10 mm. The histogram height and color reflect the strength of the NRF events. The incident beam direction for this sample was from left to right.*

The simulation results show a linear trend for the thin targets (0.2 cm) as given by Eq. (4.17) and a subsequent saturation behavior for the NRF yield that slightly increases in the case of backward scattering. This increase may be a result of notch re-filling of the resonant window of the incident beam by the atomic attenuation of γ-rays with energies greater than ($E_{resonant}$ + $\Gamma_D/2$), which could slightly increase the number of resonant photons and this correction is not taken into account in the reaction yield model. By contrast, for the opposite trend in the case of forward scattering, this can be attributed to the thicker targets causing an increased the attenuation of the incident beam and the self-absorption of the scattered NRF γ-rays as well the effect of the solid angle caused by, in which the case of the NRF RY model the detector being aligned with the center of target. Therefore, and as shown in Fig. 6.9, the NRF γ-rays coming from the first layers of the target cause large approach in the NRF RY model for significantly thicker targets.

112
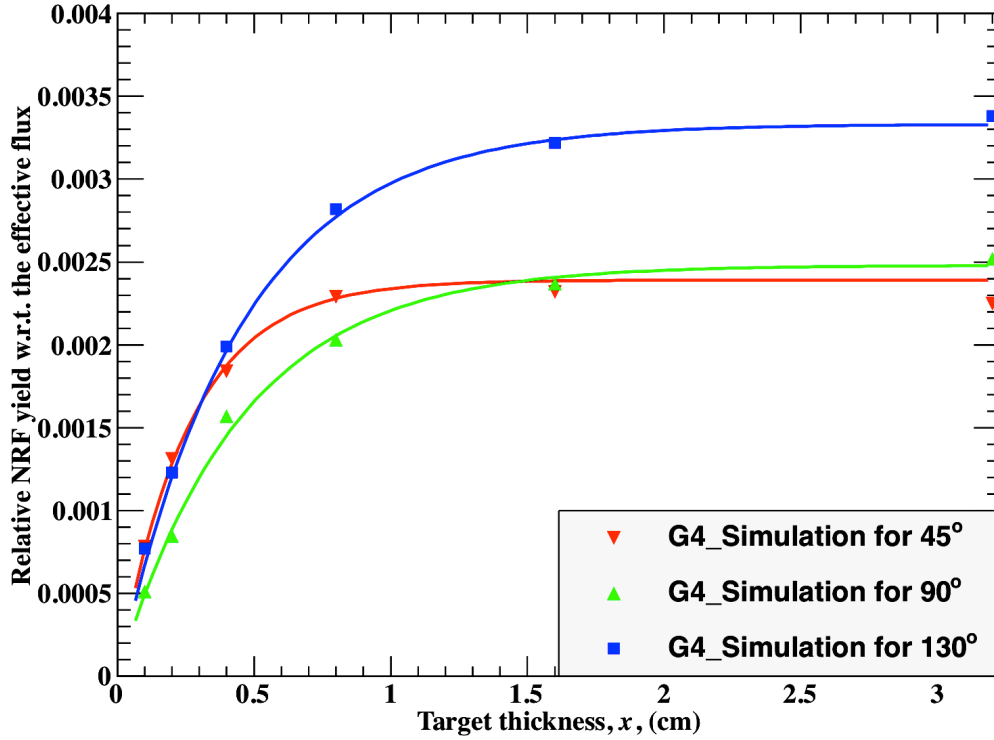
Fig. 6.10: *Relative NRF reaction yield with respect to the effective incident flux and the target thickness, x = 1, 2, 4, 8, 16, and 32 mm for the [235]U resonance state of 1733 keV. There are three data sets for the scattered NRF γ-rays: the first set was compiled for the 45° scattering angle, or forward scattering; the second set was compiled for the 90° scattering angle; and the last set was compiled for the 130° scattering angle, or backward scattering. The solid lines represent the NRF RY model for the three scattering angles.*

The NRF RY model may represent a good approach for determining the half-value layer $X_{1/2}$, which corresponds to the half maximum value of the NRF RY. For example, in the case of [235]U at a resonance energy of 1733 keV with an absorption coefficient equal to 1.99 cm^{-1} and a scattering coefficient at a scattering angle of 130° of 1.48 cm^{-1}, the total attenuation coefficient is 3.47 cm^{-1}, and therefore, $X_{1/2}$ = 0.20 cm. The difference between the count rates of backward and forward scattering is caused by attenuation, self-absorption through the target and the interaction location. In addition, the Compton scattering is dominant for forward angles relative to back scattering angles as

shown in Fig. 6.11. In the case of 90° scattered NRF γ-rays, the count rate is entirely dependent on the solid angle of the detector and the geometry/diameter of the target, which determines the scattering attenuation. In conclusion, for inspection system using the NRF technique, an optimum angle for the detection system setup could be one of the backward angles relative to the incident interrogation beam.
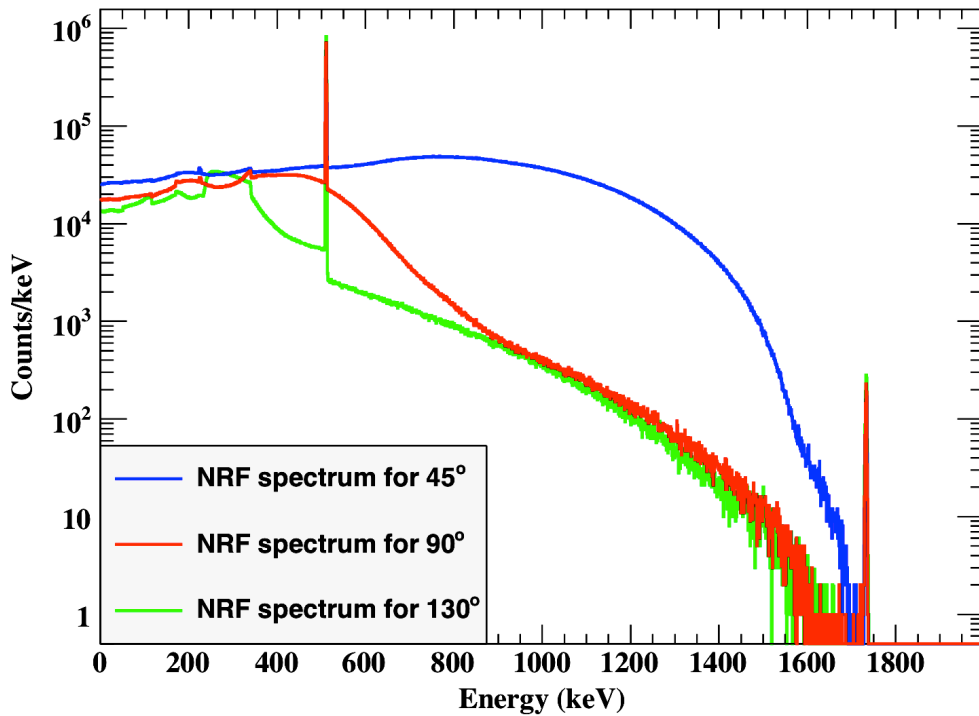
Fig. 6.11: *The NRF energy spectra of ^{235}U at resonance energy of 1733 keV for a target thickness of 32 mm. There are three spectra for the different scattering angles as following: (1) Forward scattering at 45º – blue spectrum. (2) 90º scattering – green spectrum. (3) Backward scattering at 130º – red spectrum.*

6.2   NRF Experiment on ^{238}U

The motivation for this experiment was to study the dependence of the NRF yield of the ^{238}U nuclear material as a function of the target thickness (on the order of mm in thickness). Additionally, the incident γ-ray energy is in region of interest at approximately 2 MeV. The second goal was to test the ability of the LaBr$_3$:Ce detector array to measure the NRF excitation levels of the ^{238}U in the region of its self-activity of 2 MeV. The third goal was to validate the NRF RY model for the low energy region with a relatively small thickness compared with the lead experiment. The Forth goal was to validate of the GEANT4 simulation code for the NRF interaction by the experimental results, as well verification the code by the NRF RY model. Finally, propose a new technique/method to estimate the NRF cross-section that is based on the NRF RY model, which significantly more precisely than the common method. One of the advantages of the proposed method is that it does not require the absolute values of the incident flux, the detection efficiency of the detection system, and the effective angular distribution of the scattered NRF γ-rays to calculate the NRF cross-section, in contrast to the common method that requires these absolute values.

To this end, an NRF experiment was performed using a LCS γ-ray beam at the HIγS facility at Duke University. The different thicknesses of the depleted uranium (DU) targets were irradiated by the LCS γ-ray beam with an incident beam energy of ~2.475 MeV. The scattering NRF γ-rays were measured using the HPGe detector array positioned at scattering angles of 90$^{\text{o}}$ relative to the incident γ-ray beam. In addition, a backward detector array

of the 8 LaBr$_3$:Ce detectors was used beside the array of the HPGe detector. Each LaBr$_3$:Ce detector was 1.5 inches in diameter by 3.5 inches in length. The NRF RY model is introduced to interpret the experimental data. A Monte Carlo simulation using GEANT4 was performed to simulate the NRF interaction over a wide range of the target thicknesses of the ^{238}U.

6.2.1   Experimental Setup

The NRF experiment was performed at the High Intensity γ-ray Source (HIγS) facility [50] at Duke Free Electron Laser Laboratory (DFELL). The HIγS facility is based on the Compton backscattering of the free electron laser (FEL) photons with the electrons stored in a storage ring. The LCS γ-beam that irradiated the target was generated with a nearly 100% circular-polarized photon with an energy of approximately 2.475 MeV and with a high intensity γ-ray with an average flux of approximately 3×10^5 γ/s/keV for all of the runs. The γ-beam is collimated with a circular lead collimator that is 19.05 mm in diameter, which is located at approximately 60 m downstream from the collision point, where the electrons collide with the FEL photons and confines the beam spot to a certain size (19.05 mm) of photons, to have an energy spread (FWHM) of approximately 5% on the target.

Four NRF measurements were performed on eight disks from the depleted uranium (DU), which has density of 19.1 g.cm^{-3}. Each disk of the DU is 25.4 mm in diameter and is approximately 0.6 mm in thickness with a mass of approximately 6.5 g; each disk is encased within a thin plastic sealant, as shown in Fig. 6.12.

Table 6.1

Run summary of the NRF measurements for the different thicknesses of the depleted *uranium (DU) target. Eight foils from the DU target were conducted in these measurements. The total mass of each target is presented with units of g and its total thickness in units of mm. Each target has a cylindrical shape with a diameter of ~25.4 ±0.5 mm. The uncertainties in DU masses and the thicknesses are approximately 1%.*

#Run	#Foils	Mass (g)	Thickness (mm)
1	2	12.42	1.287
2	4	26.08	2.703
3	6	39.72	4.117
4	8	53.67	5.563
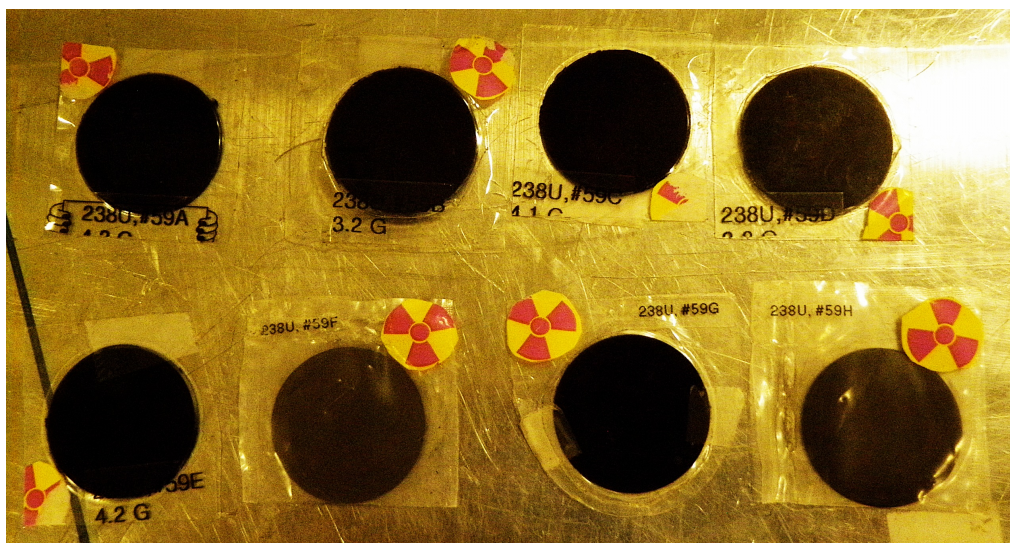
Fig. 6.12: *The photograph of the eight DU disks used in the NRF measurements of the [238]U. The thickness and mass of each foil is summarized in Table 6.1.*

A target is assembled in four sets with 2, 4, 6, or 8 disks stacked together, and the summary of the runs is presented in Table 6.1. Each set of the DU was placed within an evacuated acrylic tube to decrease the scattering of the

117

incident γ-rays by the air, which extended approximately 1.5 m upstream from the detector setup.

Fig. 6.13 shows the experimental setup of the NRF measurements. The scattering NRF γ-rays spectra were measured with the two detection systems of HPGe and the LaBr$_3$:Ce detector array, with a total hours on-beam of the LCS γ-ray source of ~32.5 h. Three HPGe detectors, each with 60% relative efficiency and energy resolution is approximately 0.19% (~2.52 keV, FWHM) at 1332 keV, were placed downstream from the collimator and positioned at a scattering angle of 90° relative to the incident beam. The standoff from the ^{238}U target was configured with two of the detectors in a vertical direction and the other detector in a horizontal direction. The detectors were positioned 10 cm away from the center of the target. Two absorber sheets of copper (3.2 mm) and lead (4.0 mm) were placed in the front of each detector to attenuate the low energy background.

The eight LaBr$_3$:Ce detectors (the Saint-Gobain BrilLanCe 380, 3.81 cm in diameter and 7.62 cm in length) connected to a 1.5″ photomultiplier (R9420, Hamamatsu) were positioned at the backward angle with an angle of 154° relative to the incident beam direction. The distance from the target center to each of the LaBr$_3$:Ce detectors was 12.2 cm. The schematic diagram of the entire NRF experimental setup is shown in Fig. 6.13. Fig. 6.14 presents the close geometry of the DU target with the HPGe detector array with the γ-ray tracking that was simulated using GEANT4.
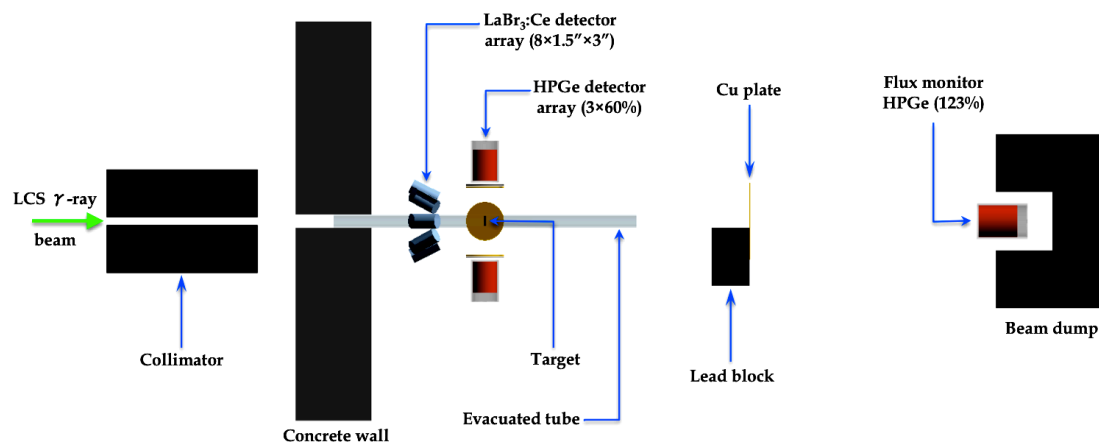
Fig. 6.13: *Schematic side view of the experimental setup of the NRF measurements of the ^{238}U at the HIγS facility at Duke University. The two detectors array setup was used with the 3 HPGe and the 8 LaBr₃:Ce detectors.*
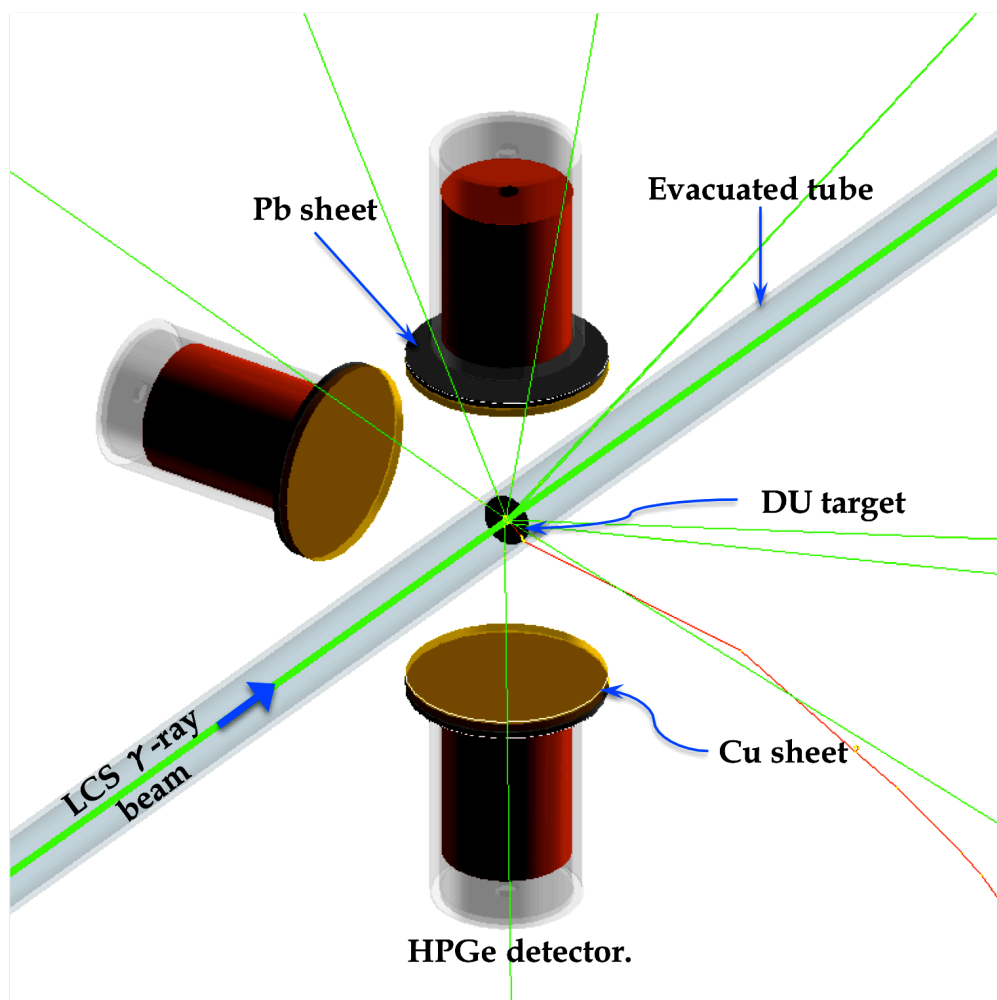
Fig. 6.14: *The close geometry for the DU target with the HPGe detector array of the NRF simulation setup, with the γ-ray track simulated using the Monte Carlo Radiation Transport, GEANT4.*

The energy calibration of all of the measured spectra was performed by the natural room background lines namely, the [40]K γ-ray line with an energy of 1460.8 keV and the [208]Tl γ-ray line with an energy of 2614.5 keV. The detection efficiency of all of the detectors was evaluated by placing a standard γ-ray source ([56]Co) at the target position with γ-ray energies of 846.8 keV, and 1037.8 keV through 3253.5 keV. The efficiency of the flux-monitor detector was determined by positioning a [56]Co source to the copper plate.

6.2.2   Energy and Flux Measurements

The incident beam energy was measured in a large volume by the HPGe detector with a 123% relative efficiency, which was placed in the beam axis prior to measuring the scattering NRF γ-rays. The lead attenuators were placed at the collision section to protect the HPGe from the high-count rate of direct measurement.

After measuring the beam energy, the HPGe (123%) detector (flux monitor) was moved out of the beam axis and placed at an angle of 8.6° relative to the beam axis in the horizontal direction, as shown in Fig 6.15. The absolute beam flux on the target was measured during the data acquisition of each run using the measurement of the Compton scattered γ-rays from a Cu-scatter placed downstream in the beam path. As the scatter the copper plate of 1.1 mm in thickness was placed directly in the beam path, approximately 100 cm downstream from the target setup and approximately 165 cm upstream from the flux monitor.
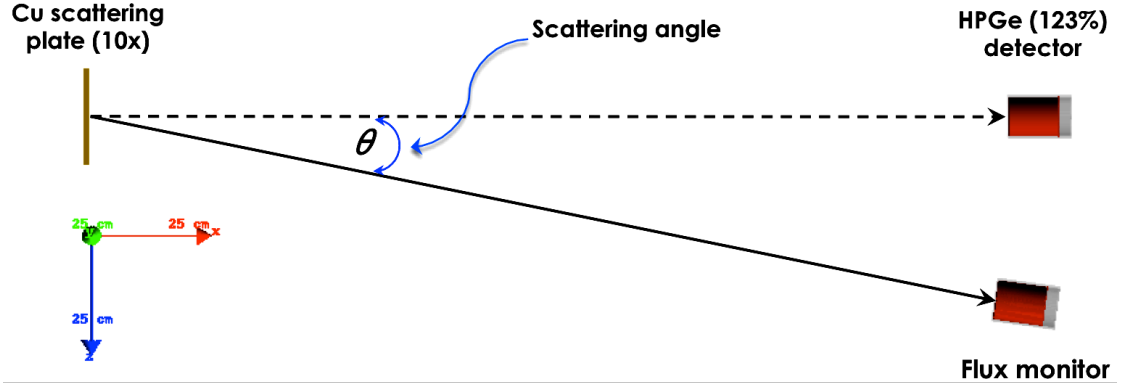
Fig. 6.15: *Schematic top view of the flux monitor in the positions of measuring the beam energy and in the accumulated γ-ray flux and the copper scattering plate (the thickness of the Cu-plate in the graph is magnified to 10x).*

The incident photon flux Φ_i on the target can be calculated by the number of counts in the scattered photo-peak, which is measured with the flux monitor at the scattering angle of 8.6°. Fig. 6.16 shows an example of the scattered flux spectrum for an incident energy of 2475 keV. The double Gaussian fitting isolates the scattered photo-peak and the Compton edge. The total photon flux can be calculated using the scattered photo-peak area A_s and the scattering Compton cross-section $\sigma_{cs}(E_s, \theta_s)$, which can be calculated using Eq. (2.5), with a scattering angle θ_s, described according to the following equation:

$$\Phi_i = \frac{A_s(E_s)/t}{\sigma_{cs}(E_s, \theta_s) \cdot n_{cu} \cdot \varepsilon(E_s, \Omega)} \tag{6.1}$$

where t is the measurement of the live time, $\varepsilon(E_s)$ is the intrinsic photo-peak efficiency of the flux monitor at the scattering γ-ray energy E_s, and n_{cu} indicates the Cu-plate areal density, which is given by the following equation:

121
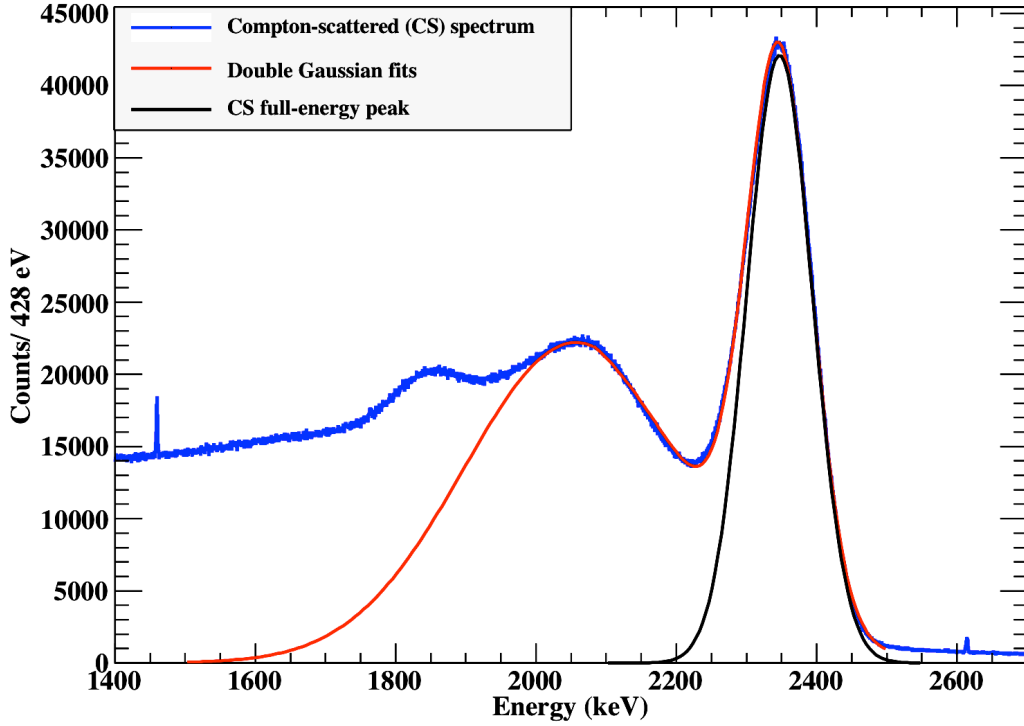
Fig. 6.16: *The Compton scattered energy spectrum at the incident beam energy of 2475 keV from a scatter Cu-plate (1.1-mm-thick) with an angle of 8.6°. The Compton scattered full energy photo-peak obtained by a double Gaussian fit to the photo-peak of the source spectrum to isolate the true photo-peak from the Compton edge.*

$$n_{cu} = \frac{\rho_{Cu} \cdot l \cdot N_a}{M_{Cu}} \tag{6.2}$$

where ρ_{Cu} is the copper density, l is the plate thickness, M_{Cu} indicates the atomic mass of Cu, and N_a is Avogadro's number. The flux calculations are corrected to the attenuation through the DU targets and the scatter of the Cu-plate (1.1-mm-thick) along with the detection dead time.

The error propagation in the flux was deduced by the relative standard error in the following form:

$$\frac{\Delta(\Phi_i)}{\Phi_i} = \sqrt{\left(\frac{\Delta(A_s)}{A_s}\right)^2 + \left(\frac{\Delta(\sigma_{cs})}{\sigma_{cs}}\right)^2 + \left(\frac{\Delta(n_{cu})}{n_{cu}}\right)^2 + \left(\frac{\Delta(\varepsilon)}{\varepsilon}\right)^2} \qquad (6.3)$$

where:

$\dfrac{\Delta(\Phi_i)}{\Phi_i}$ is the relative error in the effective incident flux,

$\dfrac{\Delta(A_s)}{A_s}$ is the relative error in the scattered photo-peak-area, which is obtained from the fitting of the photo-peak,

$\dfrac{\Delta(\sigma_{cs})}{\sigma_{cs}}$ is the relative error in the scattering Compton cross-section, which depends on the scattering energy and angle,

$\dfrac{\Delta(n_{cu})}{n_{cu}}$ is the relative error in the areal density of the Cu-plate, which depends on the plate thickness and its density, and

$\dfrac{\Delta(\varepsilon)}{\varepsilon}$ is the relative error in the detection efficiency of the flux monitor, which depends on the energy, and the solid angle, which is a function of the detector radius, and the distance between the detector and the Cu-plate.

6.2.3   NRF Spectra with the HPGe Detector Array

Fig. 6.17 presents an example of the summed energy spectra of the NRF γ-rays for the three HPGe detectors at a scattering angle of 90° for the run #2 (4 foils of the DU with a total thickness of approximately 2.7 mm). All of the measured spectra of the NRF are calibrated and rebind to a common energy bin (0.864 keV) and are subtracted from a non-linear background that is estimated by the Statistics-sensitive Non-linear Iterative Peak-clipping (SNIP) [75-77] algorithm, as shown by the red curve in Fig. 6.17.
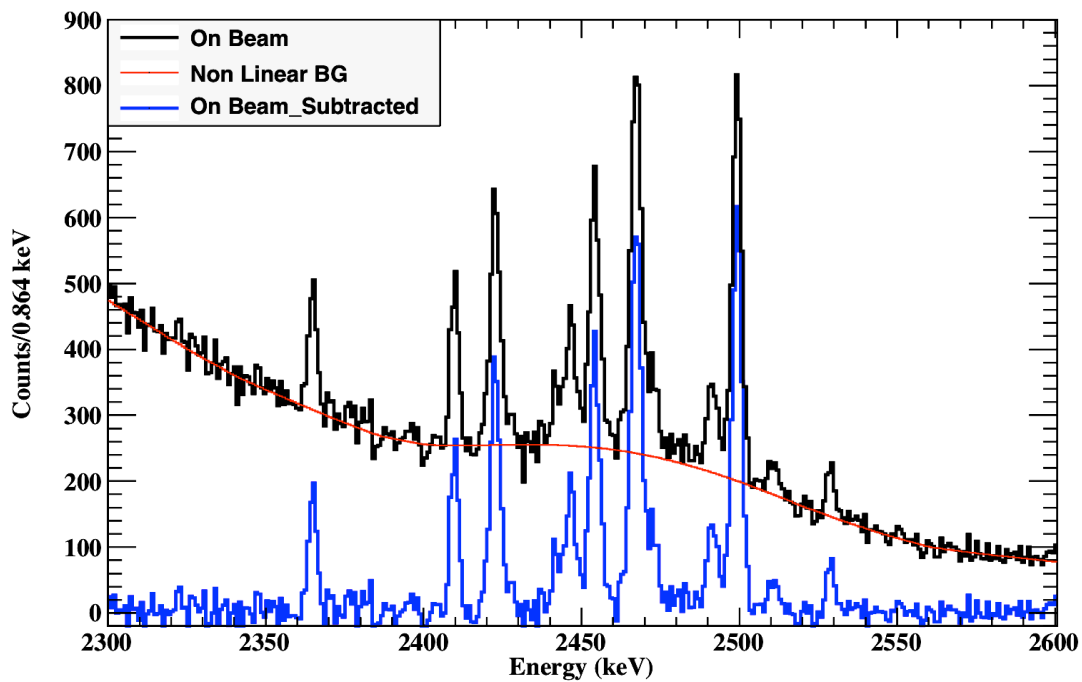
Fig. 6.17: *The sum of the experimental energy spectra of the scattering NRF γ-rays with an angle of 90°. The on-beam spectrum is indicated by the black spectrum. The subtracted energy spectrum from a non-linear component of the BG, which is estimated by the SNIP algorithm, is shown by the blue spectrum.*

Fig. 6.18 presents the NRF excitation levels of ^{238}U at approximately 2.5 MeV after being subtracted from the non-linear BG. This figure contains 12 peaks; one-peak is from the target-background of the ^{238}U that originated

from the ²¹⁴Bi γ-line with an energy of 2447 keV, and 11 of the NRF peaks are not observed in the room and target-background spectrum in the interested energy region; thus, we consider all of the peaks are from the ²³⁸U target during the (γ, γ′) interaction. The 11 NRF peaks include three pairs with an energy difference of 45 keV. This result could be attributed to three of their transitions of (2410, 2468, and 2499 keV) to the ground-state with the spin sequence of $(0 \rightarrow 1 \rightarrow 0)$ and the other three of (2365, 2423, and 2454 keV) to the first exited state at the 45 keV level with the spin sequence of $(0 \rightarrow 1 \rightarrow 2)$. This energy difference of 45 keV is not observed for the remainder of the transitions; thus, the transition could be directly to the ground state, see the schematic diagram for the NRF transitions in Fig. 6.19.
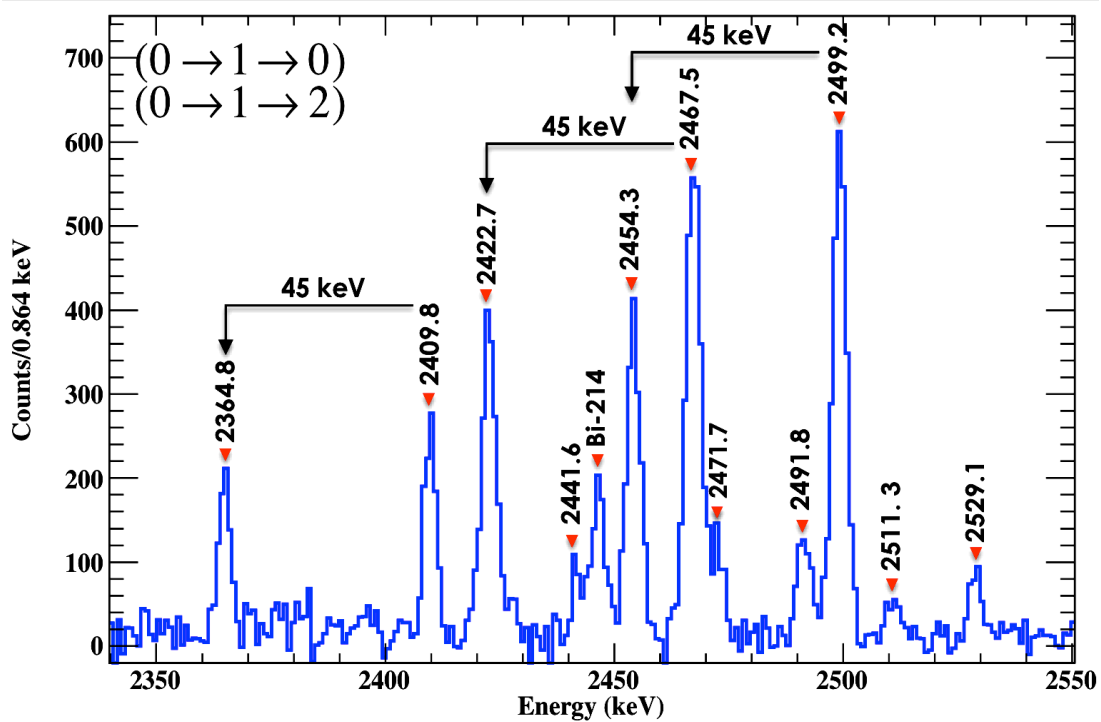
Fig. 6.18: *Subtracted NRF excitation levels spectrum of the ²³⁸U at approximately 2.5 MeV. There are 11 NRF-peaks with 1 target-background-peak for ²¹⁴Bi at 2447 keV. Four NRF peaks are newly observed in these measurements. There are three transition pairs with an energy difference of 45 keV.*
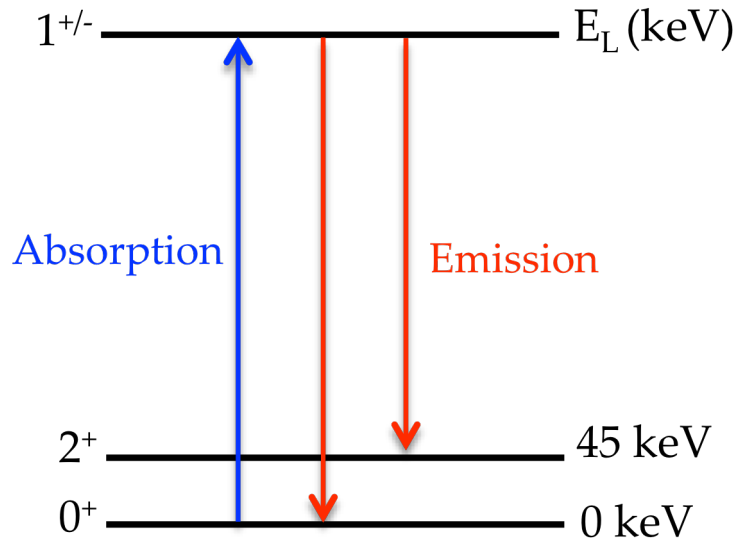
Fig. 6.19: *Schematic energy diagram of the NRF transitions of dipole* $(0 \rightarrow 1 \rightarrow 0)$, *and quadrupole* $(0 \rightarrow 2 \rightarrow 0)$ *for* ^{238}U.

6.2.3.1 *NRF Yield vs. the Target Thickness*

Fig. 6.20 presents the result of the NRF yield versus the target thickness of the four different thicknesses (Table. 6.1) of the DU target. We selected the NRF state of 2468 keV, which has been measured in a previous study [78-80]. The NRF yield versus the target thickness shows a linear increasing yield with an increasing target thickness (up to ~3mm) and then it shows the saturation tendency. The Monte Carlo simulations using the developed GEANT4 code were performed for the different thicknesses of 0.5, 2, 4, 6, 8, 10, 12, 16, and 20 mm with a diameter of 25.4 mm to discuss the wider thickness range behavior of the NRF yield. As shown in Fig. 6.20, the simulation results have a good agreement with the experimental results. Note that the NRF cross-section that is used in the GEANT4 simulation was obtained from the fitting results of the experimental data.
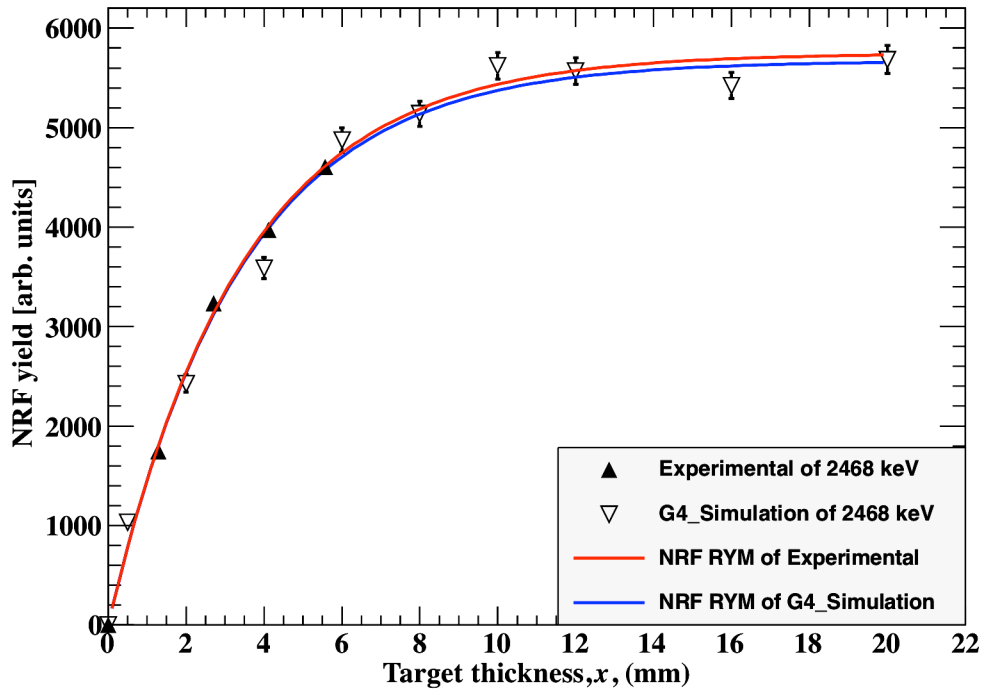
Fig. 6.20: *The NRF yield dependence on the target thickness of ^{238}U in the state of 2468 keV. The experimental results of the four measurements for the different thicknesses of the DU. The simulation results for a wide range of the different thicknesses, x = 0.5, 2, 4, 6, 8, 10, 12, 16, and 20 mm.*

The NRF RY model was applied to the experimental and the simulation results. According to Eq. (4.12), the NRF RY model can be expressed in the form of the fitting parameters C_0, C_1, and C_2, as follows, and can then be used to fit the experimental or the simulation results. In the case of the backward or forward scattering with a scattering angle of θ, the parameters are as follows:

$$Y = C_0 \cdot \frac{1 - e^{-(C_1[1+\sec(\theta)]+C2)x}}{C_1[1+\sec(\theta)]+C2}.$$

(6.4)

In contrast, for the scattering NRF γ-rays with an angle of 90°, the following equation is applied:

127

$$Y = C_0 \cdot \frac{1 - e^{-(2C_1 + C_2)x}}{2C_1 + C_2} e^{-C_1 \cdot r} \, , \tag{6.5}$$

where

$$C_0 = \Phi_i \cdot \Gamma_D \cdot N \cdot \sigma_{NRF}(E_r) \cdot W(\theta) \cdot \varepsilon(E_r) \cdot \frac{\Omega}{4\pi} \cdot \prod_k \exp(-\mu_k x_k) \, , \tag{6.7}$$

$$C_1 = \mu_e(E_r) \, , \text{ and } C_2 = \mu_{NRF}(E_r) \, .$$

The term $\prod_k \exp(-\mu_k x_k)$ is the multiplicand of the attenuations of the absorbers, k, that are situated in front of the detector.

Using these equations, we can determine the total attenuation factor from the fitting parameters and the NRF attenuation factor from the parameter C_2, therefore, the NRF cross-section is determined using C_2. The NRF cross-section is correlated to the NRF attenuation factor according to the following equation:

$$\mu_{NRF}(E_r) = \frac{N_a}{M_{IOI}} \sigma_{NRF}^{ij} \, , \tag{6.8}$$

where σ_{NRF}^{ij} represents the cross-section of the NRF transition line j of the ith isotope, and M_{IOI} is the atomic mass of the IOI.

6.2.3.2 *Effective Thickness and Attenuation Length*

The attenuation length is equal to the maximum effective length of the NRF interaction within the target, as presented by Eq. (4.14). For example, for the resonance level of 2.468 MeV, the attenuation factor of the atomic

128

interaction at the γ-energy of 2.468 MeV is 0.852 cm^{-1} (where the atomic attenuation can be calculated from the XCOM [81] database or using GEANT4, which are derived from the evaluated photon data library (EPDL97), stating that the photon cross sections should be accurate with less than 1% uncertainty [82]; thus, the second method is used), the total attenuation factor according to the experimental fitting is 2.91 cm^{-1}, and the attenuation factor for the NRF interaction is determined as 1.21 cm^{-1}. Thus, the total attenuation length is 3.43 mm, whereas it is only 4.85 mm for the absorption component. However, the maximum effective thickness for the NRF interaction through the DU at any thickness ≥ (x^{Max} = 25 mm) is 3.43 mm according to Eqs. (4.13 and 4.14). Consequently, the total attenuation length through the DU target is equal to the maximum effective length for the NRF interaction at the maximum thickness of 25 mm for a resonance state of 2.468 MeV.

6.2.3.3 *NRF Cross-Section Calculations*

We should emphasis that the NRF RY model can determine the NRF cross-section based on the attenuation factor of the NRF interaction, which is determined from the fitting parameters of the experimental saturation curve. The attenuation factor for the NRF excitation level of 2.468 MeV of ^{238}U is 1.21 cm^{-1}, as discussed in the previous subsection. Therefore, the NRF cross-section for a state of 2.468 MeV of ^{238}U is 50.4±3.3 b.eV for an absolute temperature of 300 K (or 51.4±3.3 b.eV for an effective temperature of 312 K that is based on the Debye temperature of the metallic uranium of 207 K [83]). However, the NRF cross-section of this level is 38 b.eV [78], 61 b.eV [79] or 80

b.eV [80], as previously reported. The value determined by the NRF RY model is over the range of these values and similar to the value reported in the ENSDF [79]. In addition, Fig. 6.21 represents a comparison between the attenuation by the Compton, atomic, and NRF interaction through the uranium target for the γ-ray energy 2468 keV.
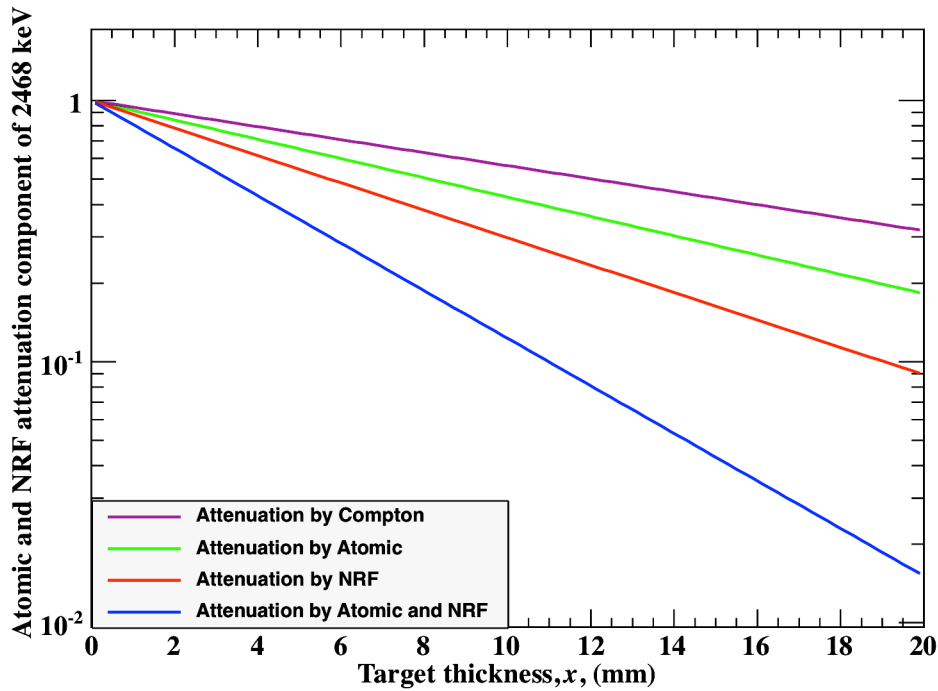
Fig. 6.21: Attenuation curves of the incident γ-ray energy of 2468 keV through the uranium target. The "Compton and Atomic" curves represent the attenuation expected for the non-resonant 2468 kev γ-rays. The "NRF" attenuation curve represents the expected attenuation for the resonant γ-ray. As well, the attenuation by the atomic and the NRF (non-resonant and resonant photons) interaction is presented.

Consequently, we propose a new technique to determine the NRF interaction cross-section based on the saturation-curve fitting by the NRF RY model to directly extract the NRF attenuation factor and, thereafter, the NRF cross-section. The merit of this method is that we can avoid many systematic

errors that occur in the NRF experiments. Additionally, the absolute values of the parameters of C_0, such as the incident flux, detector efficiency and so on, are not required in this case.

The known/common method to calculate the observed integrated NRF cross-section by the experimental parameters is given by the following equation:

$$I_s = \frac{A_{IOI}(E_r)/t}{\Phi_i \cdot n_{IOI} \cdot W_e(\theta) \cdot \varepsilon(E_r)}$$

(6.9)

where $A_{IOI}(E_r)$ is the peak area of the γ-ray line of the isotope of interest (IOI) of the state of energy E_r. The value t denotes the measuring live time, and Φ_i indicates the effective incident flux within the resonant window of the state of interest, given by Eq. (6.1). $W_e(\theta)$ indicates the effective angular distribution of the scattering NRF γ-rays according to the dipole or quadrupole transition of the NRF (as described in section 2.6.3). $\varepsilon(E_r)$ is the detection efficiency of the detector at the scattering energy of E_r. The value n_{IOI} is the areal density of the IOI, which is given by the following equation:

$$n_{IOI} = \frac{\rho \cdot l \cdot N_a}{M} \cdot \delta$$

(6.10)

where ρ is the target density, l is the target thickness, M is the atomic mass of the IOI, and δ denotes the abundance/fraction of the IOI within the target composition.

The common method is based on a single measurement; thus, the absolute values presented in Eq. (6.7) or (6.9) are required to evaluate the cross-section, including the incident flux per eV, the effective angular distribution of the scattering NRF γ-rays, the detection efficiency, and so on. Therefore, the uncertainties in the common method are numerous due to all of the parameters presented in Eq. (6.4) or (6.5), which have three constant parameters C_0 (Eq. (6.7)), C_1 and C_2, and the two variables of the NRF yield (Y) and the target thickness (x). Thus, the uncertainty (error propagation) in the NRF cross-section due to the absolute measurement can be expressed according to the following equation:

$$\frac{\Delta(\sigma_{NRF})}{\sigma_{NRF}} = \left[\left(\frac{\Delta(Y)}{Y} \right)^2 + \left(\frac{\Delta(x)}{x} \right)^2 + \left(\frac{\Delta(\Phi_i)}{\Phi_i} \right)^2 + \left(\frac{\Delta(N)}{N} \right)^2 + \left(\frac{\Delta(W(\theta))}{W(\theta)} \right)^2 \right.$$
$$\left. + \left(\frac{\Delta(\varepsilon(E_r))}{\varepsilon(E_r)} \right)^2 + \left(\frac{\Delta(\mu_e(E_r))}{\mu_e(E_r)} \right)^2 + \left(\frac{\Delta(\mu_{NRF}(E_r))}{\mu_{NRF}(E_r)} \right)^2 \right]^{1/2}$$

(6.11)

where:

$\dfrac{\Delta(\sigma_{NRF})}{\sigma_{NRF}}$ is the relative error in the NRF cross-section,

$\dfrac{\Delta(Y)}{Y}$ is the relative error in the NRF photo-peak area (yield), which is obtained from the fitting of the NRF peak area,

$\dfrac{\Delta(x)}{x}$ is the relative error in the target thickness. Where, The uncertainties in DU target thicknesses are approximately 1%.

$\dfrac{\Delta(\Phi_i)}{\Phi_i}$ is the relative error in the incident effective flux in the resonant window, which is calculated using Eq. (6.3),

$\dfrac{\Delta(N)}{N}$ is the relative error in the areal density that depends on the target thickness and the abundance of the IOI in the target composition,

$\dfrac{\Delta(W(\theta))}{W(\theta)}$ is the relative error in the effective angular distribution that depends on the spin sequence and the scattering angle,

$\dfrac{\Delta(\varepsilon(E_r))}{\varepsilon(E_r)}$ is the relative error in the detection efficiency for the detector array that is used in the measuring scattering NRF γ-rays, which depends on the detector radius and the target-detector-distance,

$\dfrac{\Delta(\mu_e(E_r))}{\mu_e(E_r)}$ is the relative error in the atomic attenuation factor of the target material for the incident beam energy, and,

$\dfrac{\Delta(\mu_{NRF}(E_r))}{\mu_{NRF}(E_r)}$ is the relative error in the NRF attenuation factor for the resonant state.

In contrast, the uncertainty (error propagation) in the cross-section that is extracted from the saturation-curve fitting of the NRF yield, using the fitting function of Eq. (6.4) or (6.5), is derived from the error in the attenuation factors of $\sigma(\mu_e)$ and $\sigma(\mu_{NRF})$, which are determined by the uncertainty in the parameters C_1 and C_2 (directly determined from the fitting). Therefore, the uncertainty in the NRF cross-section, $\sigma(\sigma_{NRF})$, can be addressed using the following equation:

$$\frac{\Delta(\sigma_{NRF})}{\sigma_{NRF}} = \sqrt{\left(\frac{\Delta(Y)}{Y}\right)^2 + \left(\frac{\Delta(x)}{x}\right)^2 + \left(\frac{\Delta(\mu_e(E_r))}{\mu_e(E_r)}\right)^2 + \left(\frac{\Delta(\mu_{NRF})}{\mu_{NRF}}\right)^2} \qquad (6.12)$$

The uncertainty in C_1 and C_2, which are obtained by the fitting, could include the uncertainty in the variables of the NRF yield (Y – NRF peak area) and the target thickness, which were included in the plotted data. Thus, the uncertainty in the NRF cross-section, in this case, is simply given according to the equation:

$$\frac{\Delta(\sigma_{NRF})}{\sigma_{NRF}} = \sqrt{\left(\frac{\Delta(\mu_e(E_r))}{\mu_e(E_r)}\right)^2 + \left(\frac{\Delta(\mu_{NRF})}{\mu_{NRF}}\right)^2} \tag{6.13}$$

Fig. 6.22 shows the saturation curves of the scattering NRF γ-rays (NRF-yield) versus the target thickness of the ^{238}U target for the 11 NRF transitions as presented in Table 6.2.
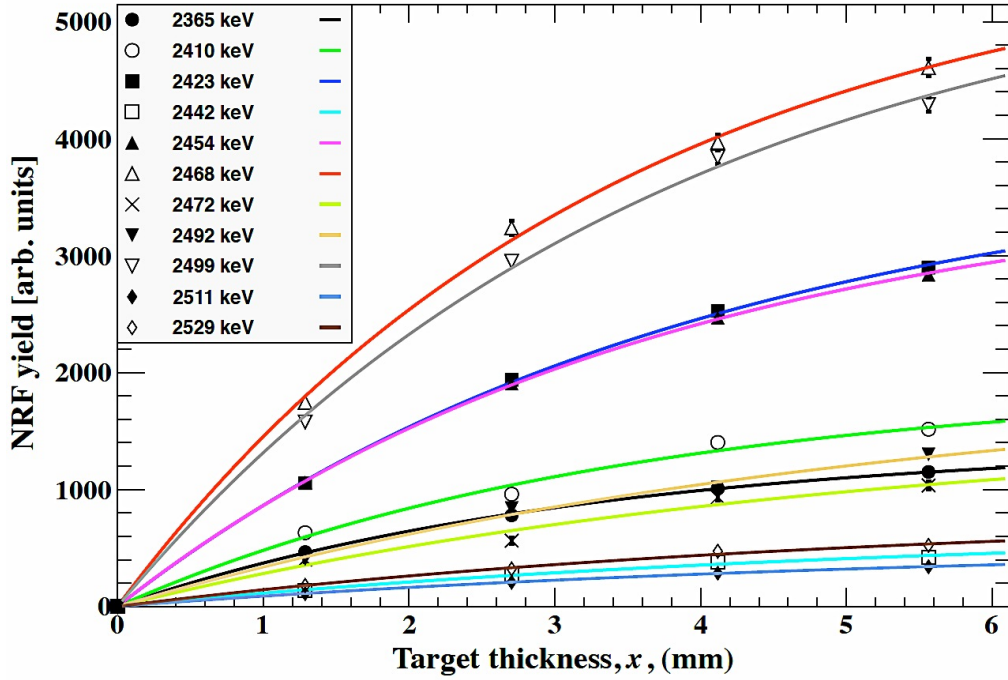
Fig 6.22: *The saturation curves of the scattering yield of the NRF transitions of ^{238}U at approximately 2.5 MeV versus the target thickness. Four NRF measurements for the different target thickness of the DU with 11 NRF transition levels.*

Table 6.2 presents the NRF transitions for the γ-rays of ^{238}U at approximately 2.5 MeV, for which the incident beam energy is 2.48 MeV with an energy width (FWHM) of 5%. In addition, the attenuation factors of the atomic and the NRF interaction, which are extracted from the fitting parameters of the scattering yield of the NRF transitions with the target thickness, are presented in the third and fourth columns. The total attenuation length (or the maximum effective length) is presented in the fifth column. The last two columns present the calculations of the NRF cross-section transitions by both of the methods determined from the absolute measurement (common method) using Eq. (6.9) and from the NRF attenuation factor that was obtained from the fitting for the saturation curve of the NRF yield (proposed method) using Eq. (6.5).

The NRF cross-section deduced by both of the methods shows that they are consistent with each other within their uncertainties. Moreover, the cross-sections calculated by the saturation method show slightly higher values than the other method. The difference in the values estimated by the two methods arises from the precise correction for the attenuation and the self-absorption by the thickness dependency estimation of the incident γ-ray for the proposed method. Consequently, the scattering yield with the thickness dependence measurements of the NRF with the RY model could introduce the precise estimation (relative to the common method) for the NRF cross-section without any of the absolute measurements, thus, reducing the uncertainty. In this study, we detected 11 NRF peaks, with certain peaks demonstrating new values for the NRF cross-section transitions and with another NRF transition showing nearly the same values as the previous data [7-9] of the cross-section within the uncertainty. In addition, 4 NRF transitions are newly observed, and these four resonant levels are presented in Table 6.2, marker by an asterisk.

Table 6.2

The NRF excitation energies (E_γ) and their Doppler widths (Γ_D) of ^{238}U at an effective temperature of 312 K are presented in the first and second columns. The third to fifth columns present the attenuation factors for the atomic (μ_e) and the NRF (μ_{NRF}) interactions along with the attenuation length (χ_0) or the maximum effective thickness $(x^{max}_{effctive})$ for the NRF γ-rays. The last two columns present the integrated NRF cross-sections calculated according to the fitting of the NRF yield using the NRF RY model and by the common method using Eq. (6.9). The last column is calculated for the target thickness of 1.287 mm of run# 1. The uncertainties in the atomic attenuation factors are less than 1% according to the EPDL97 [82]*.*

E_γ (keV)	Γ_D (eV)	μ_e (cm^{-1})	μ_{NRF} (cm^{-1})	$x^{max}_{effctive} \| \chi_0$ (mm)	I_s (b.eV) NRF RY model	I_s (b.eV) Common method
2365	1.939	0.8591	1.36±0.21	3.25	54.1±4.4	44.1±4.9
2410	1.976	0.8557	1.12±0.15	3.53	45.6±3.1	37.1±3.9
2423	1.986	0.8547	0.81±0.13	3.96	34.0±2.8	33.0±3.5
2442*	2.002	0.8534	0.12±0.10	5.48	4.9±2.1	3.9±1.9
2454*	2.012	0.8525	0.97±0.16	3.75	40.8±3.4	38.5±3.8
2468	2.023	0.8516	1.21±0.16	3.43	51.4±3.3	47.4±4.3
2472*	2.027	0.8512	0.31±0.13	4.98	12.8±2.7	10.1±2.9
2492	2.043	0.8500	0.19±0.12	5.29	8.2±2.5	7.5±2.7
2499	2.049	0.8495	1.11±0.16	3.56	46.8±3.3	45.5±4.1
2511*	2.059	0.8488	0.10±0.08	5.57	4.3±1.7	4.1±1.9
2529	2.073	0.8477	0.27±0.13	5.10	11.6±2.7	9.5±2.7

* The NRF excitation levels are newly observed for ^{238}U.

Note that the NRF cross-section was set to the simulation code obtained from the fitting results of the current experimental data, which is shown in Fig. 6.20. The simulation results show a good agreement with the experimental results at this cross-section, as presented in Fig. 6.20. Moreover, the distribution of the NRF events through the target obtained by GEANT4 is presented in Fig. 6.23. Fig. 6.23 indicates a 3-D view of the NRF events through the ^{238}U target with a thickness of 20 mm and a diameter of 25.4 mm. A projection of the NRF events on the target thickness is shown in Fig. 6.24 (a); this graph simply shows the attenuation curve for the NRF interaction through the target thickness. In addition, the projection of the NRF events on the target diameter is presented in Fig. 6.24 (b), which shows the distribution of the NRF events across the target diameter.
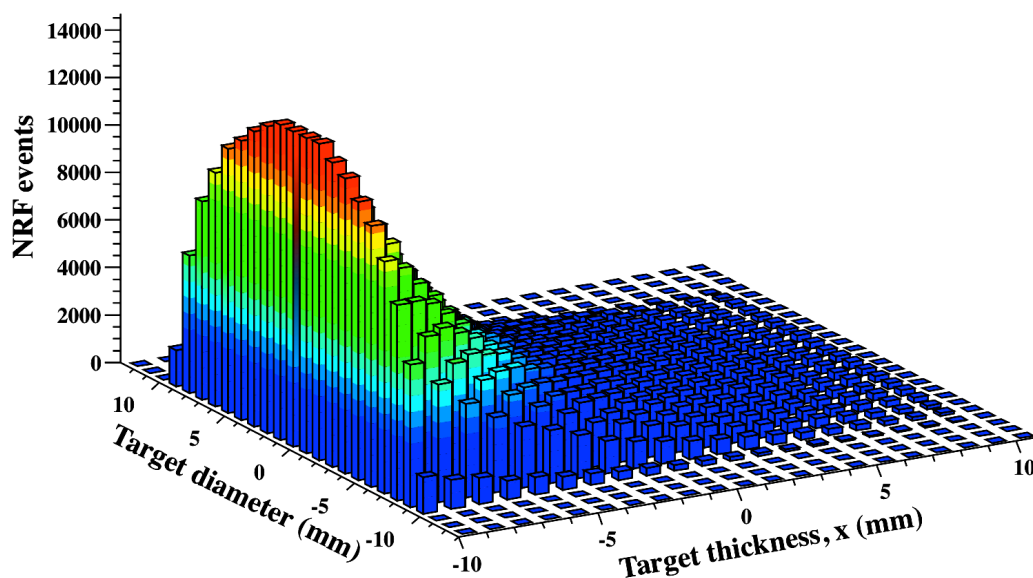
Fig. 6.23: *The NRF events profile through the ^{238}U target with a thickness of 20 mm and a diameter of 25.4 mm. It representation of a 3-D map for the NRF events within the target.*
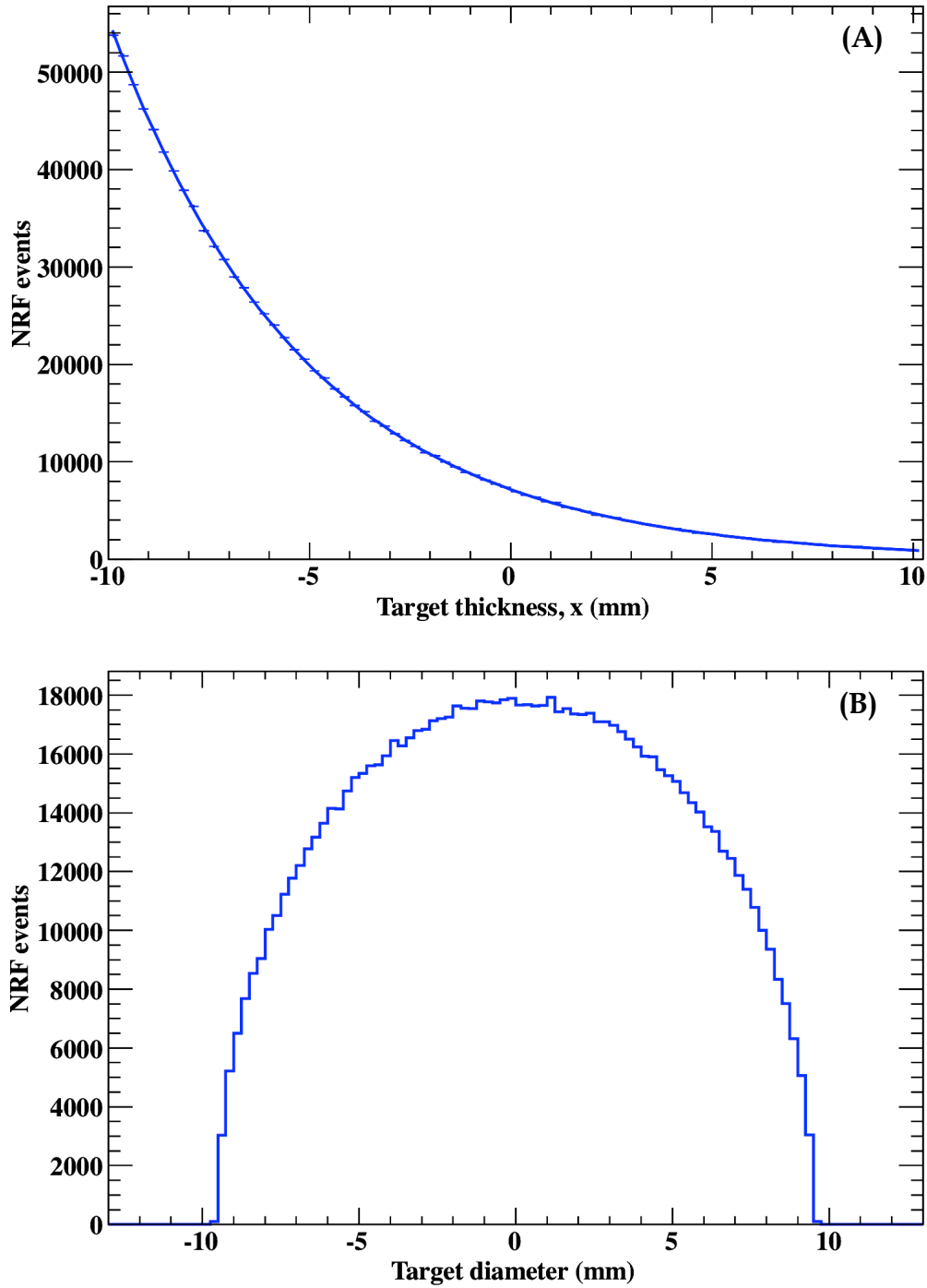
Fig. 6.24: *The NRF events projections through the* ^{238}U *target with a thickness of 20 mm and a diameter of 25.4 mm.* **(A)** *1-D X-projection of the NRF events on the target thickness, and* **(B)** *1-D Y-projection of the NRF events on the diameter of the target.*

6.2.4   NRF Spectra with the LaBr₃:Ce Detector Array

We analyzed the measured NRF spectra using the LCS γ-rays at the HIγS facility using the developed code that was presented in chapter 5 for the energy response function. Fig. 6.25 shows the measured beam spectrum (on-beam) and the analyzed spectra over the energy region of interest of the NRF γ-rays. This figure shows that it is difficult to extract the γ-lines of the resonance peaks from LaBr₃:Ce in the 2 MeV because of the multiple alpha peaks due to the self-activity within the detector.

The process that was performed on the source spectrum (on-beam) is as follows: first, subtract the source spectrum from the estimated ERF of the background of LaBr₃:Ce; second, subtract the non-linear background that was estimated using the SNIP [75-77] algorithm, achieved using the ROOT analysis program; third, identify the energy peaks in the bump using the multiple Gaussian fitting with the energy given by the HPGe detector and the energy resolution of LaBr₃:Ce of the energy peaks in this region. Note that we could use the energy of the NRF level from the reference papers to identify the NRF peaks.

As well, Fig. 6.26 shows the NRF γ-ray peaks, which indicate the nuclear levels of the ²³⁸U target over this energy range of approximately 2.5 MeV. The eight observed lines correspond to eight nuclear levels, three pairs with an energy difference of 45 keV, indicating three transitions of (2410, 2468, and 2499 keV) to the ground state and three transitions of (2365, 2423, and 2454 keV) to the first excited state at 45 keV. The scattering peak in Fig. 6.26 corresponds to the direct scattering from the incident γ-beam.
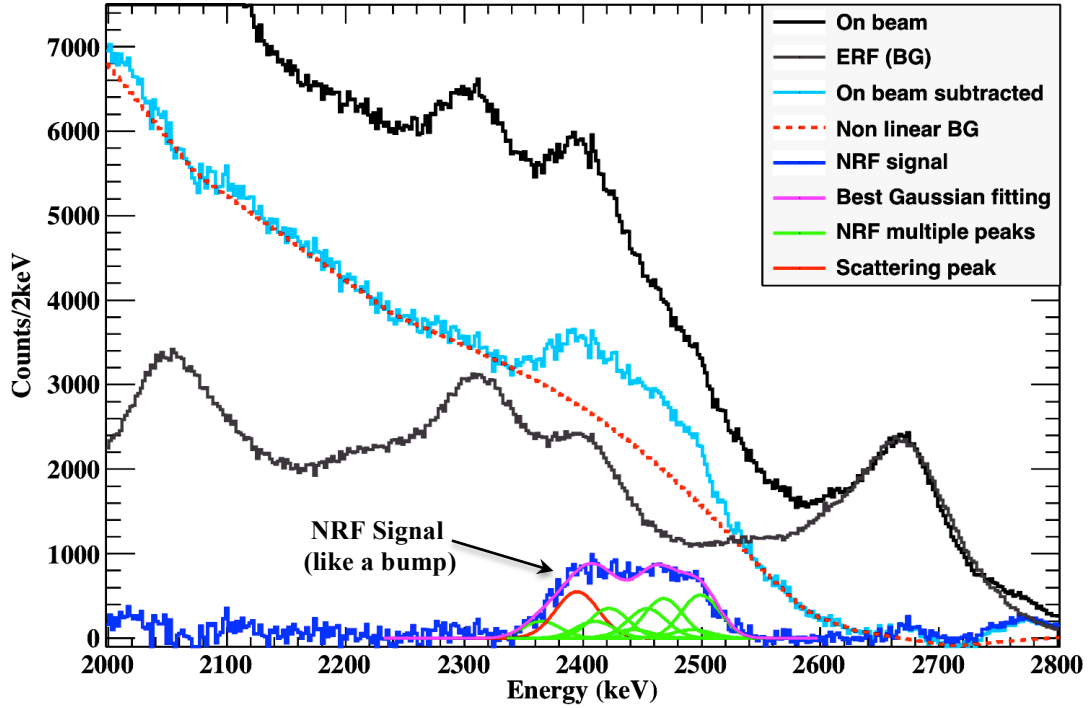
Fig. 6.25: *The on-beam spectrum of the NRF interaction of ^{238}U, the estimated ERF of the background spectrum of the LaBr$_3$:Ce detector, the subtracted on-beam spectrum from the ERF (background) indicated by the subtracted on-beam, the non-linear background estimation for the subtracted on-beam spectrum, and the NRF γ-ray lines after subtracting the non-linear background.*

The 11 NRF γ-rays were observed using the HPGe detectors are shown in Fig 6.18 around the incident beam energy. Nearly all of the detected lines using the HPGe detectors were measured using the LaBr$_3$:Ce detector array, except for the three lines of 2472, 2511 and 2529 keV because of their weak strength.

The integrated NRF cross-sections of the ^{238}U levels at approximately 2.5 MeV using the LaBr$_3$:Ce and HPGe detectors and the available reference data are presented in Table 6.3. The obtained cross-sections using the LaBr$_3$:Ce and HPGe detectors are consistent with one another within the statistical uncertainties.
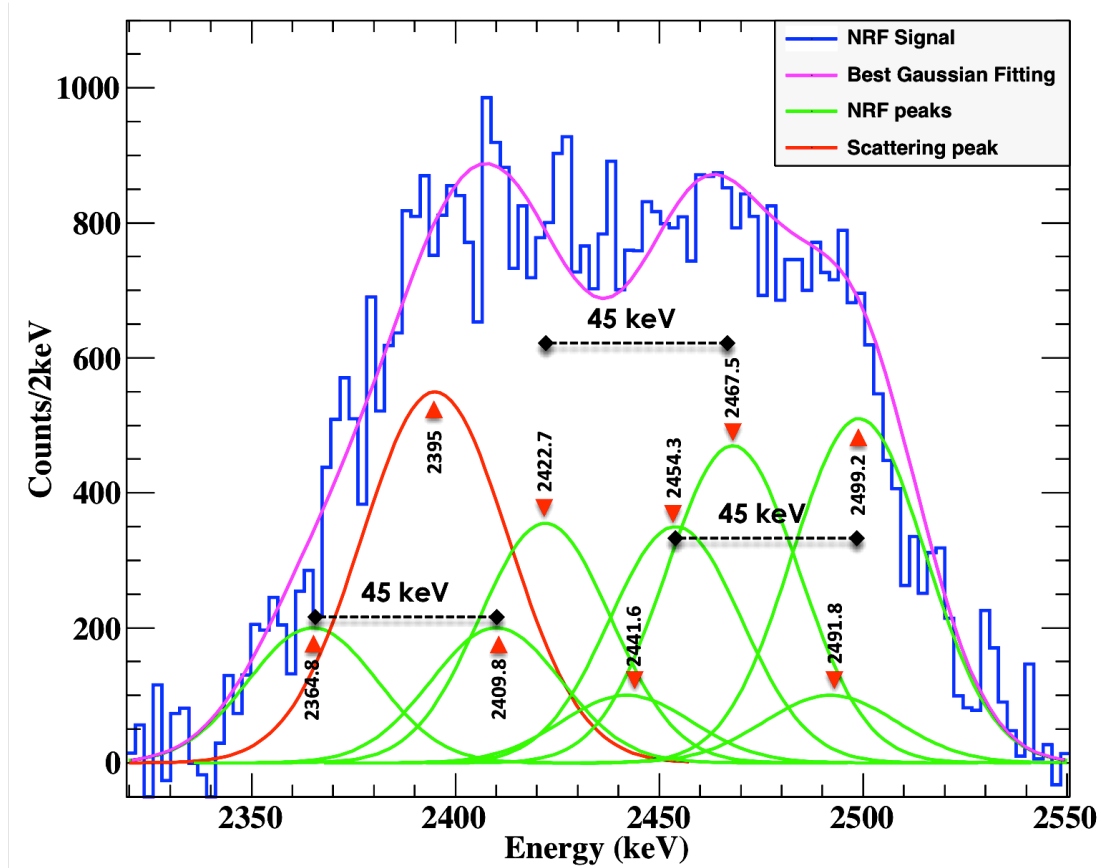
Fig. 6.26: The NRF γ-ray spectrum with the multiple Gaussian fitting of the ^{238}U isotope. The eight Gaussian peaks correspond to eight nuclear states in the ^{238}U isotope. There are six lines that form three pairs with separation energies of approximately 45 keV, 2499.2 (2454.3), 2467.5 (2422.7), and 2409.8 (2364.8) keV. The scattering peak corresponds to the direct scattering from the incident beam by a scattering angle of approximately 6.75°.

The 2468 keV NRF level, with an integrated cross-section that was expected to be the strongest level, was at approximately 80 b.eV [80] in ^{238}U in this energy region. However, the present result showed a value of 47±5 (38±5) b.eV for HPGe (LaBr₃:Ce), which is consistent with the integrated cross-section of 38 b.eV reported by B.J. Quiter, *et al.* [78]. The integrated cross-section of the 2409.8 keV NRF level is ~23 b.eV, which is close to that previously reported by S.L. Hammond, *et al.* [80]. Note that there are four

new levels of 2442, 2454, 2472 and 2511 keV. Two of these levels were measured using both of the detectors.

Summary of the integrated cross-sections of the ^{238}U isotope at approximately 2.5 MeV measured using an LaBr$_3$:Ce detector array and an HPGe detector array as a benchmark for the data.

E_γ (keV)	I_s (b.eV)		
	HPGe (60%)	LaBr$_3$:Ce (1.5″×3″)	Previous data
2365	44±5	39±5	44±6 [80]
2410	37±4	23±4	18±2 [80], 33 [78]
2423	33±4	36±5	12±1 [9]
2442	3.9±1.9	6.8±2.1	-
2454	39±4	27±4	-
2468	47±5	38±5	38 [78], 80±8 [80]
2472	10.1±2.9	-	-
2492	7.5±2.7	8.2±2.3	9±1 [80]
2499	46±4	44±5	32±2 [80]
2511	4.1±1.9	-	-
2529	9.5±2.7	-	12±2 [80]

Consequently, the LaBr$_3$:Ce detector is applicable for measuring the NRF excitations even for the heavy materials that have a close excisions levels, such as ^{238}U – separation energy is about 45 keV, which is less than the detector energy resolution. Additionally, the LaBr$_3$:Ce is useful to measure the NRF excitations even under the self-activity in the 2 MeV region, which

contaminates the NRF-spectrum by the multiple alpha-peaks. Thus, the LaBr$_3$:Ce detector could be a candidate for the detector system of the SNM inspection system

6.3 Conclusion

The dependence of the NRF reaction yield on the target thickness was studied. The NRF measurements from four different thicknesses, 1.287, 2.703, 4117, and 5.563 mm, of ^{238}U were performed at the HIγS facility. The NRF yield shows a saturation behavior for the NRF interaction with the target thickness. The NRF RY model was deduced for interpreting the saturation behavior of the NRF yield.

Moreover, the Monte Carlo simulation by GEANT4 was conducted for the NRF interaction to evaluate a wide range of thicknesses. The simulation results were consistent with the experimental results for the same transition level of 2468 keV. The analytical model of the NRF RY can reproduce the experimental and the simulation results. The simulation code is validated by the experimental result as well; it is verification by the NRF RY model.

The ultimate outcome for this method was the precise estimation of the NRF cross-section without any absolute measurements of the photon flux, detection efficiency, and so on. This method precisely addresses the attenuation of the incident γ-rays due to the atomic and nuclear absorption and the self-absorption of the emitted NRF γ-rays. The NRF cross-sections were deduced by the absolute measurement from the saturation curve of the scattering yield of the NRF versus the target thickness.

Extraction of the integrated cross-sections of the NRF excitations at approximately 2.5 MeV was successfully demonstrated. The integrated cross-section of the 2468 keV NRF level in ^{238}U was deduced as ~40 b.eV, which is consistent with the previously reported result. We measured four new NRF levels for the ^{238}U at approximately 2.5 MeV. The feasibility of using a LaBr$_3$:Ce detector to measure the NRF excitation levels of ^{238}U was investigated by applying the ERF simulation. Therefore, the LaBr$_3$:Ce detector could be an alternative detector in an inspection system for SNMs requiring a large number of detectors.

CHAPTER 7

Summary, Conclusion, and Realistic

Model

7.1 Summary and Conclusion

This dissertation presents the essential calculations to optimize the detection system for the SNMs based on the NRF using the LCS γ-ray source. A Monte Carlo radiation transport simulation code using the GEANT4 toolkit was developed to examine the NRF interaction considering the emission transitions, the angular distribution, the recoil energy, and the thermal motion of the nuclei. Based on the Monte Carlo and analytical calculations, the measurements of the NRF γ-rays at the backwards angles, with respect to the interrogating beam direction, minimize the background due to the atomic scattering with NRF yields that are significantly high relative to a comparable setup with a measurement of the forward–directed photons. Moreover, the characteristics of the incident flux on the interrogation material of ^{235}U in terms of the energy spread (FWHM) and the incident photon number

demonstrated that the NRF yield significantly increased linearly with a reduction in the energy spread of the incident beam and with an increasing flux.

The dependency of NRF yield at the target thickness was shows a saturation trend with the target thickness. An analytical model for the NRF reaction yield was deduced to interpret the behavior of the saturation curve of the NRF yield. This saturation attributed to the attenuation of the incident beam prior to the NRF interaction and the self-absorption of the resonant emissions through the target before leaving it to progress toward the measuring system.

We further examined this saturation phenomena using the NRF experiments performed on the ^{208}Pb and ^{238}U. The experiment on ^{208}Pb was at a relatively high resonant energy of 7.3 MeV on several of the targets with a thickness on the order of cm. Next we performed the experiment on the nuclear material of ^{238}U at a relatively low energy of 2.5 MeV for measurements on the different target thicknesses on the order of mm. For studying in a wide range of the target thickness for both of the experiments, the MC simulation was performed. All of the experimental and simulation data were consistent with each other and demonstrated that the NRF yield was saturated with the target thickness due to attenuation and the self-absorption processes. From this point, the calculation shows that the NRF measurements at the backward angles relative to the incident beam are better than the other scattering angles because the attenuation and the self-absorption are significantly reduced with the backward angles, as well, the

146

mainly NRF reaction yield is coming from the first layer of the target.

For the detector type, we studied the feasibility of the LaBr$_3$:Ce detector for measuring very close NRF excitation levels (9 peaks) of ^{238}U over a short energy range of 200 keV with the developed analysis code based on the energy response function developed by GEANT4. The NRF cross-sections of the ^{238}U excitation levels measured with the LaBr$_3$:Ce detector shows a good agreement with that measured with the HPGe detector as a benchmark. Consequently, the LaBr$_3$:Ce detector could be an alternative detector to the HPGe detector in the inspection system.

Finally, we conclude that the detection system should be placed at the backward angles from the viewpoint of the following: atomic scattering, resonant emissions (scattering NRF γ-ray, angular distribution of the NRF γ-rays), and the target thickness. In a realistic case, the inspection target could be thicker than that used in the experiments with an additional shield surrounding the nuclear material (at least the wall of the container cargo); therefore, the attenuation would be significant. Thus, the incident beam should be sufficiently intense to reduce the inspection time. Furthermore, in the next section, the MC simulation GEANT4 is performed for the nearly realistic case of cargo container.

7.2 MC Simulation for the Realistic Inspection System

7.2.1 Simulation Setup

The MC simulation GEANT4 was performed for the 1 kg of the HUE (93% - ^{235}U) with a 7% of ^{238}U with a box shape at the center of a standard 20′

container (20′ in length, 8′ in width, and 8′ 6″ in height). The container wall is assumed with an iron metal with a thickness of 5 mm.

As a result of the preceding study in chapter 3, the detector system was positioned at a backward angle 180º with respect to the incident beam. The detection system was a detector array which consists of a 100 LaBr$_3$:Ce detectors (10 × 10 detector matrix with a space 10 mm). In this simulation we examined 3 different crystal sizes, 1.5″ × 3″, 3″ × 3″, and 3.5″ × 4″, to assessment the performance of detection system for the different crystal size. In addition the detector in pixel shape with side length 3″ is calculated to comparing with common detector shape of the cylinder. The detector array was placed a 1.5 m from target/container center.

The interested level in ^{235}U is 1733 keV, which has a cross-section ~30 b.eV. Thus, the interrogation beam is irradiated the target using the LCS γ-ray energy 1733 keV with assuming the energy spread with ΔE/E = 1% of the incident energy. Moreover a different energy spread also is calculated such as 5%, as well, the very small energy spread with σ = 10 eV. The beam size is assumed to have a diameter of 2 cm. The integrated incident γ-photons number was 2 × 10^9 which corresponds to nearly 3 × 10^6 photon/sec over a 10 minutes irradiation.

The geometry configuration for the target inside the container as well the detection system with and without the γ-ray tracking is displayed in the Fig 7.1 for a different viewpoint. Although the simulation can treat any kind of obstacles inside the cargo, we assumed the cargo without load in this demonstration.

(A)

20' Container

Target
(HEU)

LCS γ-ray

LaBr detector
array (100)

(B)
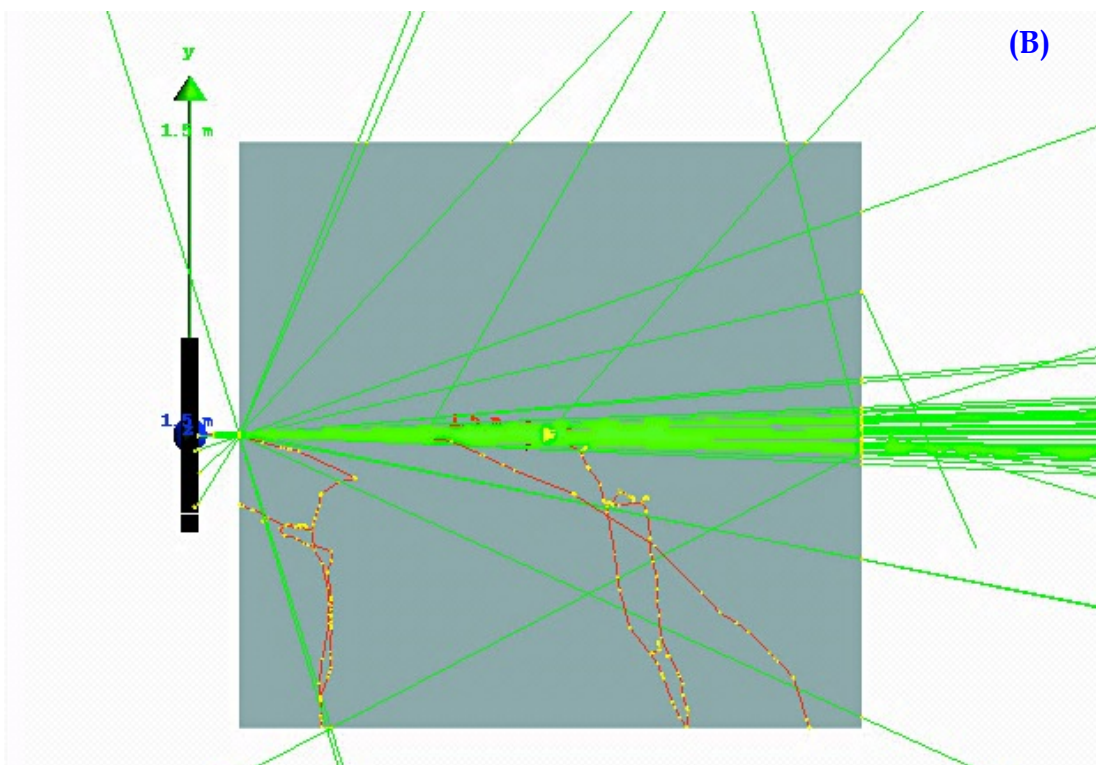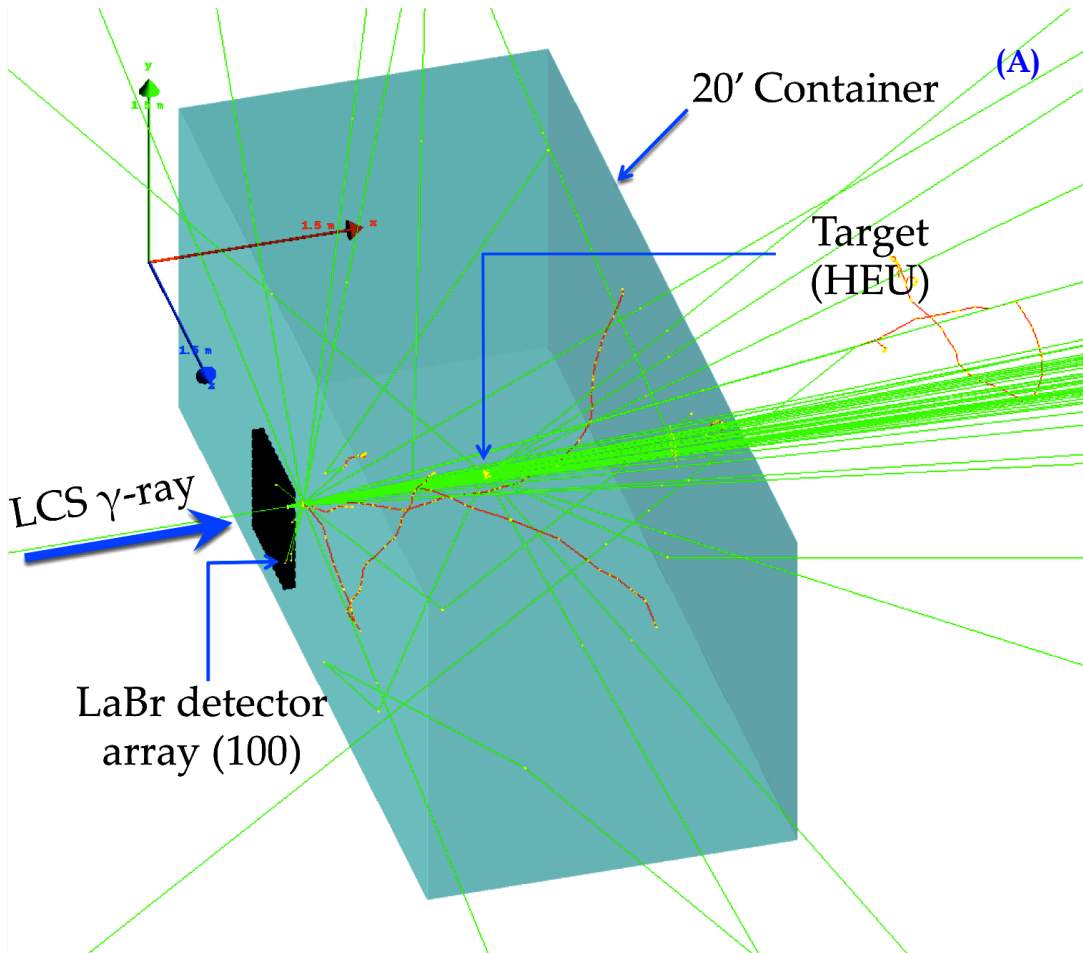
Continue
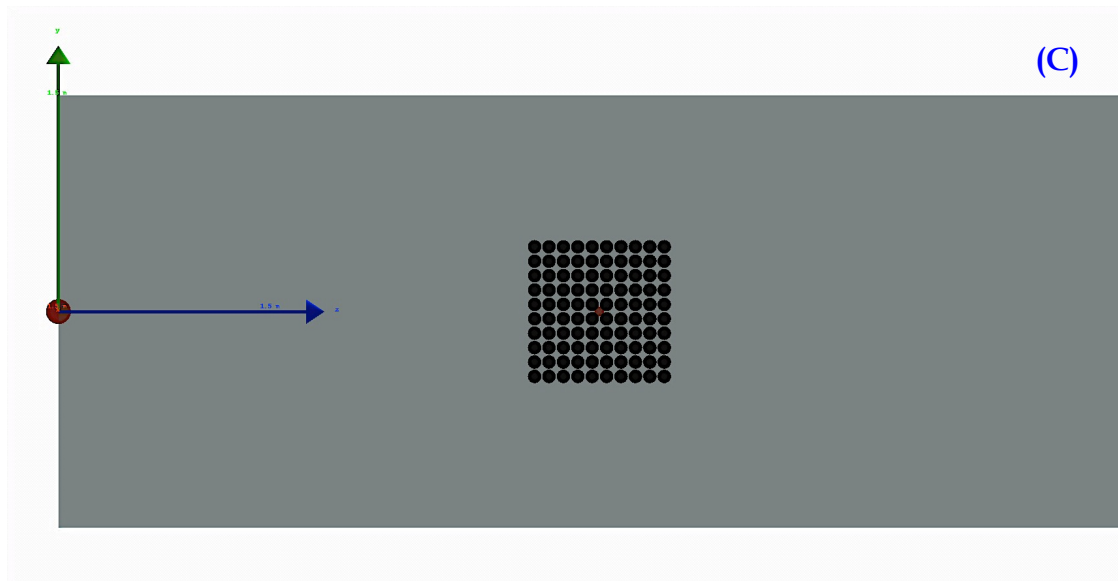
Fig. 7.1: *The geometer configuration of the 1 kg of the HEU (93%) at the center of the 20′ container with the detection system of the 100 LaBr$_3$:Ce detector that is constructed as a matrix array (10 × 10) at 1.5 m from the target center.* ***(A)*** *3-D view for the system with the γ-ray tracking of the interaction.* ***(B)*** *2-D view for the system from the backside of the container.* ***(C)*** *2-D for the side view of the system, which clearly shows the detector array of the LaBr$_3$:Ce (3″ × 3″).*

7.2.2   Simulation Results and Discussion

Fig. 7.2 shows the simulated energy spectra of the HEU that measured by 3 different detector array of the LaBr$_3$:Ce with spread of incident energy was 1%. It is clear that NRF peaks observed in detector arrays are separated from the background events due to atomic scattering γ-rays as expected in previous section.
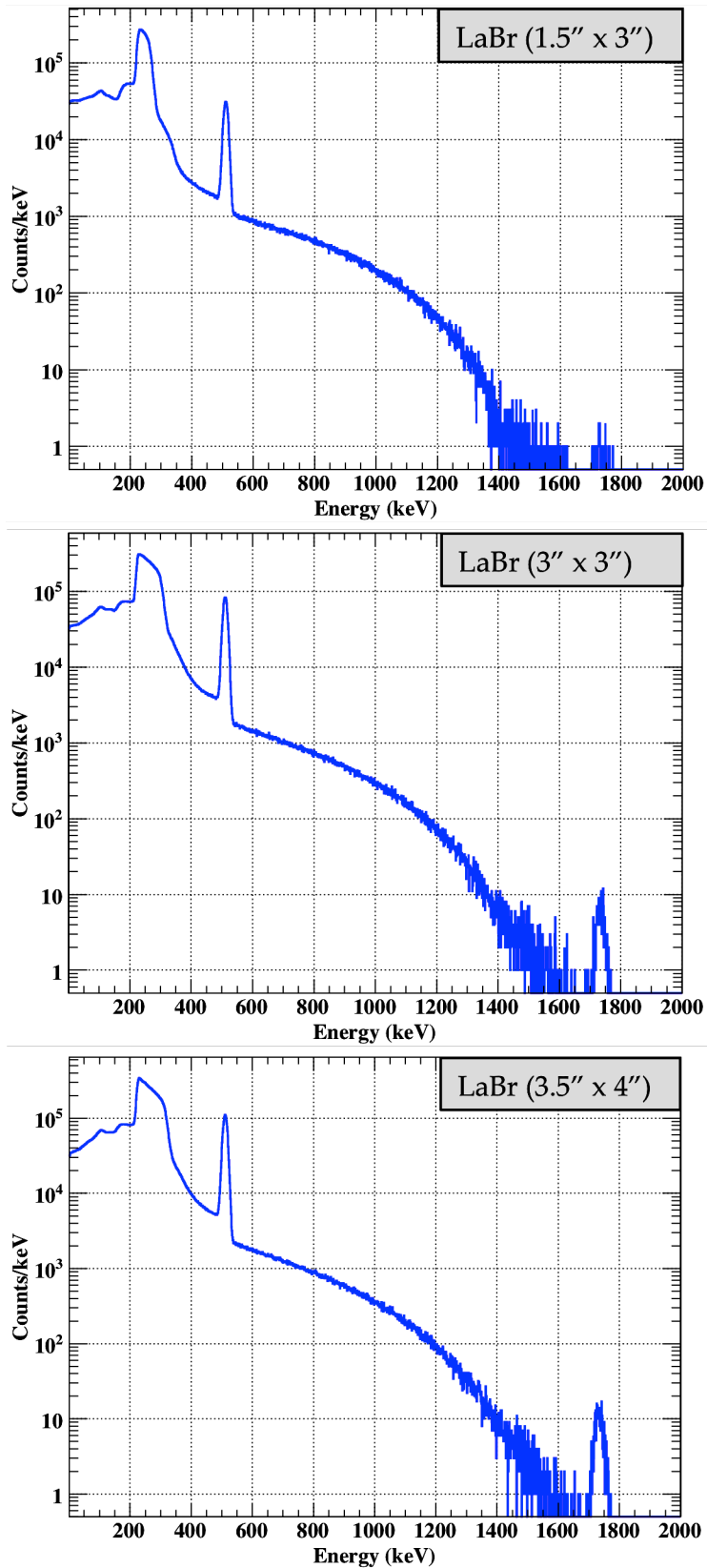
Fig. 7.2: *The comparison between the NRF energy spectra of HEU (^{235}U -1733 keV) that measured with the different crystal size of the LaBr₃:Ce in which the detector array is consist of a 100 detector. The incident energy spread was 1% at FWHM of 1733 keV.*

Table 7.1 indicates the summary of the simulation result for all runs, which was performed for the different incident energy spread and different LaBr$_3$:Ce crystal size and shape. The simulation results showed that the NRF yield from the large size of the detector unit is the larger than that from small one. Whereas, the detector array with the detector size of (3″ × 3″) is about 6 times better than with the small size of (1.5″ × 3″) to detect the scattering NRF γ-rays, while is the half with respect to the detector size of (4.5″ × 3″) for the same detector shape. Moreover, the detector array with the detector unit in pixel shape (3″- side length) exhibits good effectiveness to detect the scattering NRF γ-rays than the same size of the detector in cylindrical shape (3″ in diameter by 3″ in the length) by about 130%.

It should be noted that the difference in the NRF yield from different crystal size is explained by the detection efficiency of each detector. For example, the detection efficiency of 3″ × 3″ detector is about 6 time larger than 1.5″ × 3″ one in 1733 keV γ-rays emitted isotropically from a target. We should mention that the energy resolution of different crystal size of LaBr$_3$:Ce detector should be different. For instant, a small crystal should be better energy resolution. In this simulation, however, we assumed the same energy resolution, which was deduced from the 1.5″ × 3″ LaBr$_3$:Ce, for all detector sizes. We can conclude that a 100 LaBr$_3$:Ce detector array could measure the 1733 keV NRF γ-rays from the 1 kg of the HEU hidden in the 20′ container within a certain time.

The summary of the NRF yield for the different LaBr$_3$:Ce crystal size and shape as well, different energy spread of the incident beam energy of 1733 keV. The NRF reaction yield events at the interaction point were approximately 5.1×10^7, 7×10^4, and 1.4×10^4 for the three different values of ΔE/E of the incident beam of 1.36×10^{-3}, 1, 5 %, respectively.

LaBr crystal size	ΔE/E (FWHM)		
	1.36×10^{-3}% (23.55 eV)	1% (17.33 keV)	5% (86.65 keV)
1.5″×3″ – Cyl.	26170	30	7
3″×3″ – Cyl.	160094	230	42
3″ – Pixel	210455	296	62
3.5×4″ – Cyl.	281588	414	87

7.2.3 Conclusion

GEANT4 calculation has been performed for a realistic model of the inspection system for a standard 20′ container. The detector system consists of 100 (10 × 10) LaBr$_3$:Ce detectors. Different crystal sizes and different incident energy spread have been studied assuming a 1 kg HEU located in the center of the cargo. As the result, the NRF yield measured with large detector size array is larger than small one. Thus, the detector array with a large detector size is preferable and efficient to measure the scattering NRF γ-rays than the small size. Additionally the box or the pixel shape of the detector is more effectiveness than the cylindrical shape in the inspection system of the NRF. Consequently we can demonstrate the ability of the

LaBr$_3$:Ce detector array with a 100 detector to measure the NRF γ-rays from 1 kg HEU at the backward angle of 180°. Further studies on the NRF yield estimation in various loading conditions will be continues by using modified GEANT4 code.

Appendix A

GEANT4 Simulation Main Classes of

the NRF Interaction

```cpp
// ****************************************************************
// GEANT4 DetectorConstruction class: source file
// Class Description
// This class to construct the detector system and the target geometry and materials
// ****************************************************************

#include "DetectorConstruction.hh"
#include "DetectorMessenger.hh"
#include "JAEAGeDetectorConstruction.hh"

#include "Materials.hh"
#include "CalorimeterSD.hh"

#include "globals.hh"
#include "G4RotationMatrix.hh"
#include "G4Material.hh"
#include "G4Box.hh"
#include "G4SubtractionSolid.hh"
#include "G4Tubs.hh"
#include "G4UnionSolid.hh"
#include "G4AssemblyVolume.hh"
#include "G4LogicalVolume.hh"
#include "G4PVPlacement.hh"
#include "G4Transform3D.hh"
#include "G4TransportationManager.hh"
#include "G4SDManager.hh"
#include "G4RunManager.hh"

#include "G4VisAttributes.hh"
```

```cpp
#include "G4Colour.hh"

#include "G4SystemOfUnits.hh"
#include "G4ios.hh"
#include <iomanip>
#include "G4GeometryManager.hh"
#include "G4PVReplica.hh"

//-----------------------------------------------------------------------------
DetectorConstruction::DetectorConstruction()
,defaultMaterial(NULL)
,solidWorld(NULL)
,logicWorld(NULL)
,physiWorld(NULL)
,calorimeterSD(NULL)
{
  // default parameter values of the calorimeter
  CalorSizeX  = 66.4 * cm;
  CalorSizeY  = 80.0 * cm;
  CalorSizeZ  = 13.4 * cm;
  CalorPosX   = 0 * cm;

  ComputeCalorParameters();

  // create commands for interactive definition of the calorimeter
  detectorMessenger = new DetectorMessenger(this);
}

//-----------------------------------------------------------------------------
DetectorConstruction::~DetectorConstruction()
{
  delete detectorMessenger;
}
//-----------------------------------------------------------------------------
G4VPhysicalVolume* DetectorConstruction::Construct()
{
  DefineMaterials();
  return ConstructCalorimeter();
}
//-----------------------------------------------------------------------------
void DetectorConstruction::DefineMaterials()
{
  //This function illustrates the possible ways to define materials
  Materials* materialConstruction = new Materials;
  materialConstruction-> Construct();

  //default materials of the calorimeter
  defaultMaterial          = G4Material::GetMaterial("Air");
  ContMaterial             = G4Material::GetMaterial("Iron");
  DetectorMaterial         = G4Material::GetMaterial("LaBr3");
  ShieldMaterial                   = G4Material::GetMaterial("Lead");
```

```cpp
  PlateMaterial                = G4Material::GetMaterial("Copper");
  TargetMaterial          = G4Material::GetMaterial("enrichedUranium");
}
//-------------------------------------------------------------------------
G4VPhysicalVolume* DetectorConstruction::ConstructCalorimeter()
{
 // complete the Calor parameters definition
  ComputeCalorParameters();


 //-------------------------------------------------------------------------
 //                         World
 //-------------------------------------------------------------------------
  solidWorld = new G4Box("World",                              //its name
                     WorldSize/2., WorldSize/2., WorldSize/2.);     //its size

  logicWorld = new G4LogicalVolume(solidWorld,              //its solid
                             defaultMaterial,                //its material
                               "World");                     //its name

  physiWorld = new G4PVPlacement(0,                          //no rotation
                                G4ThreeVector(),             //at (0,0,0)
                                "World",                      //its name
                                logicWorld,                   //its logical volume
                                NULL,                         //its mother  volume
                                false,                        //no boolean operation
                                0);                           //copy number
  logicWorld->SetVisAttributes (G4VisAttributes::Invisible);
 //-------------------------------------------------------------------------
 //                         Target
 //-------------------------------------------------------------------------
  G4double box_size  = 3.7476  *cm;

  solidTarget = NULL; logicTarget = NULL; physiTarget = NULL;

  solidTarget = new G4Box("TargetSolid",                     //its name
                     box_size/2., box_size/2., box_size/2.); //its size

  G4RotationMatrix* rotTar = new G4RotationMatrix;
  rotTar-> rotateY(90.0*deg);

logicTarget = new G4LogicalVolume(solidTarget,              //its solid
                              TargetMaterial,               //its material
                              "Target");                    //its name

  physiTarget = new G4PVPlacement(rotTar,                    //no rotation
                               G4ThreeVector(0.,0.,0.),     //at (0,0,0)
                               "Target",                     //its name
                                logicTarget,                 //its logical volume
                                physiWorld,                  //its mother  volume
                                false,                       //no boolean operation
                                0);                          //copy number
```

157

```cpp
//------------------------------------------------------------------------
//        Scintillation Detector - LaBr3:Ce   (3" x 3")
//------------------------------------------------------------------------
 G4double DetSizeD = 7.62 *cm;          // detector diameter
 G4double DetSizeL = 7.62 *cm;          // detector length


   solidDet = NULL; logicDet = NULL; physiDet = NULL;


  // detector shape:
  solidDet = new G4Tubs("Det",                          //its name
                        0 , DetSizeD/2, DetSizeL/2., 0, CLHEP::twopi);


  // detector logic (material):
  logicDet = new G4LogicalVolume(solidDet,         //its solid
                                 DetectorMaterial,  //its material
                                 "Det");            //its name
//------------------------------------------------------------------------
//           Detector Array – detector position
//------------------------------------------------------------------------
      G4double DetGap = 10./2. *mm;   // detector gap
      G4int    NDet   = 10;                 // No. of Detectors per arrow (Square Matrix)
      G4int    DetID  = 0;                  // detector ID
      G4double x1        = -1.5 * m;        // detector array – target distance

   G4RotationMatrix* DetRot = new G4RotationMatrix;
   DetRot -> rotateY(90.0*deg);          // detector orientation

   G4double y1 = (DetSizeD+DetGap)/2.*(NDet-1);

   for(int i=0;i<NDet;i++) {

   G4double z1 = (DetSizeD+DetGap)/2.*(NDet-1);

    for(int j=0;j<NDet;j++)
    {
     DetID = (j + 1) + (i * NDet);

     physiDet = new G4PVPlacement(DetRot,                       // rotation
                          G4ThreeVector(x1, y1 , z1),
                          "Det",                   //its name
                          logicDet,                //its logical volume
                          physiWorld,              //its mother  volume
                          false,                   //no boolean operation
                          DetID);                  //copy number

        z1 = z1 - (DetSizeD+DetGap);
         }
        y1 = y1 - (DetSizeD+DetGap);
        }
```

```cpp
//---------------------------------------------------------------------
//                   Container  Cargo
//---------------------------------------------------------------------
      G4double Cont_L1  =       6.0960 *m;      // 20' 0"
      G4double Cont_W1 =        2.4384 *m;      // 08' 0"
      G4double Cont_H1 =        2.5908 *m;      // 08' 6"
      G4double ContThickness = 5. *mm;
      G4double Cont_L2  =       Cont_L1 - ContThickness;
      G4double Cont_W2 =        Cont_W1 - ContThickness;
      G4double Cont_H2 =        Cont_H1 - ContThickness;

      box1 = NULL; box2 = NULL; logicCont = NULL; physiCont = NULL;

       box1 = new G4Box("Box1", Cont_L1/2., Cont_W1/2., Cont_H1/2.);
       box2 = new G4Box("Box2", Cont_L2/2., Cont_W2/2., Cont_H2/2.);

      G4RotationMatrix* rotCont = new G4RotationMatrix();
      rotCont-> rotateY(90.*deg);

       G4SubtractionSolid* container = new G4SubtractionSolid("Box1-Box2", box1, box2);

      logicCont  = new G4LogicalVolume(container,              //its solid
                                       ContMaterial,           //its material
                                       "Container");           //its name

      physiCont = new G4PVPlacement( rotCont,                   //rotation
                                     G4ThreeVector(0.,0.,0.),   //at (0,0,0)
                                     logicCont,                 //its logical volume
                                     "Container",               //its name
                                     logicWorld,                //its mother  volume
                                     false,                     //no boolean operation
                                     0);                        //copy number
//---------------------------------------------------------------------
//                   Sensitive Detectors
//---------------------------------------------------------------------
 G4SDManager* SDman = G4SDManager::GetSDMpointer();

 if(!calorimeterSD) {
  calorimeterSD = new CalorimeterSD("CalorSD", this);
  SDman->AddNewDetector( calorimeterSD );
 }

 G4AssemblyVolume* assembly = new G4AssemblyVolume();

 JAEAGeDetectorConstruction* aHPGeDetector = new JAEAGeDetectorConstruction();
 aHPGeDetector->Construct(assembly);

 // aHPGeDetector->SetSensitiveDetector(calorimeterSD);         // SD --> Ge
 logicDet->SetSensitiveDetector(calorimeterSD);                 // SD --> LaBr
```

```cpp
//-------------------------------------------------------------------
//                    Visualization attributes
//-------------------------------------------------------------------

  G4VisAttributes* TargAtt = new G4VisAttributes(true, G4Color(0.0, 0.4, 1.0));
  TargAtt->SetForceSolid(true);
  logicTarget->SetVisAttributes(TargAtt);

  G4VisAttributes* DetAtt = new G4VisAttributes(true, G4Color(.8, .8, .8, 0.5));
  DetAtt->SetForceSolid(true);
  logicDet->SetVisAttributes(DetAtt);

  G4VisAttributes* ContAtt = new G4VisAttributes(true, G4Color(173./255., 216./255.,
  230./255.));
  ContAtt ->SetForceSolid(true);
  logicCont->SetVisAttributes(ContAtt);


//----------------------------------------------------
//always return the physical World
//----------------------------------------------------
  PrintCalorParameters();
  return physiWorld;
}
//----------------------------------------------------
void DetectorConstruction::PrintCalorParameters()
{
  G4cout << "\n------------------------------------------------------------\n"
//       << "---> The calorimeter is " << NbOfLayers << " layers of: [ "
      << TubeLength/mm << "mm of " << TubeMaterial->GetName()
//       << " + "
//       << GapThickness/mm << "mm of " << GapMaterial->GetName() << " ] "
      << "\n------------------------------------------------------------\n";
}
//----------------------------------------------------
void DetectorConstruction::SetCaskMaterial(G4String materialChoice)
{
  // search the material by its name
  G4Material* pttoMaterial = G4Material::GetMaterial(materialChoice);
  if (pttoMaterial){
    TubeMaterial = pttoMaterial;
    logicTarget->SetMaterial(pttoMaterial);
    PrintCalorParameters();
  }
}
//----------------------------------------------------
void DetectorConstruction::SetCaskHeight(G4double val)
{
  // change Cask thickness and recompute the calorimeter parameters
  TubeLength = val;
}
//----------------------------------------------------
```

160

```cpp
void DetectorConstruction::SetCalorSizeX(G4double val)
{
  // change the transverse size and recompute the calorimeter parameters
  CalorSizeX = val;
}
//----------------------------------------------------
void DetectorConstruction::SetCalorSizeY(G4double val)
{
  // change the transverse size and recompute the calorimeter parameters
  CalorSizeY = val;
}
//----------------------------------------------------
void DetectorConstruction::SetCalorPosX(G4double val)
{
  // change the longitudinal position
  CalorPosX = val;
}
//----------------------------------------------------
void DetectorConstruction::SetLowerEnergyRange(G4double val)
{
  // change the Lower energy range of HIT collection
  LowerEnergyRange = val;
}
//----------------------------------------------------
void DetectorConstruction::SetDetectorResolution(G4double val)
{
    detRes = val ;
}
//----------------------------------------------------
void DetectorConstruction::UpdateGeometry()
{
  G4RunManager::GetRunManager()->DefineWorldVolume(ConstructCalorimeter());
}
////////////////////////////////////////////////////////////////////////////////////


// ****************************************************************
// GEANT4 DetectorConstruction class: header file
// ****************************************************************

#ifndef DetectorConstruction_h
#define DetectorConstruction_h 1
#include "G4VUserDetectorConstruction.hh"
#include "globals.hh"

class G4Box;
class G4SubtractionSolid;
class G4Union;
class G4EllipticalTube;
class G4Tubs;
class G4LogicalVolume;
```

```cpp
class G4VPhysicalVolume;
class G4Material;
class G4UniformMagField;
class DetectorMessenger;
class CalorimeterSD;

#include "G4SystemOfUnits.hh"
#include "G4ios.hh"
#include <iomanip>
#include "G4GeometryManager.hh"
//------------------------------------------------------
class DetectorConstruction : public G4VUserDetectorConstruction
{
  public:

    DetectorConstruction();
    ~DetectorConstruction();

  public:

    void SetCaskMaterial (G4String);
    void SetCaskHeight (G4double);

    void SetCalorSizeX (G4double);
    void SetCalorSizeY (G4double);
    void SetCalorPosX  (G4double);

    void SetLowerEnergyRange(G4double);

    G4VPhysicalVolume* Construct();
    void SetDetectorResolution(G4double);
    G4double GetDetectorResolution() { return detRes; };

    void UpdateGeometry();

  public:

    void PrintCalorParameters();

    G4double GetWorldSize()     {return WorldSize;};

    G4double GetCalorSizeX()    {return CalorSizeX;};
    G4double GetCalorSizeY()    {return CalorSizeY;};
    G4double GetCalorSizeZ()    {return CalorSizeZ;};

    G4Material* GetCaskMaterial() {return TubeMaterial;};
    G4double   GetCaskRadius()  {return OuterRadius;};
    G4double   GetCaskHeight()  {return TubeLength;};

    G4double   GetLowerEnergyRange() {return LowerEnergyRange;};
```

```cpp
  const G4VPhysicalVolume* GetphysiWorld() {return physiWorld;};
  const G4VPhysicalVolume* GetCask()    {return physiTube;};

private:

  G4Material*    defaultMaterial;
  G4double       WorldSize;

  G4Material*    TargetMaterial;
  G4Material*    ContMaterial;

  G4Material*    DetectorMaterial;
  G4double       DetSizeD, DetSizeL;

  G4double       CalorSizeX, CalorSizeY, CalorSizeZ;
  G4double       CalorPosX;

  G4double         CaskSizeYZ;
  G4double         CaskSizeX;

  G4Box*                 solidWorld;     //pointer to the solid World
  G4LogicalVolume*       logicWorld;     //pointer to the logical World
  G4VPhysicalVolume*   physiWorld;     //pointer to the physical World

  G4Box*                 solidTarget;
  G4LogicalVolume*       logicTarget;
  G4VPhysicalVolume*           physiTarget;

  G4Box*                 box1;
  G4Box*                 box2;
  G4LogicalVolume*       logicCont;
  G4VPhysicalVolume*           physiCont;

  G4Tubs*                solidDet;
  G4LogicalVolume*       logicDet;
  G4VPhysicalVolume*           physiDet;

  G4EllipticalTube*      solidCalor;   // pointer to the solid calorimeter
  G4LogicalVolume*       logicCalor;   // pointer to the logical calorimeter
  G4VPhysicalVolume*           physiCalor[3][6];

  DetectorMessenger* detectorMessenger;   //pointer to the Messenger
  CalorimeterSD*    calorimeterSD;         //pointer to the sensitive detector

  G4double  LowerEnergyRange;

private:

  void DefineMaterials();
  void ComputeCalorParameters();
  G4VPhysicalVolume* ConstructCalorimeter();
```

```cpp
};
//----------------------------------------------------
inline void DetectorConstruction::ComputeCalorParameters()
{
  // Compute derived parameters of the calorimeter

  WorldSize   = 20. * m;  //
}

#endif
////////////////////////////////////////////////////////////////////////////////////////


// ****************************************************************
// GEANT4 Materials class: source file
// Class Description
// This class to construct the elements, isotopes, and materials, which used in the geometry.
// ****************************************************************

#include "Materials.hh"
#include "G4Material.hh"

#include "G4SystemOfUnits.hh"
#include "G4ios.hh"
#include <iomanip>
#include "G4GeometryManager.hh"
// =================================================================
////////////////////////
Materials::Materials()
////////////////////////
{
}
////////////////////////
Materials::~Materials()
////////////////////////
{
}
//////////////////////////
void Materials::Construct()
//////////////////////////
{
  G4double A, Z;
  G4int   iZ, N;
  // --------------------------------------------------------------------
  //                      Elements
  // --------------------------------------------------------------------
  G4Element* elH  = new G4Element("Hydrogen","H",  Z=1.,   A= 1.00794    *g/mole);
  G4Element* elC  = new G4Element("Carbon", "C",   Z=6.,   A=  12.011     *g/mole);
  G4Element* elN  = new G4Element("Nitrogen","N",  Z=7.,   A=  14.00674  *g/mole);
  G4Element* elO  = new G4Element("Oxygen", "O",   Z=8.,   A=  15.9994    *g/mole);
  G4Element* elNa = new G4Element("Sodium", "Na",  Z=11., A=  22.989768 *g/mole);
```

164

```cpp
G4Element* elAl = new G4Element("Alminum", "Al",  Z=13., A=  26.98        *g/mole);
G4Element* elSi = new G4Element("Silicon", "Si",    Z=14., A=  28.0855      *g/mole);
G4Element* elAr  = new G4Element("Argon",   "Ar",    Z=18., A= 39.948  *g/mole);
G4Element* elCa  = new G4Element("Calcium", "Ca",   Z=20., A= 40.078  *g/mole);
G4Element* elFe  = new G4Element("Iron",    "Fe",    Z=26., A= 55.847  *g/mole);
G4Element* elCu  = new G4Element("Copper",  "Cu",    Z=29., A= 63.546  *g/mole);
G4Element* elZr  = new G4Element("Zirconium","Zr",   Z=40., A=91.224    *g/mole);
G4Element* elSn  = new G4Element("Tin",      "Sn",    Z=50., A= 118.710 *g/mole);
G4Element* elI   = new G4Element("Iodine",  "I",      Z=53., A= 126.904 *g/mole);
G4Element* elCs  = new G4Element("Cesium",  "Cs",    Z=55., A= 132.905 *g/mole);
G4Element* elLa  = new G4Element("Lanthanum","La", Z=57., A= 138.905 *g/mole);
G4Element* elBr  = new G4Element("Bromine", "Br",    Z=35., A= 79.904  *g/mole);
G4Element* elCe = new G4Element("Cerium",  "Ce",    Z=58., A= 140.116  *g/mole);


// ----------------------------------------------------------------------
// Materials
// ----------------------------------------------------------------------
G4double density, massfraction, abundance;
G4int natoms, nel;
// ----------------------------------------------------------------------
// B4C
  G4Isotope* iB11 = new G4Isotope("B11", iZ= 5, N= 11, A= 11.01*g/mole);
  G4Isotope* iB10 = new G4Isotope("B10", iZ= 5, N= 10, A= 10.01*g/mole);
  G4Isotope* iC6  = new G4Isotope("C6",   iZ= 6, N= 12, A= 12.011*g/mole);

G4Element* elB11  = new G4Element("Boron 11", "B11", nel= 1);
  elB11->AddIsotope(iB11, abundance= 100. *perCent);
  G4Element* elB10  = new G4Element("Boron 10", "B10", nel= 1);
  elB10->AddIsotope(iB10, abundance= 100. *perCent);
  G4Element* elC6  = new G4Element("Carbon 6", "C6", nel= 1);
  elC6->AddIsotope(iC6, abundance= 100. *perCent);

  density = 2.52 * g/cm3;
  G4Material* B4C = new G4Material("B4C", density, nel= 3);
  B4C-> AddElement(elB11, 0.64);
  B4C-> AddElement(elB10, 0.16);
  B4C-> AddElement(elC6 , 0.20);
  // ----------------------------------------------------------------------
// High Enriched Uranium (HEU)
  G4Isotope* iU235 = new G4Isotope("U235", iZ= 92, N= 235, A= 235.01*g/mole);
  G4Isotope* iU238 = new G4Isotope("U238", iZ= 92, N= 238, A= 238.03*g/mole);

  G4Element* elU238  = new G4Element("Uranium 238", "U238", nel= 1);
  elU238->AddIsotope(iU238, abundance= 100. *perCent);
  G4Element* elU235  = new G4Element("Uranium 235", "U235", nel= 1);
  elU235->AddIsotope(iU235, abundance= 100. *perCent);

  density = 19.05 * g/cm3;
  G4Material*  enrichedUranium= new G4Material("enrichedUranium", density, nel= 2);
  enrichedUranium->AddElement(elU238, 0.07);
  enrichedUranium->AddElement(elU235, 0.93);
```

```cpp
  // -------------------------------------------------------------
// LaBr3
  density= 5.1 *g/cm3;
  G4Material* LaBr3 = new G4Material("LaBr3", density, nel=3);
  LaBr3->AddElement(elLa, 24.875/100);
  LaBr3->AddElement(elBr, 74.625/100);
  LaBr3->AddElement(elCe, 0.5/100);
  // -------------------------------------------------------------
// temperature of experimental hall is controlled at 27 degree.
  const G4double expTemp= CLHEP::STP_Temperature+27.*kelvin;
  // -------------------------------------------------------------
// vacuum
  density= CLHEP::universe_mean_density;
  G4Material* Vacuum= new G4Material("Vacuum", density, nel=2);
  Vacuum-> AddElement(elN, .7);
  Vacuum-> AddElement(elO, .3);
  // -------------------------------------------------------------
// Water
  density = 1.000*g/cm3;
  G4Material* H2O = new G4Material("Water", density, nel=2);
  H2O->AddElement(elH, natoms=2);
  H2O->AddElement(elO, natoms=1);
  // Overwrite computed mean Excitation Energy with ICRU recommended value
  H2O->GetIonisation()->SetMeanExcitationEnergy(75.0*eV);
  // -------------------------------------------------------------
// Air
  density= 1.2929e-03 *g/cm3;  // at 20 degree
  G4Material* Air= new G4Material("Air", density, nel=3,
      kStateGas, expTemp);
  G4double ttt= 75.47+23.20+1.28;
  Air-> AddElement(elN,  massfraction= 75.47/ttt);
  Air-> AddElement(elO,  massfraction= 23.20/ttt);
  Air-> AddElement(elAr, massfraction=  1.28/ttt);
  // -------------------------------------------------------------
// Iron
  A= 55.847 *g/mole;
  density= 7.87 *g/cm3;
  new G4Material("Iron", Z=26., A, density);
  // -------------------------------------------------------------
// Germanium
  A = 72.59 * g/mole;
  density = 5.323 * g/cm3;
  G4Material* Ge = new G4Material("Germanium", Z=32., A, density);
  // -------------------------------------------------------------
  // Lead
  A= 207.2 * g/mole;
  density= 11.35 *g/cm3;
  new G4Material("Lead", Z=82., A, density);
  // -------------------------------------------------------------
// Aluminum
  A= 26.98 *g/mole;
```

```cpp
  density= 2.70 *g/cm3;
  new G4Material("Al", Z=13., A, density);
 // -------------------------------------------------------------
  // Copper
 A= 63.546 *g/mole;
 density= 8.96 *g/cm3;
 new G4Material("Copper", Z=29., A, density);
}
/////////////////////////////////////////////////////////////////////////////////////////
```

```cpp
// *******************************************************************
// GEANT4 Materials class: header file
// *******************************************************************

#ifndef MATERIALS_H
#define MATERIALS_H
#include "globals.hh"
// ================================================================
class Materials {

public:
 Materials();
 ~Materials();

 void Construct();
};

#endif
/////////////////////////////////////////////////////////////////////////////////////////
```

```cpp
// *******************************************************************
// GEANT4 PhysicsList class: source file
// Class Description
// This class contains implementations of the models of physical interactions.
// *******************************************************************

#include "PhysicsList.hh"
#include "PhysicsListMessenger.hh"
#include "G4ParticleDefinition.hh"
#include "G4ParticleWithCuts.hh"
#include "G4ProcessManager.hh"
#include "G4ProcessVector.hh"
#include "G4ParticleTypes.hh"
#include "G4ParticleTable.hh"
#include "G4Material.hh"
#include "G4ios.hh"
#include "G4UnitsTable.hh"
#include "G4SystemOfUnits.hh"

 // --------------------------------------------------------------
```

```cpp
PhysicsList::PhysicsList():  G4VUserPhysicsList()
{
 currentDefaultCut = defaultCutValue = 1.0*um;
 cutForGamma       = defaultCutValue;
 cutForElectron    = defaultCutValue;
 cutForProton      = defaultCutValue;

 pMessenger = new PhysicsListMessenger(this);

 SetVerboseLevel(1);
}
// ---------------------------------------------------------------
PhysicsList::~PhysicsList()
{
}
 // ---------------------------------------------------------------
void PhysicsList::ConstructParticle()
{
 // In this method, static member functions should be called
 // for all particles which you want to use.
 // This ensures that objects of these particle types will be
 // created in the program.

 ConstructBosons();
 ConstructLeptons();
 ConstructMesons();
 ConstructBaryons();
}
// ---------------------------------------------------------------
void PhysicsList::ConstructBosons()
{
 // pseudo-particles
 G4Geantino::GeantinoDefinition();
 G4ChargedGeantino::ChargedGeantinoDefinition();

 // gamma
 G4Gamma::GammaDefinition();

 // optical photon
 G4OpticalPhoton::OpticalPhotonDefinition();
}
 // ---------------------------------------------------------------
void PhysicsList::ConstructLeptons()
{
 // leptons
 G4Electron::ElectronDefinition();
 G4Positron::PositronDefinition();
}
// ---------------------------------------------------------------
void PhysicsList::ConstructMesons()
{
```

```cpp
 //  mesons
}
// -------------------------------------------------------------
void PhysicsList::ConstructBaryons()
{
//  barions
}
// -------------------------------------------------------------
void PhysicsList::ConstructProcess()
{
  AddTransportation();
  ConstructEM();
  ConstructPhotoNuc();
  ConstructGeneral();
}
// -------------------------------------------------------------
// Gamma
#include "G4ComptonScattering.hh"
#include "G4GammaConversion.hh"
#include "G4PhotoElectricEffect.hh"
//#include "G4RayleighScattering.hh"

// e- & e+
#include "G4eMultipleScattering.hh"
#include "G4eIonisation.hh"
#include "G4eBremsstrahlung.hh"
#include "G4eplusAnnihilation.hh"

// Mu
#include "G4MuMultipleScattering.hh"
#include "G4MuIonisation.hh"
#include "G4MuBremsstrahlung.hh"
#include "G4MuPairProduction.hh"

// Hadrons
#include "G4hMultipleScattering.hh"
#include "G4hIonisation.hh"
#include "G4ionIonisation.hh"
  // -------------------------------------------------------------
void PhysicsList::ConstructEM()
{
  theParticleIterator->reset();
  while( (*theParticleIterator)() ){
   G4ParticleDefinition* particle = theParticleIterator->value();
   G4ProcessManager* pmanager = particle->GetProcessManager();
   G4String particleName = particle->GetParticleName();

   if (particleName == "gamma") {
    // gamma
    pmanager->AddDiscreteProcess(new G4GammaConversion());
```

```
        pmanager->AddDiscreteProcess(new G4ComptonScattering());
        pmanager->AddDiscreteProcess(new G4PhotoElectricEffect());
//      pmanager->AddDiscreteProcess(new G4RayleighScattering());

    } else if (particleName == "e-") {
      // electron
      pmanager->AddProcess(new G4eMultipleScattering(),  -1, 1, 1);
      pmanager->AddProcess(new G4eIonisation(),          -1, 2, 2);
      pmanager->AddProcess(new G4eBremsstrahlung(),      -1, 3, 3);

    } else if (particleName == "e+") {
      // positron
      pmanager->AddProcess(new G4eMultipleScattering(),  -1, 1, 1);
      pmanager->AddProcess(new G4eIonisation(),          -1, 2, 2);
      pmanager->AddProcess(new G4eBremsstrahlung(),      -1, 3, 3);
      pmanager->AddProcess(new G4eplusAnnihilation(),     0,-1, 4);

    /*/ Muon
    } else if( particleName == "mu+" ||
             particleName == "mu-" ) {
      pmanager->AddProcess(new G4MuMultipleScattering,    -1, 1, 1);
      pmanager->AddProcess(new G4MuIonisation,           -1,-1, 1);
      pmanager->AddProcess(new G4MuBremsstrahlung,       -1,-1, 2);
      pmanager->AddProcess(new G4MuPairProduction        -1,-1, 3);

    //
    } else if ((!particle->IsShortLived()) &&
             (particle->GetPDGCharge() !=0.0) &&
             (particle->GetParticleName() != "chargedgeantino")) {
      // all others charged particles except geantino
      pmanager->AddProcess(new G4hIonisation,            -1,-1,1);
    */
    }
  }
}

  // --------------------------------------------------------------------

#include "G4Decay.hh"

void PhysicsList::ConstructGeneral()
{
 // Add Decay Process
 G4Decay* theDecayProcess = new G4Decay();
 theParticleIterator->reset();
 while( (*theParticleIterator)() ){
  G4ParticleDefinition* particle = theParticleIterator-> value();
  G4ProcessManager* pmanager = particle->GetProcessManager();
  if (theDecayProcess->IsApplicable(*particle)) {
    pmanager-> AddProcess(theDecayProcess);
    // set ordering for PostStepDoIt and AtRestDoIt
```

```cpp
      pmanager-> SetProcessOrdering(theDecayProcess, idxPostStep);
      pmanager-> SetProcessOrdering(theDecayProcess, idxAtRest);
    }
  }
}
//------------------------------------------------------------------------
//    Photo Nuclear Process
//------------------------------------------------------------------------
//#include "G4PhotoNuclearProcess.hh"
//#include "G4GammaNuclearReaction.hh"
#include "NRFInteractions.hh"
void PhysicsList::ConstructPhotoNuc()
{
  theParticleIterator->reset();
  while( (*theParticleIterator)() ) {
    G4ParticleDefinition* particle = theParticleIterator->value();
    G4ProcessManager* pmanager = particle->GetProcessManager();
    G4String particleName = particle->GetParticleName();

    if (particleName == "gamma") {
      pmanager->AddDiscreteProcess(new NRFInteractions);
    }
  }
}


  // --------------------------------------------------------------------

void PhysicsList::SetCuts()
{
  // reactualise cutValues
  if (currentDefaultCut != defaultCutValue)
    {
     if(cutForGamma    == currentDefaultCut) cutForGamma    = defaultCutValue;
     if(cutForElectron == currentDefaultCut) cutForElectron = defaultCutValue;
     if(cutForProton   == currentDefaultCut) cutForProton   = defaultCutValue;
     currentDefaultCut = defaultCutValue;
    }

  if (verboseLevel >0){
    G4cout << "PhysicsList::SetCuts:";
    G4cout << "CutLength : " << G4BestUnit(defaultCutValue,"Length") << G4endl;
  }

  // set cut values for gamma at first and for e- second and next for e+,
  // because some processes for e+/e- need cut values for gamma
  SetCutValue(cutForGamma, "gamma");
  SetCutValue(cutForElectron, "e-");
  SetCutValue(cutForElectron, "e+");

//  SetCutValueForOthers(defaultCutValue);
```

```cpp
  if (verboseLevel>0) DumpCutValuesTable();
}
// ------------------------------------------------------------------

void PhysicsList::SetCutForGamma(G4double cut)
{
  cutForGamma = cut;
  SetParticleCuts(cutForGamma, G4Gamma::Gamma());
}

void PhysicsList::SetCutForElectron(G4double cut)
{
  cutForElectron = cut;
  SetParticleCuts(cutForElectron, G4Electron::Electron());
}

void PhysicsList::SetCutForPositron(G4double cut)
{
  cutForPositron = cut;
  SetParticleCuts(cutForPositron, G4Positron::Positron());
}

void PhysicsList::SetCutForProton(G4double cut)
{
  cutForProton = cut;
  SetParticleCuts(cutForProton, G4Proton::Proton());
}

G4double PhysicsList::GetCutForGamma() const
{
  return cutForGamma;
}

G4double PhysicsList::GetCutForElectron() const
{
  return cutForElectron;
}

G4double PhysicsList::GetCutForProton() const
{
  return cutForGamma;
}
/////////////////////////////////////////////////////////////////////////////////

// *****************************************************************
// GEANT4 PhysicsList class: header file
// *****************************************************************
#ifndef PhysicsList_h
#define PhysicsList_h 1
#include "PhysicsListMessenger.hh"
#include "G4VUserPhysicsList.hh"
```

```cpp
#include "globals.hh"
// ---------------------------------------------------------------------
class PhysicsList: public G4VUserPhysicsList
{
  public:
    PhysicsList();
   ~PhysicsList();

  protected:
    // Construct particle and physics
    void ConstructParticle();
    void ConstructProcess();

    void SetCuts();

  public:
    // Set/Get cut values
    void     SetCutForGamma(G4double);
    void     SetCutForElectron(G4double);
    void     SetCutForPositron(G4double);
    void     SetCutForProton(G4double);
    G4double  GetCutForGamma() const;
    G4double  GetCutForElectron() const;
    G4double  GetCutForProton() const;

  protected:
    // these methods Construct particles
    void ConstructBosons();
    void ConstructLeptons();
    void ConstructMesons();
    void ConstructBaryons();

  protected:
  // these methods Construct physics processes and register them
    void ConstructGeneral();
    void ConstructEM();
    void ConstructPhotoNuc();

  private:
    G4double cutForGamma;
    G4double cutForElectron;
    G4double cutForPositron;
    G4double cutForProton;
    G4double currentDefaultCut;

    PhysicsListMessenger* pMessenger;
};

#endif
///////////////////////////////////////////////////////////////////////////
```

```cpp
// ********************************************************************
// GEANT4 Physics-->NRFInteractions class: source file
// Class Description
// This class describes the photon interaction with
// NRF interaction with its cross section or the atomic interactions with its cross sections
// As well the nuclear recoil after the NRF interaction - Hani Negm 2012-2014
// ********************************************************************

#include "NRFInteractions.hh"
#include "G4EnergyLossTables.hh"
#include "G4UnitsTable.hh"
#include "G4SystemOfUnits.hh"
#include "G4ios.hh"
// ------------------------------------------------------------------------
using namespace std;
NRFInteractions::NRFInteractions(const G4String& processName,
   G4ProcessType type):G4VDiscreteProcess (processName, type),
   CrossSecFactor(1.)
{
//  SetProcessSubType(15);
  theCrossSectionDataStore = new NRFCrossSectionDataStore();
  G4int numEle = G4Element::GetNumberOfElements();
  for (G4int i = 0; i< numEle; i++) {
   NRFCrossSectionData * aGammaData
    = new NRFCrossSectionData((*(G4Element::GetElementTable()))[i]);
   theCrossSectionDataStore->AddDataSet(aGammaData);
  }
}
// ------------------------------------------------------------------------
// Destructor
NRFInteractions::~NRFInteractions() // (empty) destructor
{
  delete theCrossSectionDataStore;
}
// ------------------------------------------------------------------------
G4bool NRFInteractions::IsApplicable(const G4ParticleDefinition& particle)
{
  return ( &particle == G4Gamma::Gamma() );
}
// ------------------------------------------------------------------------
void NRFInteractions::BuildPhysicsTable(const G4ParticleDefinition&)
// Build cross section and mean free path tables
{ //here no tables, just calling PrintInfoDefinition
  PrintInfoDefinition();
}
// ------------------------------------------------------------------------
G4double NRFInteractions::GetMeanFreePath(const G4Track& aTrack,
                      G4double, G4ForceCondition*)

// returns the photon mean free path in GEANT4 internal units
// (MeanFreePath is a private member of the class)
```

```cpp
{
  const G4DynamicParticle* aDynamicGamma = aTrack.GetDynamicParticle();
  G4Material* aMaterial = aTrack.GetMaterial();

  MeanFreePath = ComputeMeanFreePath(aDynamicGamma, aMaterial);

  return MeanFreePath;
}
// ------------------------------------------------------------------------
G4double NRFInteractions::ComputeMeanFreePath(const G4DynamicParticle* aDynamicGamma,
                                G4Material* aMaterial)

// Computes and returns the photon mean free path in GEANT4 internal units
{
  const G4ElementVector* theElementVector = aMaterial->GetElementVector();
  const G4double* NbOfAtomsPerVolume = aMaterial->GetVecNbOfAtomsPerVolume();

  G4double SIGMA = 0 ;

  for ( size_t i=0 ; i < aMaterial->GetNumberOfElements() ; i++ )  {
    SIGMA += NbOfAtomsPerVolume[i] *
      ComputeCrossSectionPerAtom(aDynamicGamma, (*theElementVector)[i]);
  }

  return SIGMA > DBL_MIN ? 1./SIGMA : DBL_MAX;
}
// ------------------------------------------------------------------------
G4double NRFInteractions::GetCrossSectionPerAtom(
                  const G4DynamicParticle* aDynamicGamma,
                  const G4Element*       anElement)

// gives the total cross section per atom in GEANT4 internal units
{
  G4double crossSection =
      ComputeCrossSectionPerAtom(aDynamicGamma, anElement);

  return crossSection;
}
// ------------------------------------------------------------------------
G4double NRFInteractions::ComputeCrossSectionPerAtom(const G4DynamicParticle* aDynamicGamma,
              const G4Element* anElement)

// Calculates the microscopic cross section in GEANT4 internal units.
// Total cross section parametrisation from H.Burkhardt
// It gives a good description at any energy (from 0 to 10**21 eV)
{

  G4double CrossSection =
```

```
      theCrossSectionDataStore->GetCrossSection(aDynamicGamma, anElement, 0);

  CrossSection *= CrossSecFactor; // increase the CrossSection by  (by default 1)
  return CrossSection;
}
// ------------------------------------------------------------------------
void NRFInteractions::SetCrossSecFactor(G4double fac)
// Set the factor to artificially increase the cross section
{
  CrossSecFactor = fac;
  G4cout << "The cross section for NRF Interaction is artificially "
       << "increased by the CrossSecFactor=" << CrossSecFactor << G4endl;
}
// ------------------------------------------------------------------------
G4VParticleChange* NRFInteractions::PostStepDoIt( const G4Track& aTrack,
                           const G4Step&  aStep)
//
//
{
  aParticleChange.Initialize(aTrack);
  G4Material* aMaterial = aTrack.GetMaterial();

  // current Gamma energy and direction
  const G4DynamicParticle* aDynamicGamma = aTrack.GetDynamicParticle();
  G4double Egam = aDynamicGamma->GetKineticEnergy();
  G4ParticleMomentum GammaDirection = aDynamicGamma->GetMomentumDirection();

  // select randomly one element constituting the material
  const G4Element* anElement = SelectRandomAtom(aDynamicGamma, aMaterial);

  if ( ! theCrossSectionDataStore->IsApplicable(aDynamicGamma, anElement) )
   return  G4VDiscreteProcess::PostStepDoIt( aTrack, aStep );

  G4ParticleMomentum aMomentumDirection =
   theCrossSectionDataStore->GetMomentumDirection(aDynamicGamma, anElement);

// HN ---------------------------------------------------------------->
// Calculate the recoil energy of interested isotope
   G4double  AtomicMass = anElement->GetA() / CLHEP::g /CLHEP::mole;
   G4double  AtomicMassUnit = 931.494 *MeV;
   G4double energy = aDynamicGamma->GetKineticEnergy() / CLHEP::MeV;
   G4double E_Recoil = energy*energy / (2. * AtomicMass * AtomicMassUnit);
   G4double NRF_Energy = energy - E_Recoil;
   Egam = NRF_Energy; // change the enregy of emitted gamma ray by recoil energy

 //   G4cout << "-->Materil: " << aMaterial->GetName() << "  -->GammaEnregyBeforNRF
(keV): " << energy / CLHEP::keV << "  -->RecoilEnergy (eV): " << E_Recoil / CLHEP::eV << "  --
>NRF GammaEnregy (keV): " << Egam / CLHEP::keV << G4endl;

  // HN   <-------------------------------------------------------------
```

```cpp
// NRF gamma ray properties:
G4DynamicParticle* aParticle = new G4DynamicParticle(
    G4Gamma::Gamma(), aMomentumDirection, Egam);

aParticleChange.SetNumberOfSecondaries(1);
aParticleChange.AddSecondary(aParticle);

aParticleChange.ProposeMomentumDirection( 0., 0., 0. ) ;
aParticleChange.ProposeEnergy( 0. ) ;
aParticleChange.ProposeTrackStatus( fStopAndKill ) ;

return G4VDiscreteProcess::PostStepDoIt( aTrack, aStep );
}
// ----------------------------------------------------------------------
G4Element* NRFInteractions::SelectRandomAtom(
                    const G4DynamicParticle* aDynamicGamma,
                        G4Material* aMaterial)
{
 // select randomly 1 element within the material, invoked by PostStepDoIt
 const G4int NumberOfElements        = aMaterial->GetNumberOfElements();
 const G4ElementVector* theElementVector = aMaterial->GetElementVector();
 if (NumberOfElements == 1) return (*theElementVector)[0];

 const G4double* NbOfAtomsPerVolume = aMaterial->GetVecNbOfAtomsPerVolume();

 G4double PartialSumSigma = 0. ;
 G4double rval = G4UniformRand() / MeanFreePath;

 for ( G4int i=0 ; i < NumberOfElements ; i++ ){

  PartialSumSigma += NbOfAtomsPerVolume[i] *
         GetCrossSectionPerAtom(aDynamicGamma, (*theElementVector)[i]);
  if (rval <= PartialSumSigma) {
    return ((*theElementVector)[i]);
  }
 }
 G4cout << " WARNING !!! - The Material '"<< aMaterial->GetName()
    << "' has no elements, NULL pointer returned." << G4endl;
 return NULL;
}
// ----------------------------------------------------------------------
void NRFInteractions::PrintInfoDefinition()
{
 G4cout << G4endl << GetProcessName() << ":  " << "gamma->gamma process"
  /* <<  GetProcessSubType() */<< G4endl;
}
/////////////////////////////////////////////////////////////////////////////////
```

```
// ********************************************************************
// GEANT4 Physics-->NRFInteractions class: header file
// ********************************************************************

#ifndef NRFInteractions_h
#define NRFInteractions_h 1
#include "G4ios.hh"
#include "globals.hh"
#include "Randomize.hh"
#include "G4VDiscreteProcess.hh"
#include "G4PhysicsTable.hh"
#include "G4PhysicsLogVector.hh"
#include "G4Element.hh"
#include "G4Gamma.hh"
#include "G4Electron.hh"
#include "G4Positron.hh"
#include "G4Step.hh"
#include "NRFCrossSectionDataStore.hh"
// -----------------------------------------------------------------------
class NRFInteractions : public G4VDiscreteProcess

{
  public:  // with description

    NRFInteractions(const G4String& processName ="NRF",
            G4ProcessType type = fPhotolepton_hadron);

   ~NRFInteractions();

    G4bool IsApplicable(const G4ParticleDefinition&);
      // true for Gamma only.

    void BuildPhysicsTable(const G4ParticleDefinition&);
      // here dummy, the total cross section parameterization is used rather
      // than tables,  just calling PrintInfoDefinition

    void PrintInfoDefinition();
      // Print few lines of information about the process: validity range,
      // origine ..etc..
      // Invoked by BuildThePhysicsTable().

    void SetCrossSecFactor(G4double fac);
      // Set the factor to artificially increase the crossSection (default 1)

    G4double GetCrossSecFactor() { return CrossSecFactor;}
      // Get the factor to artificially increase the cross section

    G4double GetMeanFreePath(const G4Track& aTrack,
                G4double previousStepSize,
                G4ForceCondition* condition);
      // It returns the MeanFreePath of the process for the current track :
```

```
    // (energy, material)
    // The previousStepSize and G4ForceCondition* are not used.
    // This function overloads a virtual function of the base class.
    // It is invoked by the ProcessManager of the Particle.

  G4double GetCrossSectionPerAtom(const G4DynamicParticle* aDynamicGamma,
                    const G4Element*        anElement);
   // It returns the total CrossSectionPerAtom of the process,
   // for the current DynamicGamma (energy), in anElement.

  G4VParticleChange* PostStepDoIt(const G4Track& aTrack,
                  const G4Step& aStep);
   // It computes the final state of the process (at end of step),
   // returned as a ParticleChange object.
   // This function overloads a virtual function of the base class.
   // It is invoked by the ProcessManager of the Particle.

  virtual
  G4double ComputeCrossSectionPerAtom(const G4DynamicParticle* aDynamicGamma,
                    const G4Element* anElement);

  G4double ComputeMeanFreePath (const G4DynamicParticle* aDynamicGamma,
               G4Material* aMaterial);

 private:

  G4Element* SelectRandomAtom(const G4DynamicParticle* aDynamicGamma,
               G4Material* aMaterial);

 private:

  // hide assignment operator as private
  NRFInteractions& operator=(const NRFInteractions &right);
  NRFInteractions(const NRFInteractions& );

 private:

  G4double LowestEnergyLimit ;    // low  energy limit of the tables
  G4double HighestEnergyLimit ;   // high energy limit of the tables

  G4double fminimalEnergy;        // minimalEnergy of produced particles

  G4double MeanFreePath;          // actual MeanFreePath (current medium)
  G4double CrossSecFactor;        // factor to artificially increase
                     // the cross section
  NRFCrossSectionDataStore*   theCrossSectionDataStore;

};
// ------------------------------------------------------------------------
#endif
////////////////////////////////////////////////////////////////////////////
```

```cpp
// *****************************************************************
// G4 Physics class--> NRFCrossSectionData: source file
// for Nuclear Resonance Fluorescence cross sections
// Created: N. Kikuzawa, Japan Atomic Energy Agency, 24-NOV-06
// Modified by Hani Negm to include the angular distribution
// for the polarization effect. 2012 -2014
// *****************************************************************

#include "NRFCrossSectionData.hh"
#include <vector>
#include <sstream>
#include <algorithm>
#include <fstream>
#include "G4StokesVector.hh"
#include "G4PolarizationHelper.hh"
#include "G4StokesVector.hh"
#include "Randomize.hh"
#include "G4RandomDirection.hh"
#include "G4SystemOfUnits.hh"
#include "G4ios.hh"
#include "G4NistManager.hh"

//----------------------------------------------------------------------//
void NRFCrossSectionData::Init(G4Element* anElement)
{
  if (!getenv("NRFDATA")) {
    G4cout << "NRFCrossSectionData - Warning: "
           << "Please setenv NRFCrossSections to point to the NRF cross-section files."
           << G4endl;
    return;
  }

  theName = anElement->GetName();
  theN = anElement->GetN();
  theZ = anElement->GetZ();
  theLastSpin = 0;
  theLastParity = 0;
  hasCrossSectionData = false;
  theLevelData = new LevelData;

  G4String dirName = getenv("NRFDATA");
  dirName = dirName + "/CrossSection/";
  std::ostringstream streamName;
  streamName << dirName << "z" << (G4int)theZ << ".a" << (G4int)theN;
  G4String file = streamName.str();
  std::ifstream NRFCrossSectionDataFile(file);

  if( !NRFCrossSectionDataFile ) {
    G4cout << "NRFCrossSectionData - Warning: "
```

```cpp
          << " cannot find cross section data file : " << "z" << theZ
          << ".a" << theN << G4endl;
    return;
  }

  char inputChars[80]={' '};
  G4String inputLine;
  while(!NRFCrossSectionDataFile.getline(inputChars, 80).eof())
  {
    inputLine = inputChars;
    inputLine = inputLine.strip(1);

    if (inputChars[0] != '#' && inputLine.length() !=0) {
      G4double a(0.0), b(0.0), d(0.0), e(0.0), f2(0.0);
//    G4int b(0);
      G4String c(' ');
      std::istringstream tmpStream(inputLine);
      tmpStream >>a >> b >> c >> d >> e >> f2;

      MyLevelData* aLevelData = new MyLevelData();
      aLevelData->Excite = a * keV;
      aLevelData->Spin = b;
      aLevelData->Width = d * eV;
      aLevelData->CrossSection = e * microbarn * MeV;
      aLevelData->F2 = f2;
      if (c == (G4String)("+")) {
        aLevelData->Parity = 1;
      } else if (c == (G4String)("-")) {
        aLevelData->Parity = -1;
      } else {aLevelData->Parity = 0;}
      theLevelData->push_back(aLevelData);
    }

    if (theLevelData->size() > 0 ) {
      hasCrossSectionData = true;
    }
  }
  NRFCrossSectionDataFile.close();

  theGroundStateSpin = theLevelData->at(0)->Spin;
  theGroundStateParity = theLevelData->at(0)->Parity;

  if (theLevelData->size() > 0 ) PrintLevelData();
}

//-------------------------------------------------------------------//
G4double
NRFCrossSectionData::GetCrossSection(
  const G4DynamicParticle* aDynamicGamma,
  const G4Element*, G4double
)
```

```cpp
{
  theLastCrossSection = DBL_MIN;
  if( hasCrossSectionData == false ) return theLastCrossSection;

  theLastMomentumDirection = aDynamicGamma->GetMomentumDirection();

// G4double SigmaGamma = 0.0;

  for (G4int i = 0; i< G4int(theLevelData->size()) ; i++) {
    if ( std::abs(aDynamicGamma->GetKineticEnergy() - theLevelData->at(i)->Excite)
        < theLevelData->at(i)->Width * 0.5 )
    {
      theLastSpin = theLevelData->at(i)->Spin;
      theLastParity = theLevelData->at(i)->Parity;
      theLastCrossSection
        = theLevelData->at(i)->CrossSection / theLevelData->at(i)->Width;
//      theLastMomentumDirection = ComputeMomentumDirection(aDynamicGamma);
      if (GetVerboseLevel() > 0) {
        G4cout
          << " = " << theName << " =  "
          << "Gamma-ray Energy = "<< aDynamicGamma->GetKineticEnergy() / keV
          << " keV; "
          << " CrossSection = " << theLastCrossSection / microbarn << " ubarn"
          << G4endl;
        G4ThreeVector aDirection = aDynamicGamma->GetMomentumDirection();
        G4cout << "( X, Y, Z ) = ( " << aDirection.x() << ",  "
            << aDirection.y() << ",  " << aDirection.z()
            << " )  == ";
        G4ThreeVector aPolarization = aDynamicGamma->GetPolarization();
        G4cout << "( X, Y, Z ) = ( " << aPolarization.x() << ",  "
            << aPolarization.y() << ",  " << aPolarization.z()
            << " )"<< G4endl;
      }
      return theLastCrossSection;
    }
  }
  return theLastCrossSection;
}

//G4int k=0;   // Counter

//----------------------------------------------------------------------//
G4ThreeVector
NRFCrossSectionData::ComputeMomentumDirection(
  const G4DynamicParticle* aParticle
)
{
  G4double aSpin   = 0;
  G4int aParity    = 0;
  G4double F2;
```

```cpp
      for (G4int i = 0; i < G4int(theLevelData->size())  ; i++) {
        if ( std::abs(aParticle->GetKineticEnergy() - theLevelData->at(i)->Excite)
            < theLevelData->at(i)->Width * 0.5 )

    //    G4cout <<"k = " << k <<  G4endl;    // Counter
    //     k=k+i;    // Counter
        {
          aSpin = theLevelData->at(i)->Spin - theGroundStateSpin;
          aParity = theLevelData->at(i)->Parity * theGroundStateParity;
           F2 = theLevelData->at(i)->F2;
       }
      }


      G4double greject(1.5);
      G4double cosTheta;
      G4ThreeVector aLastMomentumDirection = aParticle->GetMomentumDirection();

      G4StokesVector aPolarization = aParticle->GetPolarization();

       //NRF transition

       G4ThreeVector aMomentumDirection = aParticle->GetMomentumDirection();
  //    aPolarization.SetPhoton();

           do {
         aLastMomentumDirection = G4RandomDirection();
         cosTheta = std::cos(aLastMomentumDirection.getTheta());
         aLastMomentumDirection.rotateUz(aMomentumDirection);

         G4ThreeVector aPolarizationFrame
          = G4PolarizationHelper::GetFrame(aMomentumDirection, aPolarization);
         G4ThreeVector nInteractionFrame
          = G4PolarizationHelper::GetFrame(aMomentumDirection, aLastMomentumDirection);
         G4double cosPhi1 = nInteractionFrame * aPolarizationFrame;
         G4double Phi1 = std::acos(cosPhi1);

         G4double P2=.5*(3*cosTheta*cosTheta-1);
          G4double P22 = 0.0;
          if ( std::abs(aPolarization.mag() - 1.) < 1.e-6) {
           P22=3*(1-cosTheta*cosTheta);
          } else {
            P22= 0.0;
          }
            greject = 1 + F2*F2*(P2 + aParity*0.5*cos(2*Phi1)*P22);

         if (greject < 0 || greject > 1.5) {
          G4cout << " ERROR ::" << G4endl;
         }

       } while (greject < 1.5*G4UniformRand());
```

```cpp
   //  G4cout << "Last Momentum Direction (x,y,z,):" << aLastMomentumDirection << G4endl;

   return aLastMomentumDirection;
}


//----------------------------------------------------------------------//
void
NRFCrossSectionData::DumpPhysicsTable(const G4ParticleDefinition &)
{
  PrintLevelData();
}


//----------------------------------------------------------------------//
void NRFCrossSectionData::PrintLevelData()
{
  G4cout << "----- Material = " << theName << " ----- "<<G4endl;
  if (theLevelData->size() == 0) {
    G4cout << "*** Warning *** No level Data ";
    return;
  }
  for (G4int i = 0; i < G4int(theLevelData->size()) ; i++) {
    G4String aParity;
    if( theLevelData->at(i)->Parity > 0){
      aParity = "+";
    } else if ( theLevelData->at(i)->Parity < 0) {
      aParity ="-";
    } else {
      aParity = " ";
    }
    G4cout
      << i << ": Level(keV)= " << std::setw(5)<< theLevelData->at(i)->Excite/keV
      << " " << theLevelData->at(i)->Spin << aParity
      << ", Width(eV)= " << std::setw(5) << theLevelData->at(i)->Width / eV
      << ", CrossSection(ubarn MeV)= "
      << theLevelData->at(i)->CrossSection /microbarn /MeV
      << ", F2= " << theLevelData->at(i)->F2
      << G4endl;
  }
  G4cout << "---------------------------------------------- "<<G4endl;
}
////////////////////////////////////////////////////////////////////////////////////////
```

```cpp
// *****************************************************************
// GEANT4 physics class--> NRFCrossSectionData -- header file
// Created: N. Kikuzawa, Japan Atomic Energy Agency, 24-NOV-06
// The last update: N. Kikuzawa, JAEA, 24-NOV-06
// Modified by Hani Negm to include the angular distribution
// for the polarization effect.  2012 -2014
// *****************************************************************

#ifndef NRFCrossSectionData_h
#define NRFCrossSectionData_h 1
#include "G4VCrossSectionDataSet.hh"
#include "G4DynamicParticle.hh"
#include "G4Element.hh"

class MyLevelData {
public:
  G4double  Excite;
  G4double  Spin;
  G4int     Parity;
  G4double  Width;
  G4double  CrossSection;
  G4double  F2;

};

class NRFCrossSectionData : public G4VCrossSectionDataSet
{
public:

 NRFCrossSectionData(G4Element* anElement) // Constructor @@??
 {
//   verboseLevel = 1;
   Init(anElement);
 }

 ~NRFCrossSectionData() {}

 G4bool IsApplicable(const G4DynamicParticle* aParticle,
             const G4Element* anElement)
 {
  G4bool result = false;
  if( anElement->GetZ() == theZ && anElement->GetN() == theN)
   result = true;
  return result;
 }

 void Init(G4Element* anElement);

 G4double GetCrossSection(const G4DynamicParticle* aDynamicGamma,
             const G4Element* anElement=0,
             G4double T=0.);
```

185

```
  G4ThreeVector GetMomentumDirection( const G4DynamicParticle *aParticle) {
   return ComputeMomentumDirection(aParticle);
  };

  void BuildPhysicsTable(const G4ParticleDefinition&) {}

  void DumpPhysicsTable(const G4ParticleDefinition&);

  G4double  GetZ()   {return theZ;};
  G4double  GetN()   {return theN;};
  G4String  GetName() {return theName;};
  G4double  GetLastSpin()  {return theLastSpin;};
  G4int     GetLastParity() {return theLastParity;};

private:
  G4int    GetFunctions(G4double a, G4double* y, G4double* z);
  G4String  theName;
  G4double  theN;
  G4double  theZ;
  G4double  theLastCrossSection;
  G4double  theLastSpin;
  G4double  theGroundStateSpin;
  G4int     theLastParity;
  G4int     theGroundStateParity;
  G4ThreeVector theLastMomentumDirection;
  G4bool    hasCrossSectionData;

  typedef std::vector<MyLevelData*> LevelData;
  LevelData* theLevelData;

  void PrintLevelData();
  G4ThreeVector ComputeMomentumDirection(const G4DynamicParticle* aParticle);
  void SetVerboseLevel(G4int i) { verboseLevel = i; };
  G4int GetVerboseLevel() { return verboseLevel; };

};
#endif
/////////////////////////////////////////////////////////////////////////////////


// ***************************************************************
// GEANT4 physics class-->NRFCrossSectionDataStore: source file
// N. Kikuzawa, 05-Feb-07
// ***************************************************************

#include "NRFCrossSectionDataStore.hh"
#include "G4HadronicException.hh"

G4bool NRFCrossSectionDataStore::IsApplicable(
  const G4DynamicParticle* aDynamicGamma,
```

```cpp
  const G4Element* anElement)
{
  for (G4int i = NDataSetList-1; i >= 0; i--) {
    if (DataSetList[i]->IsApplicable(aDynamicGamma, anElement))
      return true;
  }
  return false;
}
//--------------------------------------------------------------------------//
G4double
NRFCrossSectionDataStore::GetCrossSection(
  const G4DynamicParticle* aDynamicGamma,
  const G4Element* anElement,
  G4double aTemperature
)
{
//  theLastMomentumDirection = aDynamicGamma->GetMomentumDirection();
  if (NDataSetList == 0)
  {
    throw G4HadronicException(__FILE__, __LINE__,
     "NRFCrossSectionDataStore: no data sets registered");
    return DBL_MIN;
  }
  for (G4int i = NDataSetList-1; i >= 0; i--) {
    if (DataSetList[i]->IsApplicable(aDynamicGamma, anElement)){
      G4double crossSection = DataSetList[i]->GetCrossSection(aDynamicGamma);
      return crossSection;
    }
  }
  throw G4HadronicException(__FILE__, __LINE__,
          "NRFCrossSectionDataStore: no applicable data set found "
          "for particle/element");
  return DBL_MIN;
}
//--------------------------------------------------------------------------//
G4ThreeVector NRFCrossSectionDataStore::GetMomentumDirection(
  const G4DynamicParticle* aDynamicGamma,
  const G4Element* anElement)
{
  G4double AtomicZ = anElement->GetZ();
  G4double AtomicN = anElement->GetN();
  G4ThreeVector aMomentumDirection = aDynamicGamma->GetMomentumDirection();

  for (G4int i = NDataSetList-1; i >= 0; i--) {
    if (DataSetList[i]->GetZ() == AtomicZ && DataSetList[i]->GetN() == AtomicN){
      aMomentumDirection = DataSetList[i]->GetMomentumDirection(aDynamicGamma);
      return aMomentumDirection;
    }
  }
  throw G4HadronicException(__FILE__, __LINE__,
          "NRFCrossSectionDataStore: no applicable data set found "
```

```
              "for particle/element");
//  theLastMomentumDirection = GetMomentumDirection();
  return aMomentumDirection;
}
//-----------------------------------------------------------------------//
void
NRFCrossSectionDataStore::AddDataSet(NRFCrossSectionData* aDataSet)
{
  DataSetList.push_back( aDataSet );
  NDataSetList++;
}
//-----------------------------------------------------------------------//
void
NRFCrossSectionDataStore::
BuildPhysicsTable(const G4ParticleDefinition& aParticleType)
{
  if ( NDataSetList > 0 ) {
    for (G4int i = 0; i < NDataSetList; i++) {
      DataSetList[i]->BuildPhysicsTable(aParticleType);
    }
  }
}
//-----------------------------------------------------------------------//
void
NRFCrossSectionDataStore::
DumpPhysicsTable(const G4ParticleDefinition& aParticleType)
{
  if (NDataSetList == 0) {
    G4cout << "WARNING - NRFCrossSectionDataStore::"
        <<"DumpPhysicsTable: no data sets registered"<<G4endl;
    return;
  }
  for (G4int i = NDataSetList-1; i >= 0; i--) {
    DataSetList[i]->DumpPhysicsTable(aParticleType);
  }
}
///////////////////////////////////////////////////////////////////////////////////

// ****************************************************************
// GEANT4 physics class-->NRFCrossSectionDataStore -- header file
// N Kikuzawa, JAEA, 29-JUN-09
// Class Description
// This is the class to which to register data-sets. You can get the instance
// from energy hadronic process, and use its 'AddDataSet(...)' method to tailor
// the cross-sections for your application.
// ****************************************************************

#ifndef NRFCrossSectionDataStore_h
#define NRFCrossSectionDataStore_h 1
```

```cpp
#include "G4ParticleDefinition.hh"
#include "G4DynamicParticle.hh"
#include "G4Element.hh"
#include "NRFCrossSectionData.hh"

class NRFCrossSectionDataStore
{
public:

  NRFCrossSectionDataStore() :
    NDataSetList(0), verboseLevel(0)
  {
  }
  ~NRFCrossSectionDataStore()
  {
  }
  G4double GetCrossSection(const G4DynamicParticle* aDynamicGamma,
              const G4Element* anElement, G4double aTemperature=0.);
/*
  G4double GetCrossSection(const G4DynamicParticle*,
              const G4Isotope*, G4double aTemperature);

  G4double GetCrossSection(const G4DynamicParticle*,
              G4double Z, G4double A, G4double aTemperature);
 // to replace GetMicroscopicCrossSection
  G4double GetCrossSection(const G4DynamicParticle*, const G4Material*);

*/
  G4bool IsApplicable( const G4DynamicParticle* aDynamicGamma,
              const G4Element* anElement);

  void AddDataSet(NRFCrossSectionData*);

  void BuildPhysicsTable(const G4ParticleDefinition&);

  void DumpPhysicsTable(const G4ParticleDefinition&);

  G4double GetLastSpin() { return theLastSpin;};
  G4int GetLastParity() { return theLastParity;};
  G4ThreeVector GetMomentumDirection( const G4DynamicParticle* aDynamicGamma,
                   const G4Element* anElement);

private:

  std::vector<NRFCrossSectionData*> DataSetList;
  G4int NDataSetList;
  G4int verboseLevel;

  G4double theLastCrossSection;
  G4ThreeVector theLastMomentumDirection;
  G4double theLastSpin;
```

```
  G4int theLastParity;
};

#endif
```
// ***
// ***
// ***

```
#===========================================
# Macro file for the initialization the NRF code
# and generate the LCS gamma ray beam
# Hani Negm_NRF_LCS_GPS
#===========================================

# Sets some default verbose
/control/verbose 1
/run/verbose 1
/tracking/verbose 0
/material/verbose 0
/process/verbose 0
/event/verbose 0

#===========================================
/NRF/phys/setCuts 100 um
/NRF/calor/setLowerEnergy 10 keV
/NRF/calor/update

#===========================================
# Set the histograms to the detector system
/histo/setHisto 01  2000  1.  2000. keV
/histo/setHisto 02  2000  1.  2000. keV
/histo/setHisto 03  2000  1.  2000. keV
/histo/setHisto 04  2000  1.  2000. keV
/histo/setHisto 05  2000  1.  2000. keV
/histo/setHisto 06  2000  1.  2000. keV
/histo/setHisto 07  2000  1.  2000. keV
/histo/setHisto 08  2000  1.  2000. keV

#===========================================
# LCS gamma ray beam

#/gps/source/intensity 1.

# Particle type
/gps/particle            gamma
#
# The beam energy is in Gaussian profile
/gps/ene/type            Gauss
/gps/ene/mono            1733 keV
/gps/ene/sigma           7.36 keV       # 1% (17.33 keV)
#
```

```
# The beam spot is centered at the origin and is
# of 1d gaussian shape with a xx mm
/gps/pos/type          Beam
/gps/pos/shape         Circle
/gps/pos/radius        10     mm
#/gps/pos/sigma_r      0.1    mm
/gps/pos/centre        -1.4  0  0  m
#
# The incident surface is in the y-z plane
/gps/pos/rot1          0. 1. 0.
/gps/pos/rot2          0. 0. 1.
#
# The beam is travelling along the x-axis with xx degrees dispersion
/gps/ang/rot1          0 0 1
/gps/ang/rot2          0 1 0
/gps/ang/type          beam1d
#/gps/ang/sigma_r      1. deg

/gps/polarization      0  1  0
#/gps/pos/paralp       90 deg

/histo/setFileName     data_file_name

# Integrated incident flux
/run/beamOn            2000000000     # 2E9
#
#==========================================
#          END – GOOD LUCK – H. NEGM
#==========================================
```

191

Bibliography

1. "Nuclear Technology Review 2012," *IAEA, VIENNA*, 2012.

2. "Nuclear Technology Review 2013," *IAEA, VIENNA*, 2013.

3. ATOMIC ENERGY ACT OF 1954, "An Act for the development and control of atomic energy," *Be it enacted by the Senate and House of Representatives of the United States of America in Congress assembled*.

4. J. Medalia, "North Korea's 2009 Nuclear Test: Containment, Monitoring, Implications," *Congressional Research Service* 7-5700, R41160, 2010.

5. Vladimir A. Orlov, "Illicit Nuclear Trafficking & the New Agenda," *Bulletin IAEA* 46/1, 2004.

6. "Isotope Explorer," *LBNL Nuclear Science Division*, 2003, website, http://ie.lbl.gov/ensdf/.

7. "Table of Isotopes," *LBNL Nuclear Science Division*, 2003, website, http://ie.lbl.gov/toi/.

8. W. Bertozzi, R. J. Ledoux, "Nuclear resonance fluorescence imaging in non-intrusive cargo inspection," *Nucl. Inst. Meth. Phys. Res. B*, vol. 241, pp. 820-825, 2005.

9. W. Bertozzi, S.E. Korbly, R.J. Ledoux, W. Park, "Nuclear resonance fluorescence and effective Z determination applied to detection and imaging of special nuclear material, explosives, toxic substances and contraband," *Nucl. Inst. Meth. Phys. Res. B,* vol. 261, pp. 331-336, 2007.

10. D.A. Close, L.A. Franks, S.M. Kocimski, "The application of thermal neutron capture gamma rays to matrix identification in a transuranic waste assay system based on an electron accelerator," *Nucl. Inst. and Meth. in Phys. Res. A*, vol. 220, pp. 531-536, 1984.

11. M. Haruyama, M. Takase, H. Tobita, "Improvement of Detection Limit in 14 MeV Neutron Direct Interrogation Method by Decreasing Background," *J. Nucl. Sci. Technol.*, vol. 45, pp. 432-440, 2008.

12. J. Pruet, D.P. McNabb, C.A. Hagmann, F.V. Hartemann, C.P.J. Barty, "Detecting clandestine material with nuclear resonance fluorescence," *J. Appl. Phys.*, vol. 99, pp. 123102(1-11), 2006.

13. H. Ohgaki, H. Toyokawa, K. Kudo, N. Takeda, T. Yamazaki, "Generation and application of laser-Compton gamma-ray at ETL," *Nucl. Inst. Meth. Phys. Res. A*, vol. 455, pp. 54-59, 2000.

14. F.V. Hartemann, W.J. Brown, D.J. Gibson, S.G. Anderson, A.M. Tremaine, P.T. Springer, A.J. Wootton, E.P. Hartouni, C.P. Barty, "High-energy scaling of Compton scattering light sources," *Phys. Rev. ST Accel. Beam*, vol. 8, pp. 100702(1-17), 2005.

15. K. Kawase, M. Kando, T. Hayakawa, I. Daito, S. Kondo, T. Homma, T. Kameshima, H. Kotaki, L.M. Chen, Y. Fukuda, A. Faenov, T. Shizuma, M. Fujiwara, S. V. Bulanov, T. Kimura, T. Tajima, "Sub-MeV tunably polarized X-ray production with laser Thomson backscattering," *Rev. Sci. Instrum.*, vol. 79, pp. 053302(1-8), 2008.

16. H. Ohgaki, T. Kii, K. Masuda, R. Hajima, T. Hayakawa, T. Misawa, P. Cheol-Ho; T. Shizuma, K. Kawase, M. Kando, H. Toyokawa, "Conceptual Design of a Nuclear Material Detection System Based on the Neutron / Gamma-ray Hybrid Approach," *Proc. of IEEE HST 2010*, pp. 525-529, 2010.

17. H. Ohgaki, T. Kii, K. Masuda, M. Omer, T. Misawa, C. H. Pyeon, R. Hajima, T. Hayakawa, T. Shizuma , M. Kando, I. Daito, H. Toyokawa, "Proposal of a Non-Destructive Detection System for Hidden Nuclear Materials Based on a Neutron/Gamma-ray Hybrid System," *J. of the Korean Physical Society*, vol. 59, no. 5, pp. 3155-3159, 2011.

18. H. Ohgaki, M. Omer, H. Negm, T. Hori, T. Kii, Kai Masuda, M. Kando, I. Daito, T. Misawa, C. Pyeon, S. Fujimoto, R. Hajima, T. Hayakawa, T. Shizuma, M. Fujiwara, F. Sakai, S. Hee Park, "Non-destructive inspection system for special nuclear material using inertial electrostatic confinement fusion neutrons and Laser Compton Scattering Gamma-rays," *Proc. of IEEE HST 2012*, pp. 666-671, 2012.

19. R.L. Hirsch, "Inertial-Electrostatic Confinement of Ionized Fusion Gases," *J. Appl. Phys.*, vol. 38, pp. 4522-4534, 1967.

20. G.H. Miley, L. Wu, H.J. Kim, "IEC-based neutron generator for security inspection system," *J. Radioanal. Nucl. Chem.*, vol. 263, pp. 159–64, 2005.

21. F.R. Metzger, "Resonance Fluorescence in Nuclei," *Prog. in Nuc. Phys.*, vol. 7, pp. 54-88, 1959.

22. U. Kniessl, H.H. Pitz, A. Zilges, "Investigation of nuclear structure by resonance fluorescence scattering," *Prog. Part. Nucl. Phys.*, vol. 37, pp. 349-433, 1996.

23. N. Kikuzawa, R. Hajima, N. Nishimori, E. Minehara, T. Hayakawa, T. Shizuma, H. Toyokawa, H. Ohgaki, "Nondestructive Detection of Heavily Shielded Materials by Using Nuclear Resonance Fluorescence with a Laser-Compton Scattering γ-ray Source," *Appl. Phys. Express*, vol. 2, pp. 036502(1-3), 2009.

24. J.H. Hubbell, "Photon Cross Sections, Attenuation Coefficients, and Energy Absorption Coefficients From 10 keV to 100 GeV," *NSDRS-NBS 29*, pp. 1-85, 1969.

25. J.H. Hubbell, W.J. Veigele, E.A. Briggs, R.T. Brown, D.T. Cromer, R.J. Howerton, "Atomic Form Factors, Incoherent Scattering Functions, and Photon Scattering Cross Sections," *J. Phys. Chem. Ref. Data* 4, pp. 471-616, 1975.

26. J.H. Hubbell, "Polarization Effects in Coherent and Incoherent Photon Scattering: Survey of Measurements and Theory Relevant to Radiation Transport Calculations," *NISTIR* 4881, 1992.

27. J.H. Hubbell, "Bibliography and Current Status of K, L, and higher Shell Fluorescence Yields for Computations of Photon Energy-Absorption Coefficients," *NISTIR* 89-4144, 1994.

28. J.H. Hubbell, "Tables of X-ray Mass Attenuation Coefficients and Mass Energy-Absorption Coefficients 1 keV to 20 MeV for Elements $Z=1$ to 92 and 48 Additional Substances of Dosimetric Interest," *NISTIR* 5632, 1995.

29. J.H. Hubbell, "An Examination and Assessment of Available Incoherent Scattering S-Matrix Theory, also Compton Profile Information, and Their Impact on Photon Attenuation Coefficient Compilations," *NISTIR* 6358, 1999.

30. H. Hirayama, "Photon Interactions and Cross Sections," *Advanced Monte Carlo on Radiation Physics, Particle Transport Simulation and Applications* 2000.

31. E. Frytag, "Strahlenschutz an hochenergiebschleunigern," (G. Braum, Karlsruhe, 1072).

32. O. Klein and Y. Nishina, "Ueber die Streuung von Strahlung durch freie Elektronen nach der neuen relativistischen Ouantenelektrodynamik von Dirac," *Z. Physik*, vol. 52, pp. 853-868, 1929.

33. R.D. Evans, "Compton Effect," *Corpuscles and Radiation in Matter II, Springer Berlin Heidelberg*, vol. 6/34, pp. 218-298, 1958.

34. L.J. Curtis, "Atomic Structure and Lifetimes: A Conceptual Approach," *Cambridge University Press*, ISBN-IO O-521-53635-9, 2003.

35. D.J. Griffiths, "Introduction to Quantum Mechanics," *Prentice-Hall*, p. 155. ISBN 0-13-124405-1, 1995.

36. W. Heitler, "The Quantum Theory of Radiation," *Oxford Univ. Press, Oxford*, 1954.

37. P.P. Kane, L. Kissel, R.H. Pratt, S.C. Roy, "Elastic scattering of γ-rays and X-rays by atoms," *Physics Reports*, vol. 140, pp. 75-159 1986.

38. ICRU Report 33, "Radiation Quantities and Units," *International Commission on Radiation Units and Measurements*, Washington D.C. USA issued 15 April, pp. 25, 1980.

39. W.E. Lamb, "Capture of Neutrons by Atoms in a Crystal," *Phys. Rev.*, vol. 55, pp. 190–197, 1939.

40. L.W. Fagg, S.S. Hanna, "Polarization measurements on nuclear gamma rays," *Rev. Mod. Phys.*, vol. 31, pp. 711-758, 1959.

41. K. Siegbahn, "α, β, γ – Spectroscopy," *North Holland, Amsterdam*, 1965.

42. A.H. Wapstra, G.J. Nigh, R. van Lieshout, "Nuclear Spectroscopy Tables," *North Holland, Amsterdam*, 1959.

43. H. Negm, M. Omer, R. Kinjo, Y.W. Choi, K. Yoshida, H. Zen, T. Hori, T. Kii, K. Masuda, H. Ohgaki, "Monte Carlo Calculations of γ-rays Angular Distribution Scattering from [11]B in (γ, γ) Interaction," *Zero-Carbon Energy Kyoto 2012 Springer Japan*, Chapter 21, pp. 197-203, 2013.

44. H. Negm, M. Omer, H. Zen, T. Kii, K. Masuda, T. Hori, H. Ohgaki, R. Hajima, N. Kikuzawa, T. Shizuma, T. Hayakawa, I. Daito, H. Toyokawa, "Optimization of Geometric Configuration of Detector System for Non-destructive Assay Using Nuclear Resonance Fluorescence Technique With Laser Compton Backscattering," *Proc. of IEEE NSS/MIC 2013*, pp. 1-4, 2013.

45. S. Agostinelli et al., "Geant4 – a simulation toolkit," *Nucl. Inst. Meth. Phys. Res. A*, vol. 506, pp. 250-303, 2003.

46. J. Allison et al., "Geant4 Developments and Applications," *IEEE TNS*, vol. 53 (1), pp. 270-278, 2006.

47. Geant4: website, Geant4 10.0: Physics Reference Manual 2013, and Geant4 10.0: Application Developers Guide 2013, http://geant4.cern.ch, http://geant4.web.cern.ch/geant4/UserDocumentation/UsersGuides/PhysicsReferenceManual/fo/PhysicsReferenceManual.pdf, and http://geant4.web.cern.ch/geant4/UserDocumentation/UsersGuides/ForApplicationDeveloper/html/index.html

48. T. Hayakawa, N. Kikuzawa, R. Hajima, T. Shizuma, M. Seya, H. Ohgaki, K. Toshiteru, M. Omer, M. Fujiwara, "Development of simulation code for NDA using nuclear resonance fluorescence with laser Compton scattering gamma-rays," *Proc. of INMM 52th Annual Meeting 2011*, pp. 17-21, 2011.

49. J.A. Bearden, A.F. Burr, "Reevaluation of X-Ray Atomic Energy Levels," *Rev. Mod. Phys.*, vol. 39, pp. 125-142, 1967.

50. H.R. Weller, M.W. Ahmed, H. Gao, W. Tornow, Y.K. Wu, M. Gai, and R. Miskimen, "Research opportunities at the upgraded HIγS facility," *Prog. Part. Nucl. Phys.*, vol. 62, 257-303, 2009.

51. W. Bertozzi, J.A. Caggiano, W.K. Hensley, M.S. Johnson, S.E. Korbly, R.J. Ledoux, D.P. McNabb, E.B. Norman, W.H. Park, and G.A. Warren, "Nuclear resonance fluorescence excitations near 2 MeV in U^{235} and Pu^{239}," *Phys. Rev. C*, vol. 78, pp. 041601(1-5), 2008.

52. E. Kwan, G. Rusev, A.S. Adekola, F. DoÅNnau, S.L. Hammond, C.R. Howell, H.J. Karwowski, J.H. Kelley, R.S. Pedroni, R. Raut, A.P. Tonchev, W. Tornow, "Discrete deexcitations in ^{235}U below 3 MeV from nuclear resonance fluorescence," *Phys. Rev. C*, vol. 83, pp. 041601(1-5), 2011.

53. O. Yevetska, J. Enders, M. Fritzsche, P. von Neumann-Cosel, S. Oberstedt, A. Richter, C. Romig, D. Savran, K. Sonnabend, "Dipole strength in the ^{235}U(γ, γ) reaction up to 2.8 MeV," *Phys. Rev. C*, vol. 81, 044309(1-6), 2010.

54. H. Negm, I. Daito, H. Zen, T. Kii, K. Masuda, T. Hori, H. Ohgaki, R. Hajima, T. Shizuma, T. Hayakawa, H. Toyokawa, "A Study of the nuclear resonance fluorescence reaction yield dependence on the target thickness of ^{208}Pb," *Proc. of NPNSNP 2014, World Scientific proceeding*, *to be published*.

55. H. Negm, H. Ohgaki, I. Daito, T. Hayakawa, H. Zen, T. Kii, K. Masuda, T. Hori, R. Hajima, T. Shizuma, N. Kikuzawa, "Reaction yield dependence of the (γ, γ') reaction of ^{238}U on the target thickness," *J. Nucl. Sci. Technol*. 2014, http://dx.doi.org/10.1080/00223131.2014.980348.

56. H. Negm, M. Omer, H. Zen, I. Daito, T. Kii, K. Masuda, T. Hori, H. Ohgaki, R. Hajima, T. Hayakawa, T. Shizuma, N. Kikuzawa, H. Toyokawa, "Monte Carlo Simulation of Response Function for LaBr$_3$(Ce) detector and Its Internal-Activity," *Proc. of IEEE ANIMMA 2013*, 1-5, 2013.

57. W. Bertozzi, R. Ledoux, "Nuclear resonance fluorescence imaging in non-intrusive cargo inspection," *Nucl. Inst. Meth. Phys. Res. B*, vol. 241, pp. 820-825, 2005.

58. R. Hajima, T. Hayakawa, N. Kikuzawa, E. Minehara, "Proposal of Nondestructive Radionuclide Assay Using a High-Flux Gamma-Ray Source and Nuclear Resonance Fluorescence" *J. Nucl. Sci. Technol.*, vol. 45, pp. 441-450, 2008.

59. T. Hayakawa, H. Ohgaki, T. Shizuma, R. Hajima, N. Kikuzawa, E. Minehara, T. Kii, H. Toyokawa, "Nondestructive detection of hidden chemical compounds with laser Compton-scattering gamma ray," *Rev. Sci. Instrum.*, vol. 80, pp. 045110(1-5), 2009.

60. T. Hayakawa, N. Kikuzawa, R. Hajima, T. Shizuma, N. Nishimori, M. Fujiwara, M. Seya, "Nondestructive assay of plutonium and minor

actinide in spent fuel using nuclear resonance fluorescence with laser Compton scattering γ-rays," *Nucl. Inst. Meth. Phys. Res. A,* vol. 621 (1-3), pp. 695-700, 2010.

61. E.V.D. van Loef, P. Dorenbos, C.W.E. van Eijk, K. Kramer, H.U. Gudel, "High-energy-resolution scintillator: Ce^{3+} activated $LaBr_3$," *Appl. Phys. Lett.*, vol. 79, pp. 1573-1575, 2001.

62. E.V.D. van Loef, P. Dorenbos, C.W.E. van Eijk, K Krämer, H.U. Güdel, "cintillation properties of $LaBr_3$:Ce^{3+} crystals: fast, efficient and high-energy-resolution scintillators." *Nucl. Inst. Meth. Phys. Res. A*, vol. 486, pp. 254-258, 2002.

63. M. Omer, H. Negm, H. Ohgaki, I. Daito, T. Hayakawa, M. Bakr, H. Zen, T. Hori, T. Kii, K. Masuda, R. Hajima, T. Shizuma, H. Toyokawa, N. Kikuzawa, "Analysis of nuclear resonance fluorescence excitation measured with $LaBr_3$(Ce) detectors near 2 MeV" *Nucl. Inst. Meth. Phys. Res. A*, vol. 729, pp. 102-107, 2013.

64. M. Omer, H. Negm, H. Zen, I. Daito, T. Kii, K. Masuda, H. Ohgaki, R. Hajima, T. Shizuma, T. Hayakawa, N. Kikuzawa, "Nuclear Resonance Fluorescence of ^{235}U Measured with High-Resolution $LaBr_3$(Ce) Scintillation Detectors," *Jpn. J. Appl. Phys.*, vol. 52 (10), pp. 106401(1-4), 2013.

65. A.A. Sonzogni, "Nuclear Data Sheets for A = 138," *Nuclear Data Sheets* vol. 98 (3), 515-664, 2003.

66. J.K. Hartwell, R.J. Gehrke, "Observations on the background spectra of four $LaCl_3$(Ce) scintillation detectors," *App. Radiat. Isot.*, vol. 63 (2), pp. 223-228, 2005.

67. B. Milbrath, R. Runkle, T. Hossbach, W. Kaye, E. Lepel, B. McDonald, L. Smith, "Characterization of alpha contamination in lanthanum trichloride

scintillators using coincidence measurements," *Nucl. Inst. Meth. Phys. Res. A*, vol. 547 (2-3), pp. 504–510, 2005.

68. R. Nicolini, F. Camera, N. Blasi, S. Brambilla, R. Bassini, C. Boiano, A. Bracco, F. Crespi, O. Wieland, G. Benzoni, "Investigation of the properties of a 1"x1" LaBr$_3$:Ce scintillator," *Nucl. Inst. Meth. Phys. Res. A*, vol. 582 (2), pp. 554–561, 2007.

69. Radioactive decay in GEANT4,
http://www.space.qinetiq.com/geant4/rdm

70. J.K. Tuli, "ENSDF: Evaluated Nuclear Structure Data File," *Brookhaven National Lab Report*, BNL-NCS-51655-01/02-Rev, 2001.

71. R. Brun, F. Rademakers, "ROOT - An object oriented data analysis framework," *Nucl. Inst. Meth. Phys. Res. A*, vol. 389, pp. 81-86, 1997. See also http://root.cern.ch/.

72. M. Ciemata, D. Balabanski, M. Csatlos, J.M. Daugas, G. Georgiev, J. Gulyas, M. Kmiecik, A. Krasznahorkay, S. Lalkovski, A. Lefebvre-Schuhl, R. Lozeva, A. Maj, A. Vitez, "Measurements of high-energy g-rays with LaBr3 : Ce detectors," *Nucl. Inst. Meth. Phys. Res. A*, vol. 608, 76-79, 2009.

73. G.F. Knoll, "Radiation Detection and Measurement," *Wiley, New York*, 2000.

74. S. Miyamoto, Y. Asano, S. Amano, D. Li, K. Imasaki, H. Kinugasa, Y. Shoji, T. Takagi, T. Mochizuki, "Laser Compton back-scattering gamma-ray beamline on NewSUBARU," *Radiation Measurements*, vol. 41, S179–S185, 2007.

75. C.G. Ryan, E. Clayton, W.L. Griffin, S.H. Sie, D.R. Cousens, "SNIP, a statistics-sensitive background treatment for the quantitative analysis of PIXE spectra in geoscience applications" *Nucl. Inst. Meth. Phys. Res. B*, vol. 34, pp. 396-402, 1988.

76. M. Morháč, J. Kliman, V. Matoušek, M. Veselský, I. Turzo, "Background elimination methods for multidimensional gamma-ray spectra," *Nucl. Inst. Meth. Phys. Res. A*, vol. 401, pp. 113-132, 1997.

77. D.D. Burgess, R.J. Tervo, "Background estimation for gamma-ray spectroscopy," *Nucl. Inst. Meth. Phys. Res. A*, vol. 214, pp. 431-434, 1983.

78. B.J. Quiter, B.A. Ludewigt, V.V. Mozin, C. Wilson, S. Korbly, "Transmission nuclear resonance fluorescence measurements of ^{238}U in thick targets," *Nucl. Inst. Meth. Phys. Res. B*, vol. 269, pp. 1130–1139, 2011.

79. ENSDF: Evaluated Nuclear Structure Data File, http://www.nndc.bnl.gov/useroutput/AR_8B40BC15B5AF5D6D865E7A25FE4CAF6C_1.html

80. S.L. Hammond, A.S. Adekola, C.T. Angell, H.J. Karwowski, E.Kwan, G. Rusev, A.P. Tonchev, W. Tornow, C.R. Howell, J.H. Kelley "Dipole response of ^{238}U to polarized photons below the neutron separation energy," *Phys. Rev. C*, vol. 85, pp. 044302(1-12), 2012.

81. M.J. Berger, J.H. Hubbell, S.M. Seltzer, J. Chang, J.S. Coursey, R. Sukumar, D.S. Zucker, "XCOM: Photon Cross Sections Database, NIST Standard Reference Database 8 (XGAM)," available online at http://physics.nist.gov/PhysRefData/Xcom/Text/XCOM.html.

82. D.E. Cullen, J.H. Hubbell, L. Kissel, "EPDL97: the Evaluated Photon Data Library, '97 Version," *UCRL-504000*, vol. 6, Rev. 5, 1997.

83. C. Kittel, "Introduction to Solid State Physics," *7th edition. John Wiley Sons, Inc. New York*, Chapter 5, 1996.

Publication List

I. Peer reviewed publications in scientific journals or international conference:

1. H. Negm et al., "A Study of the nuclear resonance fluorescence reaction yield dependence on the target thickness of ^{208}Pb," *Proc. of NPNSNP 2014, World Scientific proceeding*, *to be published*.

2. H. Negm et al., "Reaction yield dependence of the (γ, γ') reaction of ^{238}U on the target thickness," *J. Nucl. Sci. Technol*. 2014. http://dx.doi.org/10.1080/00223131.2014.980348

3. H. Negm et al., "Study on Detector Geometry for Active Non-destructive Inspection System of SNMs by Nuclear Resonance Fluoresce," *Proc. of IEEE HST 2014, Submitted*.

4. H. Negm et al., "Energy response function of a LaBr$_3$:Ce detector using GEANT4 and the feasibility of using LaBr$_3$:Ce in a nuclear materials assay," *Nucl. Instru. Meth Phys. Res. A*, *Submitted*.

II. Peer reviewed publications as chapter in book:

5. H. Negm et al., "Monte Carlo Calculations of γ-rays Angular Distribution Scattering from 11B in (γ, γ) Interaction," *Zero-Carbon Energy Kyoto 2012 Springer Japan*, Chapter 21, pp. 197-203, 2013.

III. International conference proceedings:

6. H. Negm et al., "Monte Carlo Simulation of Response Function for LaBr$_3$(Ce) detector and Its Internal-Activity," *2013 IEEE 3rd International conference on Advancements in Nuclear Instrumentation Measurement Methods and their Applications* (*ANIMMA*), Marseille, France, 23-27 June 2013, pp. 1-5.

7. H. Negm et al., "Optimization of Geometric Configuration of Detector System for Non-destructive Assay Using Nuclear Resonance Fluorescence Technique With Laser Compton Backscattering," *2013 IEEE Nuclear Science Symposium and Medical Imaging Conference* (*NSS/MIC*), Seoul, Korea, 27 Oct. – 2 Nov. 2013, pp. 1-4.

IV. Oral/Poster presentation in international conference or domestic meetings:

8. H. Negm et al., "Geant4 Simulation of Nuclear Resonance Fluorescence from ^{11}B," *2012 IEEE Symposium on Radiation Measurements and Applications* (*SORMA*), Oakland, San Francisco, California, USA, 14-17 May 2012.

9. H. Negm et al., "Monte-Carlo Simulation of Nuclear Resonance Fluorescence in GEANT4," *2012 4th International Symposium of Energy Science in the Age of Global Warming of the Kyoto University Global COE Program and the JGSEE/CEE-KMUTT*, Bangkok, Thailand, 21-22 May 2012.

10. H. Negm et al., "A Study Of The Nuclear Resonance Fluorescence Reaction Yield Dependence On The Target Thickness Of Special Nuclear

Materials," *Atomic Energy Society of Japan Spring Meeting*, Kinki University, Osaka, Japan, 26-28 Mar. 2013.

11. H. Negm et al., "Monte Carlo Simulation Of Nuclear Resonance Fluorescence in light of Laser-Compton Scattering γ-Ray Source." *Atomic Energy Society of Japan Fall Meeting*, Hachinohe Institute of Technology, Aomori, Japan, 3-5 Sep. 2013.

12. H. Negm et al., "Study on Target Thickness Dependence on NRF Yield for ^{208}Pb at 7332 keV," *Atomic Energy Society of Japan Spring Meeting*, Tokyo City University, Tokyo, Japan, 26-28 Mar. 2013.

13. H. Negm et al., "Thickness Dependence on the NRF Yield for U-238," *Atomic Energy Society of Japan Fall Meeting*, Kyoto University, 8-10 Sep. 2014.